Collagen remnants in ancient bone

Thesis submitted in accordance with the requirements of the University of Liverpool for the degree of Doctor in Philosophy

by Brian Daniel Thomas

October 2018

List of contents

Acknowledgements

This work would have proved impossible without the guidance and encouragement of handfuls of helpers. The following individuals proved especially generous. Foremost, my mother Jane Thomas taught me to write well, inculcated an appreciation for science, and along with my father Col. Stanley Thomas, stimulated excellence in work and life. If forced to dedicate this thesis to just one person, it would be my mom. My wife Michele has likewise offered unwavering and vital encouragement throughout the entire research and writing process, as have our children Semper, Salah, Abby, Noah, and Verity. Next, I could not imagine a better supervising professor than Professor Stephen Taylor, without whose expertise, encouragements and practical suggestions not one word of this thesis would have been penned.

Dr. Kate Luby-Phelps and Abhi Bugde trained me on the confocal microscope used to produce the images shown in Chapter 3. Dr. Ethan McBride guided me in FTIR instrumentation for Chapter 4. Dr. Kevin Anderson did some heavy lifting to achieve the results in Chapter 5. My cohort at the University of Liverpool Dave McIntosh contributed key arguments in Chapter 6. Hugo Miller conveyed data used in Chapters 6 and 7. In addition, several generous research supporters wish to remain unnamed. Dr. Bea Clack taught me the three P's: patience, perseverance, and persistence. Finally, each coauthor named in Appendix 3.1 played an important role in the publication of our key *Bone Reports* paper.

Abstract

Ancient bone collagen retains valuable information. Radiocarbon dating, thermal dating, species identification, cladistics analyses, and paleodietary reconstruction efforts all use bone collagen from ancient samples. Experimentally derived models of the temperature-dependent collagen half-life and thus of collagen's expected shelf life under optimum preservation conditions currently stand at odds with literature reports of collagen remnants in bones with great apparent ages. These issues cause debate about bone collagen longevity. The situation highlights a need to better understand bone collagen preservation conditions and thus to apply new analytical tools to ancient and modern bone samples. In response, this study applies established techniques to ancient bone for the first time. Appropriate samples of ancient bone were first collected and catalogued. They include specimens ranging from Medieval to Paleozoic settings and involve partnerships with six permanent repositories.

This thesis describes the novel application of second-harmonic generation (SHG) imaging, an established technique in biomedical science, to ancient bone. In this study, four separate and independent techniques confirmed that SHG reliably detects trace amounts of collagen protein in certain Medieval and Ice Age bone samples. Additional results indicate that SHG detects faint traces of collagen in unexpectedly old bone samples, including dinosaur bones. The technique demonstrated a high degree of sensitivity to small amounts of collagen, plus the potential to explore the micromorphology of collagen decay in bone and other collagenous tissues.

The second novel application was Fourier-transform infrared (FTIR) spectroscopy. Recent studies demonstrated its usefulness for bone collagen content estimates in forensic analyses of bone remains. This study extended its application to Medieval, Ice Age, Cretaceous, Jurassic, and Devonian samples and found a general trend of diminishing

collagen signal with older bones. FTIR was also used for the first time to assess bone collagen integrity in an artificial decay experiment. In addition, the applicability of Raman spectroscopy to ancient bone was explored.

Accelerator mass spectrometry (AMS) was also used to measure stable and unstable carbon ratios in many of the same ancient bone samples used above. AMS ^{13}C results brought forth two main conclusions. They confirmed the accuracy of preliminary results obtained using a recently developed portable quadrupole mass spectrometer (QMS) to detect stable isotopes including ^{13}C and ^{12}C ratios from the bioapatite fraction of Medieval bone. They also confirm for the first time a co-occurrence of primary (i.e., original to the organism) isotopic signatures in fossil bones with primary organic signatures. Analysis of published Cretaceous vertebrate fossils with biological stable isotope ratios matched this co-occurrence. Finally, the first AMS ^{14}C results from Cretaceous bone collagen are presented. ^{14}C results discriminated between modern, medieval, Roman era, and ice age, but not between Cretaceous and Jurassic time frames. Overall results suggest that the application of novel techniques like SHG will help detect and further characterise ancient bone collagen. Also, low cost, nearly nondestructive tools like FTIR and QMS show promise to aid continued discoveries of original isotope ratios and biological remnants like bone collagen in fossils from widening geographic and geological ranges.

Chapter 1: On ancient bone collagen and other biochemicals in fossils

Contents

Figures

Tables

Bone structure

This thesis describes new uses of established techniques, and progress on instrumentation development, to examine ancient bone proteins. A proper understanding of ancient bone begins with structure. Bone is the defining connective tissue of all vertebrates. It consists of living cells such as osteocytes and their interconnected dendritic processes, blood vessels and blood cells, plus extensive extracellular matrix. Precisely arranged proteins combine with calcium hydroxyapatite ("bioapatite" or "apatite") to account for the rigidity and flexibility of bone. Overall, about 40% of the dry weight of bone is organic and 60% inorganic[1].

The collagen family of proteins comprises 90% the total organics of bone. It contains a high content of glycine, proline, and hydroxyproline, usually in a repeated -gly-pro-hypro-gly- pattern[2]. This arrangement of relatively small residues permits the coiled architecture of each subunit. The flexibility of this fibrous biomolecule provides bone its resilience, while bone rigid structure of the biomineral components provides compressive resistance[3]. Less abundant bone matrix proteins include osteocalcin, a protein hormone involved in signaling bone tissue growth via osteoblast activity.

Collagen occurs in over a dozen types, each suited to a structural requirement of a particular tissue or organ. Most types are non-fibrillar. The more common fibrillar types take on long, rope-like molecular conformations in tough connective tissue like bone, and include Types I, II, III, V, and X. Type I collagen fibres are the most abundant in skin, tendon, vessels, organ cortices, and fresh bone, comprise over 90% of all collagens in the human body (and is a characteristic feature of vertebrates in general), and range from 0.5-3µm thick[4]. One fibre consists of about a dozen packaged fibrils, each ranging from 10-300nm. One fibril contains many tropocollagen assemblies, each made of three parallel, crosslinked, triple helical subunits. Each Type I tropocollagen typically consists of two

identical strands (α1) hydrogen-bonded and cross-linked to a third chemically different strand (α2). During bone construction, osteoblasts generate and interweave bioapatite crystals within and around exported collagen fibres, illustrated in Fig. 1.1. Bone bioapatite crystallites take the shape of flattened rods of roughly 30Å X 400Å[5]. Collagen's abundance, insolubility in water and hence longevity, and ease of separation from bone by acid dissolution of biominerals have made it an ideal bone component for radiocarbon and stable isotope analysis[6] as well as protein sequencing for species identification in archaeological settings[7].

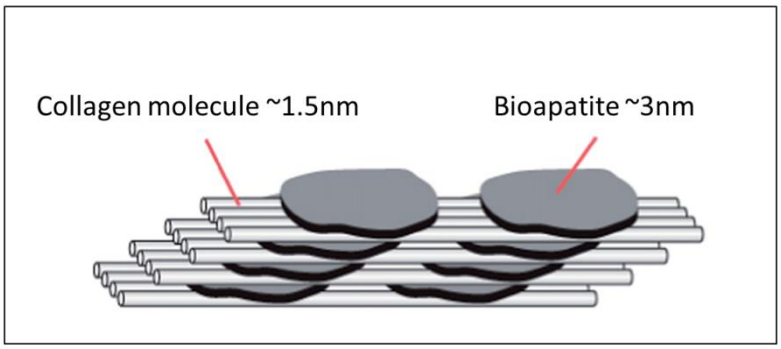

Figure 1.1 | Bone biomineral and collagenous microstructure.

Bone diagenesis

Models of bone decay *post mortem* that assume an absence of microbial biodegradation suggest that tropocollagen helices undergo chemical reactions including glycation, oxidation and hydrolysis as they decay into smaller components (e.g., amino acids, carbon dioxide, ammonia, etc.) that then disperse. Collagen fibres fray from either end, where exposure favors reactivity. In principle, the tight packing of adjacent apatite crystals hinders reactivity and preserves bone collagen[8]. Collagen fibers can interact with surrounding material, but do so under different conditions than bioapatite. Under conditions where collagen decays first, bioapatite crystals quickly disorganize and bone

quickly turns to dust. Similarly, if bioapatite undergoes dissolution before collagen decays, then its dispersal exposes collagen more readily to chemical reactants, again hastening whole bone decay. Ideal conditions for bone preservation thus dampen both the organic and inorganic decay processes. These conditions include a constant low temperature, a uniform, low hydration level with restricted percolation, and near-neutral pH. Extremes in pH react with, help solubilize, and thus hasten collagen decay[9]. Therefore, each broad setting, and even microsite variations that can occur within feet of one another in a single setting, brings its unique set of chemical, thermal, mineral, biological, pH and other conditions to bear on the complicated array of possible diagenetic fates for bone and thus bone collagen.

Field and lab observations suggest that upon deposition, any bone collagen that escapes scavenging and biodegradation decays rapidly at first, then slows to a more linear decay regime[10]. Such studies model bone collagen decay using ideal conditions, such as near-neutral pH, near sterility, and constant hydration. Even under less than ideal conditions, archaeological bone can still retain sufficient collagen for radiocarbon dating, stable isotope analysis, thermal (collagen) dating[9], and even species identification via collagen sequencing. However, paleontological (fossil) bone does not often retain sufficient collagen to relay any of those types of biological information. Recent research reviewed in detail below shows a surging interest in how long bone and bone collagen can possibly last, how long it has actually lasted, and what conditions underlie collagen longevity.

Collagen decay

The decay rate of bone collagen under ideal conditions has been well characterised experimentally. Its energy of activation (*Ea*) of 173 kJ/mol equates to a half-life of 130 ka

at 7.5°C[11,12]. Typical experiments use a two-step strategy to determine the decay rates of various proteins, including collagen. First, elevated temperatures are used to accelerate bone collagen decay, typically in a sealed glass vial. Three different experimental temperatures are required to construct an Arrhenius plot. Molecular decay is measured by various means including protein extraction and weighing, protein extraction and SDS-PAGE analysis, or protein content estimation using immunofluorescence. Each technique essentially delivers a fraction or percent protein remaining at certain time points during the typically four to eight week-long experiment. The resulting data are then plotted as the natural log of the percent remaining (or concentration of reactant) versus time in days for each of three temperatures. The slopes, obtained via linear regression analysis, are then used to calculate decay constants (k) for each temperature, using: k = -[slope].

The three resulting k values, one for each of three tested temperatures, are then plotted in a second logarithmic curve, the Arrhenius plot. It shows the natural log of each decay constant, ln(k) versus the inverse temperature, 1/T. The slope of the line of best fit through those three points is used to obtain the two unknown variables in the Arrhenius equation, namely E_a and A. E_a is the activation energy, and A is a pre-exponential factor unique to each reaction and relates in part to frequency of collisions between reactants. The slope of the Arrhenius plot equals $-E_a/R$, with R being the gas constant, 8.31446 J/(mol·K). The y-intercept of the slope from that same Arrhenius plot equals ln(A). Finally, with all variables of the Arrhenius known, a form of the Arrhenius equation is then solved algebraically for the rate constant k at any given temperature.

The Arrhenius equation relates chemical reaction rates to energy (in this case thermal) of the system. In the Arrhenius equation,

$$k = Ae^{-\mathrm{Ea}/(\mathrm{RT})} \qquad \text{Equation 1}$$

k is the rate constant, T is the absolute temperature, *A* is an experimentally determined constant related to total number of molecular collisions as noted above. The other variables are described above. The expression $e^{-Ea/(RT)}$ estimates the fraction of collisions leading to chemical reactions, where *e*= 2.718 (the base of natural logarithms).

The decay constant *k* for any reaction, like the decay of collagen, that undergoes a first order logarithmic decay and is unique to a given temperature can be expressed in terms of a half-life using:

$$t½ = \ln(2)/k \qquad \text{Equation 2}$$

The activation energy *Ea* for the decay of collagen, and biomolecules in general, remains constant, whereas the rate constant (and hence half-life) varies with temperature. An average annual temperature for the history of a buried bone is substituted for T in the Arrhenius equation (Equation 1) in order to calculate a decay rate estimate for that temperature. Buckley *et al* (2008) used 7.5°C, the average annual temperature of regions in Montana where collagen has been recovered and sequenced from dinosaur bone[11]. However, those dinosaur-containing sediments captured swamp-like flora and fauna that represent higher past temperatures[13]. Colder temperatures afford fewer molecular collisions, which equate to fewer chemical reactions and higher fidelity protein preservation.

Collagen decay rate experimental results build a temporal expectation that restricts bone collagen to archaeological time frames, yet many reports of collagen and other proteins in older-than-archaeological samples have sprinkled the paleontological literature for decades. Tension between the expectation of lability and observations of longevity has fueled steady debate over the veracity of original biochemistry remnants in fossils[14,15].

Even strictly archaeological samples display consistent disparity between thermal age and standard age assignments. The molecular integrity of bone collagen in a sample is compared to a collagen decay curve to determine its thermal age. In one study, Buckley and Collins determined thermal (collagen-based) ages for 65 archaeologically dated bones[9]. Every one showed a higher standard age than thermal age. The standard ages in their samples (range 2,500a to 1,500,000a) exceeded collagen content-based ages (range 1,584a to 144,862a) by two to tenfold. Original bone collagen in samples bearing even older standard ages highlights the mystery that underlies this disparity. By "original" is meant that the biochemical or even whole tissue under investigation came from the fossilized animal and not some contaminant like recent microbial growth. Hence, "The idea that endogenous molecules can be preserved over geological time periods is still controversial"[16]. Recent reports have sparked new interest in modes of collagen preservation and in technologies with very high collagen detection sensitivity. This thesis explores such techniques for their potential to extend the limits of protein detection in very ancient bone. Additional data thus obtained could add new insights to questions related to this controversy, such as the expected longevity of particular proteins in particular settings.

The main mechanisms proposed to extend protein preservation beyond experimental expectations centre around mineral interactions. Collins *et al* (2000)[17] found that close association of osteocalcin—a common bone protein—with bone mineral enhances its preservation potential far beyond that in aqueous solution. However, proteins in aqueous solution do not match any realistic burial and long-term protein survival scenarios. The mere observation that osteocalcin lasts longer when surrounded by minerals rather than water does not necessarily justify the conclusion that the decay model predicts or even suggests that the longevity of mineral-associated osteocalcin could enable it to persist in

fossil bone. In other words, mineral association may explain how proteins last longer in bone than in a watery 'soup', but falls short of predicting that original proteins in fossils should remain detectable until today.

Most of the preceding considerations are based on experimentally derived results coupled with reasonable deduction, but they remain theoretical enough for Collins *et al* (2002) to admit that "Biomolecular deterioration still remains a largely unexplored aspect of bone diagenesis"[6]. Even the most recalcitrant proteins have shelf-lives[18], so their descriptions in Mesozoic strata remain enigmatic[19]. The research described in this thesis focuses on technologies and applications that have arisen since that was written, and that have the potential to probe this biomolecular deterioration from new angles.

Original biochemistry in archaeological and Cenozoic specimens

A survey of older techniques for bone protein characterization sets a backdrop against which the potential virtues of new techniques can be better appreciated. Historically, bone proteins from archaeological remains have been targeted much more often than those from paleontological remains. Subfossil bone proteins can vary from abundant and easily detectable to barely present, and even absent, from archaeological settings. These observations, coupled with short protein lifespans relative to geologic time, have dissuaded investigations of bone proteins from more deeply buried fossils, for example from Mesozoic or Paleozoic Erathems. Thus, archaeological and even Upper Cenozoic bone samples often harbor abundant and dense bone proteins, all time-altered to one degree or another. Such high abundances lend themselves to analysis by crude and inefficient techniques like protein extraction and weighing on an analytical balance. More sensitive technologies are required to detect faint and highly degraded protein traces that may persist in certain rare fossil samples.

Classic techniques like immunohistochemistry have been used to identify such proteins as haemoglobin[20] and albumin[21] in archaeological bone. This technique takes advantage of antibody-antigen specific molecular interactions. Antibodies of targeted biochemicals are added to demineralized bone tissue. If the target biochemical is present, antibody binding takes place. Unbound antibodies are washed off. Fluorescent markers are then applied. They attach to the exposed end of the antigen-bound antibody molecules, and excess markers are washed off. Micrographs record fluorescence of the biomolecular *in situ* patterns.

Decades of radiocarbon dating have supplied, perhaps unwittingly for some, a robust and longstanding verification of the presence of endogenous protein in ancient bone. Collagen is routinely extracted for radiocarbon and other analyses, typically using some variation of the Arslenov method, discussed in a later chapter on radiocarbon isotope analysis. Briefly, extraction involves dissolution and removal of bone mineral in acid, followed by gelatinisation of collagen via heating under a weak acid. Researchers require analytical evidence that the collagen extracted from archaeological bone has little or no contamination in order for radiocarbon age dates to be considered valid. Therefore, rigorous and repeated tests have demonstrated the reliability of extracting primary, as opposed to external secondary or exogenous, sourcing of bone collagen. The thousands of published radiocarbon ages obtained from extraction of proteins (collagen) from mineralised tissues including shell, tooth, and bone attest to the general abundance of proteinaceous material in archaeological sites.

In addition, the presence of bone collagen is regularly confirmed by protein sequencing of archaeological samples. This process begins with protein extraction protocols similar to those used in preparation for radiocarbon dating. Protein extracts are purified then digested with a selected enzyme (a protease) known to preferentially

catalyse protein backbone hydrolysis at specific amino acid sites. The resultant mixture is separated and mass analysed typically by an integrated gas chromatography/ tandem mass spectrometry (GC/MS-MS) device. The measured molecular masses from the digested extract can then be compared with known collagen fragments so that original collagen sequences can be digitally reconstructed.

A single Siberian mammoth bone yielded 126 unique, partly intact protein types, detected by tandem mass spectroscopy. This exemplifies many Cenozoic proteins including the 'gold standard' technique of sequencing[22]. This one discovery contains far more unique protein remnants than the total collection of biochemicals found in the entire Mesozoic so far sampled, illustrating both the potential abundance of original biochemistry in Cenozoic fossils, and the disappearance of that biochemistry due to degradation over time. Another more recent report describes the oldest original animal lipid. The pygidial (preening) gland from an extinct bird captured in Germany's Messel Shale preserved still-yellow oil, now waxy[23]. Overall, the abundance of published protein sequences from recent fossil and subfossil specimens attests again to the general abundance of protein remnants in archaeological and even Cenozoic settings.

These and other methods clearly show that organic archaeological remains retain abundant endogenous organics including proteins like collagen. This fact is highlighted in research in this thesis. Some of the same technologies used to reaffirm primary collagen in archaeological bone are herein applied to older bone samples. This strategy aims to explore how well and how far those technologies can extend into older bones with presumably much less or even no collagen, and to assess by comparison the relative protein detection sensitivity of various techniques.

Few would question the reality of collagen in archaeological bones of high quality preservation. However, reports of protein remnants including collagen in paleontological

bone samples are met with widespread disapproval in certain circles. As noted in the abstract above, the subject of bone collagen longevity and persistence remains contentious on the basis of collagen decay model projections[11].

Original biochemicals and intact tissues from Mesozoic specimens

The vast majority of fossiliferous remnants of soft tissues such as skin, internal organs, body outlines, and nervous tissue occur in the fossil record as mineralisation that records only the shape, but no original biochemistry. However, original biochemicals do occur (rarely) in Mesozoic and even more rarely in Paleozoic fossil remains, as Table 1.1 documents below (p. 21).

The phrases “soft tissue,” and “soft tissue preservation” occur throughout paleontological literature, but in most cases authors intend to convey “mineralised tissue.” Often, soft parts preserve via phosphatization, sulphurization, pyritisation, or kerogenisation[24]. Authors also note preservation by silicification , carbonisation, phyllosilicate metamorphism, or apatite permineralisation[24]. Except for kerogenisation and carbonisation, these modes describe minerals that replace the original tissue. The resulting preservation records body organ outlines in whitish, reddish, and golden colors. These and other minerals can co-mingle in the same fossil, depending on mineral availability and complicated internal chemistries likely determined very early in diagenesis. More often than not, authors do not plainly distinguish “mineralised” versus “original” when they refer to soft tissue in fossils. In specimens with mineralised soft tissue, the minerals represent chemical transformations of the original, labile biochemistry into a more resistant material. Mineralisation can occur by hydrothermal action or groundwater precipitation, and even by bacterial degradation of organic components. Partial biodegradation blankets each organ with acid, which causes preferential

precipitation of nearby minerals on the order of weeks to months in laboratory experiments[25]. Extreme care is therefore required in sifting literature for those rare instances of original biochemistry.

These common mineralisation modes of soft animal part preservation do preserve gross anatomy[26,27], and in some cases microanatomy[28], but none preserve as much biological or taphonomic information as do primary protein sequences, isotope analyses of primary biominerals, or original organically preserved residual or whole tissues. This thesis focuses on original biochemistry. In addition to suggesting how future studies might apply new technologies to test diagenetic scenarios, an even more significant task is to test whether or not new applications of established technologies or altogether new technologies can increase protein detection sensitivity and efficiency enough to help resolve current controversy on bone collagen (and by extension proteins in general) longevity.

Despite the expected rarity of original biochemistry in fossils, a diligent literature search yields dozens of reports. Rather than write a book-length narrative that summarizes each published description of original biochemistry or preserved whole tissue fossil, selected examples from the longer list are described next, followed by a full compilation in Table 1.1, p. 21.

Stunningly, soft and pliable tissue was described in a *Tyrannosaurus rex* femur in 2005[29], shown in Fig. 1.2, with a follow-up report that identified specific biochemicals[30]. The specimen contained whole osteocytes, whole epithelial and erythrocyte cell-like elements, and extracellular fibrillar connective tissue. Incredulous reactions to such fresh-looking biomaterial cited bacterial contamination, and in particular that mucilaginous bacterial biofilm was mimicking vertebrate tisses[31]. In response, the original team added

more colleagues who sequenced collagen protein from the *T. rex* (Museum of the Rockies specimen MOR 1125), found in the Cretaceous Hell Creek Formation of Montana[32].

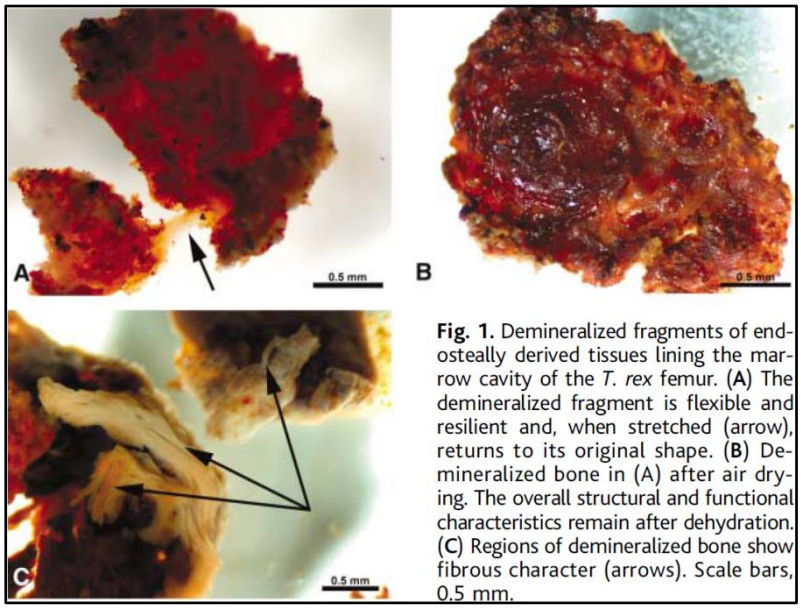

Fig. 1. Demineralized fragments of endosteally derived tissues lining the marrow cavity of the *T. rex* femur. (**A**) The demineralized fragment is flexible and resilient and, when stretched (arrow), returns to its original shape. (**B**) Demineralized bone in (A) after air drying. The overall structural and functional characteristics remain after dehydration. (**C**) Regions of demineralized bone show fibrous character (arrows). Scale bars, 0.5 mm.

Figure 1.2 | Fig. 1 from Schweitzer et al, *Science*, 2005.

A more detailed follow-up study revealed additional tyrannosaurid biochemicals from the same sample. It included results from immunofluorescence. Schweitzer and colleagues imaged proteins specific to vertebrates, including PHEX and histone H4[30]. They also applied the same vertebrate-specific protein detection procedures to a *Brachylophosaurus canadensis* (hadrosaur) femur that was extracted using sterile handling techniques from the Cretaceous Judith River Formation. In collaboration with an unbiased, external laboratory to perform collagen sequencing, the report confirmed elastin and laminin bone proteins as well as collagen[33]. An additional publication on this specimen described phenomena characteristic of modern blood vessels, including translucence, pliability, and reaction to immunological staining for collagen and other epithelial proteins.[34]

Another study published remarkable low magnification micrographs of a large, soft and pliable brownish sheet of fibrillar tissue exposed in a *Triceratops horridus* (HTC 06) horn core from the Hell Creek Formation of Northern Montana[35]. The study authors noted that no known bacterial biofilm rebounds after stretching, refuting the biofilm hypothesis. They also used scanning electron microscopy (SEM) to image osteocytes with delicate canaliculi. In collaboration with the sample repository, a portion from HTC 06 was obtained for analyses detailed in this thesis.

Polish researcher Roman Pawlicki's scientific output detailing original dinosaur tissues spanned more than three decades, included exquisite electron micrographs of bone tissue from a Gobi Desert *Tarbosaurus bataar* in 1998[36], and are ongoing[37]. The 1998 report noted, "the descriptions presented confirm that the morphology of the vascular canals in dinosaur bones and the bones of modern reptiles is the same"[36]. This sample likely represents the same *Tarbosaurus* that Pawlicki *et al* imaged using electron microscopy in 1978[38] and in a 1966 *Nature* issue that showed dinosaur collagen fibers[39]. His papers reveal osteocytes, collagen fibers, and unusually, a positive immunoassay for DNA in dinosaur osteocyte nuclei[40].

Electron microscopy was again used in 2008 to visualize exceptionally well-preserved (naturally mummified) skin from a Chinese *Psittacosaurus mongoliensis* specimen. It compared dinosaur to modern collagen fibre bundles[41]. The same researcher, South Africa's Theagarten Lingham-Soliar, published images of original skin coloration in a separate *Psittacosaurus*, also from China. Original, unaltered pigments including carotenoids and melanins were described in the specimen[42]. Researchers working in southern China reported endogenous protein from a tiny, egg-encased, Jurassic embryonic sauropod *Lufengosaurus* femur[43]. The most likely source for the protein signature that they detected was bone collagen.

A more recent example comes from what 2017 news reports called the world's best-preserved dinosaur of its kind. Canadian miners encountered the armored nodosaur *Borealopelta* upside-down in shale sand. The fossil looks more like a carcass than a rock, preserves the outline of skin, and shows every spike and nodule of the animal's dorsal surface. Spectroscopy and mass spectrometry revealed that in the skin were preserved original melanin pigments from which the animal's coloration scheme was reconstructed[44].

More examples of apparently endogenous fossil bone proteins include non-collagen protein fragment sequences from an *Iguanodon* bone housed at the Natural History Museum of London[45]. Researchers described amino acids from a New Mexico *Seismosaurus*[46] and even in fossil shells[47]. The now-dated 1980 book *Biogeochemistry of Amino Acids* noted, "work with dinosaur remains demonstrated that enough protein for analysis could often be recovered from bones and teeth as old as the Jurassic"[48]. The history of reported fossil proteins and protein constituents contrasts with the widespread concept that Mesozoic and earlier-deposited fossils all represent mineralised artifacts that contain no original biological material. In summary, many workers maintain extreme skepticism despite plenty of direct and indirect detection, using a dozen different techniques including mass spectrometry and various spectroscopic techniques used to verify proteinaceous or other biochemicals endogenous to Mesozoic strata.

Original biochemistry from Paleozoic and older specimens

Biochemicals original to Paleozoic fossils occur more rarely in the literature than Mesozoic and certainly than Cenozoic finds. Research into taphonomic modes that favour preservation of Paleozoic biota has not yet deduced adequate modes of preservation, leading to persistent controversy. An adequate taphonomy needs to explain pervasive

preservation by kerogenisation and carbonisation, among other modes, in Paleozoic fossils.

In kerogenisation, which differs from carbonisation only in its lower degree of pyrolysis, heat alters mixed original organics into a blackish residue thought to be more resistant—perhaps like coal—to the ravages of time than the original organics from which they derived. Like coalification, kerogenisation drives off water and volatiles. Many studies of carbonisation in Burgess Shale-Type (BST) fossils have determined that mineralisation processes of one sort or another, often mediated by bacterial degradation soon after the typically soft-bodied Cambrian organisms died, played a large role in preservation. A relatively recent review of the 13 most prominent BST fossil sites concluded, "However, in the great majority of cases it is a carbonaceous film alone that defines the overall morphology of the fossils"[49]. The same authors reviewed occurrences of this "carbonaceous film" (un-mineralized remains) on most continents, a distribution that resembles fossils in general.

Preservation modes like the BST also occur in more recent geologic settings, including the Cretaceous. Possibly subtle differences in sedimentation rates vary the time during which a carcass experiences sulphate-reduction microbial action that leads to pyritisation versus methanogenic microbes that lead to kerogenisation and the production of carbonaceous films[50].

Even without preservation schemes adequate to preserve original biomaterials in Paleozoic settings, a handful of cases appear in the literature. Their lower numbers in lower strata could result simply from workers not focused on original biochemicals in their specimens at hand.

The periderm of some Ordovician graptolites exhibited collagen-like structures, imaged by wide-angle X-ray diffraction in 1972 by Towe and Urbanek[51]. Graptolites

occur in Paleozoic strata and some forms are extant. They are small, worm shaped marine creatures that secrete tube-shaped organic thecae, thought to be composed of collagen or chitin. Chitin is a biochemical found in squid beaks and pens, arthropod exoskeletons, and certain fungi, where it incorporates glass-like spicules into its support structure. The researchers found a few amino acids, but not the 4-hydroxyproline or 5-hydroxylysine characteristic of collagen. The Towe and Urbanek results were thus not definitive for original collagen, but were consistent with either collagenous or chitinous residues, and suggest that graptolite fossils, which occur worldwide, warrant further investigation. Much later, definitive analyses showed that Paleozoic scorpion and false scorpion fossils retained their original exoskeletons, including chitin and chitin-associated protein[52].

The prevailing paradigm for British Columbia's Burgess Shale fossils holds that the flattened soft-bodied creatures consist merely of impressions, mineralised (for example pyritised) outlines of soft tissue, or kerogen. However, a German and Russian team used fluorescence microscopy, Fourier Transform Infrared (FTIR) microscopy, high-performance capillary electrophoresis, high pressure liquid chromatography, and mass spectroscopy to recently identify intact chitin in the Burgess sponge, *Vauxia gracilenta*[53].

Equally surprising preservation was described in still-flexible, proteinaceous marine tube worm tubes. Extracted from Siberian drill core samples of Ediacaran strata, Moczydlowska described the worm casings as not mineralised, and original to the worms[54]. Comparison revealed direct correspondence with the chitin-structural protein composition of worm casings in extant siboglinid counterparts.

Despite this extensive published literature, skepticism over original biochemical fossils persists. A 2017 report attempted to refute dinosaur-specific collagen sequences published in 2009 by showing a mismatch between expected and reported sequences, and by suggesting instrument contamination with modern sample[15]. However, it is difficult to

define an expected sequence when no living samples exist for comparison, and the instrument contamination scenario generates even more problems. It calls into question the protein sequencing methodology. Even if these collagen sequences from two fossils that also showed immunoreactivity to a handful of other proteins as well as whole tissue preservation were shown to be in error, then skeptics of original biochemistry in fossils would still need to refute dozens of biochemical detection reports throughout the scientific literature (see below). The development of new technologies or new and accessible applications of established techniques could help add more data from the fossil record in an effort to determine the accuracy and distribution of these discoveries. Increased detection efficiency could also enable future studies to test diagenetic hypotheses as proposed for various geologic, archaeologic, or geographic sites.

Five trends in over 70 original biochemistry fossil reports

Table 1.1 identifies the biochemical or other original organic component and, if available, the Genus name of the animal from which that component derived. The Table also notes geologic and geographic settings for each find. Following this, Figs 1.2-1.6 summarise trends that 70 original biochemistry fossil publications reveal. Figs 1.3, 1.4 and 1.6 are derived from Table 1.1. Five trends are identified by this compilation. They suggest target research questions that are then addressed in this thesis.

Taxon and associated biochemical	**GSA* System, Age**	**Formation, Geography**	**Year Published**
Dinosaur bone collagen & vessels	Cretaceous, Campanian	Gobi Desert, Mongolia	1966[39]
Megalosaurus egg shell protein	Jurassic, Bathonian	Rognacian Fm., S. France	1968[55]
Sauropod limb hydroxyproline	Jurassic, Kimmeridgian	Morrison Fm., CO	1968[56]
Dinosaur proteins and polysaccharides	Cretaceous, Maastrichtian	??	1974[57]

Dinosaur gelatinised collagen	Cretaceous	Western US	1976[58]
Mollusk shell glycoproteins	Cretaceous	Coon Creek Fm., Tennessee	1976[59]
"Dinosaur bones" parallel collagen fibers	Cretaceous, Campanian	Mongolia	1985[60]
Seven hadrosaurs' unfossilised bones	Cretaceous, Campanian	Upper Colville Grp., Alaska	1987[61]
Tyrannosaurus tooth hydroxyproline	Cretaceous, Campanian	Judith River Fm., Alberta	1990[62]
Diplodocus vertebra proteins	Jurassic, Upper	Morrison Fm., Brushy Basin member, NM	1991[46]
Lambeosaurus osteocalcin	Cretaceous, Campanian	Alberta	1992[63]
Various dinosaurs, organic material	Cretaceous, various	Judith River Fm., Alberta	1993[64]
Hymenaia protera (extinct tree) chloroplast DNA	Eocene, Upper	La Toca mine, Hispaniola	1993[65]
Amber insects unaltered amino acids	Cretaceous, Barremian	Dominican Amber	1994[66]
Tarbosaurus osteocyte DNA	Cretaceous, Campanian	Gobi Desert, Mongolia	1995[40]
Tyrannosaurus bone heme	Cretaceous, Maastrichtian	Hell Creek Fm., MT	1997[36]
Tyrannosaurus DNA, amino acids	Cretaceous, Maastrichtian	Hell Creek Fm., MT	1997[67]
Tarbosaurus blood vessels	Cretaceous, Campanian	Gobi Desert, Mongolia	1998[25]
Shuvuuia feathers β-Keratin	Cretaceous, Upper	Ukhaa Tolgod, SW Mongolia	1999[68]
Rahonavis (extinct bird) keratin	Cretaceous, Maastrichtian	Madagascar	1999[69]
Scelidosaurus skin layers, cells, dermal scales	Jurassic, Pleisenbachian?	Lias Group, England	2000[70]
Tyrannosaurus collagen SEM scans	Cretaceous, Maastrichtian	Lance Fm., Newcastle, WY	2001[71]
Jeholopterus skin, fibers	Cretaceous, Barremian	Yixian Fm., Ningcheng, Mongoloa	2002[72]
Iguanodon osteocalcin protein	Cretaceous, Aptian	UK	2003[45]
Micrococcus (non-spore-forming bacteria) alive in amber	Cretaceous, Aptian	Lebanese amber, Mt. Hermon, Israel	2004[73]
Tyrannosaurus soft, flexible connective tissue	Cretaceous, Maastrichtian	Hell Creek Fm., MT	2005[29]
Titanosaur egg ovalbumin	Cretaceous, Upper	Rio Colorado Fm., Bajo de la Carpa Member, Argentina	2005[74]
Enantiornithine embryo collagen	Cretaceous, Upper	Rio Colorado Fm., Argentina	2005[75]
Frog bone marrow	Miocene, Tortonian	Libros Basin infill, NE Spain	2006[76]
Tyrannosaurus collagen	Cretaceous, Maastrichtian	Hell Creek Fm., MT	2007[77-79]
Triceratops blood vessels	Cretaceous,	Hell Creek Fm., E. MT	2007[80]

	Maastrichtian		
Feather melanocytes	Cretaceous, Albian	Crato Fm., Brazil	2008[81]
Leaf fragments in mummified *Brachylophosaurus* gut	Cretaceous, Campanian	Judith River Fm., MT	2008[82]
Psittacosaurus skin fibers	Crecaceous, Barremian	Jehol Biota, Yixian Fm., Liaoning	2008[41,83]
Brachylophosaurus blood vessels, collagen sequence, elastin, laminin	Cretaceous, Campanian	Judith River Fm., MT	2009[33]
Bird feather, purple pigment	Eocene, Bartonian	Germany, Messel shale	2009[84]
Hadrosaur skin cell structures	Cretaceous, Maastrichtian	Hell Creek Fm., ND	2009[85]
Salamander muscle, whole	Miocene, Burdigalian	Ribesalbes Lagerstätte, NE Spain	2009[86]
Stegosaurus plate keratin	Jurassic, Upper	Howe Quarry, Morrison Fm., WY	2010[87]
Sinosauropteryx melanosomes	Cretaceous, Aptian	Jehol Group, China	2010[88]
Psittacosaurus skin scales and pigment	Cretaceous, Aptian	Jehol Biota, Yixian Fm., Liaoning	2010[42]
Mammal hair in amber	Cretaceous, Albian	Archingeay-Les Nouillers, Charente-Maritime, France	2010[89]
Archaeopteryx original elements	Jurassic, Tithonian	Solnhofen, Bavaria	2010[90]
Penguin melanosomes	Eocene, Priabonian	Yumaque Point, Paracas Reserve, Peru	2010[84]
Mosasaur humerus Type I collagen	Cretaceous, Maastrichtian	Ciply Chalk, Belgium	2011[91]
Scorpion chitin and chitin-associated protein	Pennsylvanian, Moscovian	Cave fill, N. Illinois	2011[52]
Eurypterid chitin and chitin-associated protein	Silurian, Upper	Williamsville Fm., Ontario	2011[52]
Pterodactylus actinofibrils	Jurassic, Upper	Solnhofen, Bavaria	2011[92]
Lizard tail skin breakdown products	Eocene, Bartonian	Green River Fm., Wyoming	2011[24]
Tyrannosaurus and *Hadrosaur* Type l collagen	Cretaceous, Maastrichtian	Hell Creek Fm., MT	2011[8]
Cuttlefish ink sac	Jurassic, Oxfordian	Blue Lias Fm., Lyme Bay, England	2012[93]
Turtle osteocytes	Jurassic, Tithonian	Mongolia	2012[94]
Tyrannosaurus and *Brachylophosaurus* actin, tubulin, histone, PHEX, DNA	Cretaceous, Maastrichtian; Campanian	Hell Creek Fm.; Judith River Fm., MT	2013[30]
Lufengosaurus embryo bone protein	Jurassic, Sinemurian	Upper Lufeng Fm., Yunnan	2013[43]
Triceratops osteocytes; soft sheets of fibrillar bone	Cretaceous, Maastrichtian	Hell Creek Fm., MT	2013[35]
Mosquito gut hemoglobin	Eocene, Lutetian	Kishenehn Fm., MT	2013[95]
Crinoid original organics	Mississippian,	Edwardsville Fm., IN	2013[96]

	Tournaisian		
Vauxia (sponge) chitin	Cambrian, Age 3	Burgess Shale, British Columbia	2013[53]
Gastropod egg chitin	Jurassic, Hettangian	Skłoby Fm., Poland	2014[97]
Sabellidites (tube worm) chitin, protein	Proterozoic, Ediacaran	Nekrasovo & Rovno Fm.'s, Russia	2014[54]
Mosasaur melanin, melanosomes	Cretaceous, Coniacian	Boquillas Fm., TX	2014[98]
Icthyosaur eumelanin in melanosomes	Jurassic, Sinemurian	Blue Lias Fm., Lyme Bay, England	2014[98]
Brachylophosaurus blood vessels, collagen sequence	Cretaceous, Campanian	Judith River Fm., MT	2015[34]
Dinosaur collagen and red blood cells	Cretaceous, Campanian	Dinosaur Park Fm., Alberta	2015[99]
Dinosaur melanosomes and pigment	Jurassic, Tithonian	Tiaojishan Fm., Liaoning	2015[100]
Rhamphyorhynchus orange claw material	Jurassic, Tithonian	Solnhofen, Bavaria	2015[101]
Proteinaceous amide groups in chert	Paleoproterozoic, Orosirian	Gunflint Fm., Ontario	2016[102]
Nothosaurus, Protanystropheus blood vessels, etc.	Triassic, Olenekian	Gogolin Fm., S. Poland	2016[37,103]
Psittacosaurus keratin in skin	Crecaceous, Barremian	Jehol Biota, Yixian Fm., Liaoning	2016[104]
Citipati (oviraptor) claw Beta-keratin	Cretaceous, Campanian	Djadokhta Fm., Mongolia	2016[67]
Dinosaur eggshell protoporphyrin, biliverdin	Cretaceous, Maastrichtian	Hougang, Tangbian, & Nanxiong Fm.'s, China	2017[105]
Lufengosaurus adult rib collagen	Jurassic, Sinemurian	Upper Lufeng Fm., Yunnan	2017[106]
Borealopelta (Nodosaur) melanin plus other biochemicals	Cretaceous, Aptian	Clearwater Fm., Alberta	2017[44]
Mammalian erythrocytes in tick gut	Upper Paleogene	El Mamey Fm., Dominican Amber	2017[107]
Brachylophosaurus collagen re-confirmed	Cretaceous, Campanian	Judith River Fm., MT	2017[108]
Messelirrisorid bird uropygial gland, yellow oil	Cenozoic, Eocene	Messel Shale, Hesse, Germany	2017[23]

Table 1.1 | Publications of Original Biochemistry in Fossils. 77 publications which show the results of more than a dozen different techniques used to detect biochemical signatures, including some techniques used in this thesis. Reports that named "soft tissues" but specified mineralisation, and reports that did not address mineralisation versus original organics, were rejected. This list is not comprehensive, but is the most complete collection of its kind, to the best of the author's knowledge. Cenozoic original biochemistry fossils are extremely under represented here (see Fig. 5 caption), since publications that dealt with the oldest, most difficult to explain, samples from Mesozoic, Paleozoic, and lower layers were instead targeted. * GSA = Geological Society of America. In publications that omitted the GSA Age, it was inferred by matching the published age date to the GSA Geologic Time Scale, version 4.0[109].

The first trend from Table 1.1 is that taxa from which researchers extract original biochemistry vary widely. It seems that no particular taxon is exempt from having organic remnants preserved as fossils. The list includes biochemistry from plants, microbes, amber-encased insects, clay-encased arthropods, sandstone- and mudstone-embedded dinosaurs, shale-bound semiaquatic reptiles and birds, fully aquatic reptiles in limestone, and perhaps most surprisingly, seafloor worm and sponge tissues found below the Cambrian. The list includes representatives from the phyla Monera, Porifera, Annellida, Plantae, Arthropoda, Mollusca (classes Gastropoda and Cephalopoda), Echinodermata, and Vertebrata (classes Mammalia, Aves, Amphibia and Reptilia.) This trend suggests that original biochemistry from additional phyla and lower level taxa await discovery.

Nor do those ancient animals' environmental niches seem to play much of a role in selection of primary organics for fossil preservation. Fossil assemblages and adaptive features of fossil forms suggest their origins from benthic, neritic, lacustrine, tropical, swampland, and perhaps semiarid terrestrial habitats. Taxa representing terrestrial biomes such as arid desert, savanna, temperate forests, taiga and tundra are rare or absent among Paleozoic and Mesozoic fossil biochemicals. However, this is due to the swampy, marine, and lacustrine environments that Mesozoic strata captured in general, and not to any specific taphonomy or diagenesis that favored or disfavored biochemical preservation. Many more dry land-living taxa occur in Cenozoic than Mesozoic deposits worldwide. Also, no dry-land taxa—with or without biochemical preservation—occur in Paleozoic strata. If another table was constructed that included Cenozoic biochemistry, it would fill many pages, and undoubtedly reveal abundant and widespread biochemical preservation of upland-living taxa[23,58]. In short, fossilized creatures from land, sea, and sky retain original biochemical remnants. Creatures from swamp, sea and sky that happen to occur

in Mesozoic strata also retain original biochemistry according to an abundant, if not widely known, body of technical literature.

A third trend that Table 1.1 reveals is that of an increased interest in, and investigation of, original biochemistry fossils in recent years. What accounts for the increase in published papers on this topic? A 2005 *Science* paper showed full-color, clear photographs of blood red tissue and still-red erythrocyte-like elements inside blood vessels extracted from the sectioned femur of "B rex" (MOR 1125), a *T. rex* named after discoverer and dig volunteer Bob Harmon [29]. He located the fossil on a Montana hillside in the Hell Creek Formation. That paper, plus a series of three follow-up reports all published in one 2007 issue of *Science*[77-79], invigorated fascination in those investigating dinosaur phylogenies as well as controversy in those familiar with the lability of biochemicals. Those papers appear to have sparked a string of similar research, as shown by the higher bars post-2005 in Fig.1.3, while simultaneously inciting vigorous demand for more definitive evidence[11] and dismissiveness from other circles[110]. Thus, more

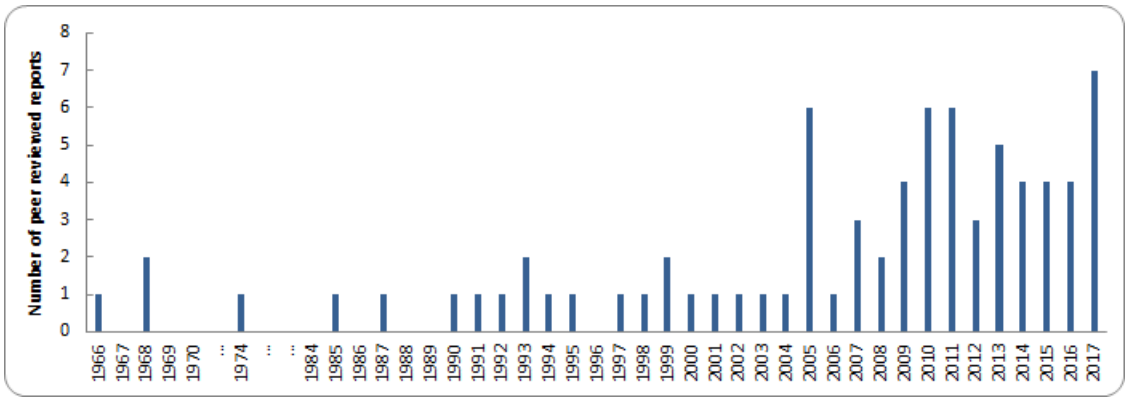

Figure 1.3 | Original Biochemistry Fossil Publications by Year. The years 1970-1973 and 1975-1984 are represented by ellipses in order to display the data legibly. This list is not perfectly comprehensive, but represents the literature accurately enough to reveal temporal trends. Investigators merely dabbled in fossil biochemistry from the 1960's until 2004. Beginning with dinosaur whole tissue discoveries in 2005, and in conjunction with the arrival of new techniques (see text), research has surged.

researchers have of late risked or suffered ire from peers all while pioneering discoveries of primary proteins and other biochemistry such as lipids[23], nucleic acids[30], and biological pigments such as melanin[111] and protoporphyrin[105] in fossils.

New techniques with the potential to nondestructively analyze labile organic fossil components have also come online of late. Workers have availed themselves of these techniques in order to gain unprecedented insights into fossil organics and what those data imply for physiology, diet, diagenesis, and other realms. These reports, including results presented in this thesis, aim to solve the mystery of the apparent longevity of labile organic structures, and to explore how far afield and how deeply buried those organics extend.

So far, data Table 1.1 reveals three trends: 1. Biochemical persistence occurs in all taxa, 2. Biochemical persistence is independent of paleoenvironment, and 3. A recent increase in investigation and published work. A fourth trend shown in Fig. 1.4.reveals preliminary geographic distribution of original biochemistry in fossils worldwide.

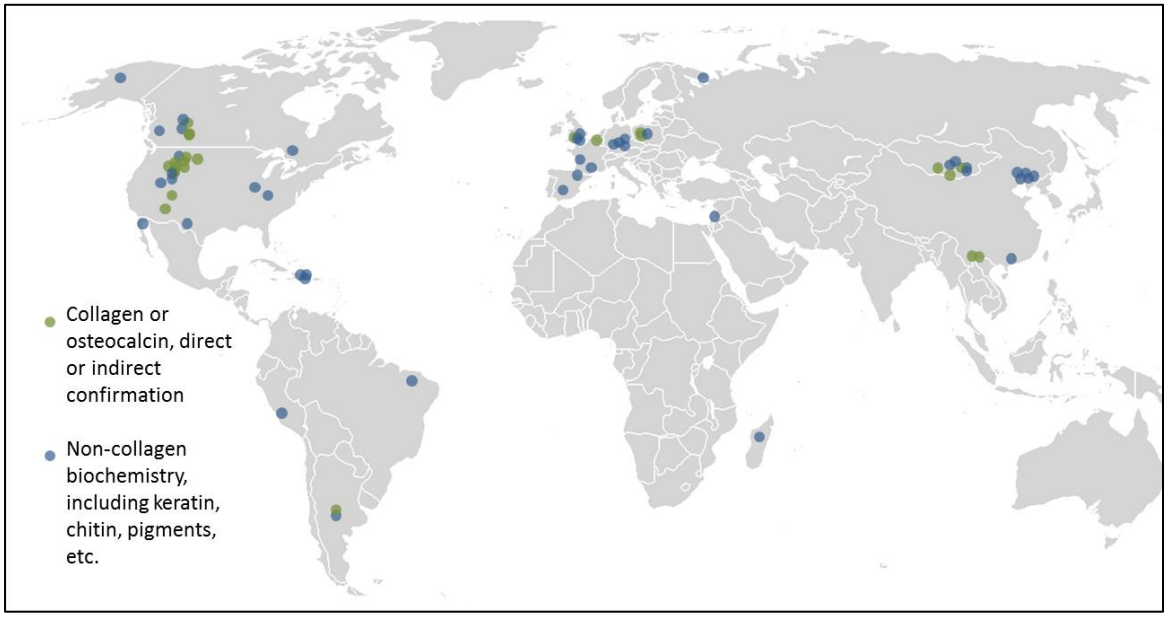

Figure 1.4 | Global Distribution of Original Biochemistry Fossils. Approximately seventy original biochemistry fossil locations show a non-random worldwide distribution. High concentrations likely reflect a combination of sample accessibility and general fossil distributions (see Fig. 1.5).

In Fig. 1.4, the bone proteins collagen and osteocalcin were marked separately from other biochemicals in fossils because this thesis focuses on bone fossils. The marked locations of original collagen versus other organics suggest future research into the extent of their overlap. Present data appear insufficient to answer this. Overlap does occur in the American West, the Gobi, and Northern Europe. However, a lack of overlap may simply mean researchers have not yet looked for, or do not have the tools to detect, collagen in locations such as China's Jehol Biota and Southern Europe. For comparison, Fig. 1.5 shows the distribution of fossils in general using the Paleobiology Database.

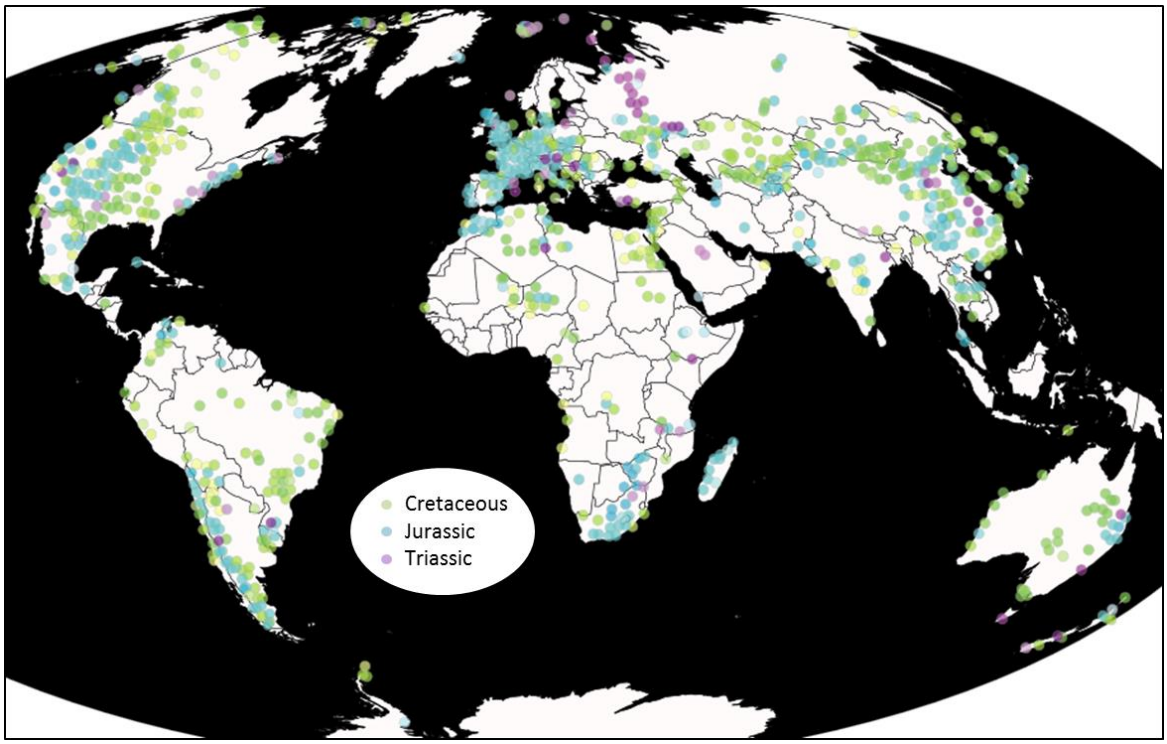

Figure 1.5 | Global Distribution of 28,834 Mesozoic Reptilia. The Paleobiology Database at paleodb.org was accessed to generate a distribution map of general fossils to compare with the distribution of biochemistry fossils from Fig. 1.4. The data were downloaded on 25 February, 2018, using the filters "Mesozoic" and "Reptilia." Comparison reveals that original biochemical fossils tend to occur wherever fossils are generally found. The 28,834 individual plotted specimens represent, in order of descending abundance, ornithischians, testudines, saurischians, theropods, avetheropods (includes birds), and other reptiles.

The occurrence of original biochemical fossils on most continents suggests that more merely await discovery on remaining continents Australia, Antarctica, and mainland Africa. Regions with few biochemistry fossils, such as Amazonia, the Sahara and Congo, and the deserts of Western Australia, coincide with regions where few fossils occur in general. This suggests that original biochemistry fossil finds may continue to populate many more fossil sites. More data would help diagnose these suggestions.

The fifth and final trend that emerges from Table 1.1 pertains to the distribution of original biochemistry fossils throughout the geologic column. The diagram shown in Fig. 1.6, here taken from the GSA Geologic Time Scale v. 4.0[109], shows (mostly sedimentary) rock layers not to be found in any single earth location, from many separate locations, here compiled graphically. All three Cenozoic rock Systems were reduced to a single bar at the top merely to show that it was not entirely forgotten in this present analysis. According to the above remarks, if the Cenozoic bar displayed a more accurate number of reports, its corresponding bar would stretch across many pages at the scale shown here. Therefore, Fig. 1.6 should only be taken to represent the current number of reports from strata deposited prior to the Cenozoic. Similarly, the entire Precambrian assemblage was reduced to the two Systems with reported original biochemistry.

Ignoring the Cenozoic, the Cretaceous System has more than double the number of original biochemistry fossil reports than from all other geologic Systems combined. This could be partly due to the lack of heating that these rocks experienced since deposition. Higher temperatures and intense hydrothermal action can transform and redistribute ancient buried carcasses. The occasional biochemicals reported from pre-Cretaceous fossils suggest that these factors avoided certain pockets of earth's crust over time.

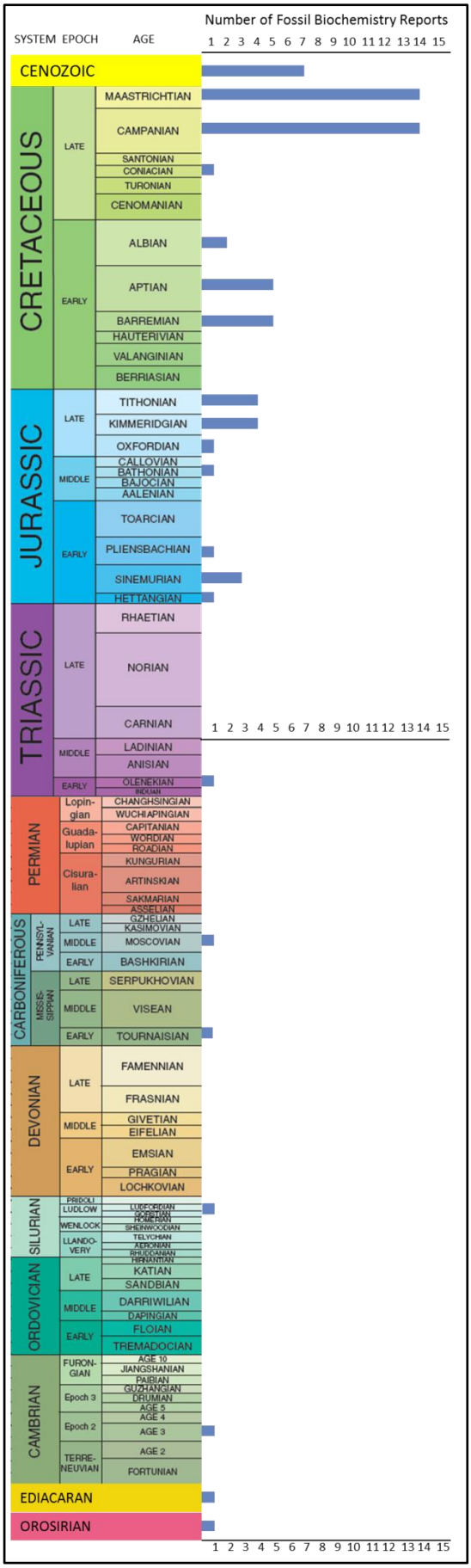

Figure 1.6 | Geological Distribution of Reported Original Biochemistry in Fossils. This chart emphasizes Mesozoic and Paleozoic rock Systems, as it condenses the entire Cenozoic at the top, and the entire Precambrian at the bottom down to merely the Ediacaran and Orosirian Systems. The data reveal a predominance of biochemistry in Cretaceous System rocks, and a persistent trickle of biochemistry elsewhere.

This geologic distribution shows that original biochemistry fossils also occur in some of the oldest strata that contain any fossils. No reports have yet described them from Permian or Devonian Systems. However, Systems that do preserve original organics or at least decayed remnants of those organics, flank both. These data suggest that original biochemical discoveries will, assuming adequate research focus and detection tools, begin to fill empty positions in the column diagram.

The five trends gleaned from Table 1.1 show that original biochemistry is geologically extensive, geographically global, and taxonomically wide-ranging. The limits are not clear, if they are present at all. The questions arise as to which rock strata have more or less biochemicals and why? Which global locations have more or less biochemicals and why? Are there any taxa that have no biochemical representation in fossils, or should investigators expect to discover original biochemicals from any kind of creature, assuming taphonomy and diagenesis were favorable to preservation? Published results suggest two hypotheses. First, geographic and stratigraphic ranges for ancient collagen will continue to increase. Second, novel instrumentation and techniques will continue to confirm existing ancient proteins and help detect them in new places.

Techniques used to verify biochemistry in fossils

Table 1.2 notes many of the techniques used to detect original biochemistry in fossils as described in the literature listed in Table 1.1. Techniques in addition to those shown here, and especially techniques that directly and non-destructively target specific biochemicals, would help to either confirm or annul the hypothesis that published spectroscopic and spectrometric techniques have indeed detected original biochemistry in Mesozoic and lower strata. In addition, most of the techniques used so far involve costly instrumentation and/or time-intensive preparation as well as considerable expertise to

Technique	**Principle of operation**	**Typical organic targets**
Collagen extraction	Dissolution of biomineral, separation and purification for weight	Collagen
Liquid Chromatography Tandem Mass Spectrometry (LC-MS/MS)	Determination of protein masses by separation according to mass/charge ratio in the first MS; ions fragmented by collision in the second MS	Any biomolecule with an analogue in database; Collagen common in protein sequencing
Quantitative X-ray Fluorescence (XRF)	Displacement of inner shell electrons by X-ray, and detection of resultant fluorescence energy differences	Elemental analysis, Oxide compound detection
Light microscopy	Magnification of intact tissue	Whole, intact tissues
Immunofluorescence	Antibody-antigen localization in situ, visualized by fluorescent dye	Any targeted proteins
Scanning Electron Microscopy (SEM)	Focused electron beam interacts with sample; backscattered electrons and characteristic X-rays detected	Position and morphology of structure
Synchrotron radiation Fourier transform infrared spectroscopy (SR-FTIR)	High brightness synchrotron light interacts with molecular structures at submicron resolution to form images by tomography	Quantity, composition, and distribution of proteins; lipid functional groups
X-ray absorption near edge structure (XANES)	Similar to SR-FTIR, but X rays target coordination structures	Elemental mapping of chelating metals
Fourier Transform InfraRed (FTIR) spectroscopy	IR light absorption by certain molecular arrangements generates characteristic spectra	Vibrational modes of specific bonds
Raman spectroscopy	Similar to FTIR but detects Stokes scattered light instead of Raleigh scatter	Vibrational modes of specific bonds
Time-of-Flight Secondary Ion Mass Spectrometry (ToF-SIMS)	Ion beam ionizes molecules from sample surface; mass of ions determined by retention time in detector	Organic molecules, e.g., amino acids
X-ray photoelectron spectroscopy (XPS)	X-ray excites atoms to emit electrons from characteristic shells; detects binding energy of electrons	Elemental composition of surface chemistry
Energy dispersive X-ray spectroscopy (EDS)	High energy beam induces sample surface to emit X-rays; electron voltage spectrum produced	Elemental composition of surface chemistry
Matrix-assisted laser desorption ionization (MALDI) mass spectrometry	Laser impinges on sample surface at an angle, ionizes particles; ions enter mass spectrometer	Total surface ions of sample, including collagen fragments

Table 1.2 | Overview of Biochemical Detection Techniques from Table 1.1 Reports.
Techniques in italics represent more direct biochemical detection methods, and those not in italics represent less direct detection methods.

operate and interpret. Therefore more user-friendly, inexpensive, and rapid techniques would facilitate widespread increase in fossil biochemical analysis.

Novel applications of established techniques and innovations toward new technologies are explored in this thesis. Before this discussion, however, the processes used to catalogue specimens and general descriptions of the specimens studied in this thesis, plus some of the partnerships with bone repositories, are described in chapter two. Chapter three then focuses on the novel application of second-harmonic generation (SHG) imaging using scanning confocal laser microscopy to fossils. The technique is well established as a valuable tool for biomedical research, but not for fossil analysis. Therefore considerable effort and further collaboration were required to establish the validity and applicability of SHG for fossil analyses. Chapter four describes FTIR and Raman spectroscopy. It combines resulting spectra taken from the archaeological and paleontological bone samples under investigation. Chapter five establishes FTIR as a novel and precise tool to assess collagen decay. In it, FTIR and SHG results from artificially decayed bone provide standards to help interpret results from actually decayed bone. Two chapters on carbon isotopes then follow. Stable carbon isotope analyses of ancient bone have some potential to inform questions about original proteins. Progress toward a field-deployable, inexpensive, and user-friendly quadrupole mass spectrometer with carbon isotope detection capability is described. Chapter six uses isotope analysis as an indirect means to investigate bone collagen by assessing the general degree of permineralisation versus preservation. Chapter seven shows how radiocarbon results inform biochemistry fossil questions and includes results that may be as challenging to interpret as original organics in fossils. The thesis concludes with some suggested means

of acquiring additional data that would help future research address questions of anomalous radiocarbon, collagen, and other biochemical fossil discoveries.

1 Guyton, A. C., Hall, J. E. & Reed Elsevier India Private, L. *Textbook of medical physiology*. (Elsevier Saunders : Reed Elsevier India Private Ltd., 2007).

2 Yang, W., Chan, V. C., Kirkpatrick, A., Ramshaw, J. A. & Brodsky, B. Gly-Pro-Arg confers stability similar to Gly-Pro-Hyp in the collagen triple-helix of host-guest peptides. *J Biol Chem* **272**, 28837-28840 (1997).

3 Shier, D., Butler, J., and Lews, R. . *Holes' Human Anatomy and Physioolgy, Tenth Edition*. 184 (McGraw Hill, 2004).

4 Naik, N., Caves, J., Chaikof, E. L. & Allen, M. G. Generation of spatially aligned collagen fiber networks through microtransfer molding. *Adv Healthc Mater* **3**, 367-374, doi:10.1002/adhm.201300112 (2014).

5 Wopenka, B., Pasteris, J.D. A mineralogical perspective on the apatite in bone. *Materials Science and Engineering C* **25**, 131-143 (2005).

6 Collins, M. J., Nielsen-Marsh, C.M., Hiller, J., Smith, C.I., Roberts, J.P., Prigodich, R.V., Wess, T.J., Csapo, J., Millard, A.R., and Turner-Walker, G. The Survival of organic matter in bone: A review. *Archaeometry* **44**, 383-394 (2002).

7 Buckley, M., Collins, M., Thomas-Oates, J. & Wilson, J. C. Species identification by analysis of bone collagen using matrix-assisted laser desorption/ionisation time-of-flight mass spectrometry. *Rapid Commun Mass Spectrom* **23**, 3843-3854, doi:10.1002/rcm.4316 (2009).

8 San Antonio, J. D. *et al.* Dinosaur peptides suggest mechanisms of protein survival. *PLoS One* **6**, e20381, doi:10.1371/journal.pone.0020381 (2011).

9 Buckley, M., and Collins, M.J. . Collagen survival and its use for species identification in Holocene-lower Pleistocene bone fragments from British archaeological and paleontological sites. *Antiqua* **1**, 1:e1 (2011).

10 Dobberstein, R. C., Collins, M.J., Craig, O.E., Taylor, G., Penkman, E.E.H., Ritz-Timme, S. Archaeological collagen: Why worry about collagen diagenesis? *Archaeological and Anthropological Science* **1**, 31-42 (2009).

11 Buckley, M. *et al.* Comment on "Protein sequences from mastodon and Tyrannosaurus rex revealed by mass spectrometry". *Science* **319**, 33; author reply 33, doi:10.1126/science.1147046 (2008).

12 Lowenstein, J. M. Immunospecificity of fossil collagens. *American Journal of Physical Anthropology* **50**, 460-460 (1979).

13 Johnson, K. R., Nichols, D.J., Hartman, J.H. The Hell Creek Formation and the Cretaceous-Tertiary Boundary in the Northern Great Plains. *Geological Society of America Special Paper* **361**, 503-510 (2002).

14 Bern, M., Phinney, B. S. & Goldberg, D. Reanalysis of Tyrannosaurus rex Mass Spectra. *J Proteome Res* **8**, 4328-4332, doi:10.1021/pr900349r (2009).

15 Buckley, M., Warwood, S., van Dongen, B., Kitchener, A. C. & Manning, P. L. A fossil protein chimera; difficulties in discriminating dinosaur peptide sequences from modern cross-contamination. *Proceedings of the Royal Society B: Biological Sciences* **284**, doi:10.1098/rspb.2017.0544 (2017).

16 Schweitzer, M. H., and Marshall, M. *The Complete Dinosaur, Second Edition*. Second edn, 281 (Indiana University Press, 2012).

17 Collins, M. J., Gernaey, A. M., Nielsen-Marsh, C. M., Vermeer, C. & Westbroek, P. Slow rates of degradation of osteocalcin; green light for fossil bone protein? *Geology*

[Boulder] **28**, 1139-1142, doi:10.1130/0091-7613(2000)028<1139:SRODOO>2.3.CO;2 (2000).

18 Briggs, D. E. & Summons, R. E. Ancient biomolecules: their origins, fossilization, and role in revealing the history of life. *Bioessays* **36**, 482-490, doi:10.1002/bies.201400010 (2014).

19 Wadsworth, C. & Buckley, M. Proteome degradation in fossils: investigating the longevity of protein survival in ancient bone. *Rapid Commun Mass Spectrom* **28**, 605-615, doi:10.1002/rcm.6821 (2014).

20 Cattaneo, C. Reliable identification of human albumin in ancient bone using ELISA and monoclonal antibodies. *American Journal of Physical Anthropology* **87**, 365-372 (1992).

21 Weser, U., Kaup, Y., Etspüler, H., Kenward, N. & Hedges, R. E. M. Biochemically and immunologically active alkaline phosphatase in archaeologically important bone samples. *Journal of Archaeological Science* **23**, 723-730, doi:10.1006/jasc.1996.0068 (1996).

22 Cappellini, E. *et al.* Proteomic analysis of a pleistocene mammoth femur reveals more than one hundred ancient bone proteins. *J Proteome Res* **11**, 917-926, doi:10.1021/pr200721u (2012).

23 O'Reilly, S., Summons, R., Mayr, G. & Vinther, J. Preservation of uropygial gland lipids in a 48-million-year-old bird. *Proceedings of the Royal Society B: Biological Sciences* **284**, doi:10.1098/rspb.2017.1050 (2017).

24 Edwards, N. P. *et al.* Infrared mapping resolves soft tissue preservation in 50 million year-old reptile skin. *Proc Biol Sci* **278**, 3209-3218, doi:10.1098/rspb.2011.0135 (2011).

25 Briggs, D. E. G., Kear, A. J., Martill, D. M. & Wilby, P. R. Phosphatization of soft-tissue in experiments and fossils. *Journal of the Geological Society of London* **150, Part 6**, 1035-1038 (1993).

26 Hou, X.-G., Stanley, G. D., Jr., Zhao, J. & Ma, X.-Y. Cambrian anemones with preserved soft tissue from the Chengjiang biota, China. *Lethaia* **38**, 193-203, doi:10.1080/00241160510013295 (2005).

27 Zhang, Z., Han, J., Zhang, X., Liu, J. & Shu, D. Soft-tissue preservation in the Lower Cambrian linguloid brachiopod from south China. *Acta Palaeontologica Polonica* **49**, 259-266 (2004).

28 Golubic, S., and H. J. Hofmann. . Comparison of Holocene and Mid-PreCambrian Entophosylidaceae (Cyanoophyta) in Stromatolitic Algal mats: Cell Division and Degradation. *The Journal of Paleontology* **50**, 1074-1082 (1976).

29 Schweitzer, M. H., Wittmeyer, J. L., Horner, J. R. & Toporski, J. K. Soft-tissue vessels and cellular preservation in Tyrannosaurus rex. *Science* **307**, 1952-1955, doi:10.1126/science.1108397 (2005).

30 Schweitzer, M. H., Zheng, W., Cleland, T. P. & Bern, M. Molecular analyses of dinosaur osteocytes support the presence of endogenous molecules. *Bone* **52**, 414-423, doi:10.1016/j.bone.2012.10.010 (2013).

31 Kaye, T. G., Gaugler, G. & Sawlowicz, Z. Dinosaurian soft tissues interpreted as bacterial biofilms. *PLoS One* **3**, e2808, doi:10.1371/journal.pone.0002808 (2008).

32 Organ, C. L. *et al.* Molecular phylogenetics of mastodon and Tyrannosaurus rex. *Science* **320**, 499, doi:10.1126/science.1154284 (2008).

33 Schweitzer, M. H. *et al.* Biomolecular characterization and protein sequences of the Campanian hadrosaur B. canadensis. *Science* **324**, 626-631, doi:10.1126/science.1165069 (2009).

34 Cleland, T. P. *et al.* Mass Spectrometry and Antibody-Based Characterization of Blood Vessels from Brachylophosaurus canadensis. *J Proteome Res* **14**, 5252-5262, doi:10.1021/acs.jproteome.5b00675 (2015).

35 Armitage, M. H. & Anderson, K. L. Soft sheets of fibrillar bone from a fossil of the supraorbital horn of the dinosaur Triceratops horridus. *Acta Histochem* **115**, 603-608, doi:10.1016/j.acthis.2013.01.001 (2013).

36 Pawlicki, R. & Nowogrodzka-Zagorska, M. Blood vessels and red blood cells preserved in dinosaur bones. *Ann Anat* **180**, 73-77 (1998).

37 Surmik, D. *et al.* Spectroscopic Studies on Organic Matter from Triassic Reptile Bones, Upper Silesia, Poland. *PLoS One* **11**, e0151143, doi:10.1371/journal.pone.0151143 (2016).

38 Pawlicki, R., and Wowogrodzka-Aagorska, M. Blood vessels and red blood cells preserved in dinosaur bones. *Annals of Anatomy* **180**, 73-77 (1978).

39 Pawlicki, R., Dkorbel, A. & Kubiak, H. Cells, collagen fibrils and vessels in dinosaur bone. *Nature* **211**, 655-657 (1966).

40 Pawlicki, R. Histochemical demonstration of DNA in osteocytes from dinosaur bones. *Folia Histochemica Et Cytobiologica* **33**, 183-186 (1995).

41 Lingham-Soliar, T. A unique cross section through the skin of the dinosaur Psittacosaurus from China showing a complex fibre architecture. *Proc Biol Sci* **275**, 775-780, doi:10.1098/rspb.2007.1342 (2008).

42 Lingham-Soliar, T. & Plodowski, G. The integument of Psittacosaurus from Liaoning Province, China: taphonomy, epidermal patterns and color of a ceratopsian dinosaur. *Naturwissenschaften* **97**, 479-486, doi:10.1007/s00114-010-0661-3 (2010).

43 Reisz, R. R. *et al.* Embryology of Early Jurassic dinosaur from China with evidence of preserved organic remains. *Nature* **496**, 210-214, doi:10.1038/nature11978 (2013).

44 Brown, C. M. *et al.* An Exceptionally Preserved Three-Dimensional Armored Dinosaur Reveals Insights into Coloration and Cretaceous Predator-Prey Dynamics. *Curr Biol* **27**, 2514-2521 e2513, doi:10.1016/j.cub.2017.06.071 (2017).

45 Embery, G. *et al.* Identification of proteinaceous material in the bone of the dinosaur Iguanodon. *Connect Tissue Res* **44 Suppl 1**, 41-46 (2003).

46 Gurley, L. R., Valdez, J. G., Spall, W. D., Smith, B. F. & Gillette, D. D. Proteins in the fossil bone of the dinosaur, Seismosaurus. *J Protein Chem* **10**, 75-90 (1991).

47 Masahiko Akiyama, a. & Ralph W. G. Wyckoff, a. The Total Amino Acid Content of Fossil Pecten Shells. *Proceedings of the National Academy of Sciences of the United States of America*, 1097 (1970).

48 Hare, P. E. & Hoering, T. C. *Biogeochemistry of amino acids*. (New York: Wiley, 1980., 1980).

49 Gaines, R. R., Briggs, D. E. G. & Zhao, Y. Cambrian burgess shale-type deposits share a common mode of fossilization. *Geology [Boulder]* **36**, 755-758, doi:10.1130/G24961A.1 (2008).

50 Oses, G. L. *et al.* Deciphering pyritization-kerogenization gradient for fish soft-tissue preservation. *Sci Rep* **7**, 1468, doi:10.1038/s41598-017-01563-0 (2017).

51 Towe, K. M. & Urbanek, A. Collagen-like Structures in Ordovician Graptolite Periderm. *Nature* **237**, 443, doi:10.1038/237443a0 (1972).

52 Cody, G. D. *et al.* Molecular signature of chitin-protein complex in Paleozoic arthropods. *Geology* **39**, 255-258, doi:10.1130/G31648 (2011).

53 Ehrlich, H. *et al.* Discovery of 505-million-year old chitin in the basal demosponge Vauxia gracilenta. *Sci Rep* **3**, 3497, doi:10.1038/srep03497 (2013).

54 Moczydłowska, M. Microstructure and Biogeochemistry of the organically preserved ediacaran metazoan sabellidites. *Journal of Paleontology* **88**, 224-239 (2014).

55 Voss-Foucart, M. F. [Paleoproteins of fossil shells of Dinosaur eggs from Upper Cretaceous deposits of Provence]. *Comp Biochem Physiol* **24**, 31-36 (1968).

56 Miller, M. F., 2nd & Wyckoff, R. W. Proteins in dinosaur bones. *Proc Natl Acad Sci U S A* **60**, 176-178 (1968).

57 de Jong, E. W., Westbroek, P., Westbroek, J. W. & Bruning, J. W. Preservation of antigenic properties of macromolecules over 70 Myr. *Nature* **252**, 63-64 (1974).

58 Wyckoff, R. W. & Davidson, F. D. Pleistocene and dinosaur gelatins. *Comparative Biochemistry and Physiology Part B: Comparative Biochemistry* **55**, 95-97 (1976).

59 Weiner, S., Lowenstam, H. & Hood, L. Characterization of 80-million-year-old mollusk shell proteins. *Proceedings of the National Academy of Sciences* **73**, 2541-2545 (1976).

60 Pawlicki, R. Metabolic pathways of the fossil dinosaur bones. Part V. Morphological differentiation of osteocyte lacunae and bone canaliculi and their significance in the system of extracellular communication. *Folia Histochem Cytobiol* **23**, 165-174 (1985).

61 Davies, K. L. Duck-Bill dinosaurs (Hadrosauridae, Ornithischia) from the North Slope of Alaska. *Journal of Paleontology* **61**, 198-200 (1987).

62 Ostrom, P. H., Macko, S.A., Engel, M.H., Silfer, J.A., Russell, D. Geochemical characterization of high molecular weight material isolated from Late Cretaceous fossils. *Advances in Organic Geochemistry* **16**, 1139-1144 (1990).

63 Muyzer, G., Sandberg, P., Knapen, M.H.J., Vermeer, C., Collins, M. Westbroek, P. . Preservation of bone protein osteocalcin in dinosaurs. *Geology* **20**, 871-874 (1992).

64 Ostrom, P. H., Macko, S.A., Engel, M.H., Russell, D. Assessment of trophic structure of Cretaceous communities based on stable nitrogen isotope analyses. *Geology* **21**, 491-494 (1993).

65 Cano, R. J., Poinar, H. N., Pieniazek, N. J., Acra, A. & Poinar, G. O., Jr. Amplification and sequencing of DNA from a 120-135-million-year-old weevil. *Nature* **363**, 536-538, doi:10.1038/363536a0 (1993).

66 Bada, J. L., Wang, X. S., Poinar, H. N., Paabo, S. & Poinar, G. O. Amino acid racemization in amber-entombed insects; implications for DNA preservation. *Geochimica et Cosmochimica Acta* **58**, 3131-3135, doi:10.1016/0016-7037(94)90185-6 (1994).

67 Moyer, A. E., Zheng, W. & Schweitzer, M. H. Microscopic and immunohistochemical analyses of the claw of the nesting dinosaur, Citipati osmolskae. *Proc Biol Sci* **283**, doi:10.1098/rspb.2016.1997 (2016).

68 Schweitzer, M. H. *et al.* Beta-keratin specific immunological reactivity in feather-like structures of the cretaceous alvarezsaurid, Shuvuuia deserti. *J Exp Zool* **285**, 146-157 (1999).

69 Mary H. Schweitzer, a. *et al.* Keratin Immunoreactivity in the Late Cretaceous Bird Rahonavis ostromi. *Journal of Vertebrate Paleontology*, 712 (1999).

70 Martill, D. M., Batten, D. J. & Loydell, D. K. A new specimen of the thyreophoran dinosaur cf. Scelidosaurus with soft tissue preservation. *Palaeontology* **43**, 549-559 (2000).

71 Armitage, M. Scanning Electron Microscope Study of Mummified Collagen Fibers in Fossil Tyrannosaurus Rex Bone. *CRS Quarterly* **38**, 61-66 (2001).

72 Wang, X., Zhou, Z., Zhang, F. & Xu, X. A nearly completely articulated rhamphorhynchoid pterosaur with exceptionally well-preserved wing membranes and 'hairs' from Inner Mongolia, Northeast China. *Chinese Science Bulletin* **47**, 226-230 (2002).

73 Greenblatt, C. L. *et al.* Micrococcus luteus -- survival in amber. *Microb Ecol* **48**, 120-127, doi:10.1007/s00248-003-2016-5 (2004).

74 Schweitzer, M. H., Chiappe, L., Garrido, A. C., Lowenstein, J. M. & Pincus, S. H. Molecular preservation in Late Cretaceous sauropod dinosaur eggshells. *Proc Biol Sci* **272**, 775-784, doi:10.1098/rspb.2004.2876 (2005).

75 Avci, R. *et al.* Preservation of bone collagen from the late Cretaceous period studied by immunological techniques and atomic force microscopy. *Langmuir* **21**, 3584-3590, doi:10.1021/la047682e (2005).

76 McNamara, M. E. *et al.* High-fidelity organic preservation of bone marrow in ca. 10 Ma amphibians. *Geology [Boulder]* **34**, 641-644, doi:10.1130/G22526.1 (2006).

77 Schweitzer, M. H. *et al.* Analyses of soft tissue from Tyrannosaurus rex suggest the presence of protein. *Science* **316**, 277-280, doi:10.1126/science.1138709 (2007).
78 Asara, J. M. *et al.* Interpreting sequences from mastodon and T. rex. *Science* **317**, 1324-1325, doi:10.1126/science.317.5843.1324 (2007).
79 Asara, J. M., Schweitzer, M. H., Freimark, L. M., Phillips, M. & Cantley, L. C. Protein sequences from mastodon and Tyrannosaurus rex revealed by mass spectrometry. *Science* **316**, 280-285, doi:10.1126/science.1137614 (2007).
80 Schweitzer, M. H., Wittmeyer, J. L. & Horner, J. R. Soft tissue and cellular preservation in vertebrate skeletal elements from the Cretaceous to the present. *Proc Biol Sci* **274**, 183-197, doi:10.1098/rspb.2006.3705 (2007).
81 Vinther, J., Briggs, D. E., Prum, R. O. & Saranathan, V. The colour of fossil feathers. *Biol Lett* **4**, 522-525, doi:10.1098/rsbl.2008.0302 (2008).
82 Justin, S. T., Karen, C., Dennis, R. B. & Nate, L. M. Probable Gut Contents within a Specimen of Brachylophosaurus canadensis (Dinosauria: Hadrosauridae) from the Upper Cretaceous Judith River Formation of Montana. *PALAIOS*, 624, doi:10.2110/palo.2007.p07-044r (2008).
83 Lingham-Soliar, T. & Wesley-Smith, J. First investigation of the collagen D-band ultrastructure in fossilized vertebrate integument. *Proc Biol Sci* **275**, 2207-2212, doi:10.1098/rspb.2008.0489 (2008).
84 Vinther, J., Briggs, D. E., Clarke, J., Mayr, G. & Prum, R. O. Structural coloration in a fossil feather. *Biol Lett* **6**, 128-131, doi:10.1098/rsbl.2009.0524 (2010).
85 Manning, P. L. *et al.* Mineralized soft-tissue structure and chemistry in a mummified hadrosaur from the Hell Creek Formation, North Dakota (USA). *Proc Biol Sci* **276**, 3429-3437, doi:10.1098/rspb.2009.0812 (2009).
86 McNamara, M. *et al.* Organic preservation of fossil musculature with ultracellular detail. *Proc Biol Sci* **277**, 423-427, doi:10.1098/rspb.2009.1378 (2010).
87 Christiansen, N. A., Tschopp, E. Exceptional stegosaur integument impressions from the Upper Jurassic Morrison Formation of Wyoming. *Swiss Journal of Geoscience* **103**, 163-171 (2010).
88 Zhang, F. *et al.* Fossilized melanosomes and the colour of Cretaceous dinosaurs and birds. *Nature* **463**, 1075-1078, doi:10.1038/nature08740 (2010).
89 Vullo, R., Girard, V., Azar, D. & Neraudeau, D. Mammalian hairs in Early Cretaceous amber. *Naturwissenschaften* **97**, 683-687, doi:10.1007/s00114-010-0677-8 (2010).
90 Bergmann, U. *et al.* Archaeopteryx feathers and bone chemistry fully revealed via synchrotron imaging. *Proc Natl Acad Sci U S A* **107**, 9060-9065, doi:10.1073/pnas.1001569107 (2010).
91 Lindgren, J. *et al.* Microspectroscopic evidence of cretaceous bone proteins. *PLoS One* **6**, e19445, doi:10.1371/journal.pone.0019445 (2011).
92 Elgin, R. A., Hone, D. W. E. & Frey, E. The extent of the pterosaur flight membrane. *Acta Palaeontologica Polonica* **56**, 99 (2011).
93 Glass, K. *et al.* Direct chemical evidence for eumelanin pigment from the Jurassic period. *Proceedings of the National Academy of Sciences of the United States of America* **109**, 10218 (2012).
94 Cadena, E. A. & Schweitzer, M. H. Variation in osteocytes morphology vs bone type in turtle shell and their exceptional preservation from the Jurassic to the present. *Bone* **51**, 614-620, doi:10.1016/j.bone.2012.05.002 (2012).
95 Greenwalt, D. E., Goreva, Y. S., Siljestrom, S. M., Rose, T. & Harbach, R. E. Hemoglobin-derived porphyrins preserved in a Middle Eocene blood-engorged mosquito. *Proc Natl Acad Sci U S A* **110**, 18496-18500, doi:10.1073/pnas.1310885110 (2013).

96 O'Malley, C. E., Ausich, W. I. & Yu-Ping, C. Isolation and characterization of the earliest taxon-specific organic molecules (Mississippian, Crinoidea). *Geology* **41**, 347-350, doi:10.1130/G33792.1 (2013).
97 Wysokowski, M. *et al.* Identification of chitin in 200-million-year-old gastropod egg capsules. *Paleobiology* **40**, doi:10.1666/13083 (2014).
98 Lindgren, J. *et al.* Skin pigmentation provides evidence of convergent melanism in extinct marine reptiles. *Nature* **506**, 484-488, doi:10.1038/nature12899 (2014).
99 Bertazzo, S. *et al.* Fibres and cellular structures preserved in 75-million-year-old dinosaur specimens. *Nat Commun* **6**, 7352, doi:10.1038/ncomms8352 (2015).
100 Lindgren, J. *et al.* Molecular composition and ultrastructure of Jurassic paravian feathers. *Sci Rep* **5**, 13520, doi:10.1038/srep13520 (2015).
101 Hone, D., Henderson, D. M., Therrien, F. & Habib, M. B. A specimen of Rhamphorhynchus with soft tissue preservation, stomach contents and a putative coprolite. *PeerJ* **3**, e1191, doi:10.7717/peerj.1191 (2015).
102 Alleon, J. *et al.* Molecular preservation of 1.88 Ga Gunflint organic microfossils as a function of temperature and mineralogy. *Nat Commun* **7**, 11977, doi:10.1038/ncomms11977 (2016).
103 Surmik, D., Rothschild, B. M. & Pawlicki, R. Unusual intraosseous fossilized soft tissues from the Middle Triassic Nothosaurus bone. *Naturwissenschaften* **104**, 25, doi:10.1007/s00114-017-1451-y (2017).
104 Vinther, J. *et al.* 3D Camouflage in an Ornithischian Dinosaur. *Curr Biol* **26**, 2456-2462, doi:10.1016/j.cub.2016.06.065 (2016).
105 Wiemann, J. *et al.* Dinosaur origin of egg color: oviraptors laid blue-green eggs. *PeerJ* **5**, e3706, doi:10.7717/peerj.3706 (2017).
106 Lee, Y. C. *et al.* Evidence of preserved collagen in an Early Jurassic sauropodomorph dinosaur revealed by synchrotron FTIR microspectroscopy. *Nat Commun* **8**, 14220, doi:10.1038/ncomms14220 (2017).
107 Poinar, G., Jr. Fossilized Mammalian Erythrocytes Associated With a Tick Reveal Ancient Piroplasms. *J Med Entomol* **54**, 895-900, doi:10.1093/jme/tjw247 (2017).
108 Schroeter, E. R. *et al.* Expansion for the Brachylophosaurus canadensis Collagen I Sequence and Additional Evidence of the Preservation of Cretaceous Protein. *J Proteome Res* **16**, 920-932, doi:10.1021/acs.jproteome.6b00873 (2017).
109 Gradstein, F. M. *The Geologic time scale 2012. [electronic book]*. (2012).
110 Pevzner, P. A., Kim, S. & Ng, J. Comment on "Protein sequences from mastodon and Tyrannosaurus rex revealed by mass spectrometry". *Science* **321**, 1040; author reply 1040, doi:10.1126/science.1155006 (2008).
111 Lindgren, J. *et al.* Interpreting melanin-based coloration through deep time: a critical review. *Proc Biol Sci* **282**, 20150614, doi:10.1098/rspb.2015.0614 (2015).

Chapter 2: Bone acquisition, cataloguing, and preparation

Contents

Figures

Tables

Curating a Collection

Prior to conducting analyses on any sizeable collection, a cataloguing system is useful to help organize, retrieve, and transfer basic collection data for each specimen. When this research project began, so few specimens were in hand that at first no local records were required. One could simply keep in mind the identity and origin of each bone. However, as the collection grew over the years, unlabeled, poorly labeled, and poorly catalogued specimens became a source of confusion that required remedy.

In addition, some journals require that all fossil or archaeological specimens described in a manuscript submitted for publication must have an accession number that ties to a permanent collection. To address these issues, three bone sample acquisition efforts arose: 1. Collaborations were developed with permanent repositories that house ancient bone collections, 2. Basic collection data was requested from each repository which were compiled for each bone (or other) sample, 3. Adequate collection data were recorded for all material from the field, and when acquiring a fossil from the open market, including any process that transferred ownership of the acquisition to a permanent repository for proper cataloguing and storage. In this way, other researchers would be able to replicate any analytical procedures—subject to the authority of the repository—performed on the same specimen.

The Society of Vertebrate Paleontology (SVP) posts a Best Practice fact sheet that outlines appropriate accessioning principles[1]. Similar ideologies should apply to archaeological as well as paleontological collections. As an example, Best Practice states that an acceptable repository should have as its aim the storage and accessibility of each fossil's contextual data for researchers to access. Without this option, the core scientific principle of falsifiability would be hindered. The SVP "strives to promote reproducibility of research results by ensuring that scientifically important vertebrate fossils and their

contextual data are placed permanently in public-trust repositories to make them always accessible for researchers seeking to verify past results and to conduct new studies[1].”

“Contextual data” include: geographic location of the find (down to Global Positioning System (GPS) coordinates if possible), stratigraphy including precise depth below ground surface (or above sea level if possible), photographs that show scale, taken while the specimen was in situ and after excavation where appropriate, plus any field identifications and field numbers. In principle, any researcher should be able to track down the specimen using the name of the repository and the accession number of the specimen noted in research publications that describe that specimen. Another important service of the museums and universities that typically comprise repositories is that of ownership. Legal rights to conduct research are required to access and study the specimens within its care.

Norton Priory, UK

Using the SVP’s philosophy of practice, collaborations with various repositories were forged. One of the first and possibly most important (for reasons that will become plain in the next chapter, which describes the use of Second Harmonic Generation Imaging of ancient bone) collection made available for this thesis project is Norton Priory. Located near the town of Runcorn in Cheshire, England, the collection is housed on the site of a medieval abbey. The abbey complex originated in the 12th century, was active for 900 years, and “is the most excavated monastic site in Europe[2].” It was discontinued in 1536 by the dissolution of the monasteries under King Henry VIII.[1]

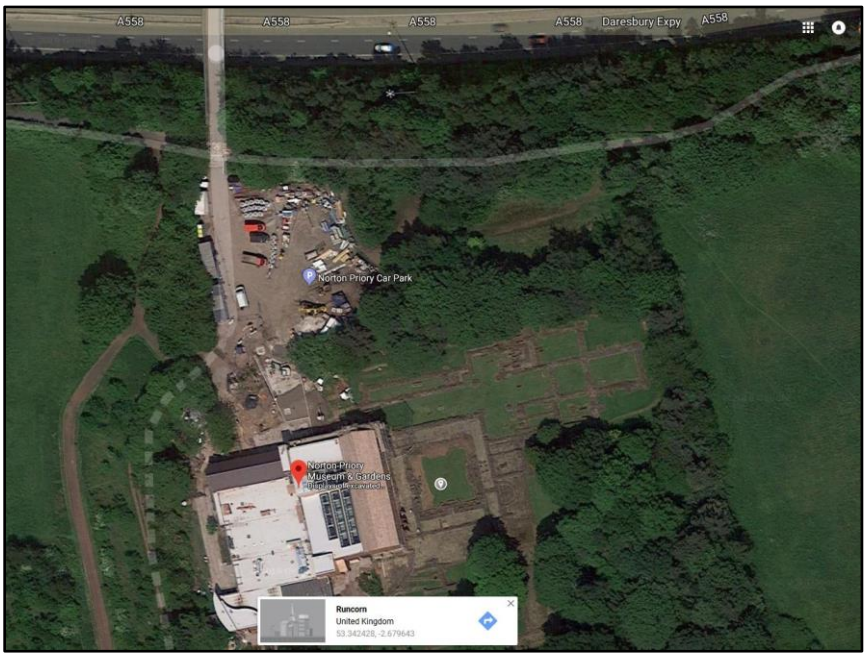

Figure 2.1 | Aerial View of Norton Priory. NP bones were excavated from approximately 53º20’32” N, 2º40’44”W.

Norton Priory houses and catalogs 70,000 medieval bones and other artifacts, with seasonal excavations ongoing. Bovine and human bone samples from Norton were generously supplied to the University of Liverpool (UoL) for this thesis research. Table 3 summarizes some relevant contextual data for the specimens loaned to the UoL from Norton Priory for this research project. Additional catalogue data that includes all bone samples used in this project are recorded in a Google document viewable via the world wide web[3].

These Norton Priory bones proved strategically important to this research. In establishing the applicability and importance of techniques that explore the primary origin of protein and isotopic remnants in ancient bone, medieval samples serve to bridge a critical time gap between modern and very ancient samples. For example, Chapter 3 will describe how four separate techniques reliably detect collagen in medieval human

Specimen number	Taxon/Description	Stratigraphy	Excav. Year	Excavator
NP71_12_9 (field#) (Acces. #: 2005.1/5/34)	*H. sapiens* ulna	Skeleton 35, Grave 34, Trench 12, context 9	1971	Greene, P.
NP71_13_9 (field #) (Acces. #: 2005.1/5/29)	*H. sapiens* fibula	Skeleton 29, Grave 28, Trench 13, context 9	1971	Greene, P.
NP73_34_81 (sk101)	*H. sapiens* rib	Trench 34, context 81	1973	Greene, P.
NP77_109_34 (field #)	Bovine radius	Trench 109, context 34	1977	Greene, P.
NP77_109_32 (field #)	?	Trench 109, context 32	1977	Greene, P.
NP77_109_5_1 (field #) (Acces. #: 2005/1/71)	Bovine radius	Trench 109, Context 5	1977	Greene, P.
NP77_109_5_2 (field #) (Acces. #: 2005/1/71)	Bovine tibia	Trench 109, Context 5	1977	Greene, P.
NP77_109_5_3 (field #) (Acces. #: 2005/1/71)	Bovine femur	Trench 109, Context 5	1977	Greene, P.
NP77_109_52 (field #)	Bovine humerus	Trench 109, context 52	1977	Greene, P.
NP14-4-402 Pagets (field#)	*H. sapiens* right femur, proximal shaft	medieval; no stratigraphy	2014	Greene, P.
NP14-4-402 Non-pagets (field #)	*H. sapiens* right femur, central shaft	medieval; no stratigraphy	2014	Greene, P.

Table 2.1 | Eleven bone specimens from the Norton Priory Collection. Column one identifies each specimen with its field and accession number, where assigned. NP means "Norton Priory". Pagets refers to a collagen-related bone disease (see text). "Sk" means "skeleton," and refers to one of the articulated skeletons. During excavation, a single field number can identify a bagged assortment of bones found in a single context. Thus, NP14-4-402 is assigned to two different human femora, one affected by an ancient form of Paget's disease and the other non-affected, or normal. Additional collection data were recorded on a larger, digitally maintained spreadsheet.

and bovine bones from Norton Priory. This step establishes for the first time the use of Second-Harmonic Generation (SHG) as a tool to investigate ancient collagen remnants in even older bone samples.

Figure 2.2 shows two disarticulated human femur bone fragments, both designated with the field number NP14_4_402 because they were excavated near to one another. These two bones were selected from re-buried remains cast off from a 1970's excavation at Norton. Archaeologist Carla Burrell of Liverpool John Moore's University selected the bones during the 2015 summer dig season as part of a research collaboration investigating Paget's disease in ancient bones. For some reason skeletons found in Norton Priory show high percentage of affected individuals over many years. In modern cases, the disease

seems to have genetic and environmental causative factors. Symptoms include bowed leg bones (femur, tibia, fibula) from weakened bone structure caused by irregular collagen fibre construction within bone tissue. One of the NP14_4_402 femurs was not affected, and the other was affected. Because of their reburial, their original contextual stratum could not be determined, and thus firm dates could not be established for these. However, they hold value even without age assignments, for example as subjects to test methods that explore ancient Paget's disease in bone. Each bone was sectioned (described below) for microscopy to ascertain if the ability of SHG to image collagen fibre structure in modern bone would reveal collagen irregularities in ancient affected versus ancient non-affected bone. Those resulting SHG images are presented in Chapter 3, while Figure 2.2 here illustrates some of the Norton Priory human samples.

Figure 2.2 | Sample of Norton Priory bones: two femurs with field number NP14_4_402. a, Femur head and partial shaft from a non-affected (i.e., non-Pagets disease) Medieval human. **b**, Partial femur shaft of a Pagets-like disease affected human, showing characteristic bowing or curvature. Both bones were supplied to the UoL for SHG imaging. Photo Credit: Dr Carla Burrell, Liverpool John Moore's University.

A rib fragment from skeleton 101, field number NP73_34_81, was particularly important in establishing SHG as a relevant and useful tool for ancient bone collagen

visualisation. Collaborators at the University of Nottingham processed the rib for protein sequencing. It belongs to one of the 130 or so articulated skeletons excavated from Norton Priory.[4] Protein sequencing is regarded as the best method and 'gold standard' for collagen-specific detection in ancient bone. Thus, Chapter 3 will show that the SHG detection of collagen from this NP73 rib fragment combined with collagen sequencing from the same rib demonstrate that SHG supplies novel information about ancient bone collagen.

Radiocarbon dates for five NP bone samples (NP77_109_34, NP77_109_32, NP77_109_5_1, NP77_109_5_2, NP77_109_5_3) were originally obtained by NP or other research entities that partnered with NP. The radiocarbon age date for one of them (NP77_109_32) is confirmed herein, using a different laboratory than the original analysis. The advantage of importing already established radiocarbon ages into this project, and confirming those analyses with new ones, is that it permits a comparative benchmark for new techniques, results, and analyses. Samples with established ages have the potential to reveal age-related isotopic differences and even to contribute results toward resolution of the ancient bone collagen debate described in Chapter 1.

University of Leicester, UK

The earliest artifacts from Norton Priory graves or middens span as far back as about AD650. Bone samples under the care of the University of Leicester are even older. The University of Leicester houses artifacts recently excavated from a Hallaton shrine.[5] The shrine consists of ritualistic burial pits just outside the village of Hallaton and just outside Castle Hill Camp[6], Leicestershire, UK, approximately 22km SE of Leicester. Castle Hill is the remains of a classic mott and bailey hill fort of post-Norman Conquest (i.e. post-AD1066) construction, but the Hallaton shrine hails from the Roman Conquest of AD43.

Figure 2.3 shows a Google maps image of the general location for the Hallaton shrine, located along the side of a low hill. British and a few Roman silver coins, a bowl, helmet, *Canus sp* carcasses and many *Sus scrofa* (wild boar) bones were buried by indigenous Celts as part of religious votive and feasting activities possibly related to the Roman invasion itself[7].

Figure 2.3 | Aerial View of Hallaton. Hallaton village is seen top right, the Norman conquest Castle Hill fort at top left, and the Roman Era votive site between and south of these. *Sus scrofa* bones were excavated from the votive site at approximately 52º33;20 N, 0º50'30" W, as estimated from Score (2012)[7].

Wild boar bone remnants from this votive site were made available to the UoL for this research. Archaeological investigations conducted by the nearby University of Leicester combined samples of a porcine metatarsal and rib, both sharing the field number XA102_2001_ 307_91_3, for carbon dating. A jaw and ischium from the same archaeological context, sharing the field number XA102_2001_98, were also carbon dated together. Both carbon ages matched and also confirm the age of the deposit based on chronological data printed on the coins associated with the burial. The analysis of collagen in NP and Hallaton bones—separated by about a millennium, firmly dated

archaeologically, and found in broadly similar burial contexts—provides relevant material to test the applicability of new techniques to investigate research questions like bone diagenesis or collagen decay in ancient bone.

Earth History Research Center, USA

The Earth History Research Centre operates under the authority of the Southwestern Adventist University system in the United States. In addition to funding and publishing research in historical biology and in paleontology and geology, the Centre curates various artifacts, mostly of paleontological interest. The centre maintains a collection of bones excavated during the 1993-1994 Pacific Gas Transmission/Pacific Gas and Electric Pipeline Expansion Project that installed a gas pipeline that spans from the US border with Canada to southern California. The locations and identities of all the fossils from this

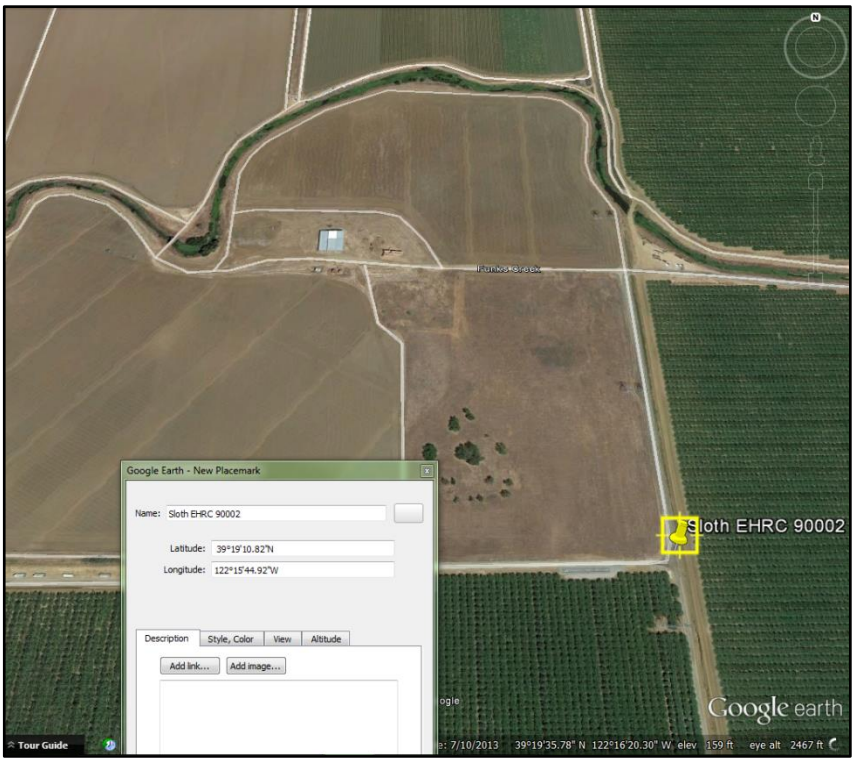

Figure 2.4 | Aerial View of site of the *Megatherium* excavation, Northern California. EHRC 90002 was found in Colusa County at approximately 39°19'11" N, 122°15'45' W in the Pleistocene Red Bluff pediment[8] under the direction of Lee Spencer in 1994.

excavation were described in an official document prepared by California-based Paleo Environmental, Inc., under the employ of Bechtel Corporation.[9] Two fossils retained from this project reached back further into the past to provide Ice Age samples for various analyses.

A fossil *Megatherium americanum* (giant ground sloth) was the most impressive fossil preserved from the whole pipeline project. Its disarticulated skeletal remnants include portions of ribs, limb bones, some vertebrae, the mandible, and most notably the entire hip girdle. Figure 2.4 Shows some of the *Megatherium* bones, designated EHRC 90002 (Earth History Research Center), and Figure 2.5 shows the hip girdle and some associated bones in storage on the campus of Southwestern Adventist University in Keane, TX. Some of the smaller, less significant bone fragments were supplied for this thesis research.

Figure 2.5 | *Megatherium americanum* EHRC 90002. a, Hip girdle. **b**, Storage drawer housing assorted sloth bones including mandible. **c**, Proximal rib breakage exposes trabecular bone, showing no sedimentary infill, and recently broken white cortical bone, showing no mineralisation. **d**, Author holds same rib as in **c**.

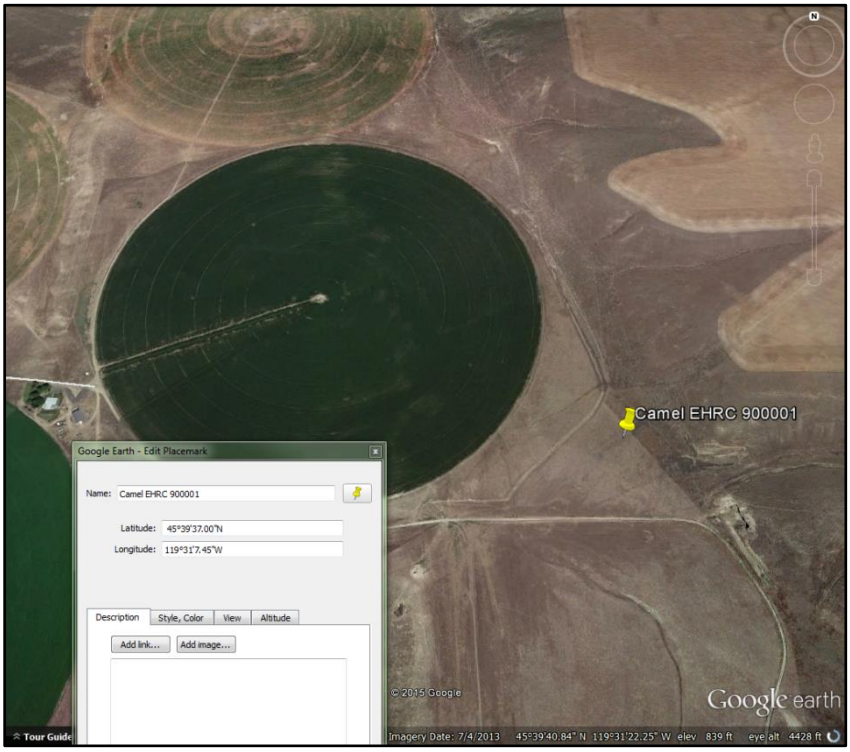

Figure 2.6 | Aerial View of site of camelid EHRC90001, Northern Oregon. EHRC 90001 was found in Morrow County, Oregon at approximately 45°39' 37" N, 116°31' 7.45" W in the Pleistocene Palouse Formation.

The accession number EHRC90001 designates few and relatively fragile remains of a camelid excavated during the PGT PG&E pipeline project. It came from the Pleistocene Palouse Formation[10], essentially a massive windblown silt deposit, in Morrow County, Oregon. The bone fragments retain grey silt matrix that loosely adhered to their exteriors and partly penetrated exposed and porous spaces within the camelid bones. Some silt was scraped off some of the bones using a clean analytical spatula and spectroscopically examined for use as an experimental control.

In addition to these two Pleistocene bone samples, two older samples of interest were acquired during the course of this research. Each sample was donated to and catalogued by the EHRC. These include a portion of a *Triceratops prorsus* brow horn, accessioned as

EHRC90003. It was excavated by John Parsons in August 2009 from the Cretaceous Lance Formation outcropping 15mi. N of Lance Creek, Wyoming, USA.

The fourth set of fossils is the only non-bone set analysed in this project. Upon the discovery that extant brachiopods use a version of collagen as their proteinaceous binding agent for the biomineralisation of shell, exposures of well-preserved fossil brachiopods were sought with the intent to acquire brachs, test the sensitivity of collagen detection

Figure 2.7 | Bones and shells curated by the Earth History Research Center (EHRC). a, Pleistocene camelid EHRC90001 shows gray coloured silt adhered to most of the unknown limb bone fragments. **b**, Pleistocene *Megatherium* EHRC90002 broken rib fragments expose what looks like still-red dried blood remnants. **c**, Devonian brachiopod *Mucrospirifer sp.* shells EHRC90004. **d**, Cretaceous *Triceratops* horn core EHRC90003 shows reddish remnants of matrix on exterior, and darkened but still porous trabecular bone.

techniques, explore their carbon isotopes, and compare any detectable with vertebrate collagen from various contexts. Six samples of extinct brachiopod *Mucruspirifer thedfordensis* were collected in 2011 from Devonian Hamilton Group exposures on the bank of the Ausable River in Ontario, Canada. They were donated to this research by excavator Martin Legaamate, and three were curated as EHRC90004. Figure 2.7 shows the four EHRC samples used during this thesis research.

Glendive Dinosaur and Fossil Museum, USA

Glendive Dinosaur and Fossil Museum (GDFM) is a privately owned museum in the city of Glendive, Montana. It conducts summertime paleontological digs in fossil-rich

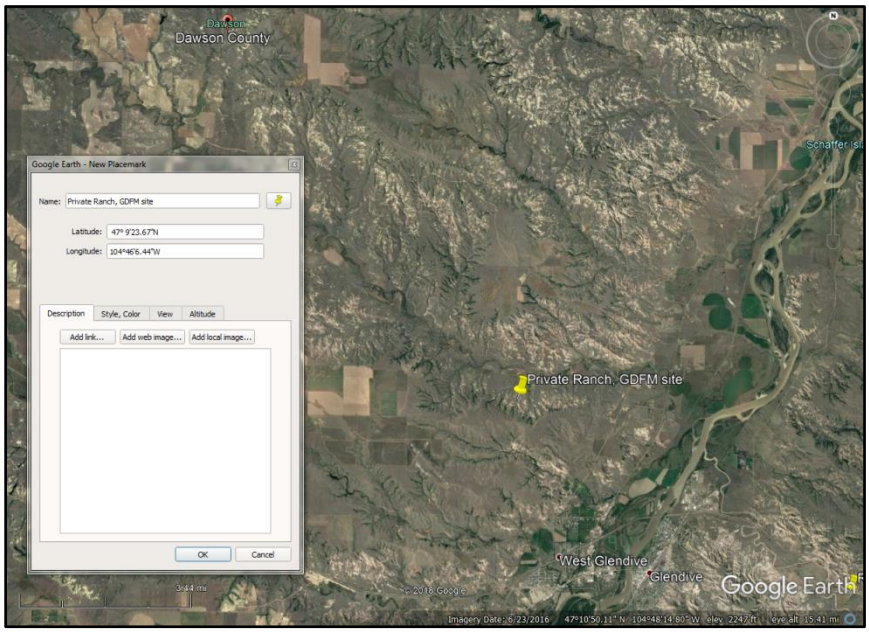

Figure 2.8 | Aerial view of a private ranch property GDFM fossil excavation site near Glendive, Dawson County, MT.

surrounding countryside, with its outcrops of the Hell Creek Formation, famous for vertebrate fossils of exceptional preservation. Figure 2.7 encompasses private ranch land in Dawson County, MT from which all specimens shown in Table 4 below except GDFM18.001 and GDFM12.004 were collected. GDFM18.001 is described below, and

GDFM12.004 was collected from museum-owned property adjacent to the city of Glendive, from which the Museum conducts its summer digs.

The Museum preserves and curates fossils mostly from its own collection efforts, and makes appropriate specimens available for research and displays. Table 4 summarizes six different dinosaur fossil fragments that the GDFM generously supplied to this research project.

Specimen number	Taxon/Description	Stratigraphy	Excav. Year	Excavator
HCTH06 (GDFM12.001)	*Triceratops sp.*/Horn core	Maastrichtian, Hell Creek	2012	Anderson, K.
GDFM03.001	*Triceratops*/Femur	Maastrichtian, Hell Creek	2003	Kline, O.
GDFM08.011	*Triceratops*/Femur	Maastrichtian, Hell Creek	2008	Kline, O.
GDFM04.001	Hadrosaurid/Femur	Maastrichtian, Hell Creek	2004	Kline, O.
GDFM18.001	*Edmontosaurus annectens*/Femur	Maastrichtian, Lance	2017	Stout, A.
GDFM12.004	Unknown/Limb fragment	Maastrichtian, Hell Creek	2012	Kline, O.

Table 2.2 | Six bone fossil specimens from the Glendive Dinosaur and Fossil Museum (GDFM) Collection. Column one identifies each specimen with its field and accession number, where assigned. HCTH06 refers to a fragment of the GDFM12.001 *Triceratops* horn core

The first and fifth entries from Table 4 represent unique situations. First, the originally intact *Triceratops horridus* brow horn core GDFM12.001 was sectioned and submitted to various entities for different analyses. HCTH06 designates a fist-sized portion of GDFM12.001 that engendered interest for bone collagen remnant exploration when a pliable sheet of apparent connective tissue plus osteocyte remnants were extracted from it and described by Armitage and Anderson (2013)[11]. A separate fragment of GDFM12.001 was donated to UoL. Some of this was sacrificed for carbon isotope

analysis, the results of which are described in chapter 6. Other portions were prepared as described below for microscopic and spectroscopic analyses.

The fifth entry in Table 4 notes GDFM18.001, which was acquired through commercial vendor and discoverer Alan Stout. He excavated the femur and supplied the GDFM with sufficient collection data to authenticate and curate the find. This *Edmontosaurus* femur was selected on the basis of two characteristics. Its white color from apparently original (not mineralized) bone material, and its porous (not infilled with sediment or mineral deposits) trabecular spaces show high quality preservation. Also, its large size increases the chances of discovering original biochemistry, and matches the large sizes of other spectacular finds already published[11-14].

Figure 2.9 | Dinosaur bones curated by the Glendive Dinosaur and Fossil Museum (GDFM). **a**, GDFM 12.004. **b**, GDFM 18.001. **c**, GDFM 03.001. **d**, GDFM 08.001. **e**, GDFM 04.001. Arrow points to the hole from which a core was extracted for carbon isotope analysis. **a** and **b** photographed and stored by the author on behalf of the University of Liverpool. **c**-**e** photographed by GDFM. **d** and **e** include a black 6in (15.24cm) ruler for scale.

Hansen Research Station, USA

Chapter 6 describes the geology of the Lance Formation as an equivalent of the Hell Creek Formation (HCF). Two reasons to consider them equivalent include the fact that they show very similar lithologies and very similar dinosaur and other fossil species. The main practical difference between the two is geographical. Given the fact that some of the most notable fossils to preserve original biochemistry were excavated from the HCF, opportunities to access both HCF through collaboration with GDFM as described above, and Lance Formation fossils were pursued.

Hansen Ranch, owned by the Hansen family and located in far East Wyoming in the Powder River Basin, includes a large segment dedicated to the Hansen Research Station (HRS). At least 50,000km^2 of bone beds contain over 16,000 catalogued and mostly disarticulated bones, teeth, and bone fragments within the HRS Cretaceous badlands deposits[15].

For almost two decades Hansen Ranch has directed an arrangement whereby fossils excavated from HRS during summer dig sessions are catalogued and stored during the remaining months of the year at facilities on the campus of Southwestern Adventist University (SWAU) in Keane, Texas. Since then, SWAU has pioneered technologies in fossil record-keeping, including the use of real-time kinematic (RTK) GPS to pinpoint the endpoints, outline, and axis of each bone to centimeter-scale precision[16]. Photographs are then mapped to a digital render of the position of each fossil *in situ*. Figure 2.9a and b show 2-D renders of the 3-D visual file. These data are used to curate three dimensional digital models called Virtual Bone Beds. They show the emplacement of each of thousands of bones thus far excavated from the dinosaur graveyards.

Table 5 shows the three HRS bone samples used in this research. In general appearance, some of the HRS dinosaur bone samples from the Lance formation are

heavier and darker than the GDFM dinosaur bone samples from the Hell Creek Formation, indicating more extensive mineralisation.

Specimen number	Taxon/Description	Stratigraphy	Excav. Year	Excavator
HRS08267	*Edmontosaurus annectens*/Unknown frag	Maastrichtian, Lance	2007	Schwartzer, L.A.
HRS26095	*Edmontosaurus annectens*/Caudal vertebrae	Maastrichtian, Lance	2017	Gray, S.
HRS19114	Unknown/limb fragment	Maastrichtian, Lance	2012	Nelson, D.

Table 2.3 | Three bone fossil specimens from the Hansen Research Station (HRS) Collection.

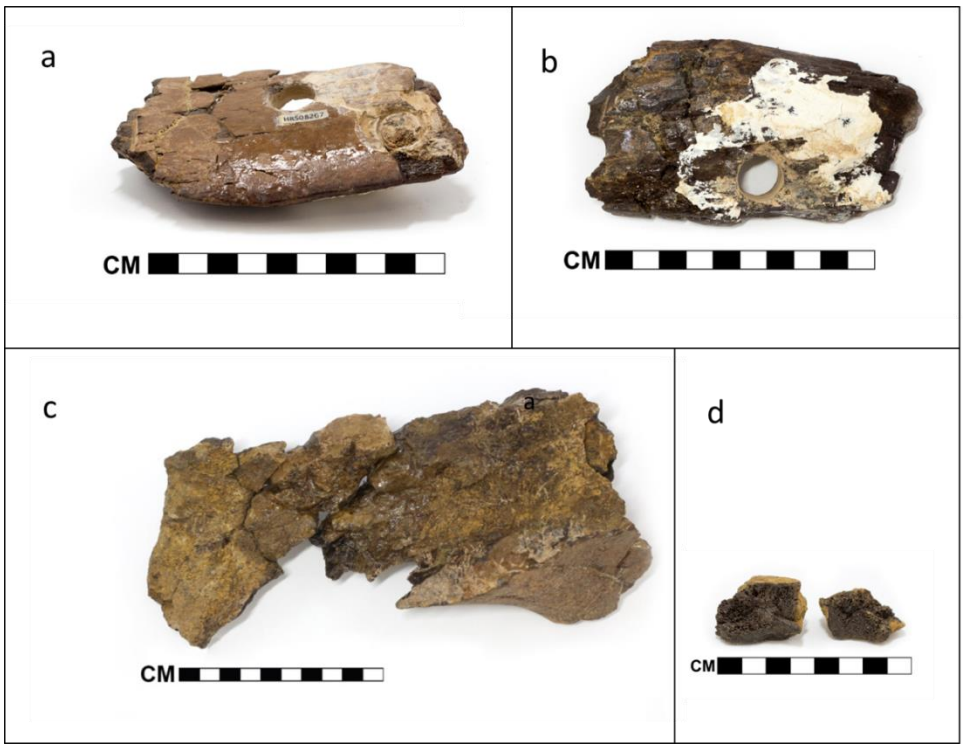

Figure 2.10 | Dinosaur bones curated by Hansen Research Station (HRS). a, HRS08267 exterior view. Shiny surface indicates cyanoacrylate residue. **b**, HRS08267 obverse, showing white PaleoPutty. Hole indicates an extraction site to access interior bone, thus avoiding treatments. **c**, HRS19114. **d**, HRS26095, also shown in Figure 2.11.

Figure 2.9 includes images captured using the photography procedures described below of the three HRS bone samples listed in Table 5. The bones were initially selected

for isotope analysis on the on the basis of their unsuitability for mounting and display. HRS houses type specimens, including a rare *Nanotyrannus*. HRS and SWAU comply fully with the International Commission on Zoological Nomenclature (ICZN) Recommendation 72, which provides guidelines for accessibility for these particularly significant fossils. For example, Recommendation 72F.3 states that "Every institution in which name-bearing types are deposited should…make them accessible for study[17]." HRS makes their collections accessible both digitally, via www.fossil.swau.edu, and physically. Figure 2.11 shows an example of some of the state-of-the-art digital representations, using HRS26095 as seen in Table 5.

Carnegie Museum, USA

Chain of custody for three tiny dinosaur bone fragments, apparent remnants of a prior project, was traced back to Carnegie Museum (CM), Pittsburgh, Pennsylvania. This is the fourth largest fossil collection in North America, with over 100,000 specimens[18]. The bones on loan were excavated among some of the first dinosaur finds in the USA, from Upper Jurassic deposits. Back then, during the famous 'Bone Wars' of the Western USA, very few records were kept as workers strove to make the next big find. As a result, catalogue data for these fossils are scarce. The online database for all CM collections recently migrated to www.idigbio.org/portal/search.

Figure 2.11 | Hansen Research Station HRS26095 visual record. a, Aerial view of excavated bones in "Triceratops 2 Quarry". Each bone and tooth's position *in situ* is digitally recorded with multiple RTK GPS measurements, shown as green circles for HRS26095. The quarry was named after the Triceratops skull visible near the bottom. **b**, HRS26095 *Edmontosaurus annectens* tail vertebra in burial context alongside other tail vertebrae. Scale bar is 1m. **c**, On-site photograph with basic field data, freely accessible online for all of over 16,000 fossils thus far excavated at HRS. Image credit: www.fossil.swau.edu. **d**, HRS26095 fragments on loan to UoL, photographed as per below, and selected for study because the peculiarly dark interior trabecular bone.

Specimen number	Taxon	Stratigraphy/Formation	Excav. Year	Excavator
CM000088	*Stegosaurus sp.*	Tithonian, Morrison	1899	Wortman, J.L.
CM021728	*Diplodocus longus*	Tithonian, Morrison	~1901-1906	Douglass, E.
CM000094	*Diplodocus carnegii*	Tithonian, Morrison	1900	Peterson, O.A./Gilmore, C.W.

Table 2.4 | Three bone fossil specimens from the Carnegie Museum (CM) Collection.

Table 6 summarizes basic data, checked against the database, for the three CM fossils on loan to UoL for this project. *Diplodocus* CM021728 came from Dinosaur National Monument, Utah. *Diplodocus* CM000094 (CM 94) and Stegosaurus CM 88 came from Sheep Creek site, Quarry D, in Wyoming. The online Specimen Record for the sauropod

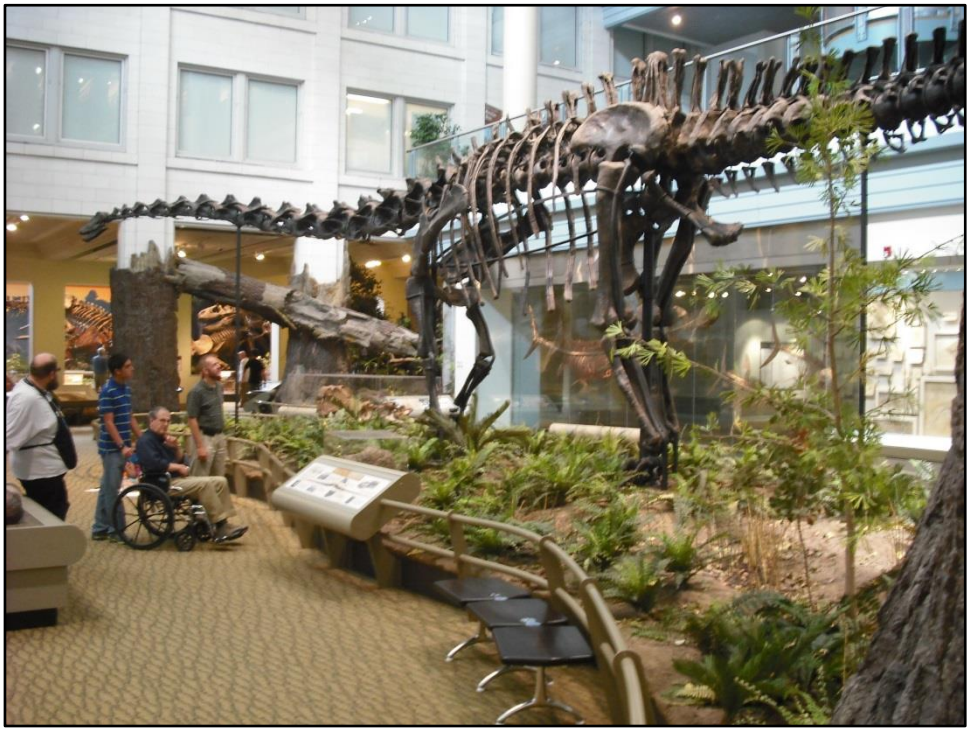

Figure 2.12 | Iconic *Diplodocus* mount at Carnegie Museum includes portions of CM000094.

Diplodocus carnegii CM000094 lists many bones under this single number. The practice of assigning a separate number to each individual bone, as has been employed by HRS

and other modern repositories, was not yet developed when these finds were catalogued before 1906. CM000094 include the entire recovered carcass, including nine cervical vertebrae, nine dorsal vertebrae, sacrum, 39 caudal vertebrae, ribs, five chevrons, scapulae-coracoids, sternal plates, ilia, pubes, ischia, left Femur, right tibia, right fibula, right astralagus (talus), and a complete right pes, or foot. Portions of CM 94 (*D. longus*) were incorporated into the iconic exhibit mount of *Diplodocus carnegii* on display for over a century, as shown in Figure 2.12. The majority of the mount is CM 84, discovered in the same location and quarry as CM 94.

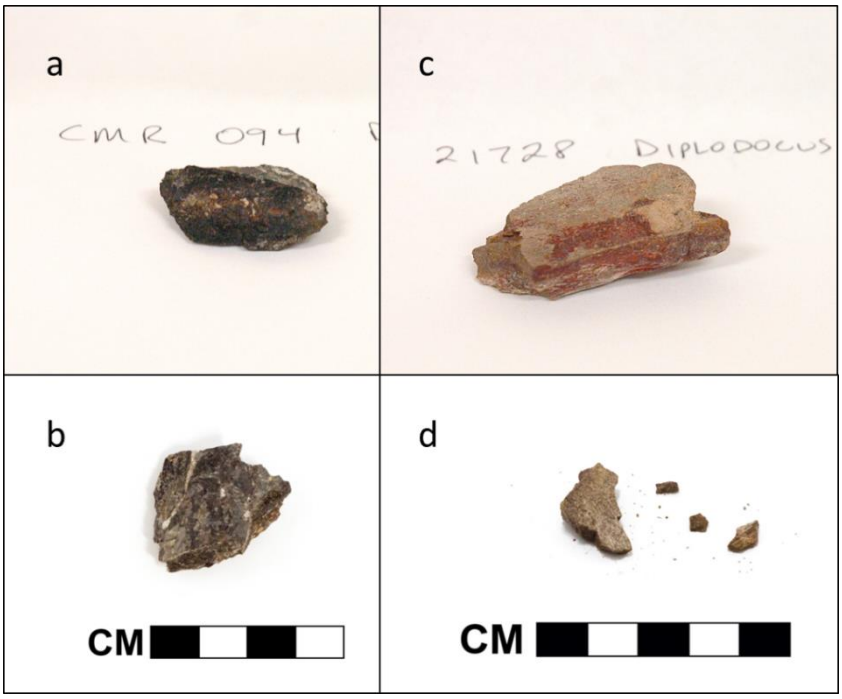

Figure 2.13 | Dinosaur bones curated by Carnegie Museum. a, CM000094 prior to sacrificing a portion for isotope analysis. **b**, CM000094 remaining after portion sacrificed for isotope analysis, and after proper photography procedures were incorporated. **c**, CM21728 prior to sacrificing a portion for isotope analysis. **d**, CM21728 remaining after portion sacrificed for isotope analysis, and after proper photography procedures were incorporated.

Figure 2.13 shows the tiny fractions that remain after destructive analyses reported herein. No part of CM 88 remains, as unfortunately what little was originally available was sacrificed for isotope analysis.

Photography

The most thorough documentation procedures for cataloguing include photographs of each item both *in situ* and, after cleaning, show metric scale. Therefore when the numbers of various bones on loan to the University of Liverpool for this project grew, it became apparent that local photography was required to properly identify collection samples. A light box of approximately $3m^3$ was constructed using reinforced cardboard repurposed from crating material. The interior was spray painted white. One large opening in the front permits the camera access to the artifacts placed inside. Each of two large windows on opposite sides was covered with a sheet of white banner paper to diffuse light, thereby reducing shadow. A hinged, paper-covered frame was affixed over the top of the light box to give the option of using unshaded or shaded light from the top.

Figure 2.14 | Light box. Construction of a light box was essential to achieve optimum lighting for sample photography of each suitable fossil fragment on loan.

A large sheet of banner paper was suspended across the back and bottom surfaces to remove corner shadows. Three OttLight (Tampa, FL) Natural Daylight LED Flex Desk Lamps, each of which emits full spectrum white light with a colour temperature of 6500K and a colour rendering index (CRI) of 96%, were positioned on the sides and top of the light box during photography. A Canon EOS 5D Mark III Digital SLR Camera equipped with a Canon EF 50mm f/1.8 STM lens was used. F-stops and ISO speeds were adjusted differently during various photo sessions. Each photograph has an accompanying file that lists these and other data. Scale bars of 10cm were printed and laminated to include beside each photographed sample. The physical scale bar, often seen out of the focal plane of the sample, was replaced with a digital scale bar using Photoshop. Photoshop was also used to white-balance each background. Ideally, each sample has its accession number painted directly onto the bone fragment's outer surface. Some partnering repositories did this with samples of sufficient size, but for samples too small to accommodate such markings, a fossil I.D. card was created and photographed alongside each sample fragment. The cards were digitally removed from each photograph prior to publication. Figure 2.15 illustrates the photography process with example photographs of a dinosaur bone and its locally-held fragment, accompanied by its I.D. card.

Bone Preparations

First, bone samples were prepared for minimally destructive protein-sensitive SHG microscopy and Raman IR spectroscopy. The collections described above supplied samples of each bone listed in the Chapter 2 Tables, plus those described in the text above and summarized in one large Google doc spreadsheet[3]. No whole bones were supplied—only bone fragments. Some samples, in particular dinosaur bones, were quite large, while most were very small and relatively fragile.

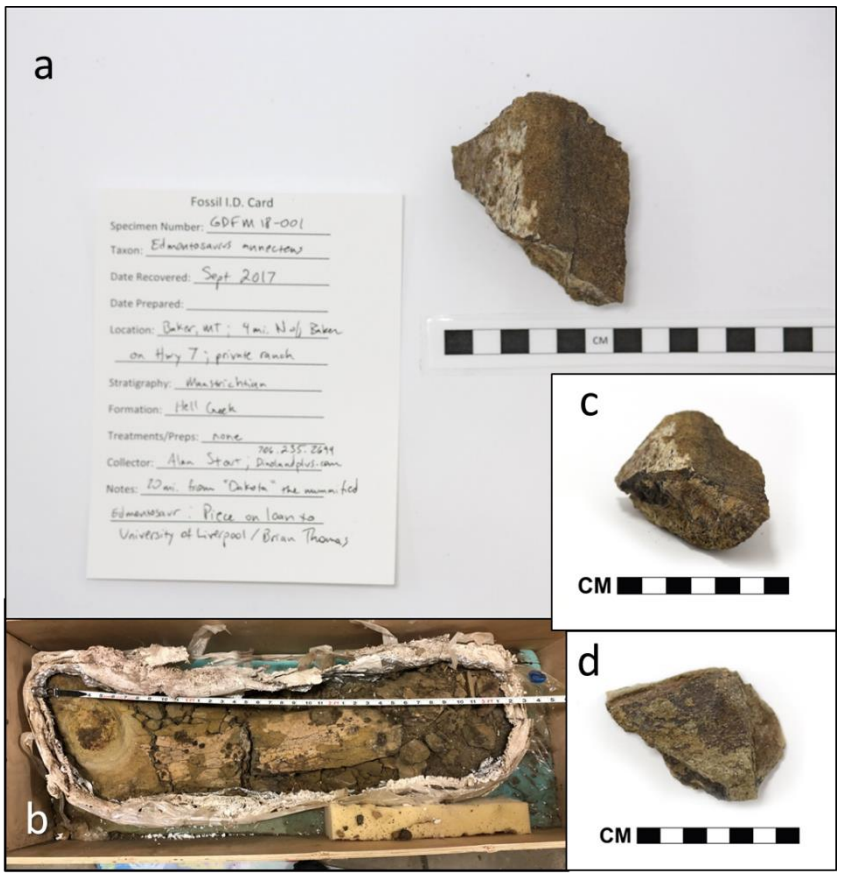

Figure 2.15 | Sample photographs, using GDFM 18.001, an *Edmontosaurus annectens* femur showing minimal mineralization. a, Unaltered photograph using light box, including its unique "I.D. Card," of the portion of GDFM 18.001 on loan. Each card records basic collection data duplicated onto a master spreadsheet. Card data include Specimen Number (Field number, Catalogue or Accession number), Taxon, Date Recovered, Date Prepared, Location (of discovery), Stratigraphy (either its geologic Age or archaeological context), Formation (geological), Treatment or Preparations (such as glues or coatings added), Collector's name, and miscellaneous Notes. **b**, GDFM 18.001 in its plaster field jacket made during excavation in September 2017 and showing a length of approximately 96.5cm. **c**, Locally held fragment of GDFM 18.001 showing a portion of still-white exterior cortical bone. Photograph shows background white-balanced and scale bar digitally inserted. **d**, Locally held fragment of GDFM 18.001 showing interior, still largely porous trabecular bone. Photograph shows background white-balanced and scale bar digitally inserted.

Large bones were first trimmed down to more manageable fractions using two main methods, each appropriate to the size, shape, and preservation state of the bone or fossil bone. In one method, a hacksaw was used to score the bone, or weaken it in one area so that a hammer blow would break off a chip. In this case, the freshly exposed interior of

the bone, not the parts exposed to the saw blade or hammer head, were used for further analyses. This method worked better for hardened, mineralised fossil bone, but due to the fracture-resistant structure of bone, resulted in very irregular sizes and shapes. In another method, a Neiko diamond dust hole saw (coring) drill bit, of ½" diameter was used to extract small cores. This method worked well for bones with moderate to very sturdy integrity, as poorly preserved or densely permineralised bones tended to powderise under the percussive force of the drill bit, even at low speeds. No lubrication was used in an effort to minimize contamination. Future attempts at coring will utilize deionised water as a lubricant for fragile or brittle samples.

Once trimmed to roughly finger or thumb tip size, each bone sample was carefully cut into thin sections using a Buehler IsoMet low speed precision cutting machine equipped with a circular diamond blade which was generously loaned by the Institute of Ageing and Chronic Disease, University of Liverpool. Where possible, level and smooth slices sized appropriately for mounting on glass microscope slides were obtained. Bone slices were mounted by facing the smoothest and flattest surface upward, then gluing the rougher surface against a standard glass slide using a cyanoacrylate glue. Both SHG images and Raman spectrographs of the glue were collected as controls. All mounted slides were stored at 3C.

Specimen number	**Taxon, description**
Holocene ↓	
NP14-4-402Pagets (field#)	*Homo sapiens* right femur, proximal shaft
NP14-4-402Non-pagets (field #)	*Homo sapiens* right femur, central shaft
NP77_109_34 (field #)	Bovine radius
NP77_109_32 (field #)	?
NP77_109_5_1 (field #)	Bovine radius

NP77_109_5_2 (field #)	Bovine tibia
NP77_109_5_3 (field #)	Bovine femur
NP71_12_9 (field#)	*Homo sapiens* ulna
NP71_13_9 (field #)	*H. sapiens* fibula
NP73_34_81 (sk101)	*H. sapiens* rib
NP77_109_52 (field #)	Bovine humerus
XA102_2001_307_91_3 metatarsal	*Sus scrofa* proximal metatarsal and 50% shaft
XA102_2001_307_91_3 Rib	*Sus scrofa* rib shaft
XA102_2001_98_jaw	*Sus scrofa* Mandible frag with erupting molar
XA102_2001_98_ischium	*Sus scrofa* Ischium (Unfused pelvis)
Pleistocene ↓	
EHRC90002	*Megatherium* Ischium frag
EHRC90001	Camelid
EHRC90005	Mammoth
Mesozoic ↓	
CM000088	*Stegosaurus*
CM021728	*Diplodocus longus*
CM000094	*Diplodocus carnegii*
HRS08267	*Edmontosaurus annectens* bone fragment
HRS26095	*Edmontosaurus annectens* Caudal vertebrae
HRS19114	Unknown
HCTH06 (GDFM12.001a	*Triceratops* horn core, 40in long
GDFM03.001	*Triceratops* femur
GDFM08.011	*Triceratops* femur
GDFM04.001	Hadrosaur femur, Hell Creek
GDFM18.001	Edmontosaurus annectens
GDFM12.004	Unknown
EHRC90003	*Triceratops* brow horn
Paleozoic ↓	

EHRC90004	*Mucrospirifer* (brachiopods)
Controls ↓	
Cyanoacrylate	
Apatite crystal	
HCF sediment	
Palouse sediment (EHRC90001)	

Table 2.5 | Total collection summary.

Each stored sample is labeled with its accession number and some basic collection data, perhaps most importantly its taxon. These were systematized to an online local specimen collection catalogue[3] with the following columns: Specimen number, Repository, Taxon/Description, Stratigraphy and Formation, Location, Date of excavation, Excavator, and Notes. Table 7 summarizes two of these 8 columns and includes all the samples used in this project, grouped by sedimentary superposition. It includes some sediment samples for negative controls (total N = 35). This catalogue of bone samples on loan to UoL facilitated efficient access for storage and further analysis.

1 Best Practice Guidelines for Repositing and Disseminating Contextual Data Associated with Vertebrate Fossils. *Society of Vertebrate Paleontology* (2016). <www.vertpaleo.org>.

2 *Norton Priory Museums and Gardens*, <nortonpriory.org> (2018).

3 Thomas, B. *Catalogue Data for Fossils on Loan to Brian Thomas/University of Liverpool*, <https://tinyurl.com/ycueoxng> (2018).

4 *The Redevelopment of Norton Priory Musuem*, <https://www.youtube.com/watch?v=FEztUrJRYNU > (2017).

5 Score, V. & Browning, J. *Hoards, Hounds and Helmets: a conquest-period ritual site at Hallaton, Leicestershire*. (University of Leicester Archaeological Services, 2011).

6 Wall, J. C. *The Victoria history of Leicestershire*. Vol. 1 259-260 (Archibald Constable and company limited, 1907).

7 Score, V. HELMETS, INGOTS AND IDOLS: AN UPDATE ON THE HALLATON FINDS. *Transactions of the Leicestershire Archaeological and Historical Society* **86**, 103-115 (2012).

8 Helley, E. J. & Jaworowski, C. *The Red Bluff Pediment--a Datum Plane for Locating Quaternary Structures in the Sacramento Valley, California*. (US Government Printing Office, 1985).
9 Paleontologic Resource Impact Mitigation on the PGT-PG&E Pipeline Expansion Project: Final Report, Vol 2., (Paleo Environmental Associates, Inc., Altadena, California, 91001, 1994).
10 Baker, V. R. Quaternary geology of the Channeled Scabland and adjacent areas. (1978).
11 Armitage, M. H. & Anderson, K. L. Soft sheets of fibrillar bone from a fossil of the supraorbital horn of the dinosaur Triceratops horridus. *Acta Histochem* **115**, 603-608, doi:10.1016/j.acthis.2013.01.001 (2013).
12 Pawlicki, R., and Wowogrodzka-Aagorska, M. Blood vessels and red blood cells preserved in dinosaur bones. *Annals of Anatomy* **180**, 73-77 (1978).
13 Schweitzer, M. H., Wittmeyer, J. L., Horner, J. R. & Toporski, J. K. Soft-tissue vessels and cellular preservation in Tyrannosaurus rex. *Science* **307**, 1952-1955, doi:10.1126/science.1108397 (2005).
14 Schweitzer, M. H. *et al.* Biomolecular characterization and protein sequences of the Campanian hadrosaur B. canadensis. *Science* **324**, 626-631, doi:10.1126/science.1165069 (2009).
15 Weeks, S. R. in *Geological Society of America Convention.* (Geological Society of America).
16 Silver, M. in *The American Surveyor* (Cheves Media, Frederick, MD, 2014).
17 Nomenclature, I. C. o. Z. in *Article 72. General provisions.* Vol. 72 (International Commission on Zoological Nomenclature, Lee Kong Chian Natural History Musuem, Singapore).
18 Henrici, A. (ed Carnegie Museum) (idigbio.org, 2016).

Chapter 3: Second-harmonic generation imaging of ancient bone collagen

Contents

Figures

Tables

Appendixes

Second-harmonic generation (SHG) imaging and collagen

SHG microscopy developed as a fortuitous offshoot of two-photon, also known as multiphoton, imaging. The latter utilises a fluorophore—typically attached chemically to a molecule of interest—and the former uses no artificial fluorophore. Both imaging techniques utilize the same basic principle. Two low energy incident photons impinge on molecules with certain electronic/structural configurations that absorb those photon energies and re-emit them as a single photon with twice the energy and half the incident wavelength.[1]

By controlling the wavelength (and thus energy) of the incident laser light and using a detector tuned to half that wavelength, a confocal microscope targets just the wavelength emitted by the molecule of interest and leaves the rest of the visual field black. In SHG imaging of almost all biological samples, including bone, the target molecule is Type 1 collagen. Chapter 1 identified Type 1 collagen as by far the most abundant bone protein. The highly organized structure of fully formed collagen emits one photon for the two it receives at particular wavelengths. For example, two photons at 920nm light excites collagen moieties to fluoresce one photon at half that wavelength, with its emissions detected from 420nm to 480nm.

Confocal microscopy utilizes a pinhole filter just prior to the detector to block out-of-focus light that would otherwise blur the image. In contrast, multiphoton microscopy including SHG can collect all light emitted from the sample, even if it gets scattered on its way to the detector, since emission occurs only from a pinpoint within the focal plane. This permits the microscope's detection setting to operate in non-descanned mode, meaning that the pinhole filter is removed. All the collected light gets assigned to the focus depth from whence it originated. This setup enables an increased signal intensity and hence image clarity from having gathered more emitted light. However, this effect is

extremely mitigated by the dramatic increase in incident light intensity required to generate the likelihood of having two photons impinge on a sample at virtually the same time and place, an effect achieved with high-voltage laser pulses. Both multiphoton and confocal microscopy raster the tightly focused beam across the sample surface to generate an image for a defined area. Figure 3.1 diagrams the comparison.

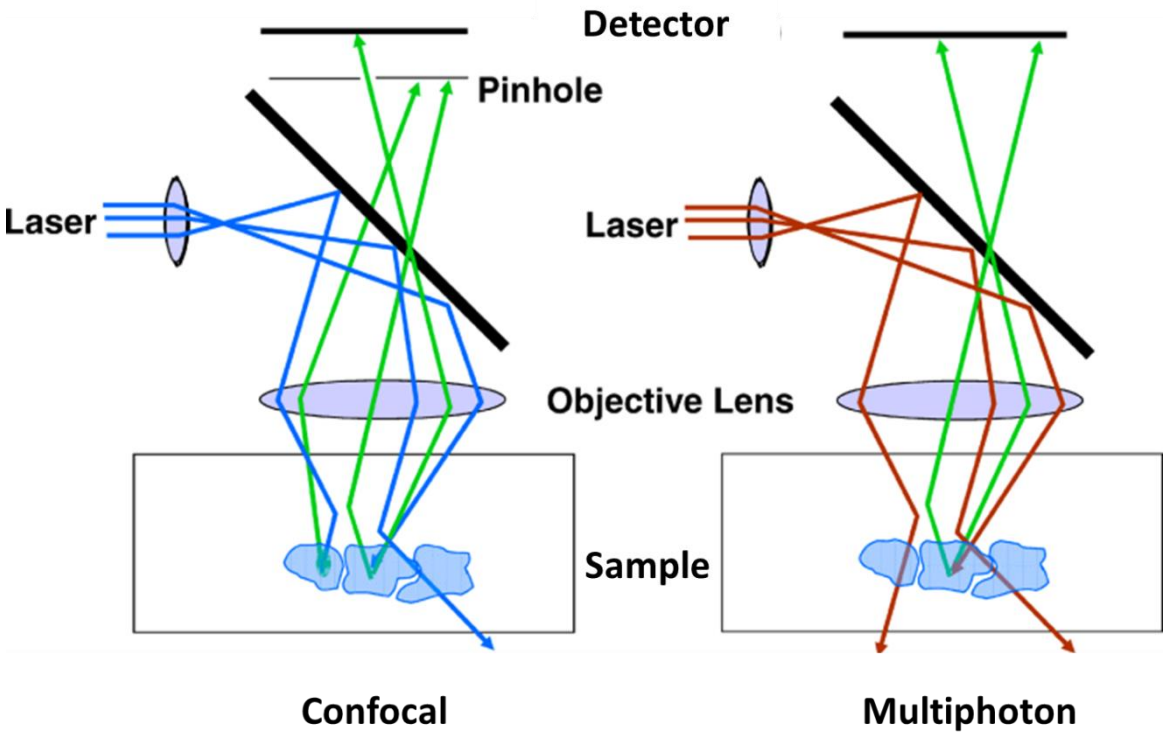

Figure 3.1 | Diagram of excitation scattering in confocal microscopy versus multiphoton microscopy. Confocal microscopy shown on the left uses a pinhole filter to reduce scattered light (green arrows) that arose from excitation that occurred outside the focal plane. Multiphoton excitation microscopy shown on the right can gather all excitation photons since the only emission occurs at the focal point. Image adapted from Piston[2].

SHG microscopy shares two general advantages with the multiphoton techniques that use fluorophores. They both permit high resolution and high contrast imaging. Another advantage of multiphoton microscopy is that it enables the collection of multiple channels simultaneously. Dichroic mirrors split light into multiple colors (wavelengths), or multiple laser light sources can be used. In either case, a separate detector is often used to collect each emitted wavelength for each channel, but an exception to this is described

below. These relatively recent technological advances have enabled multiple channel imaging to produce scores of stunning photographs of biological microstructures[3-6].

In addition to the general advantages listed above, two particular qualities make SHG imaging useful for studies of collagen structure, such as biomedical research into diseases that affect epithelial and connective tissues. SHG can penetrate a few mm into soft tissues, which is deeper than its predecessor, confocal fluorescence excitation microscopy[7]. Also, the use of lower energy (longer wavelength) incident light may reduce damage to tissues through phototoxicity[8]. SHG has been applied to fresh or live specimens in these contexts [6,9], but not yet to ancient bone.

Depth of laser light penetration into either live or ancient bone is hindered by bone biominerals. SHG explorations described below suggest that light penetration falls just short of 1mm in ancient bone. However, SHG offers three distinct advantages for ancient and fossil bone imaging. These advantages lead to ease of use and reduced cost by having fewer requirements to produce an image. First and most important for controversial fossil proteins described in Chapter 1, SHG specifically targets Type 1 collagen. Second, SHG imaging does not require adding a fluorophore (dye) to the tissue, and thus collects a direct detection of Type 1 collagen remnants in bone. Some workers have objected to the use of immunohistochemistry to detect bone collagen in dinosaur bones, for example, on the basis that it technically does not directly illuminate the primary molecule but depends on an antibody to bind to that target[10]. Direct detection in ancient and fossil bone by SHG imaging could test this type of objection.

A third distinct advantage of confocal laser scanning microscopy applied to ancient fossil bone imaging is that the technique detects very small amounts of fluorescing, or in this case multiphoton-emitting, biochemistry. In principle, older bones should have smaller amounts of endogenous protein. It is possible that SHG imaging can directly

image, without the loss of target molecules inherent in extraction protocols, traces too faint for other methods to detect at all. This project reports the first results of SHG imaging applied to ancient bone.

SHG instrumentation

SHG imaging was performed using a two-photon Zeiss 780 Upright Examiner Z1 laser scanning confocal microscope assembly, pictured in Figure 3.2. The instrument is maintained at the Live Cell CORE Imaging facility at the University of Texas Southwestern Medical Center in Dallas, Texas. A Coherent Chameleon titanium:sapphire pulsed laser was set to 920 nm for excitation of the SHG channel. Laser power at the specimen was approximately 13 mW and was selected subjectively, based on the principle of balancing increased signal with the decreased contrast that comes with increased laser power. Laser power was also selected to strike a balance between the very strong collagen signal seen in fresh bone under low power versus the very weak signal seen in ancient bone under higher power. Mounted bone samples were imaged with a Zeiss Plan-Apochromat 10×, NA =0.45 dry objective lens.

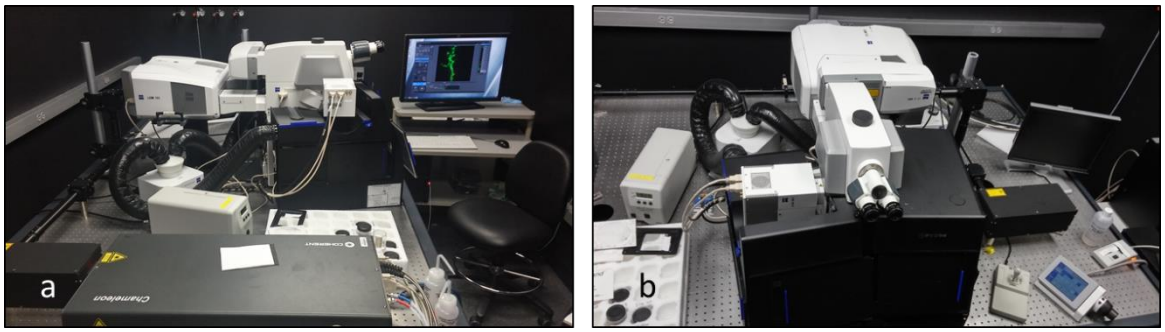

Figure 3.2 | Ziess 780 upright confocal microscope. a, Side view captures the top of the Chameleon SHG laser (dark grey box) in the foreground, the microscope upper body, and the control desk on the right. **b**, Front view of the main microscope body. The light-resistant black box that covers the stage is seen below the binocular. The multichannel Zeiss BiG detector is seen on the left side of the binocular. Black hoses outfit the light resistant box with gas and temperature exchange features for live cell imaging.

The microscope's upright configuration records reflected light detection. SHG emissions were collected from 420 to 480 nm. For most images, a second channel was collected to detect autofluorescence emissions from 500 to 550 nm. Band-pass filters were mounted in a standard P&C filtercube. The SHG emission signal was collected at 458 nm (roughly half the incident wavelength) and a parallel autofluorescent signal was collected at 760 nm using a dual channel Zeiss LSM Binary GaAsP (BiG) detector. This detector uses gallium arsenide-phospide (GaAsP) in its photomultiplier tubes. The BiG, shown in Fig 3.2, can collect images at two different wavelengths simultaneously using a beamsplitter with two integrated PMT's.

Autofluorescence reveals cellular components that include various lipopigments and vitamin derivatives[11] as well as aromatic amino acids[12] useful for comparison against collagen distribution within bone. Fig 3.3 shows a cross-section of modern cortical bone from a proximal bovine femur. An SHG-only image in Fig 3.3a compares with a composite of the SHG plus autofluorescent signals in Fig 3.3b. Modern bone retains a strong red signal that indicates dense collagen protein packing. Most of the ancient bones imaged for this project showed faint red signals that indicate small collagen traces. Therefore focal planes and bone regions for ancient bone samples were selected to include sufficient collagen to visualise within the viewing frame. For most images, frame sizes of 1932 × 1932 pixels were rastered at 5 s speed, taking the average of 4 reads per line. This setting reduces noise by averaging out random voxels in the detector.

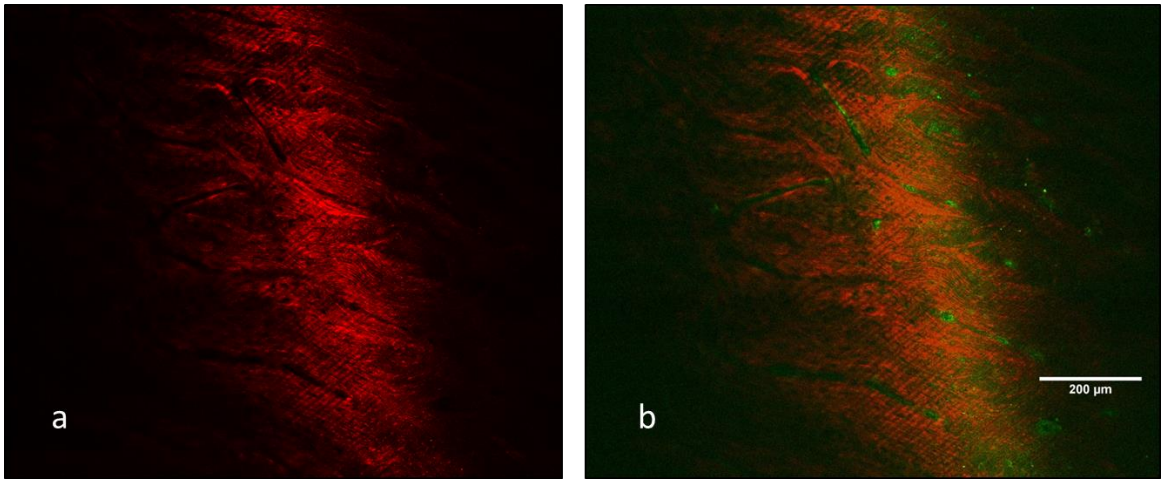

Figure 3.3 | Comparison of second-harmonic generation (SHG) only and a composite of SHG and autofluorescence channels using modern bone. Dark areas to the left and right of the colored area represent out-of-focus regions. **a**, The SHG channel shows abundant Type 1 collagen in red. **b**, The composite of both channels reveals green autofluorescent biochemical components in most of the spaces between collagen. The scale bar is 200 µm, with both images at the same scale. The intensity threshold for both channels was set from 0 to 75. Colors were artificially assigned. Narrow, diagonal, parallel lines are interpreted as Buehler diamond saw tooth marks.

Toward the end of this research project, a second instrumental setup was sought that would add perspective to ancient bone SHG images. The SHG signals from dinosaur bone were so faint and tiny that they did not communicate context. Therefore laser reflection images of bone surfaces were captured and rendered in black and white using a 561nm laser at 6.9mW power. The pinhole aperture was set to its widest setting, which spanned 79.3 µm. With the dichroic mirror removed, the detector range spanned 415-735nm. These settings basically allowed a widefield image that captured the uppermost surface of each bone sample. Fig. 3.4 uses the EHRC90002 ice age Megatherium (see Chapter 2 for details) as an example to compare the widefield image with the corresponding red/green SHG/autofluorescence image.

The widefield and SHG areas captured in Fig. 3.4 overlap exactly and were obtained in the following way. First, the upper bone surface was focused under the widefield setting described above, and an image was captured. Next, the microscope settings were changed to SHG settings without moving the stage, and after another minor focus a SHG image was captured. The most obvious feature of Fig. 3.4a is its extraordinarily

diminished red signal as compared to Fig. 3.3. This feature is explored and discussed below using many other samples, including dinosaur bone. The scarcity of collagen in ancient samples, as illustrated in Fig. 3.4a, prompted the widefield setup shown in Fig 3.4b.

General SHG observations

The comparison shown in Fig. 3.4 revealed two general observations relevant to SHG imaging of ancient bone. Arrows and circles highlight four of many regions where divots or pits occur in the bone surface. Arrows point to collagen shining through tiny gaps where apatite is absent. (See the next section and Appendix 1 for a rigorous demonstration that SHG does indeed detect ancient bone collagen.) The circles indicate

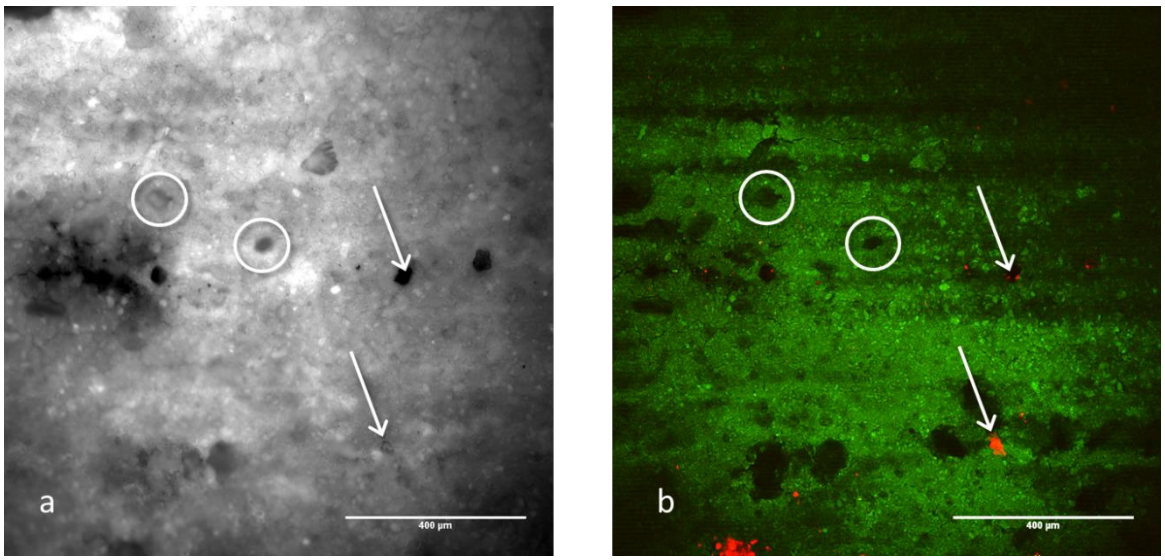

Figure 3.4 | Comparison between widefield reflectance and second-harmonic generation (SHG) images of ice age Megatherium EHRC90002. a, Widefield bone surface illuminated with 561nm laser. The intensity threshold ranged from 15 to 150. **b**, Red SHG/ green autofluorescence composite of the same bone surface as that imaged in (a). The intensity threshold was set from 0-70 for both channels. The scarcity of red signal correlates with paucity of collagen. Arrows indicate pits within which slightly subsurface collagen remnants are visible. Circles indicate pits within which no collagen appears. The scale bar is 400 µm.

two pits from which no red signal is evident. Thus, deeper, more protected microregions within bone appear to afford some measure of protection for ancient collagen. Second, the

visibility of the collagen at depth rather than upon the outermost bone surface is inconsistent with the hypothesis that the SHG signal represents contamination from some exogenous collagen source.

Another general observation from SHG images has to do with the pattern of collagenous remnants in ancient bone. Fig. 3.5 shows two typical SHG images of bones taken from British sites. The distribution of collagen remnants seems to follow a randomized pattern, with blotches of red signal sprinkled throughout the bone. These tiny remnants possibly represent areas that originally had the densest collagen deposition when the animal was buried. Fig. 3.5a dates back to the Roman invasion, and Fig. 3.5b represents a burial made about a millennium later. Since the latitude and climate were similar for these samples, the diminished collagen signal in the Roman Era porcine jaw is attributed to its longer burial time.

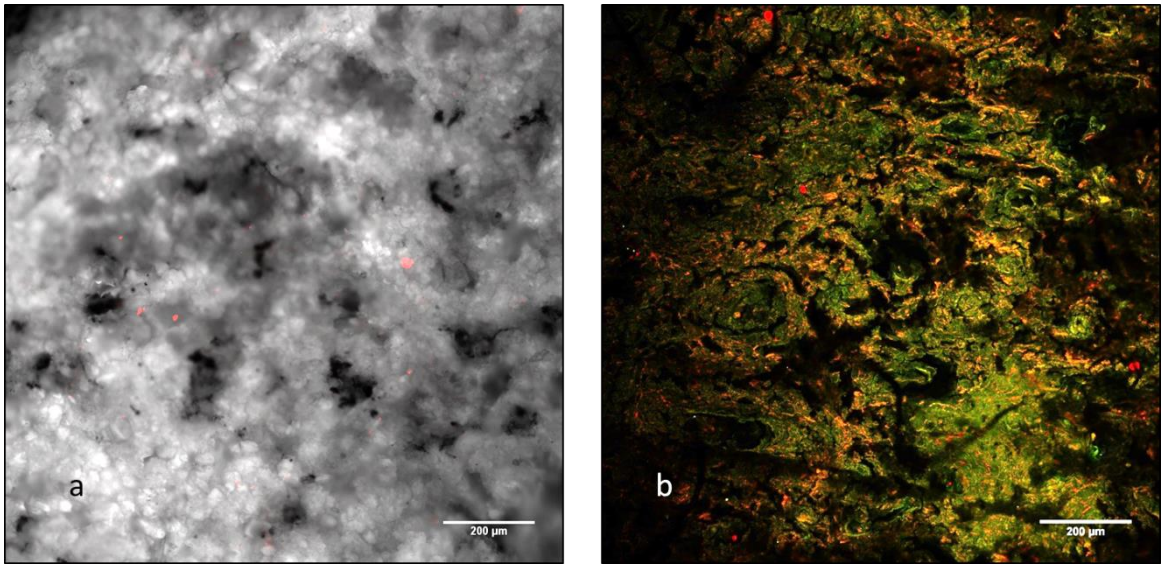

Figure 3.5 | SHG images of two typical medieval bones. a, Widefield bone surface merged with SHG channel of Roman Era porcine jaw XA102_2001_98jaw. The intensity threshold of the widefield channel ranged from 15 to 150, and that of the SHG channel from 0-75. Oddly, the XA bones from the British votive site retained almost no autofluorescent molecules, so the widefield image was merged for context. This reveals an unexplained lack of correspondence between collagen and bone surface patterns like pits. **b**, Red SHG/ green autofluorescence composite of medieval human femur NP14-4-402. Both images are to scale at 200 µm.

A final general observation from these images is that the SHG signal can vary widely in bones of similar age, and even of similar settings. For example, Fig. 3.6 includes three different views of the same bone surface taken from a Pleistocene camelid EHRC90001 and compares them with a Pleistocene Megatherium EHRC90002. The more abundant red signal in the camelid shows much higher collagen content than that which remains in the ground sloth. Although they were deposited at very roughly similar times, this pattern makes sense in light of the climate differences between the two burial sites. The camelid was deposited at latitude 45deg 39' 37", whereas the sloth was about six degrees closer to the equator at latitude 39deg 19' 10.8". Heat accelerates collagen decay, and the sloth was in a warmer climate, hence its much lower collagen signal as seen in Fig. 3.6.

SHG only detects fully formed collagen fibres, which range from 0.3-300µm in diameter[13]. This leaves the smaller collagen components (collagen fibrils, tropocollagen, and collagen-derived peptides) undetected by SHG. Thus, even though SHG is very sensitive to the presence of any fibres present[14], collagenous components could persist even in bones with no SHG signal. However, loss of target molecules through inefficiencies in collagen extraction protocols make recovery of faint traces of collagen's smaller components technically challenging. Overall, SHG imaging appears to offer the first look at the shape and distribution of *in situ* collagen in ancient bone.

Digital image processing

Zeiss Efficient Navigation (ZEN) software was used to control the microscope parameters and capture raw images into the ".czi" file format. Open source ImageJ software package Fiji[15] was used to process the images. Raw images from each channel (458 for SHG and 760 for autofluorescence) captured a full range of intensity from 0 to 255. Fiji was used to adjust pixel intensity of each channel from 0 to 75 for most images.

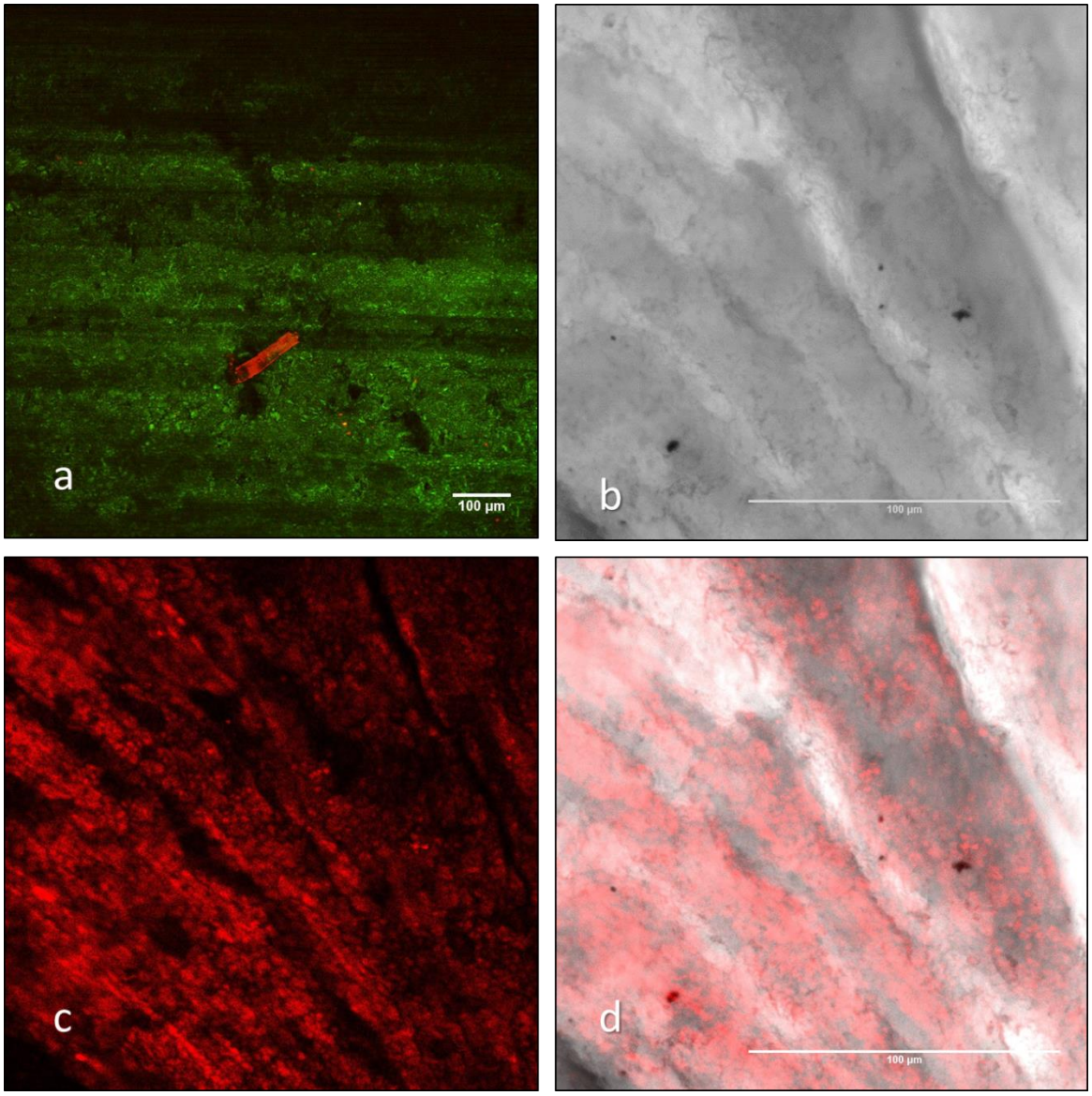

Figure 3.6 | Two Pleistocene bones from different latitudes show variable collagen preservation. a, Composite SHG/autofluorescence of EHRC90002 Megatherium fossil found at 45 degrees north latitude. The bar-shaped artifact may not represent collagen, since it does not have the same blotchy appearance characteristic of other samples, and it is much larger than the tiny red specks of more probably collagen remnants. The intensity threshold of the red channel ranged from 0 to 75, and from 0-135 for the green channel. **b**, Widefield reflectance image also of the EHRC90001 camelid fossil found at a cooler climate at 39 degrees north latitude. The intensity threshold ranged from 12-120. **c**, SHG-only image EHRC90001 shows much more collagen than (a). The intensity threshold ranged from 1-135. **d**, Composite of (b) and (c). Scale bar equals 100 µm.

Early in the course of this project, this range seemed to maximize the collagen plus organic signals against the background while adjusting as little of the original data as possible. However, this minimalist approach resulted in dim, dark images, especially of the very faint red traces in the oldest bones. Therefore, later efforts, also using Fiji, increased brightness even more. It was decided that instead of landing on a uniform pixel intensity range for all images as is common in the literature that describes images of live or modern samples, the intensity range would be adjusted to make each individual image more clearly visible. Each particular intensity range is noted in each figure caption.

Fiji was also used to merge the SHG and autofluroescence channels, and to merge SHG and widefield reflectance channels. Variations of the following procedure were used. First, the brightness ranges of each channel were adjusted individually to balance disparate intensities from the two channels for the purpose of visualizing SHG. For example, modern bone (Fig. 3.3) had so much collagen that its red SHG signal overwhelmed the autofluorescence. Older bones had dramatically less collagen content and hence dramatically dimmer SHG than autofluorescent signals. For example, Fig. 3.7 shows two differently processed ouputs from the same original image of a medieval human femur. A high intensity threshold for the autofluorescence signal colored green in Fig. 3.7a contrasts with that green signal diminished relative to the SHG colored red in Fig. 3.7b. Therefore, their hues were arranged to enhance the red SHG signal from faint collagen traces. Using the image color channels tool in Fiji, images were split or merged as appropriate. Merged images were then flattened, scale bars were added, and the resultant images were output as ".jpg" files.

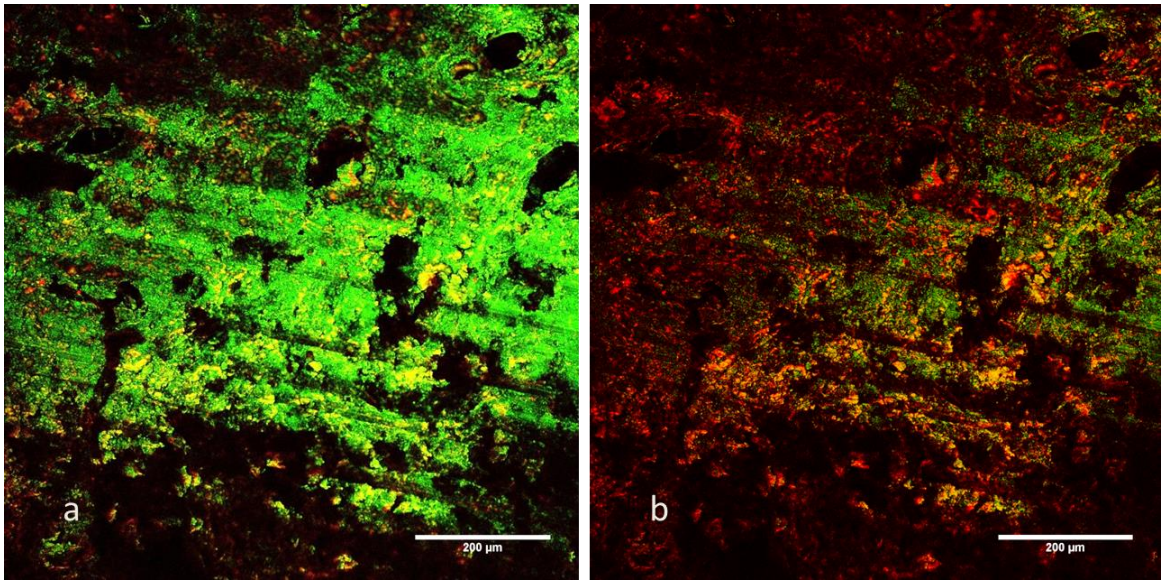

Figure 3.7 | Channel intensities emphasize various components of SHG/Autofluorescence images in medieval human femur NP14-4-402. a, Scale bar 200 µm. Red intensity threshold 0-55, green 75-255. **b**, The same source image as in a, with the same red channel intensity at 0-55, but with the green channel intensity threshold set from 150-360.

The potential for SHG imaging in combination with image processing to estimate the quantity of Type I collagen remaining in ancient bones from various times and places was illustrated using Fiji to calculate a Collagen Area Ratio (CAR) as per Chiu et al.[16]. This effort to generate a collagen decay curve used carbon dated bone samples. The results are described in the section below, "Use of SHG to construct preliminary collagen decay curve." The area of collagen was estimated as the number of "red" voxels, defined as all hues within 0-37. All other hues were excluded. All data were tabulated in a spreadsheet. Total organic area was estimated as the number of voxels of all hues in the region of interest with brightness above 20 (i.e., red and green, but not black).

To render Z-stacks as 2D images that fit the format of figures for print, each .lsm file was first converted to an 8 bit image. It was processed using the default settings on the 3D viewer plugin that comes bundled with Fiji (ImageJ 1.52b). The display setting was set to "surface plot 2D" with bounding box and coordinate systems selected. The resulting 3D image was rotated to a desired orientation and a snapshot was taken.

Does SHG detect ancient bone collagen?

An evaluation of whether or not SHG truly detects collagen in ancient samples was undertaken. Due to the controversial nature of collagen persistence in some fossil bones, the maxim that extraordinary claims require extraordinary evidence was adopted in an attempt to prove the negative case. Thus, evidence was sought for collagen contamination from microbe or animal infiltration, field handling, sample preparation, or laboratory technique. The first step in this process was to employ protein detection and collagen identification means other than SHG to help determine whether or not the SHG signals in ancient bones actually reveal proteins instead of some unknown contaminant or component. In principle, each collagen-positive result helps nullify the hypothesis of exogenous SHG-signal sourcing.

Four independent techniques were used, including the "gold standard" of protien sequencing, collagen extraction for radiocarbon dating, Fourier-transform infrared (FTIR) spectroscopy, and Raman spectroscopy. Discussion of collagen extraction for radiocarbon dating is given in Chapter 6: Radiocarbon. In brief, carbon dating was performed at least one time on one of one Paleozoic, three of nine of Mesozoic, two of three Pleistocene, and 10 of 19 Holocene specimens. Of these, radiocarbon from the collagen fraction of bone was found in zero Paleozoic, three Mesozoic, one Pleistocene one of three ice age specimens, and all 10 Holocene specimens tested. Some of those specimens with insufficient collagen were analysed for carbon isotopes within their biomineral fractions. The spectroscopic techniques and their results are described in Chapter 4: Infrared and Raman spectroscopy. In brief, these spectrographs detected faint but characteristic peaks attributed to vibrational modes of protein-specific bonds.

Three main reasons led to the selection of medieval human rib NP73_34_81 from Skeleton 101 for direct comparison between SHG, collagen extraction for radiocarbon dating, and protein sequencing. First, the bone had quality preservation, as evidenced in its tan coloration and relative integrity. Second, its more recent archaeological setting promised a higher yield from protein extraction protocols. Last, the human proteome databases are robust and facilitate accurate protein identification.

Protein sequencing was performed commercially by the Advanced Proteomics Facility at the University of Oxford. Samples were prepared in collaboration with researchers R. Layfield, D. Scott, and B. Shaw from the University of Nottingham as described in Thomas et al. (2017, appendix 1)[17]. Following Jiang et al. (2007)[18], approximately 50 mg of bone powder was demineralized in 1.2 M HCl. It was incubated sequentially with extract buffer 1 (100 mM Tris, 6 M Guanidine-HCl, pH 7.4), extract buffer 2 (100 mM Tris, 6 M Guanidine-HCl, 250 mM EDTA, pH 7.4) and finally 6 M HCl. Following each extraction step, the bone powder was pelleted by centrifugation at 16,000g for 10 min at 4 °C, then washed in deionised water. The supernatant was discarded, with the exception of the 6 M HCl extract, which was utilised later either by SDS-PAGE using a 5–20% polyacrylamide gradient gel and visualised with silver-staining, or taken forward to MS/MS analysis. For the latter the 6 M HCl extract was digested with trypsin according to a modified Filter Aided Sample Preparation (FASP) strategy[19], with subsequent LC-MS/MS analysis carried out using a Dionex RSLC nano-HPLC system and a Thermo Scientific LTQ-Orbitrap-Velos mass spectrometer following Scott et al. (2016)[20].

The .raw data file obtained from the LC-MS/MS acquisition was processed at the University of Nottingham School of Life Sciences using Proteome Discoverer (version 1.4.0.288, Thermo Scientific). Mascot (version 2.2.04, Matrix Science, Ltd.) was used for

file searching against the UniprotHuman_2015_02 database (unknown version, 67,911 entries) assuming the strict trypsin digestion[21]. The peptide tolerance was set to 10 ppm

Figure 3.8 | Collagen sequence in medieval human rib bone NP73_34_81 (SK 101). a, SDS PAGE of ~700-year-old human bone protein extract still shows a visible protein smear, consistent with endogenous collagens. **b**, SK 101 had a 59% sequence coverage of the human collagen alpha-I chain. **c**, SK 101 had a 65% sequence coverage of the human collagen alpha-II chain. From Thomas et al.[17].

and the MS/MS tolerance was set to 0.02 Da. Fixed modifications were set as alkylation of cysteine, and variable modifications set as deamidation of asparagine and glutamine, and oxidation of methionine and proline residues. Proteome Software's Scaffold Q + S version 4.4.1.1 was used to validate MS/MS based peptide and protein identifications made in Proteome Discoverer[22]. Peptide identifications were accepted if they could be established at greater than 95.0% probability, with a minimum of two peptides required for protein identification.

Protein extraction from NP73_34_81 was confirmed by SDS PAGE analysis, which demonstrated a characteristic protein 'smear', shown in Fig. 3.8a, that is consistent with the presence of collagens. Mass spectrometry-based protein sequencing revealed remarkable collagen preservation seven centuries post-burial, and identified numerous

peptide sequences corresponding to human collagen alpha-I (COL1Al, 59% sequence coverage, Fig. 3.8b) and collagen alpha-II (COL1A2, 65% sequence coverage, Fig. 3.8c).

Fig. 3.9 includes an array of SHG images of bones of various ages. They reveal a general trend of diminished SHG signal with age, consistent with the idea that SHG reveals endogenous collagen. If SHG instead indicated exogenous material, chances are slim that the material would mimic aging protein trends.

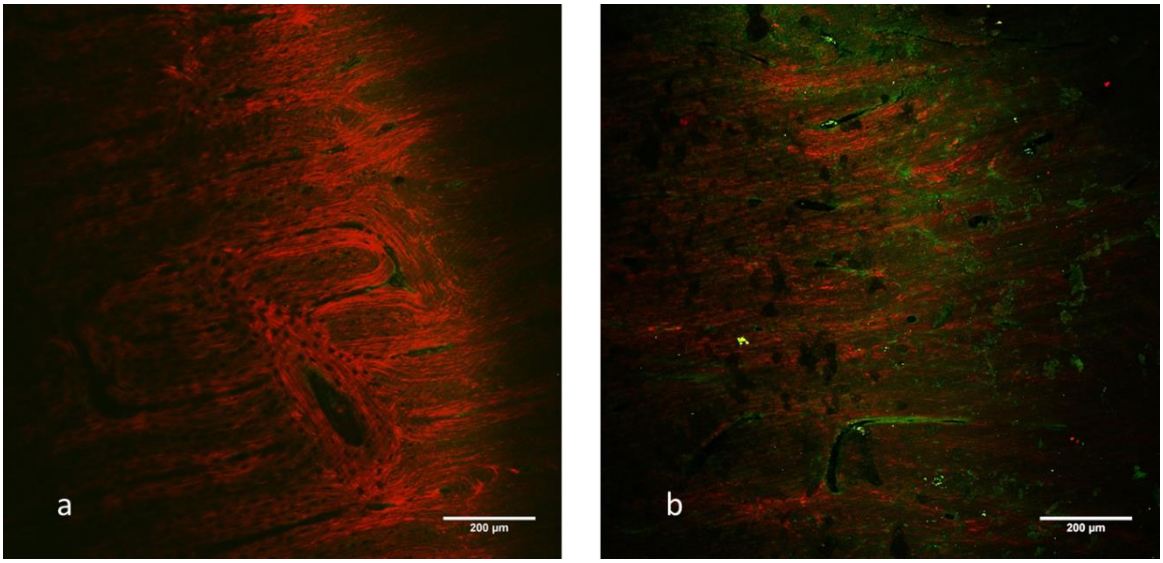

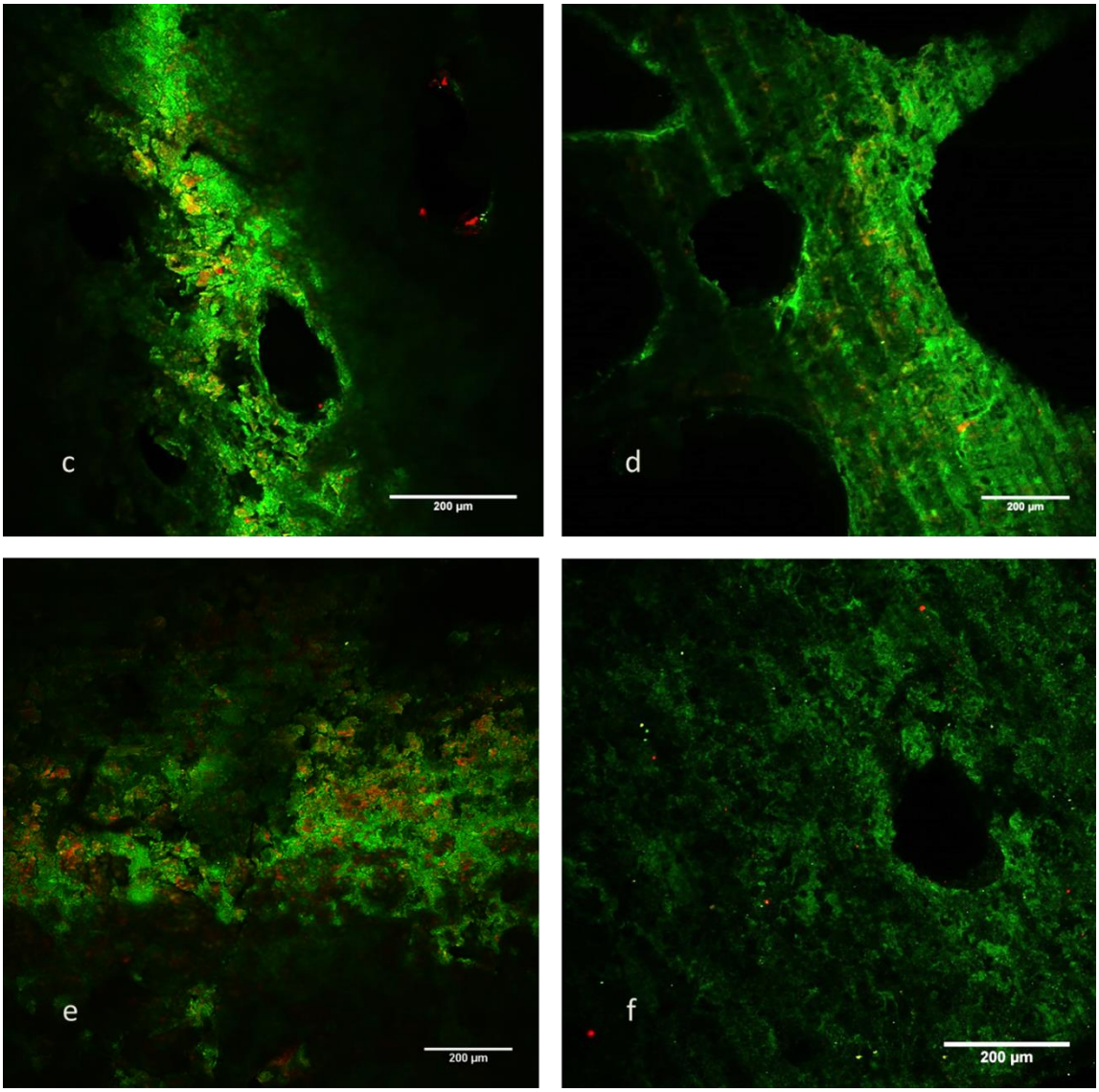

Figure 3.9 | Second-harmonic generation (SHG) images of weight-bearing and low-stress bones from four taxa. Collagen SHG detection is shown in red, and the green shows autofluorescence of mostly organic, non-collagen bone tissue constituents. The SHG (red) signal decrease with older bones is consistent with collagen decay over time. This sample set shows that SHG reveals collagen in a wide range of taxa, ages, skeletal positions, and settings. The scale bars equal 200µm. The brightness range for both red and green channels was set to 0-75. **a-d**, Weight-bearing bones. **a**, A cross-section of cortical bone from the proximal diaphysis of modern bovine femur shows dense collagen bands that encircle osteons. **b**, Norton Priory bovine tibia NP77_109_5 cortical bone shows better collagen signal than the two human samples B and C, possibly because of Paget's effect on postmortem bone decay, or differences between human burial versus trash deposition. **c**, Red collagenous remains in Norton Priory Pagetic human left ulna NP71_12_9 (SK 35) were confirmed by protein sequencing (see text). **d**, Upper Pleistocene Camelid EHRC9001 from Oregon, USA, shows barely visible collagenous remnants. **e-f**, Low-stress bones. **e**, The uneven surface of a thin section of medieval human rib bone NP73_34_81 (SK101) from Norton Priory, UK, reveals significant collagen decay relative to modern bone, as well as irregular collagen deposition, presumably due to Paget's disease. **f**, Pleistocene Megatherium ilium EHRC90002 from California, USA, shows the least collagen signal among the bones under consideration here. Figure modified from Thomas et al, 2017[17].

Among bone samples for which SHG images indicated the presence of collagen was found positive identification of protein-specific spectral characteristics (discussed later), clear collagen retrieval for radiocarbon analysis from many, and unequivocal collagen sequences from one. Taken together, these observations refute the contamination hypothesis. It was concluded that SHG does indeed detect ancient bone collagen, even very faint traces. However, this painstaking verification process did reveal rare instances where apparent SHG signals arise from non-collagenous sources. These caveats deserve description, and are given in the next section along with the results from negative controls.

Images of negative controls

One ancient bone sample showed apparent SHG signatures that lack collagen characters, thus providing a negative control. In chapter 2, Fig. 2.7 a, b reveals fine-grained, gray-colored clay matrix associated with ice age camelid EHRC90001. Fig. 3.10 shows two microscopic perpsectives of this fossil. In one, the cleaned and smooth exterior bone surface was imaged (Fig. 3.10 a, b) to reveal abundant, striated collagen in red. Diffuse margins and variable intensities of the red shapes characterize collagen. In the other, the sediment-infilled bone interior was imaged (Fig. 3.10 c, d) to reveal sedimentary grains. They show no striated pattern, solid and bright intensities, and sharp margins. Diffuse margins and variable green intensities similarly characterize autoflurescent endogenous organics at the 760 nm excitation wavelength. This discovery leads to two suggestions. First, although the 920 nm excitation wavelength set for SHG imaging does produce reflectance at ~450 nm in at least one non-biological mineral, careful attention to the shape and nature of that emission pattern is sufficient to discern between inorganic mineral and collagenous signals. Second, future practicioners of SHG

on ancient bone will need to familiarize themselves with this caveat in order to avoid the error of concluding that SHG has imaged collagen when in fact it did not.

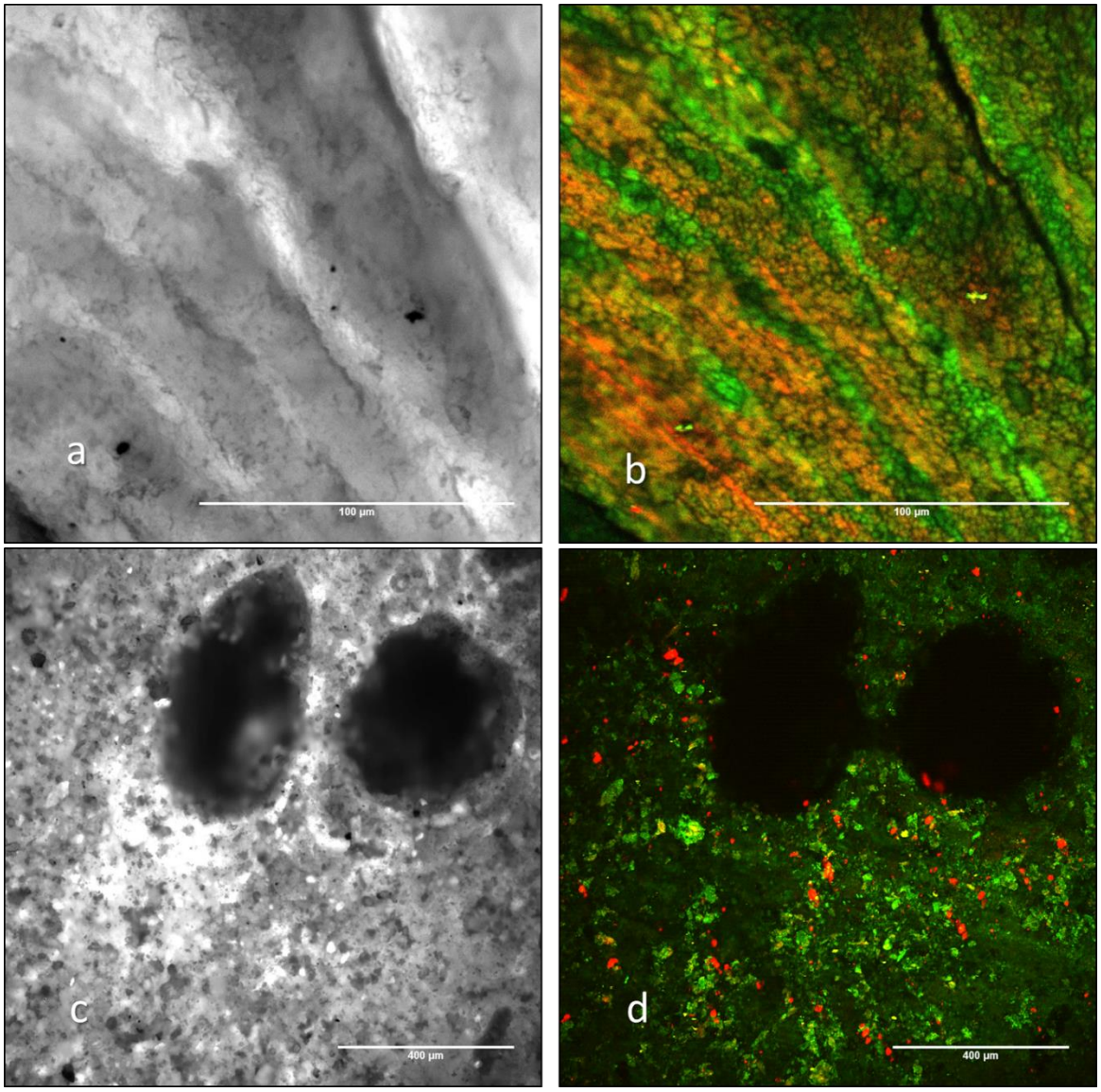

Figure 3.10 | Genuine SHG of collagenous versus negative control non-collagenous SHG signal in ice age camelid EHRC90001. a, Widefield view of lean exterior surface of cortical bone shows minimal matrix adhesion. Scale bar 100 µm; intensity threshold 30-130. **b**, Composite of SHG and autofluorescence from the same clean surface as shows linear or blotchy shapes with diffuse margins characteristic of collagen. Scale bar 100µm and green channel intensity thresholds 0-75. **c**, Widefield view of matrix-infilled bone interior shows sediment grains. Scale bar 400 µm; intensity threshold 0-170. **d**, Composite of SHG and autofluorescence from the same surface as c shows red (and green) angular shapes with sharp margins characteristic of sedimentary grains.

Apatite mineral was obtained as an additional negative control to compare with bioapatite in ancient bone. Crystals were imaged under the same microscope settings used

for all other SHG imaging, seen in Fig. 3.11. A very small (~0.5 g) crystal was imaged using the widefield settings as described in the above section “SHG instrumentation”, shown in Fig. 3.11a. It appears that crystal microsurfaces at certain angles reflect laser light. Fig. 3.11b shows a composite of SHG and autofluorescence settings. The negative result is consistent with the complete lack of organics in or on the unsterilized crystal apatite surface. This result is consistent with the hypothesis that SHG imaging detects biochemical collagen and not biomineral apatite when used to analyse ancient bone. Finally, two fossil matrices were analysed as negative controls for FTIR and Raman spectroscopy. Those results are discussed in Chapter 4: Infrared and Raman spectroscopy.

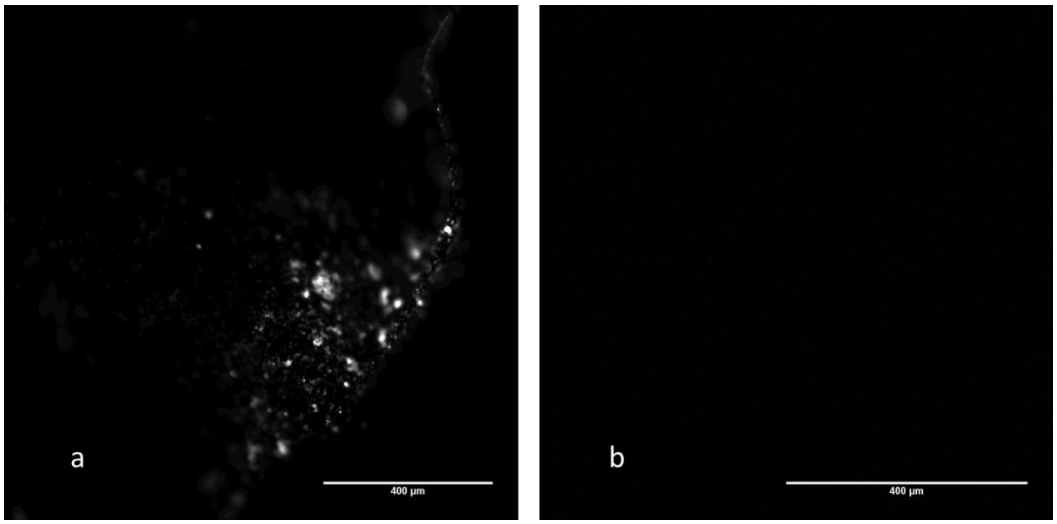

Figure 3.11 | SHG imaging of apatite mineral as a negative control . a, Widefield view of irregular crystal surface. Scale bar 400 µm; intensity threshold 0-25. **b**, Composite of SHG and autofluorescence show no signal for either channel except noise.

Use of SHG in attempt to characterise Paget’s disease of bone

In the process of collaborating with Norton Priory, an opportunity arose to explore the usefulness of SHG as a forensics tool to investigate Paget’s disease in ancient bone. The medieval human skeletons at Norton Priory show a peculiarly high rate of Paget’s-like disease symptoms, which include deformation of long bones (in particular, bowed

femurs and tibiae) and disorganised cortical bone. The disease is very rare today but ties to a defect in the deposition of collagen within bone matrix. An unfunded and informal

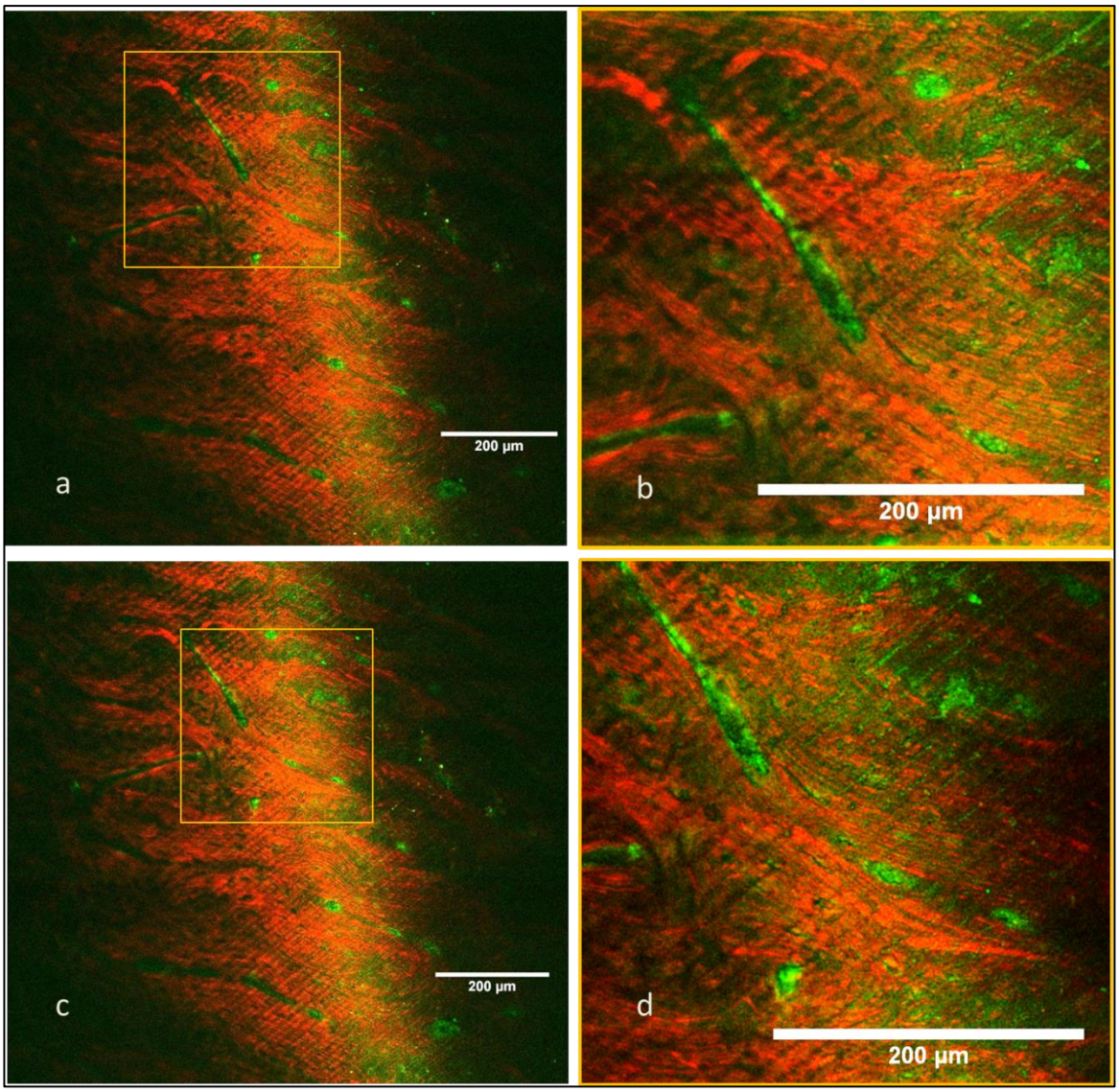

consortium of investigators named the Paget's Disease of Bone (PDB) working group

Figure 3.12 | SHG images of modern bovine bone reveal healthy and normal striated collagen structure. a, Scale bar 200 µm. Red channel intensity threshold 0-100, green channel 0-75. **b**, Close-up of area shown in gold box in a. Red channel intensity threshold 0-125, green channel 0-75. **c**, Scale bar 200 µm. Red channel intensity threshold 0-100, green channel 0-75. **d**, Area shown in gold box of c. Red channel intensity threshold 0-150, green channel 5-70.

meets biannually to discuss research objectives and results. It was suggested that SHG imaging might discern Paget's-related histological characteristics. Figure 3.12 opens this investigation by comparison with modern unaffected cortical mammal bone. SHG images

of the same modern bovine bone as shown in Fig. 3.3 were taken at two different scales two years after the image in Fig. 3.3. Both images show very similar collagen density and reveal the striated collagen that typifies healthy bone.

Three Paget's-affected and one non-affected human bones were selected, on the basis of gross morphology, by archaeologist Dr. Carla Burrell of the PDB group for processing and SHG imaging. Fig. 3.13 shows SHG images each of human femur NP14-4-402 Non-Pagetic and NP14-4-402 Pagetic (see chapter 2, Table 2.1) to contrast healthy with affected ancient bone. In general, this result shows a high intrinsic SHG signal. These two bones

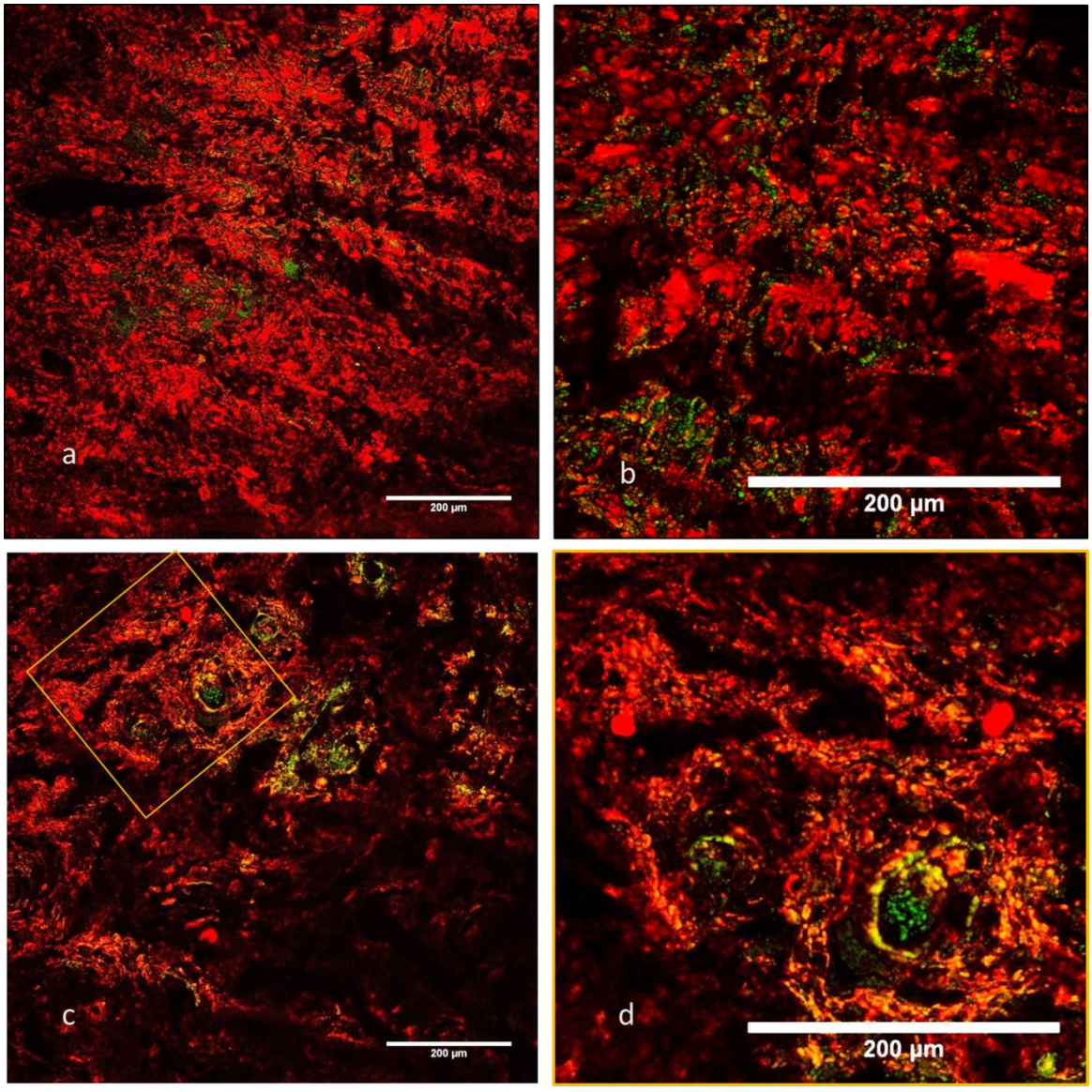

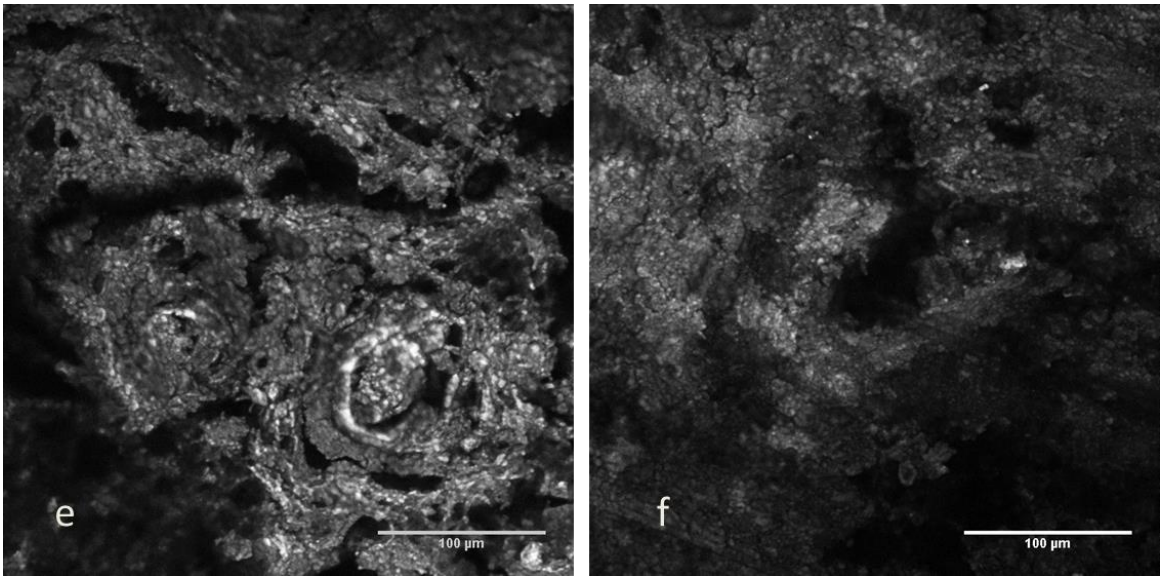

Figure 3.13 | SHG images of medieval human femur bones NP14-4-402 Non-Pagetic versus NP14-4-402 Pagetic. SHG Pagetic versus non-Pagetic bone imaging results may suggest confocal microscopy as a useful tool to identify or investigate Paget's in ancient bone. ImageJ despeckle function was applied to all six images. **a**, NP14-4-402 Non-Pagetic shows a relatively high quality collagen retention in this unstratified medieval bone from Norton Priory. Scale bar 200 µm. Red channel intensity threshold 0-55, green channel 15-360. **b**, A close-up view of a different region on the same prepared slide as a. Scale bar 200 µm. Red channel intensity threshold 0-150, green 75-360. **c**, NP14-4-402 Pagetic shows a relatively high quality collagen retention in this unstratified medieval bone from Norton Priory. Scale bar 200 µm. Red channel intensity threshold 0-75, green channel 75-360. **d**, Close-up of area shown in gold box of c. Scale bar 200 µm. Red channel intensity threshold 0-100, green channel 75-360. **e**, Autofluorescence (green) channel of NP14-4-402 Pagetic rendered in greyscale with the intensity threshold 0-200. Scale bar 100 µm. **f**, Autofluorescence (green) channel of NP14-4-402 Non-Pagetic rendered in greyscale with the intensity threshold 0-200. Scale bar 100 µm.

also showed a high ratio of SHG-to-autoflurorescent signal (results not shown). Figure 3.13 e and f isolate the autofluorescent signal of the NP14-4-402 affected and unaffected samples, respectively, and render them in greyscale. They appear to reveal more bone microstructural details than the SHG channel alone, at least for these two bones. Typical modern affected individuals have patchy, hole-filled, disorganised cortical bone structure. This might be discerned in the affected medieval bone images in Fig. 3.13 c, d, e, and f. However, variable decay since burial of within-bone organics could mimick the unhealthy bone patterning that characterizes modern PDB. Aditional samples from two separate,

affected human femur cortical bones (NP71-13-9 from skeleton of grave 28, and NP71-12-9 from skeleton 35 of grave 34, see chapter 2; see Table 2.1) are shown in Fig. 3.14. Both of these bones have the advantage over the NP14-4-404 samples of having been excavated as part of more complete skeletons from stratified contexts, and have been radiocarbon dated.

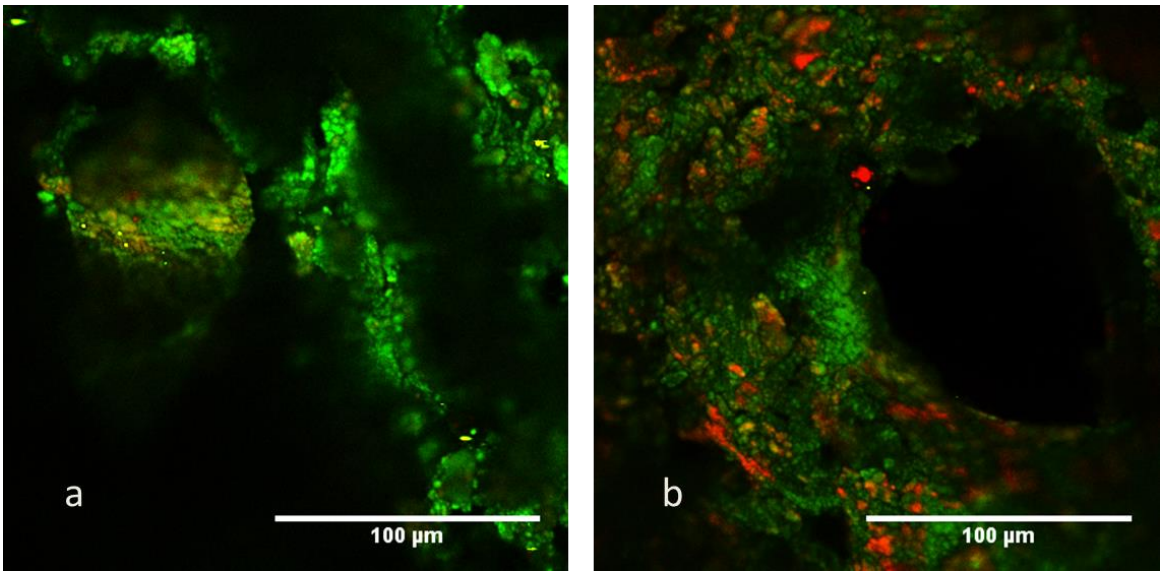

Figure 3.14 | SHG images of medieval human femur bones with Paget's-like disease. a, NP71-13-9 shows very little collagen, and its uneven surface reveals too little information to discern the usefulness of this imaging technique. Scale bar 100 µm. Red and green channel intensity threshold 0-75. **b**, NP71-12-9 does not show PDB features that could not also be explained by diagenesis. Scale bar 100 µm. Red and green channel intensity threshold 0-75.

In general, the disparity between the collagen content as guagued by the SHG signal coverage in NP71-13-9 seen in Fig. 3.14 a versus that of NP14-4-402 Non-Paget's seen in Fig. 3.14 a illustrates the wide variation in collagen and thus bone preservation from microsites even within the same location. This variability, plus the lack of an objective pattern that could discern diagenesis from disease suggests that SHG imaging may have minimal usefulness to discern histological remnants of Paget's-like diseases in ancient bone. More images from more samples, along with comparison to modern affected samples, will be needed to extract the patterns required to assess PDB.

Use of SHG to construct preliminary collagen decay curve

Artificial protein decay experiments have confirmed that bone collagen decay matches a first-order, temperature-dependent model while hydrated[23]. Diminishing collagen, primarily via hydrolysis and oxidation, accelerates gross bone structural decay. As collagen unravels, it releases its integrated plate-shaped hydroxyapatite crystallites. Bone thus becomes increasingly friable. A common method of quantifying bone collagen decay involves extraction, gelatinization, desiccation, and weighing the bone collagen fraction of total bone. Lower percent by weight collagen ratios generally correlate with older bones. This technique has even been used to generate collagen "ages," but the results conflict with other age determinations and vary considerably with depositional environment, as noted above in reference to Fig. 3.14. In addition to time, factors including hydration, soil pH and salinity, and possibly the degree of peripheral mineralization influence collagen decay. SHG offers a new, minimally destructive method to estimate collagen content in ancient bone.

The potential for SHG imaging in combination with image processing to estimate the quantity of Type I collagen remaining in ancient bones from various times and places was illustrated by estimating a CAR as per Chiu et al[24], calculated as:

CAR = (SHG area of collagen ÷ total organic area) × 100

The area of collagen was estimated as the number of "red" pixels, defined as all hues within 0-37. All other hues were excluded. Total organic area was estimated as the number of pixels of all hues in the region of interest with brightness above 20 (i.e., red

and green, but not black). CAR results for six bones were plotted against radiocarbon ages to test the feasibility of using this procedure for ancient bone collagen decay studies.

Table 3.1 lists uncalibrated radiocarbon age determinations by bone fraction. Radiocarbon ages were determined for both fractions from samples from two bones; One medieval (NP77-109-34) and one ice age (EHRC90001). They show broad agreement between the two bone fractions in these samples, even though the error bars do not overlap. These

Description	**^{14}C age bp (collagen)**	**^{14}C age bp (apatite)**
Bovine tibia NP77-109-5	573± 23 (QUBC-24093)	
Bovine radius NP77-109-5	570± 30 (Beta-368271)	
Bovine radius NP77-109-34	934± 30 (QUBC-24091)	860± 20 (UGAMS-17385)
Human left ulna NP71-12-9	840 ± 30 (Beta-425286)	
Camelid EHRC90001	12060± 89 (AA-106299)	10170± 30 (UGAMS-20474)
Megatherium EHRC90002		20050± 40 (UGAMS-20475)

Table 3.1 | Radiocarbon ages of select ancient bones. NP = Norton Priory; EHRC = Earth History Research Center; QUBC = Queen's University Belfast (CHRONO); Beta= Beta Analytic; UGAMS = University of Georgia Accelerator Mass Spectrometer (Center for Applied Isotope Studies); AA = University of Arizona (Accelerator Mass Spectrometry Lab). *Skeleton 35, Grave 34, excavated 1971, included Pagetic human left ulna NP71-12-9 as described elsewhere in this report.

kinds of results are somewhat common, especially with bones over three millennia old, as discussed in chapter 7 Radiocarbon.

Bone ID	**Cell Area (auto-fluorescence)**	**Collagen Area (SHG)**	**Collagen Area Ratio**	**Green intensity threshold**	**Red intensity threshold**
Modern bovine	338826	335435	98.9991	0-75	0-75
NP77-109-5Tibia	1876570	1418116	75.5695	0-75	0-75
NP77-109-5Radius	302510	212917	70.3834	0-75	0-75
NP77-109-34	110378	2627	2.38000	0-75	0-75
NP71-12-9	60621	1933	3.18866	0-75	0-75
EHRC90001	229550	1502	0.08003	0-75	0-75
EHRC90002	59314	30	0.05057	0-75	0-75

Table 3.2 | Collagen Area Ratio (CAR) data.

Fig. 3.15 plots collagen area ratio (CAR) versus radiocarbon age for eight bone samples from six bones that represent modern, medieval, and ice age time frames. The radiocarbon results include three bioapatite and four collagen extract determinations, as detailed in Table 3.1. The logarithmic curve associated to the data follows the formula y = 424.98x-0.81 with an R^2 value of 0.7255. This value of R^2 indicates a statistically plausible level of agreement for the relatively small data set considered and is in keeping with similar studies relating to DNA half-life in bone. Additional data would be required to test various hypotheses related to collagen decay regimes and in particular the identification of target samples from intra-comparable preservation conditions. These results illustrate one way in which future research could utilise SHG results to investigate bone collagen decay rates and regimes in various settings.

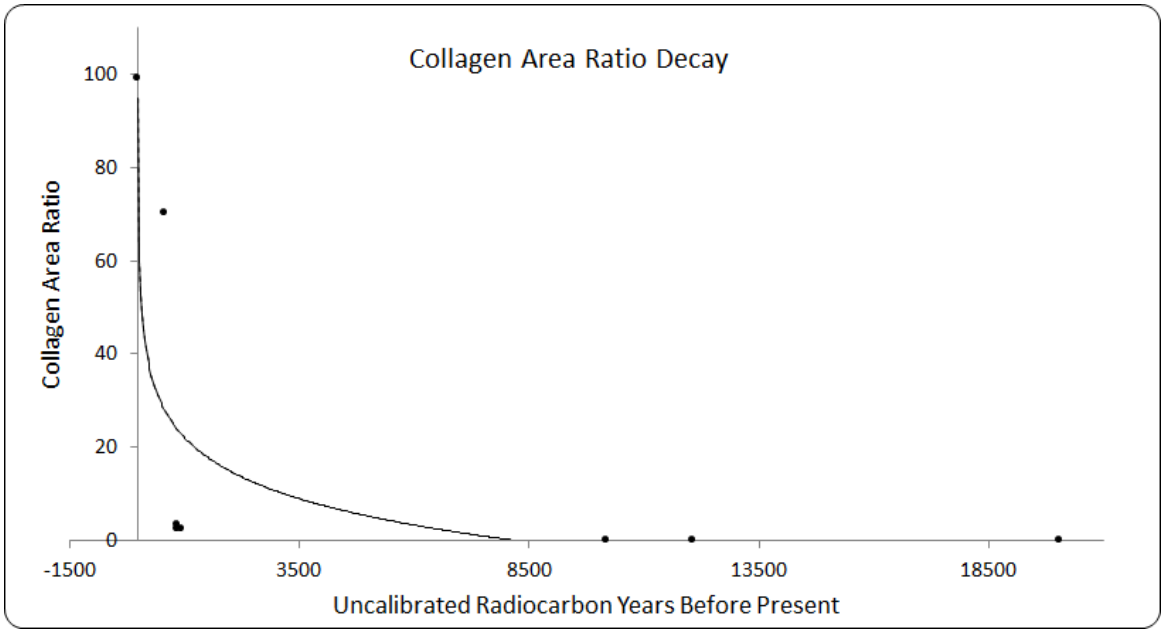

Figure 3.15 | Collagen Area Ratio Versus Radiocarbon Age. SHG-derived Collagen Area Ratios of eight radiocarbon-dated bones (shown in Table 3.1) plus one modern bone suggest that SHG could help estimate post-burial bone collagen loss rates and patterns. Radiocarbon results include four collagen and three bioapatite extracts. The data were fitted to a logarithmic curve with an R^2 value of 0.7255.

Two clear deficiencies in this analysis qualify it as preliminary research. First, the sample numbers are low. In principle, the more data the better, in any science. Ideally, several hundred data points would offer a more reliable sense of collagen decay, following Buckley et al (2008)[23]. However, the high cost of commercial radiocarbon dating and the low supply of many, datable bone samples of widely variant ages and yet similar assumed diagenetic histories curtails this kind of investigation. Second, autofluorescence is probably not the best proxy for "total organic area" in calculating CAR. Initial attempts to approximate CAR used the green channel as a rough proxy for original organic area, but subsequent SHG images of ancient bones from different sites began to reveal a lack of reliable patterning in autofluorescent signal in ancient bones. Future attempts at producing collagen decay curves from SHG image data could instead use the density of collagen in modern cortical bone as a standard "total organic area" for CAR calculations, with the caveat that pore spaces in ancient bone samples should somehow be measured and then subtracted.

SHG images of experimentally decayed blood vessels

Investigation of experimentally decayed collagen is a necessary corollary to understand if and how collagen detection techniques apply to actually decayed collagen. Toward this end, a preliminary collagen decay experiment was conducted as an initial attempt to test the feasibility of SHG to quantify collagen loss over time. Chicken blood vessels, including the proximal brachial artery and the distal radial artery from wing, and the femoral artery from leg, were used for this experiment for two reasons. First, blood vessel walls are comprised of epithelial tissue, which is over 90 percent collagen, and literature reviewed in Chapter 1 does describe controversial Mesozoic and Cenozoic skin remnants. An independent detection method has the potential to help resolve this

controversy. Second, chapter one specified the remarkable discoveries of intact blood vessels (complete with branches and red-colored erythrocyte-like elements) inside two dinosaur femora. A subsequent analysis of these kinds of vessels included a proposal that a class of iron-mediated organic chemical reactions called Fenton chemistry facilitated collagen cross-links during taphonomy, dramatically prolonging protein preservation[25]. SHG imaging plus other techniques used in this thesis have the potential to further investigate the feasibility of this hypothesis.

The iron hypothesis study compared ostrich blood vessels soaked in various purified, concentrated iron solutions to water-soaked vessels. Iron-soaked vessels remained intact at room temperature after two years, whereas water-soaked vessels biodegraded in mere weeks. As a result, this iron preservation hypothesis quickly gained renown[26]. But this hypothesis leaves plenty of room for questioning. For example, invoking a natural environment to concentrate iron contrasts with laws of diffusion. Also, this explanation does not explain why the highly reactive Fenton chemistry would cross-link more proteins than it would destroy. High temperature decay studies similar to those used to estimate bone collagen decay rates[27] could further test the iron preservation hypothesis if a technique like SHG could quantify collagen loss.

Approximately 2 cm-long segments of blood vessel were mechanically separated from dissected chicken wings and legs. One set of each was maintained untreated at room temperature for one week, and another set of each was soaked in pH 1 solution for one week at 80 °C using a Quincy Lab, Model 10 oven. The high temperature was applied as a proxy for time, to artificially decay the collagen. The low pH was applied to ensure sufficient collagen degradation to make a clear enough difference in collagen integrity for SHG imaging to detect. Finally, one blood vessel was treated 1 mg/ml for 16h at 37 C with collagenase type 1 by MP Biomedicals with the prediction that SHG imaging would

detect little or no signal. Fig. 3.16 includes SHG-only images of the following: unaged chicken wing blood vessel, unaged chicken leg blood vessel, chicken wing blood vessel in pH 1 for one week at 80C, chicken leg blood vessel in pH 1 for one week at 80C, and chicken leg blood vessel treated with collagenase.

Artificially decayed blood vessel collagen had a lower SHG intensity and coverage than that of untreated blood vessels, clearly showing that the aging treatments reduced or eliminated collagen content. The results visually confirm that SHG tracks collagen decay. This is also consistent with the conclusion noted above and in Thomas et al (2017) that SHG imaging tracks in situ collagen microdistributions in actually decayed (i.e., ancient) bone. The fact that SHG detected almost no collagen in the negative control of the blood vessel treated with collagenase confirms the efficacy of this technique in visualizing collagen.

Finally, future use of SHG to characterize artificially decayed vessel or bone collagen will benefit from quantification, using digital image processing software, of intuitively visual results like these shown in Fig. 3.16. Initial attempts to isolate and quantify SHG-only pixels have been unsuccessful. Percentages of collagen for each image shown in Fig. 3.16 were calculated using:

$$\frac{\text{(SHG-only pixels/total in-focus pixels) aged blood vessel area}}{\text{(ave. of 3 SHG-only pixels /total in-focus pixels) un-aged blood vessel area}} \times 100$$

However, estimates for total in-focus pixels were highly variable, resulting in inconsistent and uninformative ratios. Future efforts may find use of the widefield imaging settings described above to generate a more consistent estimate of the total area

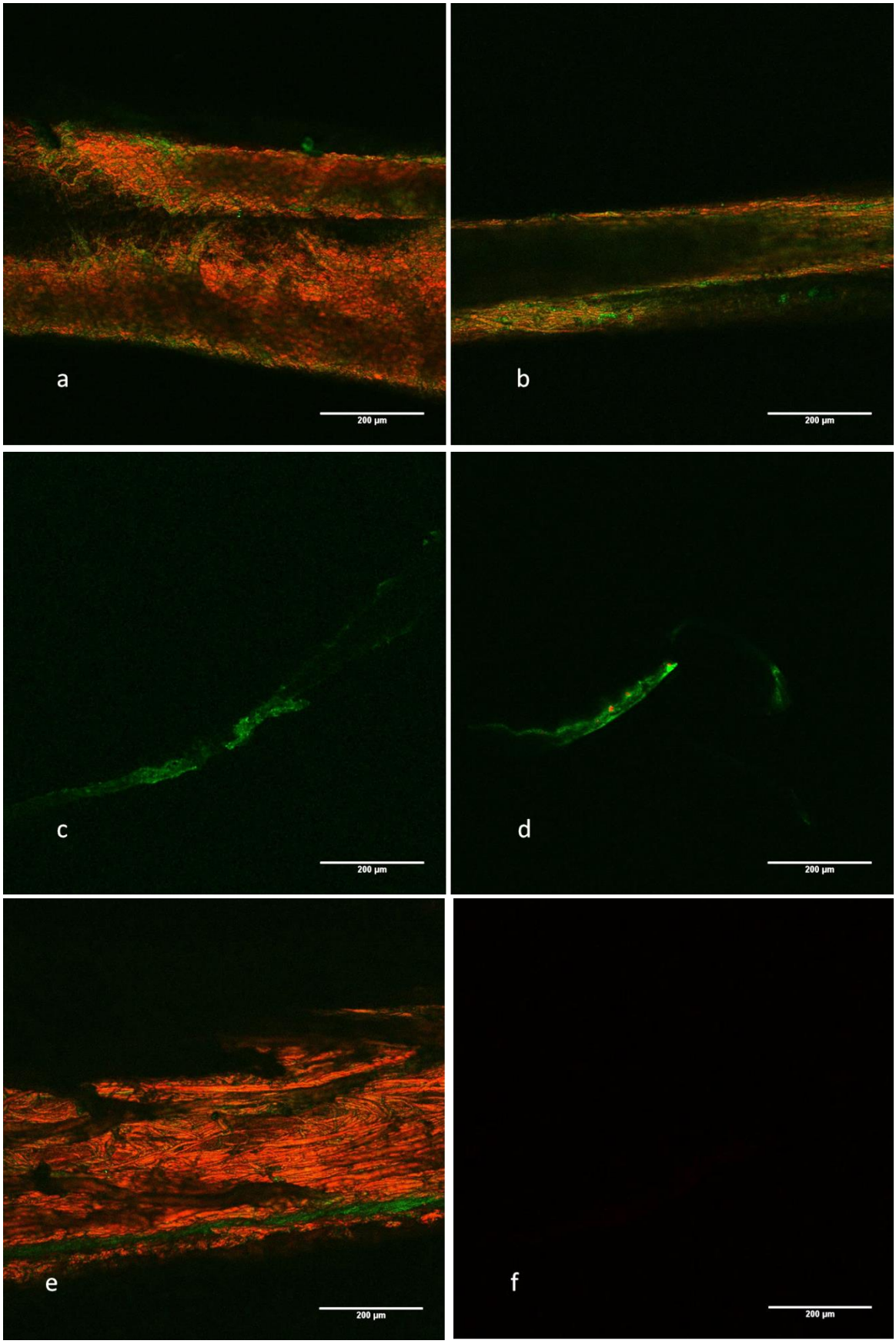

Figure 3.16 | SHG images of artificially decayed and non-decayed chicken blood vessels. Scale bars 200 µm. **a**, **b**, Untreated chicken wing blood vessel reveals patches and fibrous

structures (red) consistent with collagen. Red and green channel intensity threshold 0-75. **c**, Chicken wing blood vessel soaked for one week at pH 1 and 80 °C. Red and green channel intensity threshold 0-25. **d**, Chicken leg blood vessel treated with collagenase reveals greatly diminished collagen content. Red intensity threshold 0-35, green intensity threshold 0-75. **e**, Untreated chicken leg blood vessel. Red intensity threshold 0-33, green intensity threshold 0-50. **f**, Chicken leg blood vessel soaked for one week at pH 1 and 80 °C reveals no collagen and no autofluorescent organics remaining.

of the blood vessel, or "total in-focus pixels," for both aged and unaged samples. In addition, the irregular dimensions of each cylindrical vessel caused out-of-focus portions. Possibly a procedure for flattening each vessel on its glass slide would improve SHG signal efficiency and result in a more repeatable proxy for "total in-focus pixels."

SHG images of pre-ice age fossils

Three Mesozoic bone specimens were imaged in this study: HCTH06, GDFM03.001, and GDFM04.001. None of these bones accompanied a carcass; i.e., all were disarticulated. All had various degrees of darkening in exterior and interior coloration, suggesting some degree of diagenetic alteration. None showed features of peculiar preservation that would suggest a particular likelihood of collagen preservation except that all had mostly air-filled pores, as opposed to mineral or clay-filled, within the once blood-filled trabecular spaces. Figs. 3.17-3.22 show the first SHG images of dinosaur bones, revealing faint traces of collagen.

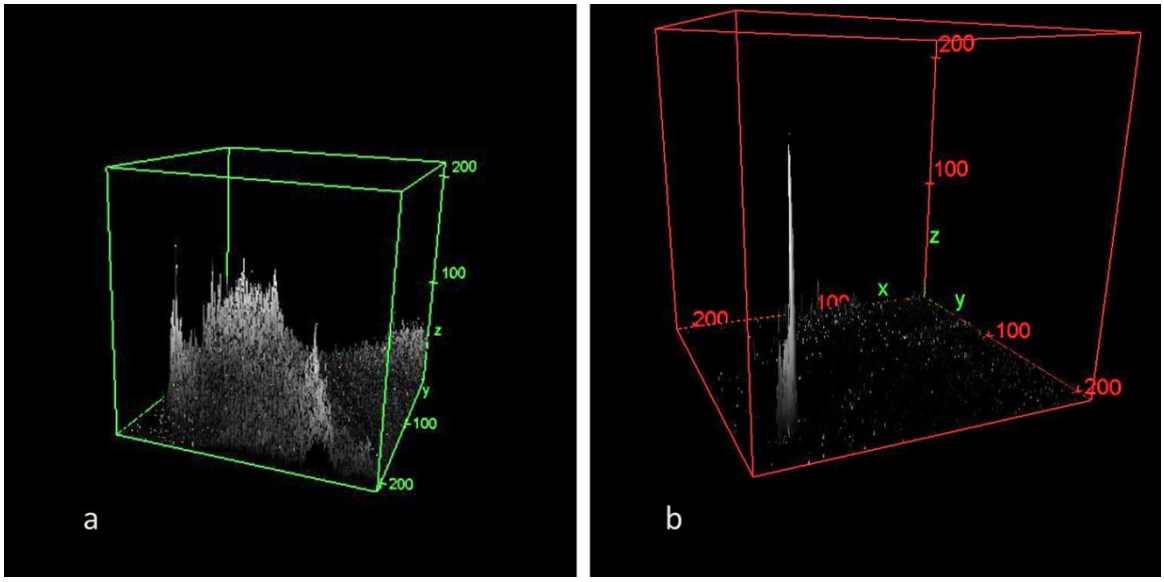

Figure 3.17 | Z-stacks of only the SHG channel for modern and fossil bone. The upper surface of each bone was digitally positioned at the bottom of each image (i.e., each one is turned upside-down) to visualize the depth of SHG penetration into, and distribution of, bone collagen. Scale in microns. **a**, Modern bovine proximal femur cortical bone cross section reveals a dens lawn of collagen. The image contains 35 slices with a voxel depth of 1.800 µm. **b**, Cretaceous Triceratops horn core HCTH06 (the same as that described by Armitage and Anderson, 2013)[28] reveals one deep and several more shallow collagenous remnants. The image contains 18 slices with a voxel depth of 1.800 µm.

Fig. 3.17 shows the result of the first attempt at SHG imaging on dinosaur bone. The image was collected as a Z-stack of 18 slices using only the SHG channel. The 2D images in Fig. 3.16 were rendered using the "3D viewer" plugin that comes bundled with ImageJ, as noted above and displayed as "surface plot 2D." Surprisingly, it did reveal some signal, albeit significantly diminished in comparison to the density of SHG signal from modern bovine bone. Fig. 3.17 inverts the bones' upper surfaces to show a collagen-like signature as a spike that penetrated about 120 microns down into the tissue. The collagen signatures in Fig. 3.17 a penetrated to the same approximate depth, consistent with the hypothesis that SHG imaging captures ancient bone collagen even from disarticulated and generally unremarkable looking Mesozoic specimens.

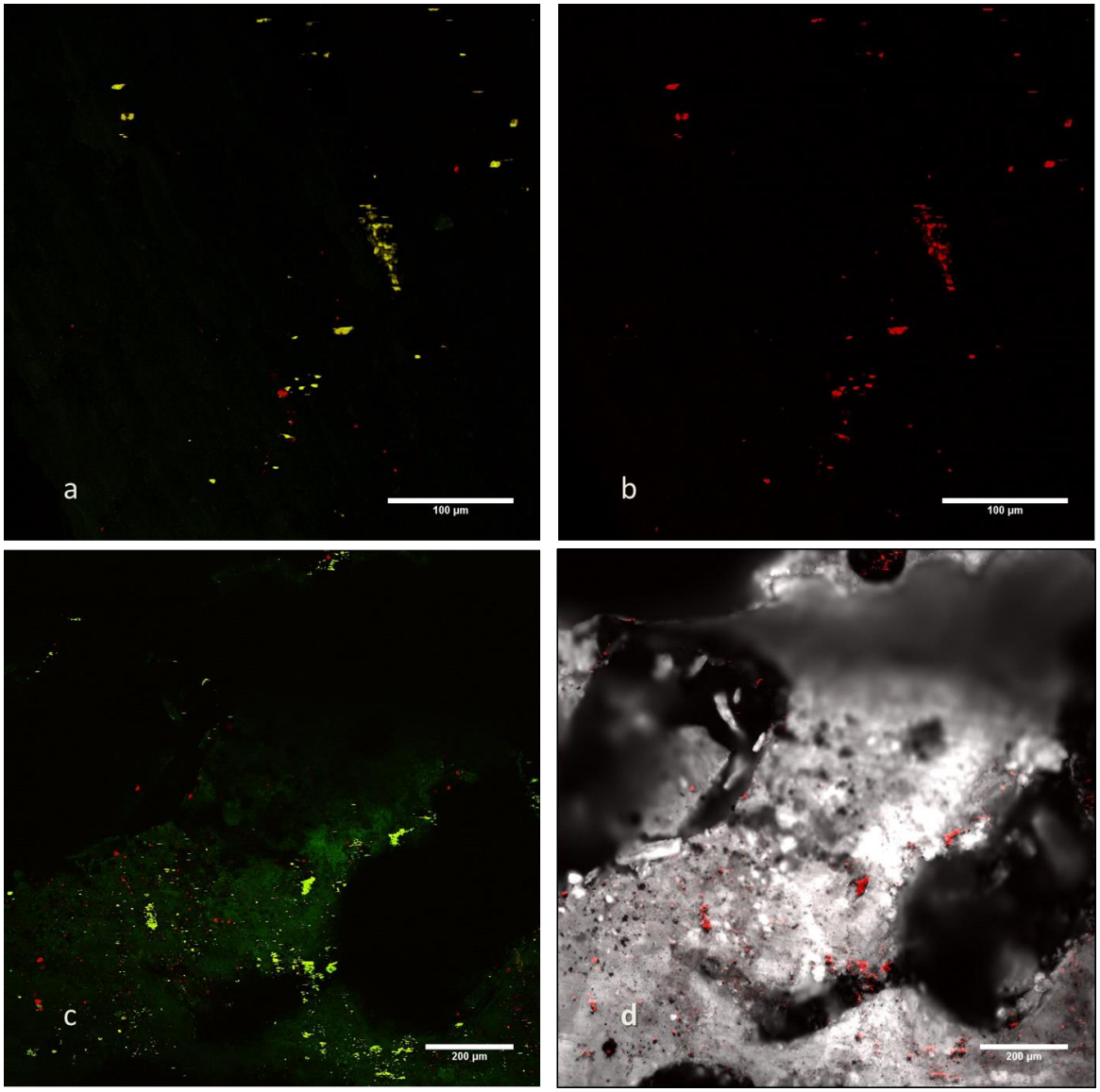

Figure 3.18 | Two internal surfaces from Triceratops femur GDFM03.001. a, **b**, Image collected in December 2017. Composite of SHG (red) and autofluorescence (green) shows similar partial overlap as that seen in modern bone (Fig. 3.3) Extremely faint signal is consistent with very highly degraded collagenous remnants. Red intensity threshold 0-25, green 0-175. Scale bar 100 µm. **c**, **d**, Separately prepared section of same bone sample imaged in May 2017. Composite of SHG (red) and widefield reveals localization of tiny collagenous remnants mostly situated within microscopic recesses of the bone's exposed surface. Scale bar 200 µm.

Two separate imaging preparations showcase two novel methods of adding context to SHG-only images of fossil bone. Fig. 3.18 a and b reveal a large degree of overlap between the faint signals in the red (SHG) and green (autofluorescence) channels. Notably, a small portion of SHG signal emerges independently of a colocalized autofluorescence signal in several spots. This pattern is visually similar to that of modern

bone as seen in Fig. 3.3, and medieval bone as seen in Figs 3.7 a and 3.9 b and c. This pattern fits the conclusion above that SHG imaging visualizes collagen remnants in ancient bone.

The hadrosaur femur GDFM04.001 holds particular intrigue as one of three Mesozoic specimens from which minute amounts of collagen were commercially extracted for radiocarbon analysis, as described in chapter 7: Radiocarbon. Fig. 2.9 e shows a photograph of this specimen. Fig. 3.18 displays snapshots from a 3D rendering of a z-stack of 38 slices taken from GDFM04.001. Whereas the 3D renders in Fig. 3.16 show only the SHG signal, the 3D renders shown in Fig. 3.18 show both the SHG and autofluorescence channels. Using the same ImageJ 3D viewer plugin, Fig. 3.19 displays visual data as a volume plot. In order to generate a higher resolution 3D render, 38 slices of one micron each were collected from GDFM04.001 instead of the 18 from HCTH06 shown in Fig. 3.17. The resulting Fig. 3.19 reveals, for the first time, the distribution in situ of collagenous remnants (shown in red) from a Mesozoic dinosaur bone specimen.

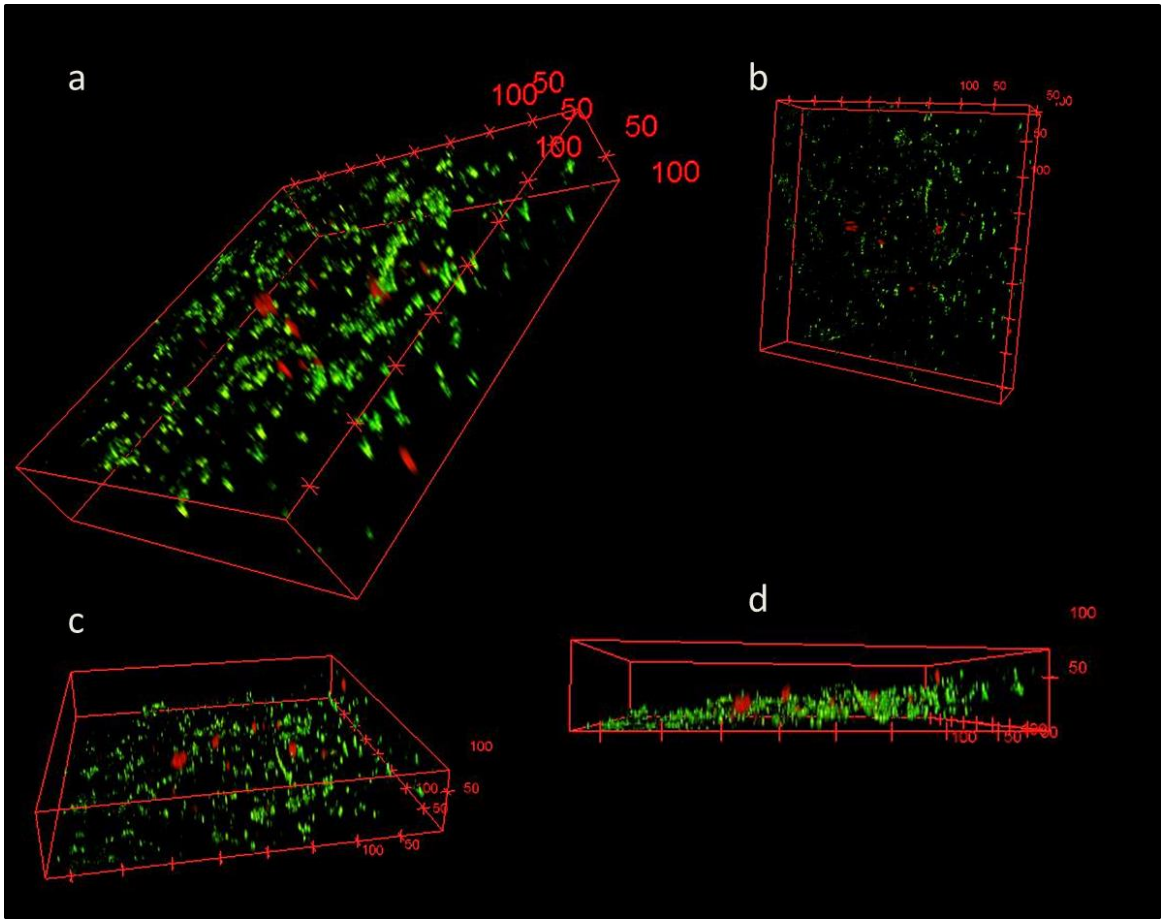

Figure 3.19 | Two internal surfaces from Triceratops femur GDFM04.001. GDFM04.001; 38 slices; Red and green 0-75. **a**, oblique; **b**, upper surface facing out. **c**, inverted **d**, side-on shows depth of laser penetration display as a volume plot.

Several 2D SHG images of GDFM04.001 were also captured. Fig. 3.20 shows one of them using a composite of SHG and autofluorescence onto a separately captured to-scale widefield view of the identical bone surface. It shows faint traces of organics in microscopic recesses and dense area overlap of the red and green channels. Both of these features characterize other ancient bone samples shown above, for example EHRC90002 shown in Fig. 3.4. Remarkably, the dinosaur material shows a similar or possibly an even higher coverage area of organic signals than the much more recently deposited ice age specimens. Possibly the historic differences in taphonomy and diagenesis can help account for the remarkable collagen preservation in unremarkable samples.

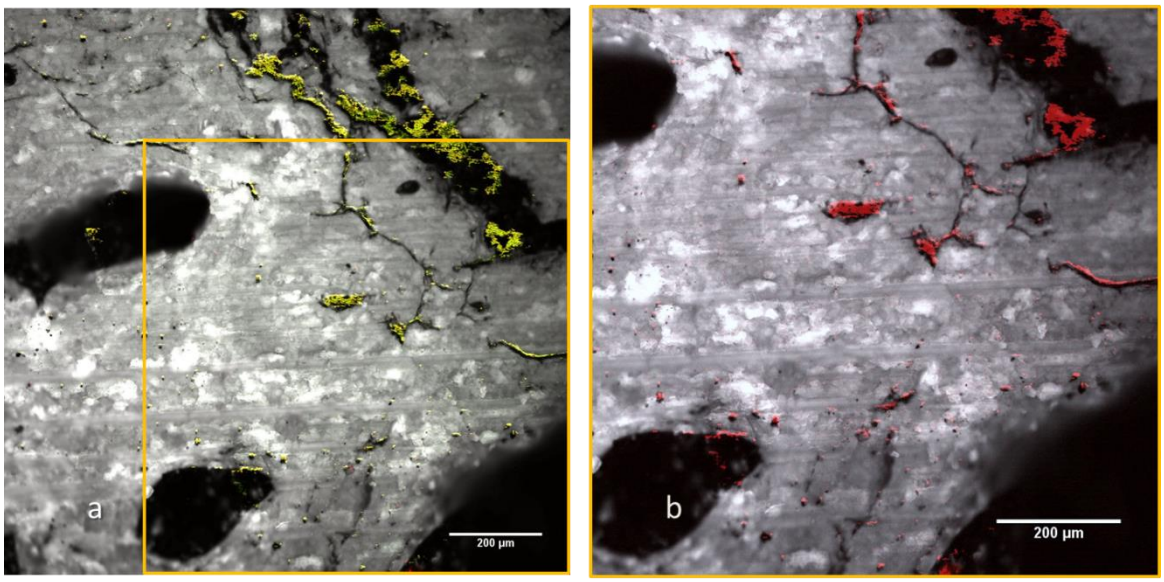

Figure 3.20 | Composite images of GDFM04.001. a, A composite of all three channels (SHG, Autofluorescence, and widefield bone surface) show a high degree of red and green overlap. Gold box indicates area of zoom for b. Red intensity threshold 0-25, green 0-255, widefield 0-75. Scale bar 200 µm. **b**, A composite of red overlaid on the widefield reveals collagen in microscopic recesses. Red intensity threshold 0-25, widefield 0-75. Scale bar 200 µm.

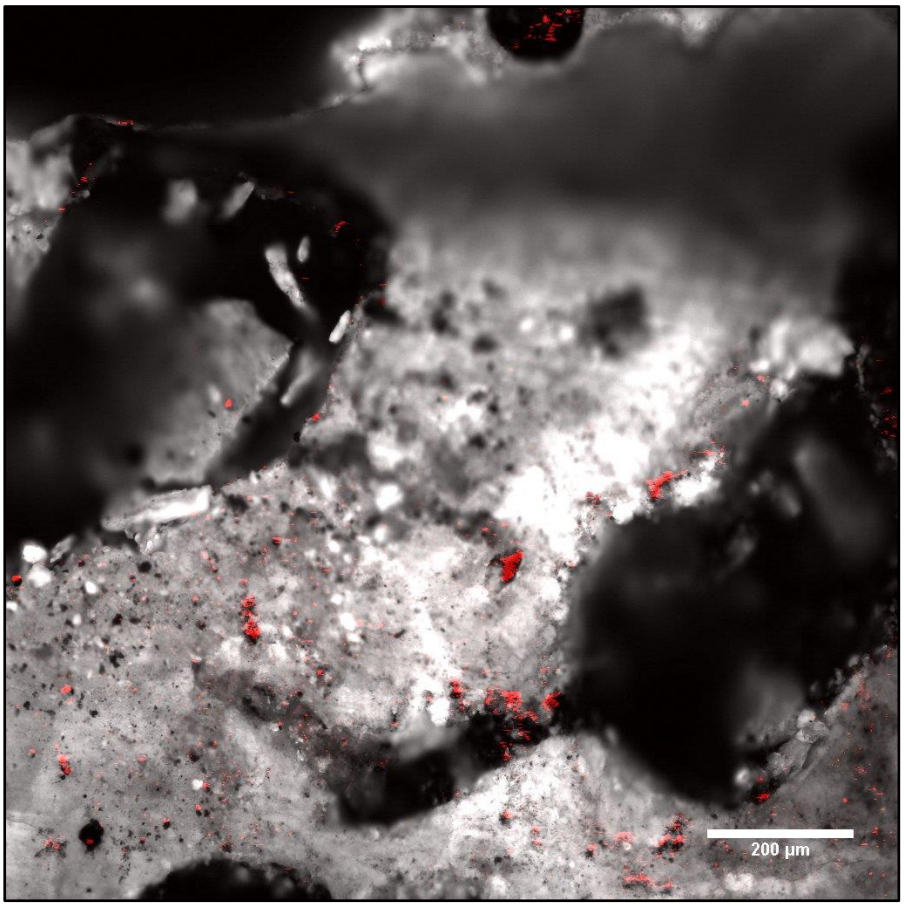

Figure 3.21 | Composite image of triceratops femur GDFM03.001. This bone was prepared by physical fragmentation instead of cutting as in Fig. 3.20. The collagen signal localizes to small pockets, similar to Fig. 3.20b.

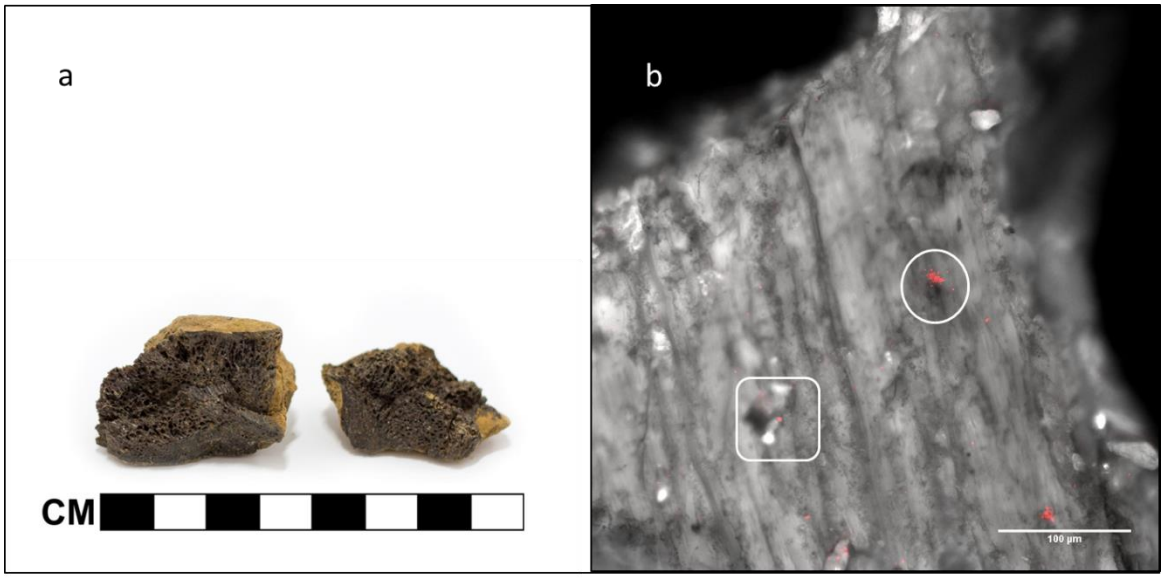

Figure 3.22 | Interior and SHG images of hadrosaur vertebra HRS26095. Like GDFM03.001 shown in Fig. 3.20, this bone was prepared by physical fragmentation to produce a small shard for microscopy. **a,** Whole bone photograph reveals darkened but still vacant trabecular spaces. **b,** SHG signals do not unequivocally localize to bone pockets. The circled collagen signal might localize to the dark divot just beneath it. The boxed, very faint collagen signal represents those that present to the bone surface.

Figs 3.17-3.21 show very small collagen-specific SHG signals in three Maastrichtian bones from the Hell Creek Formation. Table 2 from Chapter 1 showed 14 separate techniques that independently verified original biochemistry in fossil bone. In this context, the discovery that SHG also detects faint traces of collagen in fossil bone both confirms the published findings described in Chapter 1 and suggests that SHG should be added to the Table 2 list. In addition, unlike all 14 other techniques used in the literature, SHG imaging reveals a 3D distribution of collagen within the bone.

1 Strupler, M. *et al.* Second harmonic imaging and scoring of collagen in fibrotic tissues. *Optics express* **15**, 4054-4065 (2007).
2 Piston, D. W. When two is better than one: Elements of intravital microscopy. *PLoS biology* **3**, e207 (2005).
3 Ratner, D. M. *et al.* Changes in the N-glycome, glycoproteins with Asn-linked glycans, of Giardia lamblia with differentiation from trophozoites to cysts. *Eukaryotic cell* **7**, 1930-1940 (2008).
4 Bückers, J., Wildanger, D., Vicidomini, G., Kastrup, L. & Hell, S. W. Simultaneous multi-lifetime multi-color STED imaging for colocalization analyses. *Optics express* **19**, 3130-3143 (2011).

5 Wouterlood, F. G., Bloem, B., Mansvelder, H. D., Luchicchi, A. & Deisseroth, K. A fourth generation of neuroanatomical tracing techniques: exploiting the offspring of genetic engineering. *Journal of neuroscience methods* **235**, 331-348 (2014).

6 Palero, J. A., De Bruijn, H. S., Sterenborg, H. J. & Gerritsen, H. C. Spectrally resolved multiphoton imaging of in vivo and excised mouse skin tissues. *Biophysical journal* **93**, 992-1007 (2007).

7 Lichtman, J. W. & Conchello, J.-A. Fluorescence microscopy. *Nature methods* **2**, 910 (2005).

8 Denk, W., Strickler, J. H. & Webb, W. W. Two-photon laser scanning fluorescence microscopy. *Science* **248**, 73-76 (1990).

9 Brown, E. *et al.* Dynamic imaging of collagen and its modulation in tumors in vivo using second-harmonic generation. *Nature medicine* **9**, 796 (2003).

10 Buckley, M., Warwood, S., van Dongen, B., Kitchener, A. C. & Manning, P. L. A fossil protein chimera; difficulties in discriminating dinosaur peptide sequences from modern cross-contamination. *Proceedings of the Royal Society B: Biological Sciences* **284**, doi:10.1098/rspb.2017.0544 (2017).

11 Zipfel, W. R. *et al.* Live tissue intrinsic emission microscopy using multiphoton-excited native fluorescence and second harmonic generation. *Proc Natl Acad Sci U S A* **100**, 7075-7080, doi:10.1073/pnas.0832308100 (2003).

12 Monici, M. Cell and tissue autofluorescence research and diagnostic applications. *Biotechnol Annu Rev* **11**, 227-256, doi:10.1016/S1387-2656(05)11007-2 (2005).

13 Naik, N., Caves, J., Chaikof, E. L. & Allen, M. G. Generation of spatially aligned collagen fiber networks through microtransfer molding. *Adv Healthc Mater* **3**, 367-374, doi:10.1002/adhm.201300112 (2014).

14 Bancelin, S. *et al.* Determination of collagen fibril size via absolute measurements of second-harmonic generation signals. *Nature communications* **5**, 4920 (2014).

15 Schindelin, J. *et al.* Fiji: an open-source platform for biological-image analysis. *Nature methods* **9**, 676 (2012).

16 Chiu, Y.-W. *et al.* Applying harmonic optical microscopy for spatial alignment of atrial collagen fibers. *PLoS One* **5**, e13917 (2010).

17 Thomas, B. *et al.* Second-harmonic generation imaging of collagen in ancient bone. *Bone reports* **7**, 137-144 (2017).

18 Jiang, X. *et al.* Method development of efficient protein extraction in bone tissue for proteome analysis. *Journal of proteome research* **6**, 2287-2294 (2007).

19 *Filter Aided Sample Preparation (FASP) Method*, <http://www.biochem.mpg.de/226356/FASP> (

20 Scott, D. *et al.* Mass spectrometry insights into a tandem ubiquitin-binding domain hybrid engineered for the selective recognition of unanchored polyubiquitin. *Proteomics* **16**, 1961-1969 (2016).

21 Perkins, D. N., Pappin, D. J., Creasy, D. M. & Cottrell, J. S. Probability-based protein identification by searching sequence databases using mass spectrometry data. *ELECTROPHORESIS: An International Journal* **20**, 3551-3567 (1999).

22 Searle, B. C. Scaffold: a bioinformatic tool for validating MS/MS-based proteomic studies. *Proteomics* **10**, 1265-1269 (2010).

23 Buckley, M. *et al.* Comment on "Protein sequences from mastodon and Tyrannosaurus rex revealed by mass spectrometry". *Science* **319**, 33; author reply 33, doi:10.1126/science.1147046 (2008).

24 Chiu, Y. W. *et al.* Applying harmonic optical microscopy for spatial alignment of atrial collagen fibers. *PLoS One* **5**, e13917, doi:10.1371/journal.pone.0013917 (2010).

25 Schweitzer, M. H. *et al.* A role for iron and oxygen chemistry in preserving soft tissues, cells and molecules from deep time. *Proceedings of the Royal Society of London B: Biological Sciences* **281**, 20132741 (2014).

26 *Jurassic World Film Transcript*, <http://jurassicpark.wikia.com/wiki/Jurassic_World_Film_Transcript> (

27 Buckley, M. & Collins, M. J. Collagen survival and its use for species identification in Holocene-lower Pleistocene bone fragments from British archaeological and paleontological sites. *Antiqua* **1**, 1 (2011).

28 Armitage, M. H. & Anderson, K. L. Soft sheets of fibrillar bone from a fossil of the supraorbital horn of the dinosaur Triceratops horridus. *Acta Histochem* **115**, 603-608, doi:10.1016/j.acthis.2013.01.001 (2013).

Appendix 3.1: SHG imaging publication in journal *Bone Reports*.

Bone Reports 7 (2017) 137–144

Contents lists available at ScienceDirect

Bone Reports

journal homepage: www.elsevier.com/locate/bonr

Second-harmonic generation imaging of collagen in ancient bone

B. Thomas[a,*], D. McIntosh[a], T. Fildes[a,b], L. Smith[b], F. Hargrave[b], M. Islam[c], T. Thompson[c], R. Layfield[d], D. Scott[d], B. Shaw[d], C.L. Burrell[e], S. Gonzalez[e], S. Taylor[a]

[a] Mass Spectrometry Research Group, University of Liverpool, Brownlow Hill, Liverpool L69 3GJ, UK
[b] Norton Priory Museum, Runcorn WA7 1SX, UK
[c] School of Science and Engineering, Teesside University, Borough Road, Middlesbrough TS1 3BA, UK
[d] School of Life Sciences, University of Nottingham Medical School, Nottingham NG7 6HZ, UK
[e] Liverpool John Moores University, Liverpool, UK

ARTICLE INFO

Keywords:
Second-harmonic generation microscopy
Collagen type I
FTIR
Raman spectroscopy
Ancient bone

ABSTRACT

Second-harmonic generation imaging (SHG) captures triple helical collagen molecules near tissue surfaces. Biomedical research routinely utilizes various imaging software packages to quantify SHG signals for collagen content and distribution estimates in modern tissue samples including bone. For the first time using SHG, samples of modern, medieval, and ice age bones were imaged to test the applicability of SHG to ancient bone from a variety of ages, settings, and taxa. Four independent techniques including Raman spectroscopy, FTIR spectroscopy, radiocarbon dating protocols, and mass spectrometry-based protein sequencing, confirm the presence of protein, consistent with the hypothesis that SHG imaging detects ancient bone collagen. These results suggest that future studies have the potential to use SHG imaging to provide new insights into the composition of ancient bone, to characterize ancient bone disorders, to investigate collagen preservation within and between various taxa, and to monitor collagen decay regimes in different depositional environments.

1. Introduction

The collagen fraction of ancient bones holds historical information related to bone taphonomic history, and even holds some biological information about ancient life. Analyses of ancient bone collagen have included collagen extraction for radiocarbon dating, weight measurement, stable isotope analyses, and sequencing. These techniques investigate research problems such as emplacement ages (Arslanov and Svezhentsev, 1993), collagen decay regimes (Buckley et al., 2008), paleodiets (Lee-Thorp et al., 1989), and cladistics analyses (Morvan-Dubois et al., 2003), respectively. Second-harmonic generation (SHG) imaging specifically targets type I collagen, without sample destruction. It has contributed significantly to biomedical research on collagen structures (Mohler et al., 2003) and diseases through imaging tissues in vivo (Brown et al., 2003) and in modern bone (Chen et al., 2012; Ambekar et al., 2012), suggesting its potential to explore ancient bone. SHG imaging could supply new insights into the collagen composition of ancient bones, including disease characterization, extent and distribution of collagen, collagen decay characteristics, and preservation favorability of various decay environments.

1.1. Second harmonic generation imaging

SHG imaging takes advantage of the interaction between two low-energy photons with type I collagen present in bone. Collagen is structured such that it can absorb the two low energy incident photons and re-emit them as a single photon with twice the energy (frequency) at half the wavelength (Strupler et al., 2007). This non-invasive quality is attractive to biomedical researchers, since it does not require the addition of dyes such as fluorophores as does two-photon imaging that otherwise uses a very similar confocal microscope setup. Addition of dyes is not required to image collagen structure using SHG, thus protecting valuable specimens of ancient bone. Finally, two-photon and SHG imaging use low energy infrared laser light which does not burn live tissues. SHG thus appeals as a technique that captures collagen-specific images without disrupting labile biomolecular remnants endogenous to ancient bone.

Type 1 collagen fibres in fresh bone range from 0.3-3 μm thick (Naik et al., 2014). A fibre consists of a dozen or so packaged fibrils, each ranging from 10 to 300 nm. One fibril contains many assemblies of parallel, crosslinked, triple helical collagen molecules, each also called

* Corresponding author at: Department of Electrical Engineering & Electronics, Mass Spectrometry Research Group, University of Liverpool, Brownlow Hill, Liverpool L69 3GJ, UK.
E-mail addresses: brian.thomas@liv.ac.uk (B. Thomas), d.g.mcintosh@liv.ac.uk (D. McIntosh), tf@liverpool.ac.uk (T. Fildes), lyn.smith@nortonpriory.org (L. Smith), frankhargrave@nortonpriory.org (F. Hargrave), m.islam@tees.ac.uk (M. Islam), T.Thompson@tees.ac.uk (T. Thompson), robert.layfield@nottingham.ac.uk (R. Layfield), daniel.scott@nottingham.ac.uk (D. Scott), barry.shaw@nottingham.ac.uk (B. Shaw), c.l.burrell@2009.ljmu.ac.uk (C.L. Burrell), S.Gonzalez@ljmu.ac.uk (S. Gonzalez), s.taylor@liv.ac.uk (S. Taylor).

http://dx.doi.org/10.1016/j.bonr.2017.10.005
Received 16 June 2017; Received in revised form 27 September 2017; Accepted 24 October 2017
Available online 01 November 2017

tropocollagen. During degradation, collagen fibres essentially fray and disperse into their smaller components. Confocal microscopy used for SHG imaging can resolve fully formed type 1 collagen fibres, but leave fibrils and tropocollagen too small for SHG to detect even though they could remain in bone as protein remnants. SHG thus has the potential to nondestructively characterize bone collagen fibre morphology and its decay patterns over time and across various environments. Further, there is evidence that in certain bone diseases (e.g. Paget's disease), defects in molecular rearrangements of collagen type I like beta-isomerization may occur (Cloos et al., 2003), and the prospect of applying SHG to study such disorders in archaeological bone samples also remains to be explored.

1.2. SHG imaging and protein verification in ancient bones

Various techniques can be used to determine (and in some cases quantify) the presence of endogenous organics in bone. Raman spectroscopy reveals vibrational modes of characteristic molecular arrangements, including the amide bond (Penel et al., 2005). Similarly, Fourier transform infrared spectroscopy (FTIR) reveals absorption spectra characteristic of protein chemical structure (Gu et al., 2013). Protein sequences derived by tandem mass spectrometry can be matched to primary structural data in databases that include microbe versus vertebrate protein sequences as a test against exogenous protein sourcing. The physical extraction and weighing of the collagen bone fraction during sample preparation for radiocarbon dating by AMS inadvertently but directly verifies the presence of primary collagen in ancient bone. In this study we used the above four techniques to test the hypothesis that SHG can detect collagenous remnants in ancient bones from various ages, taxa, and settings. SHG imaging is thus established as an important new tool to explore specific questions about how various burial environments and histories may have influenced collagen decay patterns in different ancient bones.

2. Materials and methods

2.1. Sample descriptions

2.1.1. Geography and stratigraphy

Eight bone samples of known provenance were obtained to test the potential of SHG imaging to supply novel information about collagen type I in ancient bone from multiple localities, ages, and depositional environments. Described in more detail below, these included a modern bovine femur used as a reference. Five samples including three human (NP71_12_9, NP71_13_9, NP73_34_81) and two bovine (NP77_109_5, NP77_109_34) came from one of Europe's most excavated sites, Norton Priory, UK. Additionally, a Pleistocene *Megatherium americanum* ilium fragment (EHRC90002) from California's Northern Sacramento valley and a well-weathered Pleistocene camelid from Oregon test SHG's utility on much older bones and on sedimentary as opposed to burial settings.

Norton Priory, a historic Augustinian monastery in Cheshire, UK, included an ancient abbey active from its foundation in 1134 CE to the 16th century. Recent analysis of human burial remains excavated there beginning in the 1970s found an abnormally high incidence of skeletons affected by a disorder resembling Paget's disease of bone (Burrell et al., 2016). Paget's disease is a focal disorder characterized by disorganized histological bone structure sometimes accompanied by abnormal curvature of limb bones, especially including the femur (Aaron et al., 1992). An affected human left ulna (NP71_12_9), a rib fragment (NP73_34_81) from skeleton 101 (SK 101) and a right fibula (NP71_13_9) were selected from burials excavated in 1971 and 1973. Sample NP71_12_9 belongs to Skeleton 35, Grave 34 and sample NP73_34_81 belongs to Skeleton 101, Grave 116. AMS radiocarbon dating was successful for these individuals. The 2 σ results for Skeleton 35 presented a single date of Cal 1155–1260 CE (Cal BP 795–690) whereas Skeleton 101 presented two possible dates; Cal 1280–1320 CE (Cal BP 670 to 630) and Cal 1350–1390 CE. AMS radiocarbon dating of sample NP71_13_9, belonging to Skeleton 29, Grave 28 was unsuccessful. However, it has been estimated that this burial is from the late 14th Century (i.e. also medieval) based on the surrounding archaeology. All individuals are male and over 45 years of age. Disease-affected, as opposed to unaffected, bones were not necessary for this study but were included for two reasons. First, they were available to our group as bones from which collagen was confirmed by extraction for radiocarbon dating. Second, they illustrate the potential for future studies to implement SHG imaging as a novel means to characterize ancient bone disease.

A bovine tibia (NP77_109_5) and a bovine radius (NP77_109_34), were both excavated in 1977 from an associated midden-like deposit. Portions of each were sacrificed for radiocarbon analysis. The collagen fraction of NP77_109_5 was AMS radiocarbon (2 σ) dated to Cal 1300–1360 CE or 1380–1420 (Cal BP 650–590 or 570–530) due to two intersections of the mean radiocarbon age with the calibration curve. The collagen fraction of NP77_109_34 was AMS radiocarbon dated to Cal 1027–1161 CE (Cal BP 923–829; 2 σ). The bioapatite fraction of NP77_109_34 was radiocarbon dated by AMS to BP 860 ± 20 (not calibrated; corresponding before calibration to 1070–1110 CE). Table 1 summarizes these ages in years before present (CalBP), i.e. years before 1950, calibrated. These bovine bones explore the capacity of SHG to reveal information from unintentionally buried bones, for example how their differential diagenesis may have affected their collagen content and distribution.

The Pacific Gas Transmission/Pacific Gas and Electric (PGT-PG & E) Pipeline Expansion Project conducted in the western US during 1993–1994 contained guidelines requiring the collection and preservation of any fossils encountered while trenching over 800 miles. One of the project's largest and most complete fossils consisted of a partially complete *Megatherium* (ground sloth) taken from the Pleistocene Red Bluff Formation of Colusa County, California. Another, better-preserved Project find was an ancient camelid from the upper Pleistocene Palouse Formation in Oregon. All pipeline fossils are housed

Table 1
Radiocarbon results.

Description	^{14}C age bp (collagen)	^{14}C age bp (apatite)
Bovine tibia NP77 109 5	573 ± 23 (QUBC-24093)	
Bovine radius NP77 109 5	570 ± 30 (Beta-368,271)	
Bovine radius NP77 109 34	934 ± 30 (QUBC-24091)	860 ± 20 (UGAMS-17385)
Human left ulna NP71 12 9	840 ± 30 (Beta-425,286)	
Human rib NP73 34 81	660 ± 30 (Beta-425,288)	
Camelid fragment EHRC90001	12,060 ± 89 (AA-106299)	10,170 ± 30 (UGAMS-20474)
Megatherium femur EHRC90002		20,050 ± 40 (UGAMS-20475)

NP = Norton Priory; EHRC = Earth History Research Center; QUBC = Queen's University Belfast (CHRONO); Beta = Beta Analytic; UGAMS = University of Georgia Accelerator Mass Spectrometer (Center for Applied Isotope Studies); AA = University of Arizona (Accelerator Mass Spectrometry Lab). *Skeleton 35, Grave 34, excavated 1971, included Pagetic human left ulna NP71 12 9 as described elsewhere in this report.

at the permanent repository of the Earth History Research Center (EHRC) in Keane, Texas. A thumb-sized fragment that had already fallen from the mostly intact camelid (EHRC90001) limb bone was sectioned for SHG imaging. Its collagen fraction was AMS radiocarbon dated by the University of Arizona to 12,060 ± 89, CalBP. These Pleistocene samples explore the age range of samples that SHG can image, as well as differences between SHG and other methods (such as FTIR and physical extraction) of quantifying collagen remnants. Comparison of primary bone collagen structure from modern, medieval, and ice age bones demonstrates the applicability of SHG imaging to ancient bones varied biological and taphonomic origins.

2.1.2. Radiocarbon dating

Radiocarbon dating of bone samples was performed using four different commercial laboratories: Queen's University Belfast (CHRONO), Beta Analytic, University of Georgia Center for Applied Isotope Studies, and the University of Arizona's Accelerator Mass Spectrometry Lab. Sample preparations including acid demineralization pretreatments had slight differences, but used the industry standard acid-alkali-acid (AAA) strategy to extract and gelatinize collagen. *Megatherium* EHRC90002 had insufficient collagen for radiocarbon analysis, so the radiocarbon from the bone bioapatite was measured instead, and used to compare with two other bioapatite-derived radiocarbon ages from our small bone set. The purpose of the present study does not include precision archaeological timing of emplacement for the samples under consideration. Instead, radiocarbon results are here used primarily to confirm the presence of endogenous proteins via physical collagen extraction and secondarily to illustrate how future research on time-stamped ancient bone could benefit from SHG imaging results.

2.2. Second harmonic generation imaging

2.2.1. Sample preparation for SHG

Bone was initially sectioned by hand saw. Samples with a length of approximately 1.5 cm, measured along the axial orientation, were cross-sectioned using a Buehler Isomet low-speed saw fitted with a circular diamond-tipped blade. Bone slice thicknesses of approximately 300 μm were targeted. However, ancient bone proved brittle and fragile, resulting in some uneven wedge-shapes and non-level surfaces. Slices were mounted on glass slides. Images were collected before and after a 20 min bath in 10% acetic acid to test whether or not acid would etch biominerals to expose protein to improve SHG visualisation.

2.2.2. Second harmonic generation apparatus

SHG imaging was performed using a dedicated two-photon confocal microscope assembly at the Live Cell CORE Imaging facility at the University of Texas Southwestern Medical Center in Dallas. Mounted bone samples were imaged with a Zeiss Plan-Apochromat 10 ×, NA = 0.45 objective lens using a Zeiss Examiner Z1 two-photon excitation laser scanning confocal microscope (Carl Zeiss, Jena, Germany) coupled to a Coherent Chameleon titanium:sapphire laser (Coherent, Glasgow, UK). The laser was set to 920 nm for excitation. Laser power at the specimen was approximately 13 mW. SHG emissions were collected from 420 to 480 nm, and autofluorescence emissions were collected from 500 to 550 nm with band-pass filters mounted in a standard P & C filtercube. The SHG emission signal was collected at 458 nm (half the incident wavelength) and a parallel autofluorescent signal was collected at 760 nm using a dual channel Zeiss LSM BiG detector. The BiG can collect images at different wavelengths simultaneously. Autofluorescence reveals cellular components that include various lipopigments and vitamin derivatives (Zipfel et al., 2003) as well as aromatic amino acids (Monici, 2005) useful for comparison with collagen distribution within bone. Focal planes and bone regions were selected to include sufficient collagen to visualise within the viewing frame. Frame sizes of 1932 × 1932 pixels were rastered at 5 s speed, taking the average of 4 reads per line. Fig. 1 shows composite images of SHG in red, merged with autofluorescence in green, discussed below.

Zeiss Efficient Navigation (ZEN) software proprietary to the microscope system was used to control equipment and capture raw images in .czi file format. Open source ImageJ software package Fiji (Schindelin et al., 2012) was used to process the data, which included merging the channels and adjusting channel brightness, to produce Fig. 1. Pixel intensity from each channel (458 and 760) ranged from 0 to 255. An intensity threshold of 75 was used for both channels to maximize collagen and organic signals against the background. After merging red and green channels, the brightness ranges were adjusted to balance disparate intensities from the two channels. For example, modern bone had so much collagen that its red SHG signal overwhelmed the autofluorescence. Therefore its hues were set to 40–255 to dim the powerful SHG signal enough to visualise autofluorescence, as shown in Fig. 1A. Older bones had dramatically less collagen content and hence dramatically dimmer SHG than autofluorescent signals. Therefore, hues from Medieval and ice age bone samples were set from 20 to 255 to enhance the red SHG signal from faint collagen traces.

2.3. Raman spectroscopy

Raman spectroscopy reveals vibrational and rotational modes of various covalent bonds, which raise or lower the energy level of laser light. It has been used to characterize amide bonds in collagen (Gullekson et al., 2011). Raman spectra from five ancient bones and one modern bovine bone were collected at the Laboratory of Imaging Mass Spectrometry at the University of North Texas (UNT) in Denton. A Horiba iHR550 Imaging Spectrometer was set to full scan range of 200–2600 cm^{-1}. The instrument was calibrated every fourth scan.

2.4. Fourier transform infrared spectroscopy

FTIR spectroscopy of medieval bovine tibia NP77_109_5, ice age *Megatherium americanum* EHRC90002, and one modern bovine bone was performed at the School of Science and Engineering, Teesside University. A Perkin Elmer Spectrum 100 FTIR spectrometer with a diamond attenuated total reflectance (ATR) accessory was used to make measurements. A few mg of bone from each sample was ground with an agate mortar and pestle and then placed in contact with the ATR accessory. The SPECTRUM™ software was used to record spectra over the wavelength range 650 cm^{-1} to 2000 cm^{-1} at a spectral resolution of 4 cm^{-1}. Each spectrum was an average of 16 scans.

The ratio of the main amide peak height to the phosphate peak height represents relative amounts of collagen to bioapatite in a bone sample. Since collagen decays, its peak height should decrease over time. To confirm collagen decayed in ancient bone, FTIR spectra shown in Fig. 3 were collected from three bone samples representing modern, Medieval, and ice age time frames. All three bones were used in multiple, overlapping collagen detection techniques as described below. The degree of collagen preservation was estimated by calculating the ratio of protein-specific amide bond stretching to bioapatite-specific phosphate stretching as per Thompson et al. (2013, 2009). The carbonyl stretch of the amide bond in collagen generates a spectral peak height at 1650 cm^{-1}, and the phosphate stretch of the apatite fraction in bone generates a peak at 1035 cm^{-1}. A higher value of the carbonyl-to-phosphate peak height ratio (carbonyl/phosphate, or CO/P) corresponds to better collagen preservation.

2.5. Protein extraction and sequencing

Protein extraction from ancient bone for mass spectrometry-based sequencing (LC-MS/MS) proceeded according to the method of Jiang et al. (2007). Briefly, bone powder (~50 mg; NP73_34_81; medieval human rib) was demineralized (1.2 M HCl) and then incubated sequentially with extract buffer 1 (100 mM Tris, 6 M Guanidine-HCl, pH 7.4), extract buffer 2 (100 mM Tris, 6 M Guanidine-HCl, 250 mM

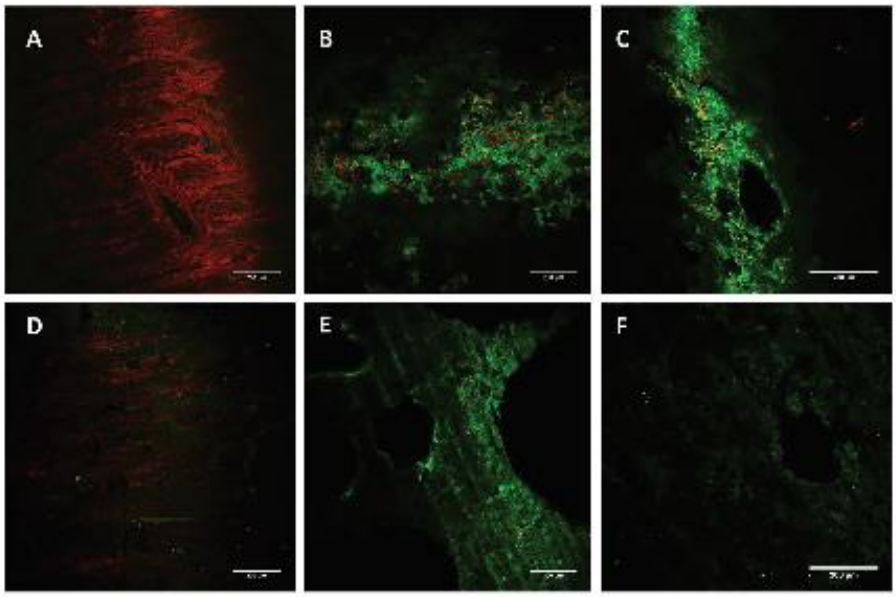

Fig. 1. Second-Harmonic Generation (SHG) images of six bones.
Collagen SHG detection is shown in red, and the green shows autofluorescence of mostly organic, non-collagen bone tissue constituents. The SHG (red) signal generally diminishes with older bones, consistent with collagen decay over time. This sample set shows that SHG reveals collagen in a wide range of taxa, ages, and settings. The scale bars equal 200 μm. The brightness range for both red and green channels was set to 0–75. A) A cross-section of cortical bone from the proximal diaphysis of modern bovine femur shows dense collagen bands that encircle osteons. B) The uneven surface of a thin section of Medieval human rib bone NP73_34_81 (SK101) from Norton Priory, UK reveals significant collagen decay relative to modern bone, as well as irregular collagen deposition, presumably due to Paget's disease. C) Red collagenous remains in Norton Priory Pagetic human left ulna NP71_12_9 (SK35) were confirmed by protein sequencing (see text). D) Norton Priory bovine tibia NP77_109_5 cortical bone shows better collagen signal than the two human samples B and C, possibly because of Paget's effect on postmortem bone decay, or differences between human burial versus trash deposition. E) Upper Pleistocene Camelid EHRC9001 from Oregon, USA shows barely visible collagenous remnants. F) Pleistocene *Megatherium* ilium EHRC90002 from California, USA shows the least collagen signal among the bones under consideration here. The, but demonstrates that SGH can collect information from a w. (For interpretation of the references to color in this figure legend, the reader is referred to the web version of this article.)

EDTA, pH 7.4) and finally 6 M HCl. Following each extraction step, the bone powder was pelleted by centrifugation (16,000*g* for 10 min at 4 °C) and washed in deionised water. The supernatant was discarded, with the exception of the 6 M HCl extract, which was utilised in subsequent analyses; either probed directly by SDS-PAGE using a 5–20% polyacrylamide gradient gel (visualised with silver-staining), or taken forward to MS/MS analysis.

For the latter the 6 M HCl extract was digested with trypsin according to a modified FASP strategy, with subsequent LC-MS/MS analysis carried out using an RSLC nano-HPLC system (Dionex, UK) and an LTQ-Orbitrap-Velos mass spectrometer (Thermo Scientific) essentially as detailed by Scott et al. (2016). The .raw data file obtained from the LC-MS/MS acquisition was processed using Proteome Discoverer (version 1.4.0.288, Thermo Scientific), with the file searched using Mascot (version 2.2.04, Matrix Science Ltd.) (Perkins et al., 1999) against the UniprotHuman_2015_02 database (unknown version, 67,911 entries) assuming the strict trypsin digestion. The peptide tolerance was set to 10 ppm and the MS/MS tolerance was set to 0.02 Da. Fixed modifications were set as alkylation of cysteine, and variable modifications set as deamidation of asparagine and glutamine, and oxidation of methionine and proline residues. Scaffold Q + S (Searle, 2010) (version 4.4.1.1, Proteome Software) was used to validate MS/MS based peptide and protein identifications from Proteome Discoverer. Peptide identifications were accepted if they could be established at greater than 95.0% probability, with a minimum of two peptides required for protein identification.

3. Results and discussion

3.1. SHG imaging captures faint signals in ancient bone

Before use of SHG imaging as a diagnostic technique for research questions pertaining to ancient bones from various settings, taxa, and ages, it first needs to be shown that the methodologies used here can reliably image the same bone component—namely collagen type 1—in modern as in ancient bone. The first step to establish this was to capture SHG images from bone samples from different settings and ages and compare them with modern bone. Fig. 1A shows typical collagen-dense (colored red) modern bovine cortical bone. Roughly concentric striated collagen fibres, perforated by small black patches that correspond to osteocyte lacunae, wrap around oval-shaped osteons. This result conforms to other SHG images of modern bone (Schrof et al., 2014). Fig. 1B–F show SHG images of ancient bones and permit, for the first time, comparison with modern bone. In all five ancient samples, the red SHG signal is greatly reduced compared to modern bone. We performed subsequent analyses to verify that these red traces correspond to primary (i.e. endogenous) and not contaminating, bone collagen.

Uneven autofluorescence patterns, particularly evident in Fig. 1B (Human rib NP73_34_81) and 1C (Human left ulna NP71_12_9), do not reflect structures inherent to the bone, but rather uneven surface samples and regions where the focal plane captured slanted surfaces. This became evident when focusing up or down brought higher or lower regions into focus. Acetic acid pretreatments of bones for image resolution improvement were inconclusive, so the application of acetic acid to bone surfaces was discontinued. Medieval human, Medieval

bovine, and Pleistocene *Megatherium* bone all show at least faint collagen traces, visible as red blotches and dots. We conclude that these represent collagenous remnants for three reasons. Firstly, the diminishing signal with increasing age generally corresponds to established collagen decay regimes as described below. Secondly, separate techniques verify protein within our bone samples, as described in the next section. Thirdly, literature consistently reports significant contributions to SHG signal from collagen type 1, which has been firmly established as the primary source in modern bone.

The hue range of 20 to 255 was chosen to strike a balance between the two channels so that each image includes both the collagen and autofluorescent signals. The same hue range was applied to all ancient bone images, but not modern bone, to equally compare collagen content across samples from a variety of burial settings and ages. Visual inspection reveals a loss of collagen signal strength over time. The three Medieval bones shown in Fig. 1B–D all have more collagen than the two Pleistocene bone shown in Fig. 1E and F. In addition, Fig. 1D shows a bovine bone of roughly the same age as the two human bones in Fig. 1B and C. These should show a similar concentration of collagen if time is the sole factor in collagen decay. However, the bovine bone shows a higher collagen concentration, possibly due to diagenetic differences between intentional burial of humans versus the midden-like setting of the discarded bovine bone.

Future studies can use SHG images of ancient bone to quantify collagen using the signal area in a single image, as per Chiu et al. (2010) who calculated a collagen area ratio (CAR) by dividing the pixels of interest (collagen) by those presumed to represent the total organic area (for example, autofluorescent pixels). Alternatively, future studies could quantify collagen volume by subtracting collagen signal from organics in 3-D rendered z-stacks like that shown below. Future studies could combine either strategy with radiocarbon or otherwise age-dated bone samples to explore collagen decay regimes in specific settings. More research will also be necessary to determine if enough collagen remains in Medieval human bones for SHG imaging to reveal disease affected or non-affected patterns.

Despite the positive identification of collagen using SHG, faint permineralisation caused slight darkening of the outermost 1.5 mm of the Pleistocene camel cortical bone EHRC90001. Dark, microscopic flecks of mineral within the bone appeared as red block shapes under SHG. Regions deeper within the original bone than about 3 mm had no dark flecks and no red block shaped signals, but they did have the same red blotches characteristic of collagenous remnants in all samples within this study. This result showed that although SHG signals can reveal collagen in ancient bone, they can also reveal mineralization, suggesting that discernment of bone microstructure and decayed collagen morphologies, and not color alone, will be important for workers to qualify ancient bone collagen using SHG.

3.2. Four techniques confirm protein in SHG-imaged ancient bone samples

Raman spectra of these ancient bones shown in Fig. 2 revealed broad shoulders instead of the sharp corresponding peaks from modern. As proteins hydrolyze and/or cross-link through diagenetic alteration and decay, and as their concentrations diminish, many of their corresponding Raman peaks lose distinctiveness of shape. Morris and Finney (2004) identified the Raman spectral peak near 1340 wavenumbers (in cm^{-1}) in modern bone as an amide III vibrational mode, and the Raman spectral peak near 1530 cm^{-1} as an amide II vibrational mode. Fig. 2 shows sharp amide peaks from modern bovine bone (blue spectrum) that indicate strong protein bond vibrations. The two ancient bone spectra include human bone NP77_109_5 to represent a typical Raman spectrum from our Medieval bone set (purple spectrum) and *Megatherium* bone EHRC90002 to represent an ice age sample. These decreased amide bonds in ancient bones include shoulders and shallow peaks relative to modern bone. The shifts in ancient bone spectral shoulders toward higher wavenumbers than the peak values from modern bone are attributed to postmortem chemical alterations. Peak height reductions over time were also observed, consistent with McLaughlin and Lednev's measured Raman peak reductions especially in the CH_2 region of turkey bone buried for 68 days (McLaughlin and Lednev, 2011). These results are consistent with diminished primary bone protein such as collagen.

FTIR in conjunction with Raman spectroscopy has been used to assess collagen quality in archaeological samples, and even to prescreen samples suitable enough for radiocarbon analysis (Boaretto et al., 2009). FTIR has also been used to characterize amino acids and amide bond signatures from blood vessel-like remains from fossils as deep as Triassic (Surmik et al., 2016). A similar technique confirmed the left-handed triple helical configuration indicative of collagen in a Jurassic sauropod rib bone (Lee et al., 2017). These demonstrate the sensitivity of the FTIR technique to detect proteinaceous signatures when applied to ancient bone samples that have been sufficiently well preserved. The blue FTIR spectrum in Fig. 3 corresponds to the same modern bone used for Raman spectroscopy (blue spectrum in Fig. 2) and SHG image (Fig. 1A). Likewise, the purple FTIR spectrum in Fig. 3 shows NP 77_109_5, the same Medieval bone as the purple Raman spectrum in Fig. 2. The green spectra in both Fig. 3 and Fig. 2 show amide bond vibration in Pleistocene camel EHRC 90002. Additionally, collagen was extracted for successful radiocarbon dating from both NP77_109_5 and EHRC 90002. Finally, Fig. 1D shows collagen in the SHG image of NP77_109_5, and Fig. 1F shows small traces of collagen (in red) within the SHG image of EHRC 90002. Fig. 3 compares modern bovine (blue spectrum) with medieval bone (purple, bovine tibia NP 77_109_5) FTIR spectra. The carbonyl peak at ~1650 cm^{-1} indicates reduced but preserved collagen in the Medieval sample. The Pleistocene sample (green spectrum in Fig. 3) is further reduced from the Medieval, again consistent with collagen loss due to decay over time.

Table 2 shows the carbonyl and phosphate FTIR peaks used to calculate CO/P ratio for the three bones in Fig. 3.

These calculations confirm what Fig. 3 also reveals: a decrease in CO/P ratios with older bone samples. This decreased collagen signal, similar to those decrease signatures seen in Raman spectra peaks that develop shoulders with age (Fig. 2) and SGH signal weakening with age (Fig. 1), are consistent with artificial protein decay experiments that show bone collagen decay matching a first-order, temperature-dependent model while hydrated (Collins et al., 1995) and confirm that these bones retain endogenous proteinaceous content.

Protein extraction from the SHG-imaged medieval human rib sample (SK 101) was confirmed by SDS PAGE analysis, which demonstrated a characteristic protein 'smear' [Fig. 4A] consistent with the presence of collagens. Mass spectrometry-based protein sequencing revealed remarkable collagen preservation seven centuries post-burial, and identified numerous peptide sequences corresponding to human collagen alpha-I (COL1A1, 59% sequence coverage) and collagen alpha-II (COL1A2, 65% sequence coverage) [Fig. 4B, C], representing both chains of collagen type I, and entirely consistent with the SHG data.

The sample preparation process for radiocarbon dating inadvertently also provides evidence for endogenous collagen remnants in ancient bone. Table 1 summarizes eight radiocarbon results from six ancient bones with varying degrees of collagen-indicating SHG signal. Three different radiocarbon dating laboratories found sufficient fractions of insoluble collagen in five of six bones. The *Megatherium* (EHRC90002) bone had insufficient collagen for radiocarbon dating, consistent with the small traces of SHG signal seen in Fig. 1F. Typical cutoff fractions for commercial radiocarbon laboratories equal approximately 1% by weight collagen/total bone (Brock et al., 2012). Fig. 1 includes SHG images of two (tibia NP77_109_5, and EHRC90001) of the five bones shown in Table 1 that contained sufficient collagen for radiocarbon analysis. One bone sample (Bovine radius NP77_109_5) was selected for a z-stack of SHG images, and is shown in Fig. 5.

In summary, results from four independent techniques verify primary protein in our ancient bone set. These results are consistent with

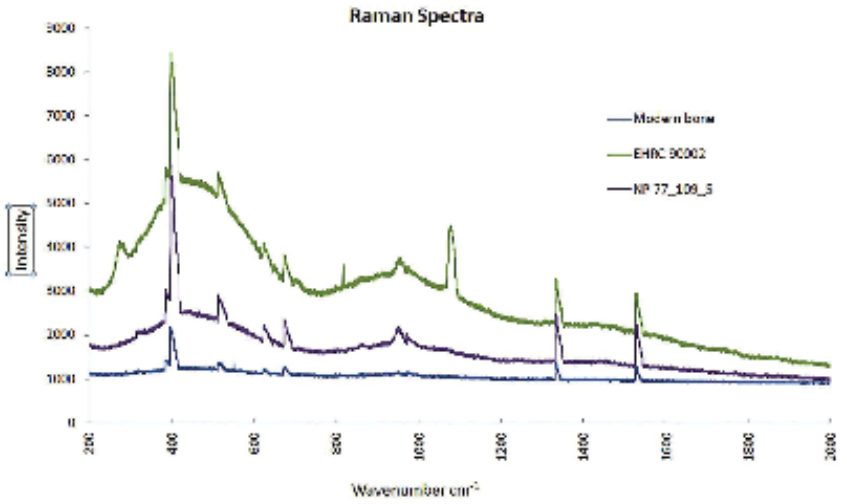

Fig. 2. Raman spectra of bone collagen amide peaks.
Modern bovine, Medieval bovine, and Pleistocene *Megatherium* bones show corresponding bone collagen amide III vibrational mode peaks near 1340 cm^{-1}, and amide II peaks near 1530 cm^{-1}. Peak heights appeared to diminish in the Pleistocene but not the medieval sample. Peak wavenumbers decreased slightly with age.

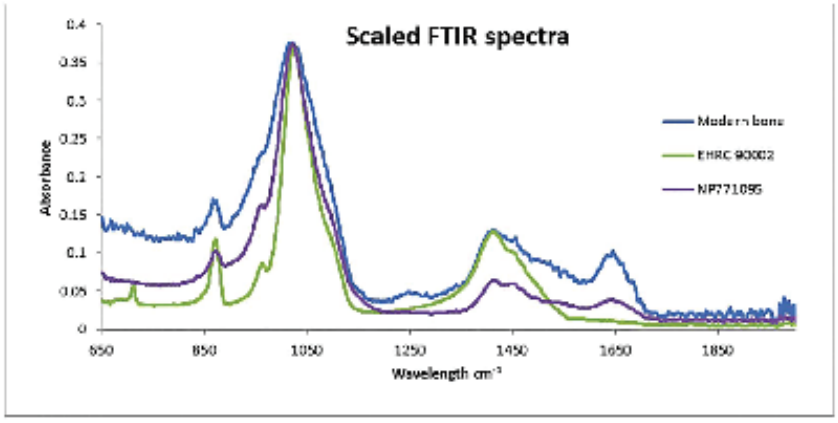

Fig. 3. FTIR spectra of three bones show collagen decay.
Modern, Medieval, and Pleistocene bones each show collagen-based carbonyl (CO) stretch peaks near 1650 cm^{-1}. These peaks decrease with age, indicating protein loss. The phosphate (P) peak at 1035 cm^{-1} stays relatively stable over time, enabling a calculation of the CO/P (essentially collagen/bioapatite) ratio as shown in Table 2.

Table 2
Carbonyl and phosphate FTIR peak values.

Bone source:	Modern	Medieval (MNP77_109_5)	Ice Age (EHRC90002)
CO (1025 cm^{-1})	0.0533	0.2212	0.3707
P (1650 cm^{-1})	0.0136	0.0217	0.0132
CO/P =	0.26	0.10	0.03

the hypothesis that SHG imaging of ancient bone detects decayed remnants of original bone collagen. Raman spectroscopy, FTIR spectroscopy, and SHG imaging all probe the chemical makeup of bone samples without the need to treat or destroy the sample. Standard radiocarbon bone sample pretreatments and protein sequencing bone sample preparations destroy small amounts of the artefacts, but they firmly secure the presence of endogenous ancient bone proteins.

3.3. 3-D SHG imaging of ancient bone

By recording SHG images at different focal planes a z-stack of images from bovine radius NP77_109_5 was collected. 75 planar SHG images, each measuring 1214 × 1214 μm, spanned a depth of 750 μm to provide a resolution of 10 μm in the z-axis. Bitplane (Oxford Instruments) Imaris image analysis software was used to collate the stack into a 3-D model (Fig. 5A) and to render the z-stack in 3-D and apply a space-filling model to both channels. As in all Fig. 1 images, the red represents collagen and green represents autofluorescence, both shown in Fig. 5A. Fig. 5B renders the green autofluorescence channel, which indicates the presence of proteinaceous and lipid residues, as a space-filled model to against which the smaller SHG signal in order to illustrate the spatial positioning of collagen remnants shown in red. The red signals in Fig. 5 indicate remnants of bone collagen type 1. SHG in

Fig. 4. Collagen sequence in Medieval human rib bone NF73.34_81 (SK 101).
A) SDS PAGE of ~700-year-old human bone protein extract still shows a visible protein smear, consistent with endogenous collagens. B) SK 101 had a 59% sequence coverage of the human collagen alpha-I chain. C) SK 101 had a 65% sequence coverage of the human collagen alpha-II chain.

bone loses resolution with depth, and did not work well beneath 1 mm. However, Fig. 5 suggests that future SHG studies can nondestructively probe for collagen almost 1 mm beneath the exposed surface of an ancient bone sample. SHG images from additional bone samples representing more continuously graded ages could reveal post-mortem type I collagen decay patterns, and images from diseased versus normal human bone could further characterise bone health in ancient populations.

4. Conclusion

Four separate protein detection techniques confirm the presence of proteinaceous organic remains in the same ancient bones from which SHG imaging captured signals consistent with endogenous collagen type I. We conclude that it is possible to visualise the distribution of tiny patches of collagen in ancient bone using SHG imaging. Our results further demonstrate that SHG imaging reveals bone collagen remnants in a wide (modern to Pleistocene) age range, which additional research could potentially expand. Finally, SHG images of Medieval bone collagen show variation in collagen preservation even from a single location (Norton Priory), suggesting its potential to explore causes of differential collagen preservation. However, collagen-like SHG signals from exogenous minerals caution that experiential knowledge of bone microstructure including collagen remnant morphologies is necessary (without the assistance of other techniques) to discern collagen in partly mineralised ancient bone. Future work can leverage digital image

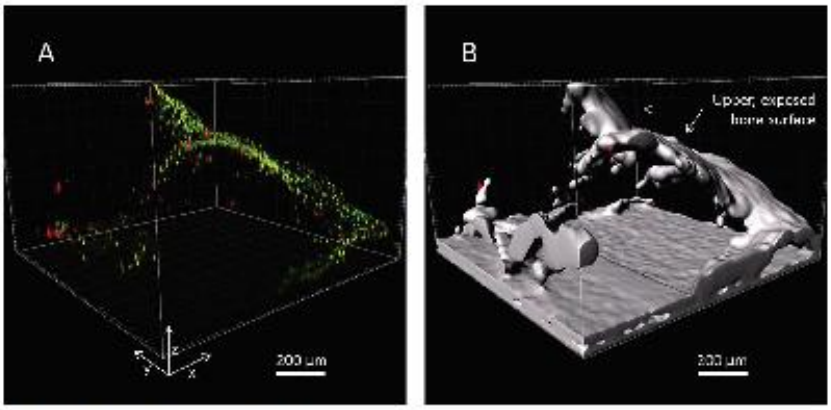

Fig. 5. SHG z-stack reveals 3-D distribution of collagen in ancient bone surface.
Medieval bovine radius NF77_109_5, radiocarbon-dated to approximately 1380 CE, shows faint collagenous remnants colored red. Areas with no color represent trabecular spaces. 75 2-D images spaced 10 µm apart spanned a depth of 750 µm, totaling a 1 mm × 1 mm × 0.75 mm volume. A) Stacked 3D image with red SHG that shows collagen remnants and green autofluorescence that shows other organics (see text). B) Imaris software was used to render a solid grey space-fill function around the green signal to reveal non-overlapping collagenous volumes. (For interpretation of the references to color in this figure legend, the reader is referred to the web version of this article.)

processing of SHG data to estimate collagen content and visualise the 3-D distribution of collagen in ancient bone surfaces up to 1 mm deep. SHG imaging holds promise as a novel and nondestructive technique to investigate collagen in ancient bones of various settings, taxa, and ages.

Acknowledgements

Protein sequencing was funded in part by the Wellcome Trust (ref. WT107720MA) and we wish to thank the Protein Nucleic Acid Chemistry Laboratory (PNACL), University of Leicester, UK, for assistance with LC-MS/MS analyses. The Live Cell Imaging lab at the University of Texas Medical Center in Dallas, including Kate Luby-Phelps, Dorothy Mundy, and Abhijit Bugde, deserve special thanks for SHG training and access to confocal equipment made available in part through NIH S10 RR029731-01. Philip Mach at the University of North Texas provided tutelage on Raman spectroscopy and Rob van 'THof at UoL for assistance with bone sectioning. Arthur Chadwick granted access to EHRC fossils curated at Southwestern Adventist University. Norton Priory Museums Trust kindly provided samples and Q-Technologies funded radiocarbon analyses.

References

Aaron, J.E., Rogers, J., Kanis, J.A., 1992. Paleohistory of Paget's disease in two medieval skeletons. Am. J. Phys. Anthropol. 89, 325–331.

Ambekar, R., Chittenden, M., Jasiuk, I., Toussaint Jr., K.C., 2012. Quantitative second-harmonic generation microscopy for imaging porcine cortical bone: comparison to SEM and its potential to investigate age-related changes. Bone 50, 643–650.

Arslanov, K.A., Svetlichnitsky, V.S., 1993. An improved method for radiocarbon dating fossil bones. Radiocarbon 3, 387–391.

Boaretto, E., Wu, X., Yuan, J., Bar-Yosef, O., Chu, V., Pan, Y., Liu, K., Cohen, D., Jiao, T., Li, S., Gu, H., Goldberg, P., Weiner, S., 2009. Radiocarbon dating of charcoal and bone collagen associated with early pottery at Uychatsyan Cave, Hunan Province, China. PNAS 106, 9595–9600.

Brock, F., Wood, R., Higham, T.F.G., Ditchfield, P., Bayliss, A., Ramsey, C.B., 2012. Reliability of nitrogen content (%N) and carbon:nitrogen atomic ratios (C:N) as indicators of collagen preservation suitable for radiocarbon dating. Radiocarbon 54, 879–886.

Brown, E., McKee, T., diTomaso, E., Pluen, A., Seed, B., Boucher, Y., Jain, R.K., 2003. Dynamic imaging of collagen and its modulation in tumors in vivo using second-harmonic generation. Nat. Med. 9, 796–800.

Buckley, M., Walker, A., Ho, S.Y.W., Yang, Y., Smith, C., Ashton, P., Oates, J.T., Cappellini, E., Koon, H., Penkman, K., Elsworth, B., Ashford, D., Solazzo, C., Andrews, P., Strahler, J., Shapiro, B., Ostrom, P., Gandhi, H., Miller, W., Rumy, B., Zylber, M.I., Gilbert, M.T.P., Prigodich, R.V., Ryan, M., Rijsdijk, K.F., Janoo, A., Collins, M.J., 2008. Comment on "protein sequences from mastodon and Tyrannosaurus rex revealed by mass spectrometry.". Science 319, 33c.

Burrell, C.L., Gonzalez, S., Smith, L., Emery, M.M., Irish, J.D., 2016. More than meets the eye: Paget's disease within archaeological remains. Am. J. Phys. Anthropol. 159, 105–106.

Chen, X., Nadiarynkh, O., Plotnikov, S., Campagnola, P.J., 2012. Second harmonic generation microscopy for quantitative analysis of collagen fibrillar structure. Nat. Protoc. 7, 654–669.

Chin, Y.-W., Lo, M.T., Tsai, M.-R., Chang, Y.C., Hsu, R.-B., H-Y, Yu, Sun, C.-K., Ho, Y.-L., 2010. Applying harmonic optical microscopy for spatial alignment of atrial collagen fibers. PLoS ONE 5, e13917.

Closs, P.A., Fledelius, C., Christgau, S., Christiansen, C., Bigaig, M., Delmas, P., Body, J.J., Garnero, P., 2003. Investigation of bone disease using isomerized and racemized fragments of type I collagen. Calcif. Tissue Int. 72, 8–17.

Collins, M.J., Riley, M.S., Child, A.M., Turner-Walker, G., 1995. A basic mathematical simulation of the chemical degradation of ancient collagen. J. Archaeol. Sci. 22, 175–183.

Gu, C., Dinesh, R.K., Katti, K.S., 2013. Photoacoustic FTIR spectroscopic study of undisturbed human cortical bone. Spectrochim. Acta A 102, 25–37.

Gullikson, C., Lucas, L., Hewitt, K., Kreplak, L., 2011. Surface-sensitive Raman spectroscopy of collagen I fibrils. Biophys. J. 100, 1837–1845.

Jiang, X., Ye, M., Jiang, X., Liu, G., Feng, S., Cai, L., Zou, H., 2007. Method development of efficient protein extraction in bone tissue for proteome analysis. J. Proteome Res. 6, 2287–2294.

Lee, Y.-C., Chiang, C.-C., Huang, P.-Y., Chung, C.-Y., Huang, T.D., Wang, C.-C., Chen, C.-I., Chang, R.-S., Liao, C.-H., Reisz, R.R., 2017. Evidence of preserved collagen in an Early Jurassic sauropodomorph dinosaur revealed by synchrotron FTIR microspectroscopy. Nat. Commun. 8, 14220.

Lee-Thorp, J.A., Sealy, J.C., van der Merwe, N.J., 1989. Stable carbon isotope ratio differences between bone collagen and bone apatite, and their relationship to diet. J. Archaeol. Sci. 16, 585–599.

McLaughlin, G., Lednev, I.K., 2011. Potential application of Raman spectroscopy for determining burial duration of skeletal remains. Anal. Bioanal. Chem. 401, 2511–2518.

Mohler, W., Millard, A.C., Campagnola, P.J., 2003. Second harmonic generation imaging of endogenous structural proteins. Methods 29, 97–109.

Monici, M., 2005. Cell and tissue autofluorescence research and diagnostic applications. Biotechnol. Annu. Rev. 11, 227–256.

Morris, M.D., Finney, W.F., 2004. Recent developments in Raman and infrared spectroscopy and imaging of bone tissue. Spectroscopy 18, 155–159.

Morvan-Dubois, G., Le Guellec, D., Garrone, R., Zylberberg, L., Bonnaud, L., 2003. Phylogenetic analysis of vertebrate fibrillar collagen locates the position of zebrafish α3(I) and suggests an evolutionary link between collagen α chains and Hox clusters. J. Mol. Evol. 57, 501–514.

Naik, N., Caves, J., Chaikof, E., Allen, M.G., 2014. Generation of spatially aligned collagen fiber networks through microstransfer molding. Adv. Healthc. Mater. 3, 367–374.

Penel, G., Delfosse, C., Descamps, M., Leroy, G., 2005. Composition of bone and apatitic biomaterials as revealed by intravital Raman microspectroscopy. Bone 36, 893–901.

Perkins, D.N., Pappin, D.J., Creasy, D.M., Cottrell, J.S., 1999. Probability-based protein identification by searching sequence databases using mass spectrometry data. Electrophoresis 20, 3551–3567.

Schindelin, J., Arganda-Carreras, I., Frise, E., Kaynig, V., Longair, M., Pietzsch, T., Preibisch, S., Rueden, C., Saalfeld, S., Schmid, B., Tinevez, J.-Y., White, D.J., Hartenstein, V., Eliceiri, K., Tomancak, P., Pijl, Cardona A., 2012. An open-source platform for biological-image analysis. Nat. Methods 9, 676–682.

Schraf, S., Varga, P., Galvis, L., Raum, K., Masic, A., 2014. 3D mapping of the collagen fibril orientation in human osteonal lamellae. J. Struct. Biol. 187, 266–275.

Scott, D., Garner, T.P., Long, J., Strachan, J., Mistry, S.C., Bottrill, A.R., Tooth, D.J., Searle, M.S., Oldham, N.J., Layfield, R., 2016. Mass spectrometry insights into a tandem ubiquitin-binding domain hybrid engineered for the selective recognition of unanchored polyubiquitin. Proteomics 16, 1961–1969.

Searle, B.C., 2010. Scaffold: a bioinformatic tool for validating MS/MS-based proteomic studies. Proteomics 10, 1265–1269.

Strupler, M., Pena, A.-M., Hernest, M., Tharaux, P.-L., Martin, J.-L., Beaurepaire, E., Schanne-Klein, M.-C., 2007. Second harmonic imaging and scoring of collagen in fibrotic tissues. Opt. Express 15, 4054–4065.

Surmik, D., Boczarowski, A., Balin, K., Dulski, M., Szade, J., Kremer, B., Pawlicki, R., 2016. Spectroscopic studies on organic matter from Triassic reptile bones, Upper Silesia, Poland. PLoS ONE 11, e0151143.

Thompson, T.J.U., Gauthier, M., Islam, M., 2009. The application of a new method of Fourier transform infrared spectroscopy to the analysis of burned bone. J. Archaeol. Sci. 36, 910–914.

Thompson, T.J.U., Islam, M., Bonniere, M., 2013. A new statistical approach for determining the crystallinity of heat-altered bone mineral from FTIR spectra. J. Archaeol. Sci. 40, 416–422.

Zipfel, W.R., Williams, R.M., Christie, R., Nikitin, A.Y., Hyman, B.T., Webb, W.W., 2003. Live tissue intrinsic emission microscopy using multiphoton-excited native fluorescence and second harmonic generation. PNAS 100, 7075–7080.

Appendix 3.2: Publication in Advances in Biotechnology and Microbiology

Advances in Biotechnology & Microbiology
ISSN 2474-7637

Juniper Publishers
key to the Researchers

Short Communication
Volume 7 Issue 2 November 2017
DOI: 10.19080/AIBM.2017.07.555708

Adv Biotech & Micro

Second-Harmonic Generation Imaging of Medieval Human Bone

Thomas B and Taylor S*

Mass Spectrometry Research Group, University of Liverpool, UK

Submission: October 06, 2017; **Published:** November 14, 2017

***Corresponding author:** Taylor S, Mass Spectrometry Research Group, University of Liverpool, UK, Tel: 0151-794-4517; Fax: 0151-794-4540; Email: s.taylor@liv.ac.uk

Keywords: Second-harmonic generation; Imaging; Collagen; Medieval bone

Short Communication

Second-harmonic generation (SHG) imaging using confocal laser microscopy has found use in biomedical investigations as a non-destructive and efficient means to examine collagen structures in animal tissues including bone [1]. The technique takes advantage of an inherent capacity for the large and highly organized coiled coil structure of collagen to absorb two low frequency (low energy) photons and re-emit them as a single photon with twice the frequency but half the wavelength. It thus permits visualizations of microscopic characteristics of collagen in tissues without adding fluorophores. However, SHG has not to our knowledge been applied to ancient bones.

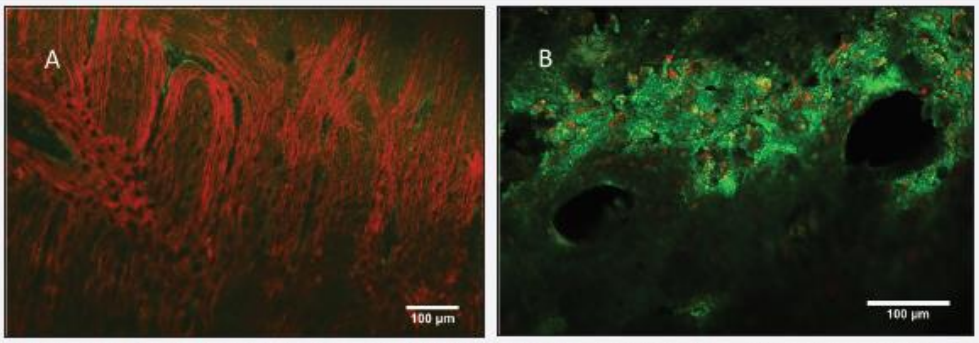

Figure 1: SHG Images of modern and ancient bone. 1A) Red SHG areas represent abundant bone collagen. Collagen striations encircle typical osteocyte structure of modern bovine cortical bone cross-section. Green areas show autofluorescent biomolecules. 1B) Medieval human left ulna cortical bone cross-section from Norton Priory (NP 71_12_9), UK, show greatly diminished collagen signals in red as expected from postmortem collagen decay.

Various techniques have revealed information about burial history and ancient life found in the collagen fraction of ancient bones. For example, workers use collagen extracts for most radiocarbon dating of bones. Stable isotopes in collagen reveal clues about paleodiets, collagen sequencing by tandem mass spectrometry enables interspecies cladistics analyses [2], and weight percent of residual collagen in ancient bone reflects age and burial dynamics [3]. Further, the growing field of molecular paleontology continues to benefit from new techniques that show particular sensitivity to trace amounts of collagen protein [4]. SHG imaging therefore holds potential to visualize collagenous remnants in ancient bone. Further, digital imaging software can mine images for trends, for example to estimate collagen content in bone.

SHG imaging of cross-sections of cortical bone from a modern bovine femur and a Medieval human left ulna (NP 71_12_9) excavated at Norton Priory, UK, was performed using a two-photon laser scanning confocal microscope outfitted for second-harmonic generation imaging. We used a Zeiss Plan-Apochromat

10X, NA =0.45 objective lens and a 920nm titanium: sapphire laser with power at the specimen of approximately 13mW for excitation. A band-pass filter from 420 to 480nm was used to collect SHG emissions, and a 500 to 550nm filter to collect auto fluorescent emissions in parallel. The SHG emission signal was collected at 458nm and autofluorescent signal was collected at 760nm using a dual channel Zeiss LSM BiG detector. Auto fluorescence reveals cellular components that include various lipo-pigments and vitamin derivatives as well as aromatic amino acids. Focal planes and bone regions were selected to include sufficient collagen to visualize within the viewing frame. Figure 1 shows composite images of modern an ancient bone with SHG in red and auto fluorescence in green.

Figure 1A shows modern bovine femur with a red (collagen) channel intensity threshold of 0-50, and a green channel intensity threshold of 0 to 75. The intensity thresholds were reversed for each channel in Figure 1B (red =0 to 75; green =0 to 50) in order to enhance the faint collagen signal in the ancient sample.

Table 1: Collagen area ratio estimates for modern and medieval bone.

	SHG Area (pixels)	Organic Area (pixels)	CAR
Modern bovine	335435	338826	99
NP 71_12_9	212917	302510	70.38

A Collagen Area Ratio (CAR) from each image was calculated according to Chiu et al. [5] using Fiji [6]. Briefly, CAR =(SHG area of collagen ÷ total organic area)x100. Red SHG plus green autofluorescence channels were combined to estimate total organic area. Areas shown in Table 1 represent averages of three images each. Future studies will likely specify alternative means of estimating collagen content that serve particular research interests, but CAR is used here to illustrate the potential of processing SHG images. Table 1 compares the average of three CAR calculations each from modern bovine and medieval human ulna NP 71_12_9. The result numerically confirms a decrease in collagen content over time that the decrease in red (collagen) signal in Figure 1 suggests.

CAR calculations of a statistically significant number of firmly dated bone samples could be used to generate collagen decay curves that investigate preservation potentials of various taxa and environments. SHG Imaging visualizes the extent and distribution of collagen fragments in Medieval bone, and image processing software can mine those images to address research questions such as collagen decay in certain taxa or settings.

Acknowledgement

The authors would like to acknowledge provision of samples of medieval bone from Norton Priory Museum Trust Ltd (NPMT Runcorn, UK) and access to SHG facilities at the University of Texas Southwestern Medical center (UTS, Dallas, USA).The authors would like to thank colleagues at the Department of Electrical Engineering and Electronics at the University of Liverpool: David McIntosh and Tom Fildes for helpful assistance. The authors acknowledge Professor Kate Luby-Phelps (UTS), MsLynn Smith and Dr Frank Hargrave (NPMT) for useful discussions. We have no conflict of interest to declare.

References

1. Ambekar R, Chittenden M, Jasiuk I, Toussaint KC (2012) Quantitative second-harmonic generation microscopy for imaging porcine cortical bone: Comparison to SEM and its potential to investigate age-related changes. Bone 50(3): 643-650.
2. Asara JM, Schweitzer MH, Freimark LM, Phillips M (2007) Protein sequences from mastodon and Tyrannosaurus Rex revealed by mass spectrometry. Science 316(5822): 280-285.
3. Buckley M, Collins MJ (2011) Collagen survival and its use for species identification in holocene-lower pleistocene bone fragments from british archaeological and paleontological sites. Antiqua 1(1): 1-7.
4. Lee YC, Chiang CC, Huang PY, Chung CY, Huang TD, et al. (2017) Evidence of preserved collagen in an early Jurassic sauropodomorph dinosaur revealed by synchrotron FTIR microspectroscopy. Nat Comm 8: 14220.
5. Chiu YW, Lo MT, Tsai MR, Chang YC, Hsu RB, et al. (2010) Applying Harmonic optical microscopy for spatial alignment of atrial collagen fibers. PLOS ONE 5: e13917.
6. Schindelin J, Arganda CI, Frise E, Kaynig V, Longair M, et al. (2012) Fiji: an open-source platform for biological-image analysis. Nat Meth 9(7): 676-682.

How to cite this article: Thomas B and Taylor S. Second-Harmonic Generation Imaging of Medieval Human Bone. Adv Biotech & Micro. 2017; 7(2): 555708. DOI: 10.19080/AIBM.2017.07.555708.

Chapter 4: Infrared and Raman spectroscopy

Contents

Figures

Tables

Rationale for use of ATR-IR and Raman spectroscopy on ancient bone

This research project involves a quest for novel technologies with potential to detect and characterise ancient bone proteins or other indicators of sub-fossilisation in ancient bone. At first, this quest focused on the two techniques that were initially available: second-harmonic generation imaging (SHG) and quadrupole mass spectrometry (QMS). Chapter 3 detailed novel results from SHG, but steep technical hurdles with QMS diverted focus elsewhere.

A fortuitous interaction with members of the Paget's Disease of ancient Bone (PDB) study group, which meets biannually at Norton Priory, introduced Fourier Transform Infrared spectroscopy (FTIR) as a third potential technique. PDB researchers from the School of Science and Engineering at Teesside University, UK, developed a procedure in 2009 to use attenuated total reflectance (ATR) FTIR (ATR-IR) spectroscopy as a forensic tool to quantify collagen content in burned bone[1,2]. The reasoning followed that if FTIR can detect collagen in bones of interest to forensics, then the same procedure might apply to much older samples, for example to any faint collagen remnants in archaeological or even fossil bone.

Soon afterward, my on-site supervisor in the United States and director of the University of North Texas Laboratory of Imaging Mass Spectrometry Guido Verbeck offered his ATR-IR device for use on ancient bone. He also suggested that if FTIR could detect remnants of endogenous organic functional groups, then possibly Raman spectroscopy could also. Both methods of infrared spectroscopy offer several advantages for ancient protein investigations. First, no two molecules show the same spectra, enabling substance identification either by comparison with spectra in proprietary libraries or by comparing spectra of known substances manually. FTIR analysis of thin sections of modern bone have been used to generate collagen-specific surface images[3].

Depending on the instrument, both are easy and inexpensive to operate. For example, hydration does not affect the IR spectra of molecules, so they can be measured in aqueous solution or at ambient humidity. Also, the peak intensities relate to the concentration of material present.

Like FTIR, Raman spectroscopy also measures bond oscillations when the frequency of the incident infrared laser matches the frequency of the stretching, bending, or wagging oscillation. Early in this project, use of Raman spectroscopy on ancient bone was unknown. After initial results were collected, further literature review revealed the use of Raman spectroscopy, though rare, to detect organic functional groups inside fossil material. Raman spectra were obtained to further investigate what they might reveal in ancient, including fossil, bone and shell, especially when compared with other techniques including SHG and FTIR on the same samples.

Further, after most of the data were collected and upon even further literature review it was discovered that Raman spectra of modern bone reveal a distinct, faint, but singular peak from hydroxyproline, which is a collagen-specific amino acid. Since this peak appears very tiny in modern bone spectra, as discussed in the last section below, it may not be discernable at all in ancient bone which has lower collagen content. But if the hydroxyproline peak is discernable in ancient bone samples, then Raman spectroscopy could become a much more widely used tool to quickly detect bone collagen, especially using a portable device.

ATR-IR and Raman spectroscopy instrumentation

FTIR was applied by the Teesside team on several of the specimens collected for this project, as described in Chapter 2. The few specimens provided to them spanned a deep stratigraphic range that included modern, medieval, and fossil bone, plus a Devonian

brachiopod shell. Some of those results were included in the *Bone Reports* paper attached to Chapter 3 as Appendix 1. The following procedures were used to collect FTIR results from ancient bone, as noted in Thomas *et al*. (2017)[4].

FTIR spectroscopy of one modern bovine bone, medieval bovine tibia NP77_109_5, ice age *Megatherium americanum* EHRC90002, Triceratops horn core HTCH06, dinosaur fragment HRS19114, Triceratops femur GDFM03.001, and hadrosaurid femur GDFM04.001 was performed at Teesside University. A Perkin Elmer Spectrum 100 FTIR spectrometer with a diamond attenuated total reflectance (ATR) accessory was used to measure the infrared spectrum of each powdered bone sample. A few mg of bone from each sample were ground with an agate mortar and pestle and then placed in contact with the ATR accessory. The SPECTRUM™ software was used to record spectra over the wavenumber range 650 cm^{-1} to 2000 cm^{-1} at a spectral resolution of 4 cm^{-1}. Each spectrum took an average of 16 scans.

The ATR accessory collects absorbance data from liquids or solids, but it only works for solids that intimately contact the crystal's upper surface. To achieve this for bone, small samples must be powderised. At Teesside, Islam and Thompson used an agate mortar and pestle to grind bone, but the mortar and pestle available at the Laboratory of Imaging Mass Spectrometry at the University of North Texas (UNT) used for subsequent tests was standard ceramic (Coors). Figure 4.1 shows the Thermo Scientific Nicolet 6700 FT-IR Spectrometer at UNT with the Smart iTX modular multiple-bounce diamond ATR accessory that was used to collect spectral data for 29 mostly ancient bone samples. Omnic software was used to record spectra over the wavenumber range 500 cm^{-1} to 4000 cm^{-1} at a spectral resolution of 4 cm^{-1}. This wider range than Thompson and Islam captured, at the cost of only a few more seconds per sample, what might someday become peaks of interest. Spectra shown in figures represent narrower ranges that zoomed in on

the peaks of immediate interest, namely that of phosphate and carbonyl. Each spectrum represented an average of 32 scans. This higher scan number slightly increased spectral resolution, again at a cost of a few more seconds per sample. Each FTIR spectrum was saved as a .csv file, then imported into the free graphing software Veusz (v. 3.0 © 2003-2018 Jeremy Sanders) for visualisation.

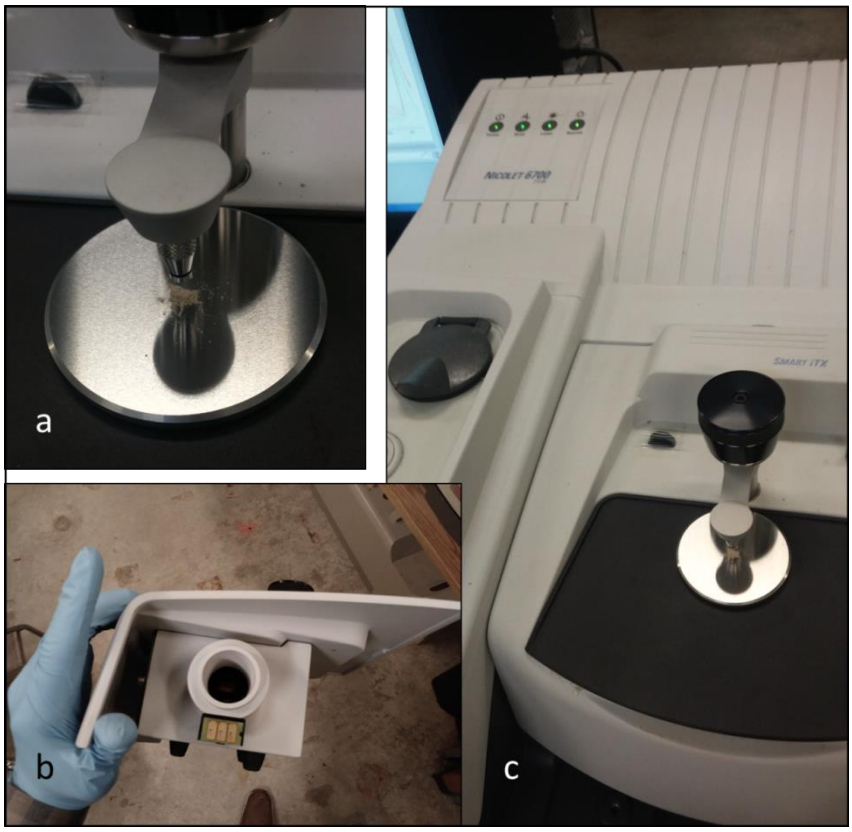

Figure 4.1 | The benchtop Thermo Scientific Nicolet 6700 FT-IR. a, Powderised ancient bone covers the diamond crystal surface beneath the anvil on the attenuated total reflectance module stage. **b**, The ATR module separated from the spectrometer exposes a tube containing the laser path. **c**, The ATR in context of the instrument.

The ratio of the main amide peak height to the phosphate peak height represents relative amounts of collagen to bioapatite in a bone sample. Because collagen decays, its peak height should decrease over time. To confirm collagen decay in ancient bone, FTIR spectra were collected from three bone samples representing modern, Medieval (NP 77_109_5), and ice age (EHRC 90002) time frames. Fig.4.2 shows the spectra for the

three bones. Thomas *et al*. (2017) used multiple collagen detection techniques to detected protein traces in most samples tested.

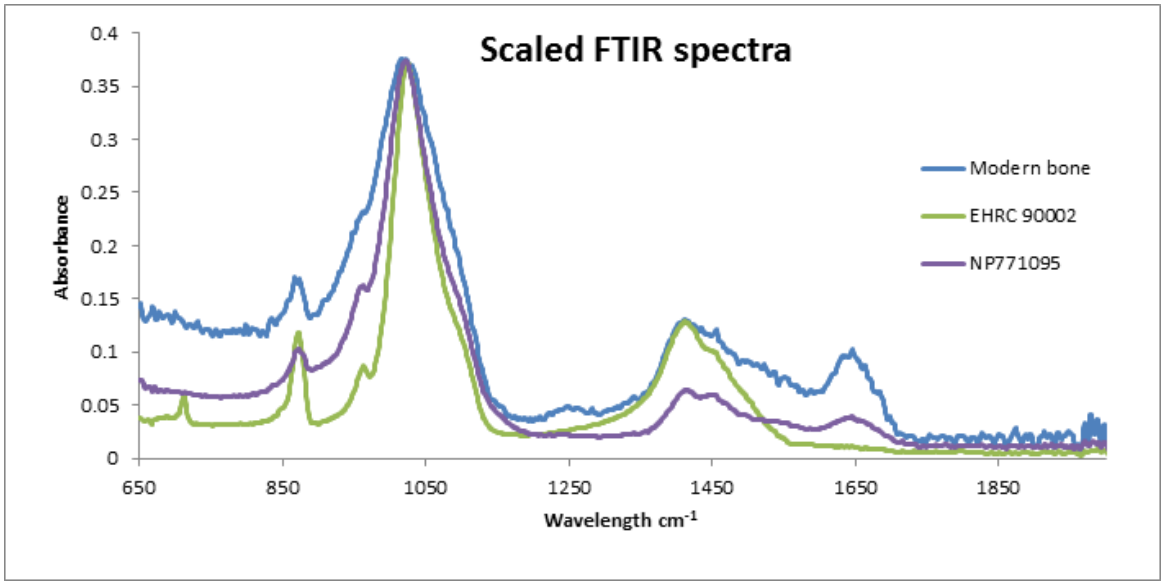

Figure 4.2 | Modern, medieval, and ice age ATR-IR spectra show evidence of collagen decay. After Thomas *et al*. (2017).

Fig. 4.2 is reproduced here from Thomas *et al*. (2017). It reveals a consistent peak height at 1035 cm-1, which corresponds to a phosphate stretch. This peak represents the crystalline, bioapatite fraction of bone that does not chemically decay over time with the systematic pattern of proteins. The peak at 1650 corresponds to a protein-specific carbonyl bond. Since Type I collagen dominates the biochemical landscape of fresh bone, and since myriad techniques have verified collagenous remnants in ancient and fossil bone, the carbonyl peak can be confidently assigned to bone collagen. Fig. 4.2 shows a systematic reduction in carbonyl peak height over time, consistent with collagen decay, except only three samples were included. Subsequent IR spectra were acquired in part to evaluate the consistency of this apparent trend.

Two preparation methods were used for Raman spectroscopy. In one, the laser was centered on a solid, smooth surface of cut and mounted cortical bone thin section. In the other, the laser was centered on a small (>0.5, <1.5 mg) sample of powdered bone. Powdered bone was carefully placed on a thin crystal constructed to cover a hole in the center of a 3-D printed, ~6 cm diameter round dish. Glass and plastics do affect Raman-scattered light a little, but crystal has virtually no effect on the light. In this configuration, incident laser passes through the crystal portion of the bottom of the dish before it impinges on the powdered sample. The Raman shift was measured as scattered light. For data collection, an Almega XR Raman spectrometer integrated to an Olympus BX51 microscope with spatial resolution down to 1 μm was used, essentially as per Huynh *et al*. (2015)[5] and shown in Fig. 4.3. An excitation source of 785 nm, at 30% of 40 mW power,

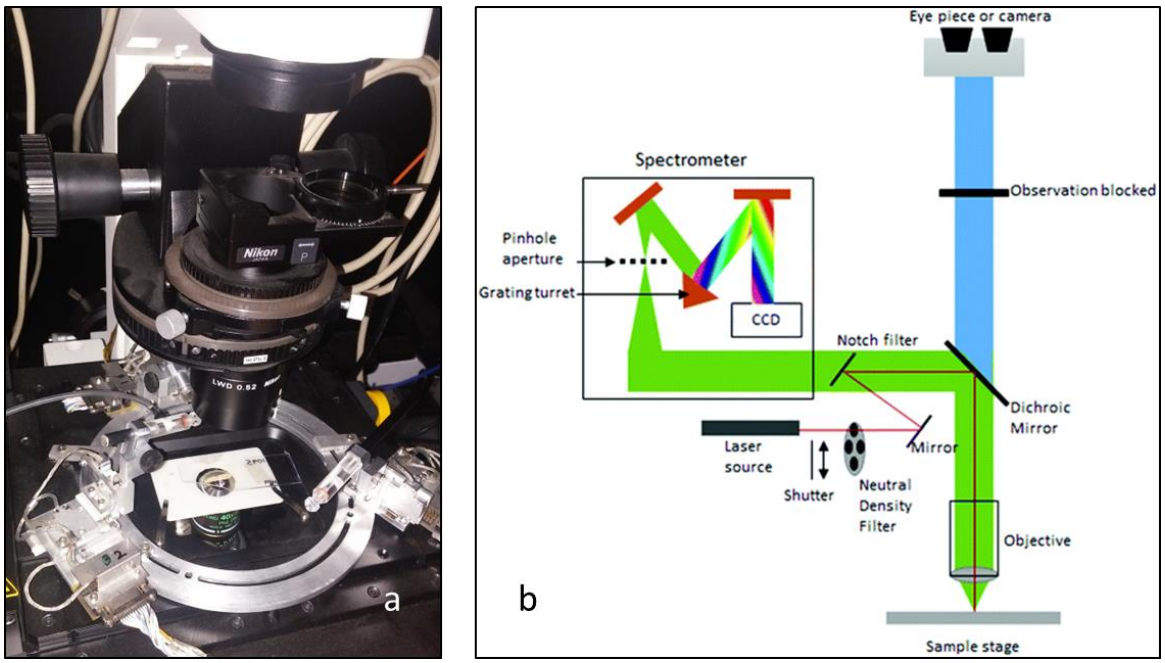

Figure 4.3 | Raman microscope and generalised setup. a, Olympus BX51 stage and objective are shown. Nanomanipulators beside the stage were not used. b, Generalised diagram of Raman microscope after Smith et al[6].

single transverse mode, high brightness diode laser was used. The laser power was not high enough to heat the samples enough to visibly affect them, whether powderised or

solid. The Raman signal was collected over the range of 1800–300 cm^{-1} using a 10x microscope objective with a numerical aperture (NA) of 0.25.

FTIR and Raman theory

Infrared spectra reveal which functional groups are present in a sample. This provides a solid starting point for identifying the chemistry, including the presence of proteins, in that sample. General infrared spectroscopy works on the principle that a chemical functional group will absorb a specific frequency of light that matches that functional group's frequency of stretching, bending, or wagging. The instrumentation's software calculates the absorbance spectrum of a sample by subtracting the light intensity absorbed by the sample from the background intensity. In FTIR spectroscopy, a broad spectrum of wavelengths is obtained for each sample all at once instead of by collecting the absorbance one wavelength at a time. Modern devices incorporate a version of the Fourier transform algorithm, which measures whether or not a frequency occurs within a particular wave function, to arrive at the unique spectrum for that specimen.

An ATR is a unique method of gathering absorbance data whereby the infrared laser interacts with a sample at a short distance away from the laser beam itself via an evanescent wave. The laser is angled at 45° to the horizontal surface of the crystal, in this case a diamond. Laser intensity is donated to the sample via evanescence that penetrates to a very shallow depth above the diamond and into the sample. The detector is sensitive to the higher intensity losses that occur at wavenumbers that correspond to vibrational modes of chemical functional groups. The ATR-IR (FTIR-ATR) is user-friendly, cost-effective, and requires only tiny amount (~0.5g) of sample.

Fig. 4.4 shows standard IR peak ranges for a variety of organic functional groups. The two groups of interest for forensic analysis of ancient bone, which estimates time

since the decease of the vertebrate, are carbonyl (green) and phosphate (orange). A protein's amide bond contains a particular chemical configuration (O=CH-NH-H) that includes a carbonyl moiety. As shown in Fig 4.4, the stretch peak for a variety of different carbonyl-containing molecular configurations occurs from 1600-1850 cm^{-1}, but from 1690-1640 cm^{-1} for the carbonyl on the amide bond, which is by definition protein-specific[7].

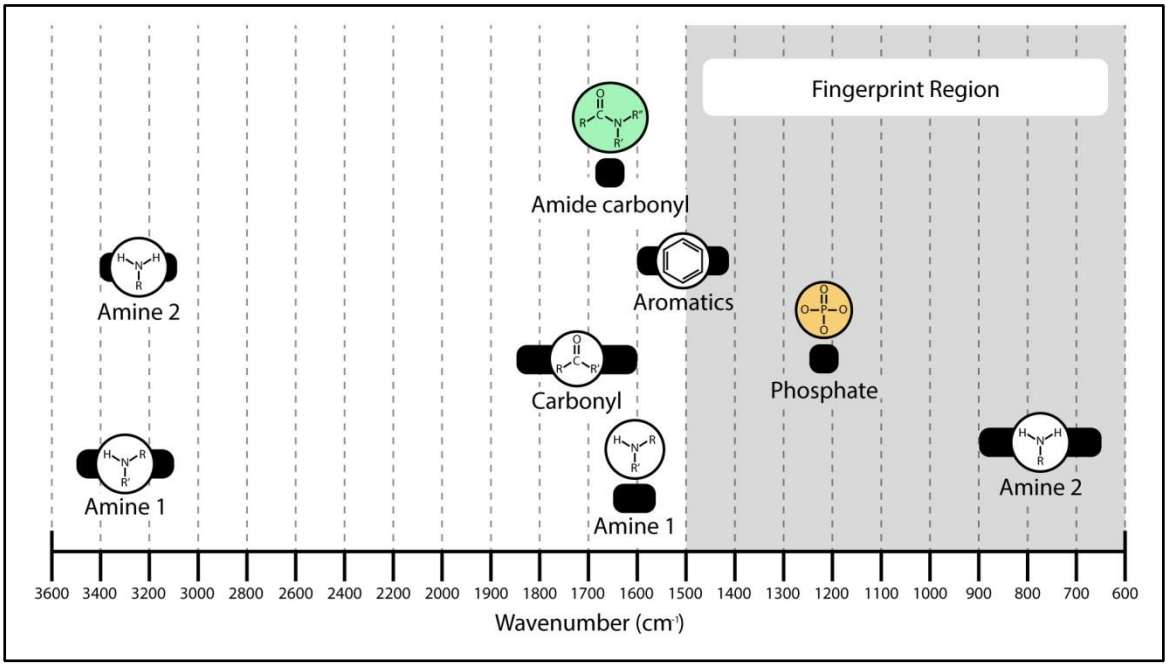

Figure 4.4 | Infrared peak ranges for functional groups of interest to ancient bone protein detection. Thompson *et al*. (2009) developed a method for estimating collagen content in bone by taking the ratio of the carbonyl (green highlight) peak height to the phosphate (orange highlight) peak height.

Degree of collagen preservation was estimated by calculating the ratio of amide bond stretching to bioapatite-specific phosphate stretching as per Thompson *et al*[1]. The carbonyl stretch of the amide bond in collagen generates a spectral peak height at ~1650 cm^{-1}, and the phosphate stretch of the apatite fraction in bone generates a peak at ~1035 cm^{-1}. A higher value of the carbonyl-to-phosphate peak height ratio (carbonyl/phosphate, or CO/P) corresponds to higher molecular integrity of collagen. Table 4.1 lists the origins of ATR-IR peaks for bone, as per Thompson *et al*[2]. Various ratios of these peak heights

have been explored in efforts to detect contamination and measure the degree of alteration of both the organic and inorganic phases of bone material.

Approximate FTIR peak wavenumber	Vibrational mode, functional group
565	ν_4 PO_4
605	ν_4 PO_4
632-650	OH group
874	ν_2 CO_3^{2-} group
960	ν_1 (PO_4) sym apatite
1028-1100	ν_3 (PO_4) apatite
1400-1551	CO_3^{2-} groups (lattice carbonate)
1630-1660	Organic tissue and water
3400	OH water
3573	OH group

Table 4.1 | Identification of typical peaks of interest on an ATR-IR spectrum of bone. ν_4 (PO_4) = O-P-O bend, ν_2 (CO_3^{2-}) = out-of-plane bend, ν_3 = P-O asymmetric stretch, ν_1 = P-O symmetric stretch.

Raman spectroscopy mirrors FTIR. They both use infrared absorbance to identify organic functional groups. However, while FTIR scans samples more quickly by irradiating them with a range of wavelengths and then using algorithms to deconstruct the peaks after the fact, the Raman device available for these studies scanned the sample iteratively. But the key conceptual difference is that whereas infrared spectroscopy measures Rayleigh scattered light, Raman spectroscopy measures the Stokes shift. With Rayleigh scattering, each emitted photon carries the same amount of energy as the incident photons. The Stokes shift measures the difference between the energy of the emitted electron and the energy of the incident, or excitation, laser light. For every Stokes-shifted photon radiated, about a million Rayleigh-scattered photons radiate.

Both techniques measure vibrational excitation. Infrared detects it directly, but Raman detects it by subtraction. The vibrational states that Raman spectroscopy probes

are the same as those that FTIR reveals, so they are similar. However, vibrations that are strong in an infrared spectrum involve a strong dipole moment and are usually weak in a Raman spectrum. Likewise, non-polar functional group vibrations that give strong Raman bands usually show weak infrared signals. Thus, use of both infrared spectroscopic techniques can provide a more complete picture of the molecular structures in a sample.

At least three tactics were explored to mitigate the potential argument that IR spectroscopy might not adequately distinguish between carbonyl stretch peaks from endogenous protein versus exogenous carbonyls. In one, careful sample preparation was used, especially the acquisition of fresh, interior, unadulterated bone material and the use of clean utensils and sterile gloves throughout. As a second tactic, multiple, independent collagen-specific detection methods were used in parallel with FTIR and Raman. These results were published in Thomas *et al*. (2017), and showed that the same bones that had unequivocal collagen also had carbonyl peaks.

These results suggested a trend that offers a third tactic. Those bone samples with visibly less pervasive SHG signals also had carbonyl peaks of decreasing heights. This trend is consistent with the well-characterized decay of bone collagen over time (see Chapter 1), and thus difficult to explain by exogenous proteinaceous sourcing, especially in view of the lack of evidence for any exogenous material being present in the freshly exposed bone interiors that were accessed for FTIR and Raman analyses.

Infrared spectroscopy does not at present differentiate between functional group sources, but the significant challenges in assigning all or even most of these carbonyl peaks to sources other than the ancient bones themselves suggests that exogenous proteinaceous sources contribute at most only a small portion of the peak heights.

FTIR spectra of modern and medieval bone

Medieval bone samples from Norton Priory were assessed using FTIR for collagen integrity. Based on the diminished collagen relative to modern bone that SHG images revealed (see Chapter 3), it was expected that FTIR should reveal a significant decrease in their CO/P ratios. Figure 4.5 combines the medieval bovine and human bone spectra alongside a modern bovine sample.

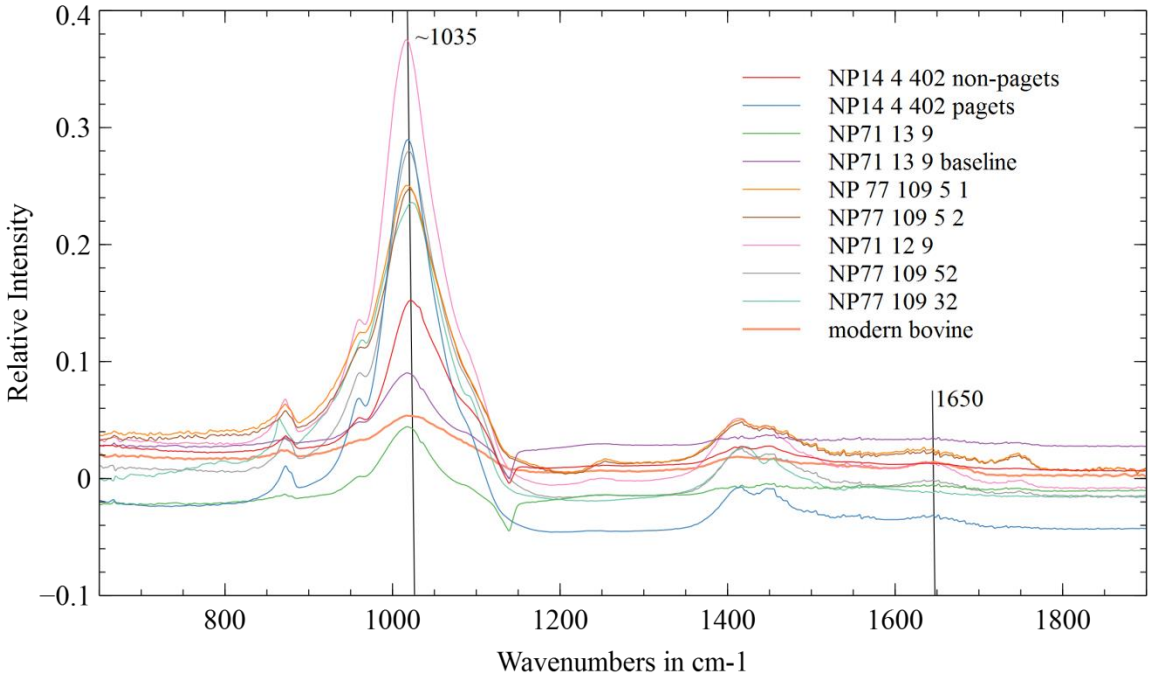

Figure 4.5 | Raw FTIR spectra for nine medieval bones. Phosphate stretch and peak intensities were picked from the highest point near 1035 cm-1, and carbonyl stretch peak intensities were picked from the peak height known from the literature for all spectra.

The most prominent peak within the region of these spectra displayed in Fig 4.5 is the bioapatite-specific phosphate P-O asymmetric stretch at 1035 cm^{-1}. This stretch describes the resonance of alternating, adjacent oxygens relative to the central phosphorus within the phosphate. The peak lies within the broader apatite peak range shown in Table 4.1. For tabulating the CO/P ratios, phosphate peak intensities were collected at the actual apex of each peak, whether or not it aligned perfectly with 1035 cm^{-1}.

The carbonyl peak was much less distinct, and looked more like a shallow mound, even in the modern bone sample. Because of this, the carbonyl relative intensity for CO/P ratios was recorded at exactly 1650 cm^{-1}. Table 4.2 below tabulates these results.

Accession number	Carbon Yrs	CO/P
XA102_2001/307 rib	2060 ± 30	0.1313549
XA102_2001/307 metatarsal		0.1130435
XA102_2001/98 jaw	2060 ± 30	0.1046114
XA102_2001/98 ischium		0.1215163

Table 4.2 | CO/P spread among associated Roman era porcine bones. Samples are described in Chapter 1 under Hallaton. Dates presented in carbon years before present, uncalibrated, with present equaling 1950 AD. The CO/P range among these four samples approximates its error.

Specific spectra in Fig. 4.4 deserve attention. The two spectra for NP77_109_5_1, a bovine radius, and NP77_109_5_2, (Table 2.1) a bovine tibia, nearly overlap, as expected from their nearly identical origin and same context and trench. At a minimum, this shows that these spectra faithfully record meaningful in-bone data. Next, the default baseline algorithm in Omnic was applied to "NP71_13_9 baseline." The function appeared to reduce peak definition and thus reduce information clarity, so it was not applied to other spectra. In comparison to modern bone, which Fig. 4.5 renders as a thicker line than the others, the relative intensities of all peaks in ancient bone samples appear exaggerated. This is due in part to the proportional shrinkage of the phosphate asymmetric stretch at 1025 cm^{-1} of modern bone relative to the much higher intensities of that same peak in ancient bone samples. A probable cause of this effect is discussed in the next section.

FTIR spectra of Roman era bone

Porcine bone samples designated "XA" originated from a 2,000 year-old Celtic Briton votive site as described in Chapter 2. Because these were buried from 7-11 centuries earlier than the medieval bones from Norton Priory, it was anticipated that the

CO/P ratios for these bones would be lower. This was the case, as the phosphate peak heights rose relative to medieval and modern bone samples (data not shown). This peak's intensity increases with crystallinity, as discussed in Thompson *et al.*[2], who observed an increase in crystallinity with heating that occurs as the original microscopic bioapatite crystals (described in Chapter 1) slowly recrystallize into larger structures during diagenesis. The diminishing phosphate peak heights in spectra in Figs 4.5 and others are consistent with the description of recrystallisation occurring over time, and thus behave as though time were a proxy for heat as it affects bone bioapatite.

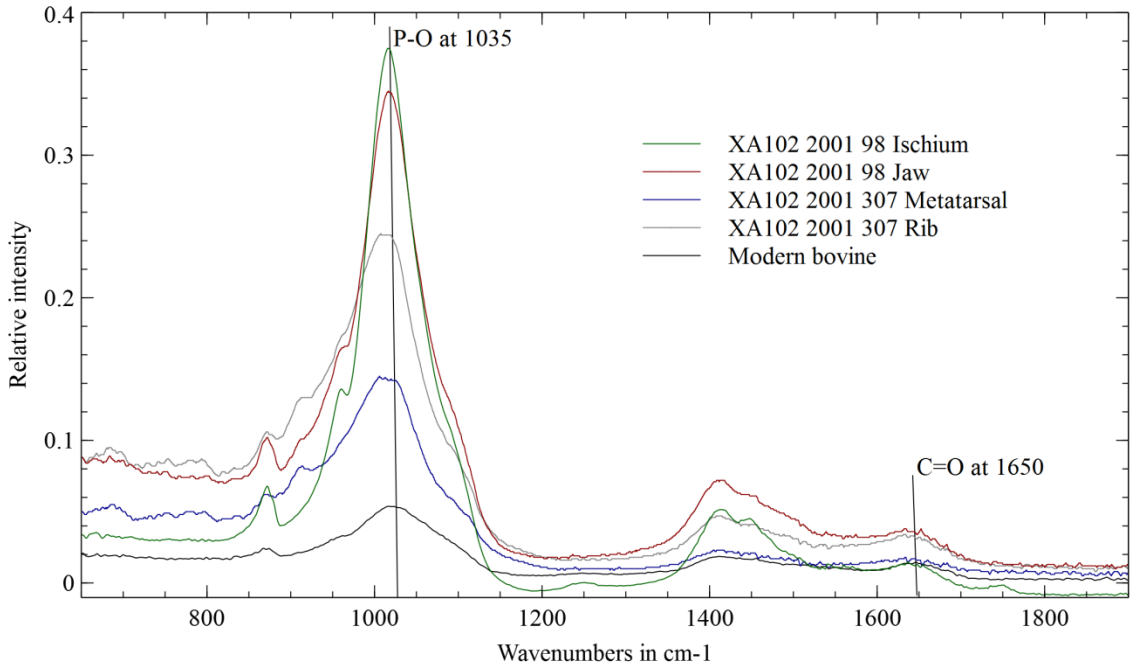

Figure 4.6 | Raw FTIR spectra for 4 Roman era bones. Porcine bones from Hallaton show increasing phosphate peak intensities even though they were carbon-dated to the same age (see Table 4.2 below).

However, the relatively wide variance in phosphate peak heights for the four Hallaton bones shown in Fig. 4.6 are inconsistent with the recrystallisation over time hypothesis since all four bones were buried at the same time and place. During aging, hydroxyapatite crystals partly dissolve and recrystallize, with the smallest crystals

disappearing and the largest crystals growing[8]. Causes for the FTIR variation in these XA samples remain uncertain, but may be due to differences in sample preparation. For example, grain size differences may have arisen from the grinding protocol, resulting in subtle changes to IR-detected crystallinity. This hypothesis was tested and the results shown in Chapter 5. In an unpublished manuscript, Kontopoulos *et al*. show systematic shifts in both peak intensity and position caused by specific bone particle sizes. The authors call the phenomenon the Particle Size Effect on ATR-FTIR analysis of bone powder, and recommend specific new protocol "that significantly improves accuracy, consistency, reliability, replicability, and comparability of the data[9]." Their protocol includes two key steps that were not taken in the current analysis: Sieve the particles to select those from 20-60 μm, and use 3-5 mg of bone powder for each of three runs. Future research on ancient bone should benefit from this protocol standardization.

However, although crystal size likely affects the CO/P ratio more than any other factor for ancient bone, variation in collagen decay plays an additional but smaller role as carbonyl moieties become oxidised. As collagen decays, it no longer barricades bioapatite crystals from migrating toward and merging with one another. Similarly, as bioapatite recrystallises, it can slowly expose collagen fibers to degradative factors like water which hydrolises organics. SHG images from Chapter 3, for example those shown in Fig 3.9, reveal highly variable collagen preservation quality from bones with very similar taphonomies. Therefore in addition to protocol variances, small differences in collagen preservation underground over time certainly affect CO/P ratios. Whatever the actual cause or causes, this result suggests that CO/P ratios are to be taken at present as only very rough proxies for bone protein decay over time.

CO/P ratios were tabulated using these spectra and are shown in Table 4.3. Of interest is the wide variance in phosphate peak height even though these bones were all

collected from the same site with evidence of simultaneous burial in a single votive offering, and bearing the same radiocarbon age. These results indicate that whatever factors led to changes in IR spectra did not alter carbon isotope ratios, for example via

Accession #	14C age, bp, apatite	14C age, bp, collagen or TOC	CO/P
Holocene ↓			
Modern		1	0.255673
NP77_109_5_2		573 ± 23	0.087243
NP71_12_9		840 ± 20 (tooth)	0.032053
NP71_13_9		650 ± 20	-0.118255
XA102_2001/307 rib		2060 ± 30	0.131355
XA102_2001/307 metatarsal		2060 ± 30	0.113043
XA102_2001/98 jaw		2060 ± 30	0.104611
XA102_2001/98 ischium		2060 ± 30	0.121516
Pleistocene ↓			
EHRC90002	20050 ± 40	insuff. coll.	0.014039
EHRC90001	10170 ± 30	12060 ± 89	0.115205
Mesozoic ↓			
CM21728	39760 ± 240	26890 ± 90 (bulk)	0.056981
HRS08267	41490 ± 160	insuff. coll.	0.171102
HCTH06 (GDFM12.001a)	41010 ± 220	33570 ± 120 (bulk)	-0.051153
GDFM03.001	24340 ± 70	30890 ± 200	0.097723

Table 4.3 | Radiocarbon results for bones samples with FTIR-based CO/P results. Data were used to plot Fig. 4.9. See Chapter two for sample identifications. Bp, "before present," with 1950 as "present." Holocene data are reported as calibrated ages, and Pleistocene and Mesozoic as uncalibrated. TOC, "Total Organic Content," refers to a generalised (i.e., not collagen-specific) extraction of organics that include collagens but exclude calcium carbonates from the biomineral. "Tooth" notes the assignment of 840 ± 20 carbon years to the skeletal remains from a tooth associated with the same individual. "Bulk" refers to a preparation that includes carbon both from organic and inorganic bone fractions.

isotope exchange, as discussed in Chapter 6. On the other hand, the variances in phosphate peak heights for these Holocene samples yield a wide range in CO/P ratios and suggest that CO/P ratios do not always vary consistently over time, as discussed in more detail below. These four bone fragments with two carbon dates provided convenient material to inform an error bar that can be included in collagen decay curve estimates

based on FTIR spectra. The range of CO/P ratios in the Hallaton bones are taken as a rough proxy for error ranges in other bones that together share the same setting and age. Accordingly, Table 4.3 shows these CO/P ratios taken from the spectra in Fig 4.5 and the range of 0.02674 suggests an error for two-millennia-old bones of ± 0.01337. This number was applied as an estimated error bar in the Y-axis for all samples used in an FTIR-based collagen decay curve shown below.

FTIR spectra of Pleistocene bone

Only three Pliestocene bones became available during the course of this research, but they fill an important chronological gap in efforts to characterize bone collagen preservation and test the applicability of various techniques to residuals of ancient bone proteins. Fig. 4.7 shows these spectra. The mammoth and *Megatherium* bones were more fragile than the camelid, consistent with two other observations that indicate the camelid remains retain higher collagen content. First, the camelid CO/P is higher than the mammoth and *Megatherium* samples, at 0.1152 versus 0.05698 and 0.0140, respectively. Second, bone samples from both the camelid and *Megatherium* were submitted to the radiocarbon dating facility at the University of Arizona, which found sufficient collagen to proceed with the camelid, but insufficient collagen in the *Megatherium*. Added to these observations is the fact that the camelid was sourced from a much higher latitude and thus a much lower average annual temperature. Since higher temperatures are the primary means of accelerating collagen decay rates, the northernmost sample ought to preserve the most collagen, and it does. The trend among these three samples is therefore consistent with the hypothesis that CO/P ratios can track collagen decay trends.

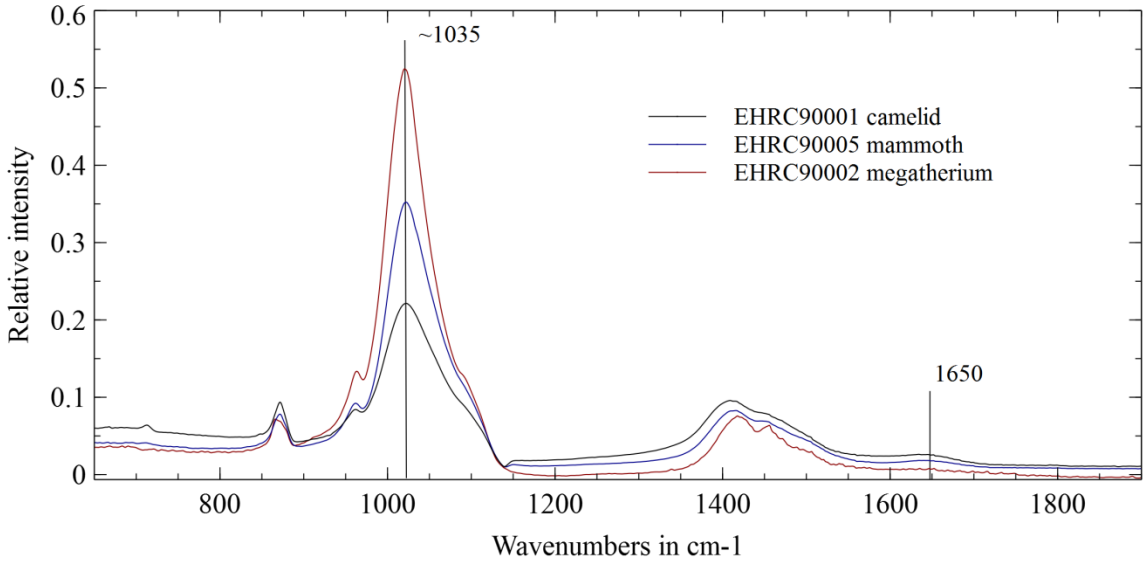

Figure 4.7 | FTIR spectra for 3 Pleistocene bones from the American west.

FTIR spectra of Mesozoic bone

The next oldest stratigraphic selections to include at this point would represent Cenozoic remains. Unfortunately none of the handful of repositories involved in this research has been willing or able to supply any catalogued Cenozoic samples. This omission presents a chronological gap in efforts to more fully characterize collagen decay over time. However, the present data are sufficient to evaluate the effectiveness of bone collagen detection tools on biochemical remnants from Mesozoic and even older sediments, as listed in Table 1.1.

The first test for the effectiveness of FTIR as an efficient ancient bone collagen detection tool was to apply it on ancient bones with unquestioned collagen remnants. These results were described in chapter 3 and published in *Bone Reports*, shown in Appendix 1. A second assessment of the method looks at peak profiles. As an example, Figs 4.5, 4.6., and Fig. 3 in Thomas *et al.*[4] compare ancient with modern bone samples to show that although peak heights differ, both ancient and modern bone reveal similar profiles. Fig 4.8 shows a third assessment. Crushed dinosaur bone from the Cretaceous

Hell Creek Fm. of Montana was scanned alongside Hell Creek matrix that was collected on site, directly adjacent to the bones. The matrix has a consistency of dirty, well-packed sand.

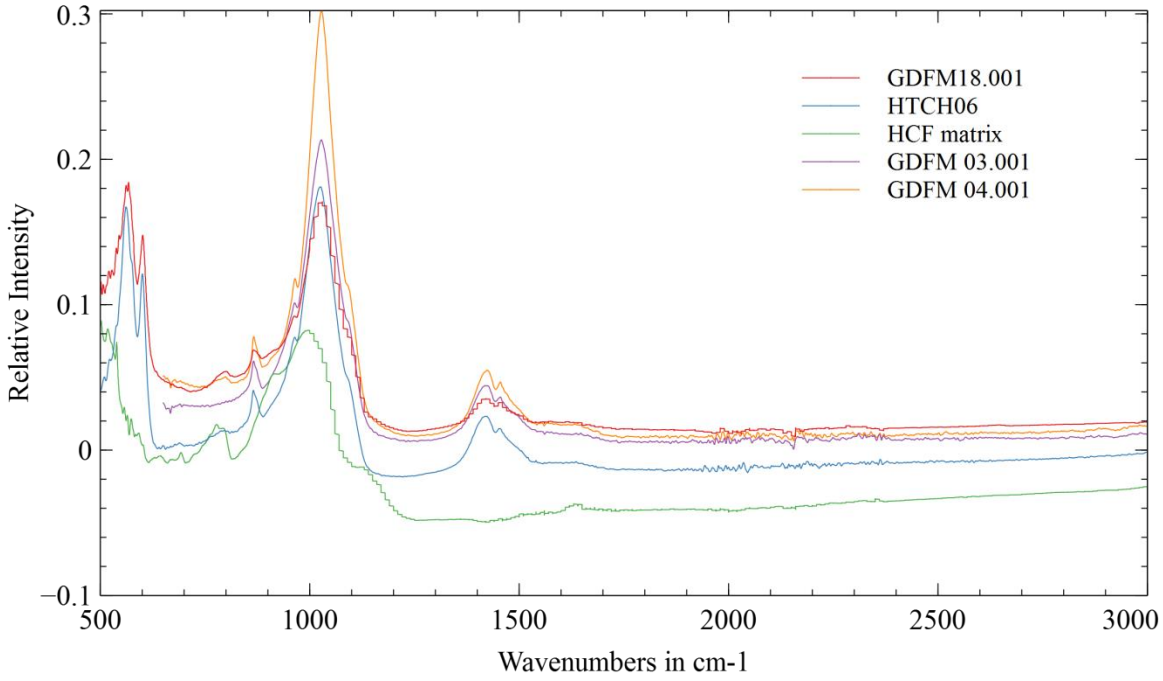

Figure 4.8 | FTIR spectra for four Mesozoic dinosaur bones from the Hell Creek Fm.

Fig. 4.8 shows four Hell Creek (Maastrichtian) bone spectra plus the Hell Creek matrix spectrum in green. A broader portion of the spectrum than Figs 4.7 and 4.6 was included, as noted on the X axis, in order to visualise additional spectral characteristics. The figure clearly shows matrix peaks not present in bone, and bone peaks not present in the matrix, consistent with their fundamentally different compositions.

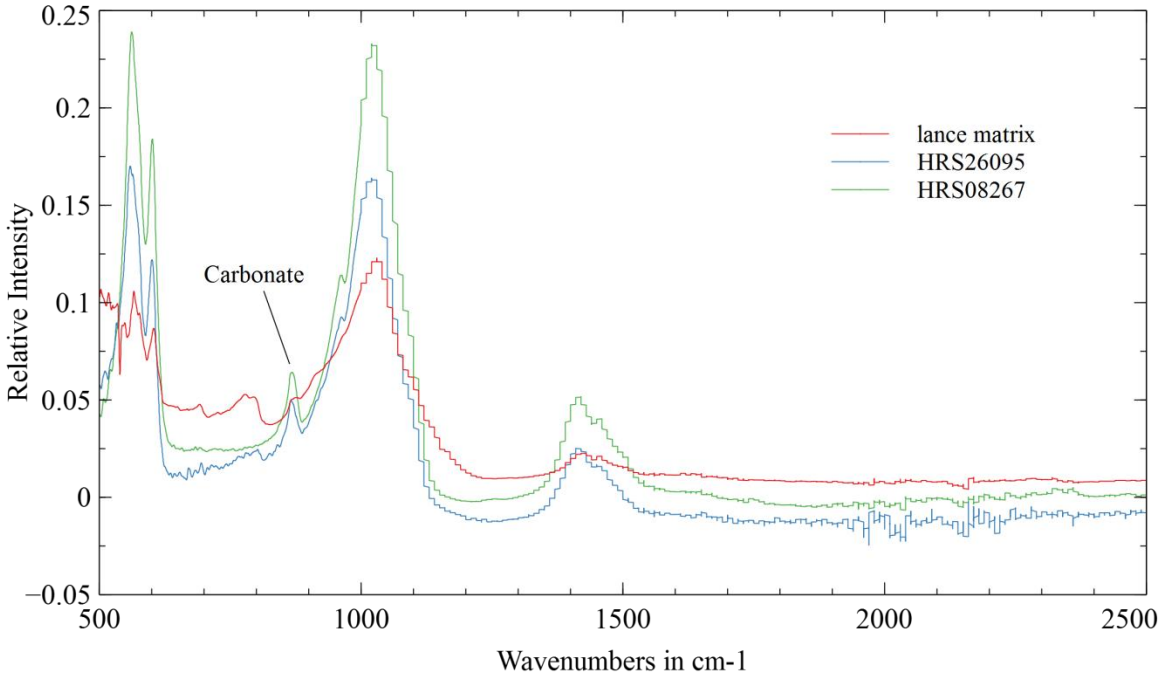

Figure 4.9 | FTIR spectra for two Mesozoic dinosaur bones from the Lance Fm. The lack of resolution above ~1000 cm^{-1} for these samples remains an anomaly, since procedures were consistent across all samples.

Similar figure to Fig. 4.8, Fig. 4.9 compares two Lance Fm. dinosaur bone spectra, also from Maastrichtian strata, with Lance matrix. As noted in Chapter 2, the Hell Creek and Lance are equivalent strata. Thus, their spectra might share similar characteristics. Figs 4.8 and 4.9 reveal a peak in the matrix spectra at 790 cm^{-1} not found in bone. This can be assigned to aluminum oxide[10]. The spectra in Fig. 4.9 reveal similar discontinuity between sediment and bones. In particular, Figs 4.8 and 4.9 have a distinct carbonate peak at 880 cm^{-111}, whereas the sediments do not. Taken together, the distinct differences between the sedimentary matrix on the one hand and all the bones on the other hand are consistent with the hypothesis that although many of these bone surfaces appear partially permineralised, their internal portions retain bone chemistry.

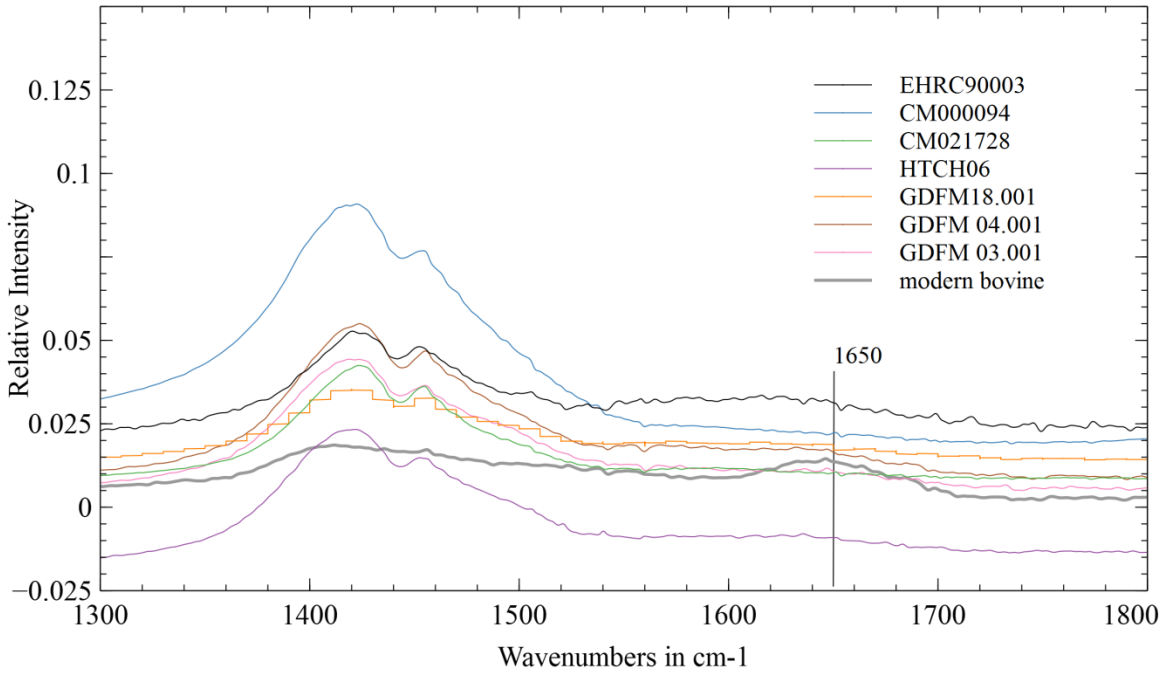

Figure 4.10 | Raw FTIR spectra of seven Mesozoic dinosaur bones. See Chapter two for sample identifications. All dinosaur spectra show much lower carbonyl (1650 cm^{-1}) peaks than modern bone, consistent with highly or entirely degraded collagens.

Finally, all Mesozoic spectra shown in Fig. 4.10 are compared to modern bone. All the Mesozoic bone samples show an increased phosphate peak intensity, discussed above in the context of medieval bones which exhibit the same feature. Fig. 4.10 includes two very darkly colored, and thus highly mineralised, Jurassic samples from Carnegie Museum (CM). Regardless of the apparent degree of mineralisation, these spectra conformed overall to those of Cretaceous remains. However, Fig. 4.10 reveals no carbonyl peak in either CM sample.

Fig. 4.10 represents a close-up of the carbonyl peak region, a key peak of interest for forensic analysis of buried bone. Both of the Jurassic CM samples, as well as possibly the Cretaceous GDFM 03.001, have no semblance of a peak at 1650, consistent with zero or almost zero collagenous content in them. The peak or hump, as seen in the modern bone spectrum colored grey, is broad and shallow and ranges from ~1610 to 1710 cm^{-1}.

Having merely two Jurassic samples are insufficient to assert any trend for the entirety of Jurassic remains. However, if additional FTIR analyses of Jurassic bone reveal flat lines that run through this broad 1650 region, then two explanations deserve discussion. First, it is possible that the additional time that Jurassic remains have lain underground prior to the later Cretaceous deposits would account for the absence of collagen, since the biochemical decays systematically over time[12]. However, multiple pre-Cretaceous indicators of primary protein remnants including collagen as listed in table 1.1 (for example the embryonic Lufengosaurus femur collagen[13]) suggest that time may not always play as critical a factor in preservation as expected. Instead or in addition, temperature plays a role according to artificial decay studies described in Chapter 1. In the discussion about Pleistocene bone results shown above in Fig. 4.6 it was suggested that samples from higher latitudes tend to retain more collagen, because of lower temperatures, than those in lower latitudes or elevations. A similar situation may exist between Glendive, MT and Dinosaur, Utah. The average annual temperature for all months in both cities is similar, with Glendive at 10.25 C, and Dinosaur at 8.72 C[14]. Although Dinosaur is lower in latitude, it is higher in elevation. Its lower average temperature would seem to suggest that it would preserve organics longer than northern Montana. However, the winter months in Montana maintain colder temperatures than those in Dinosaur. Thus, although it is certain that temperature accelerates the decay of biochemicals, it remains speculative but possible that temperature variations in the long history since burial of Mesozoic remains have influenced bone collagen preservation bias between sites.

Novel application of FTIR to collagen decay

Now that ATR-IR has been applied to ancient bone in largely an exploratory investigation, can it be said that the technique detects controversially old bone collagenous remnants in traces too tiny for traditional methods such as extraction and weighing or extraction and sequencing? One way to address this is to plot CO/P ratios from modern to ancient until they no longer drop. In theory, they should generate a curve with a decreasing ratio over time until the curve flattens. A horizontal ratio should indicate the absence of any trace of CO once the phosphate crystals have reached their maximum recrystallisations; i.e., their maximum peak heights. Thus, a preliminary ATR-IR-based collagen decay curve was constructed as per the following steps.

First, all the bone samples with either direct or indirect carbon ages were cross-referenced to those with FTIR results. Table 4.3 lists these data, which were then plotted on Fig. 4.11. The commercial laboratories that performed the isotope analyses supplied the 1-sigma errors. The radiocarbon years are presented uncalibrated, since the purpose was not to pinpoint the age of each sample, but more generally to explore any possible relationship between measured CO/P ratios and $^{14}C/^{12}C$ ratios. Radiocarbon results for Mesozoic and older samples are very rare in the literature, but not totally unprecedented. They are typically attributed to contamination, but this attribution often bears heavy explanatory burdens as will be discussed in Chapter 7. The error bars for the CO/P ratios were obtained by dividing in half the total range of values reported in Table 4.2, which is 0.0134.

Fig. 4.11 shows a plot that estimates collagen decay over time. The poor fit of the logarithmic curve to the data follow from the widely scattered CO/P ratios. Two potential causes of this scattering were discussed above, namely, differences in sample processing

and variations in phosphate recrystallisation during diagenesis. It was already well known by those familiar with field excavations that collagen preservation, which can be assessed

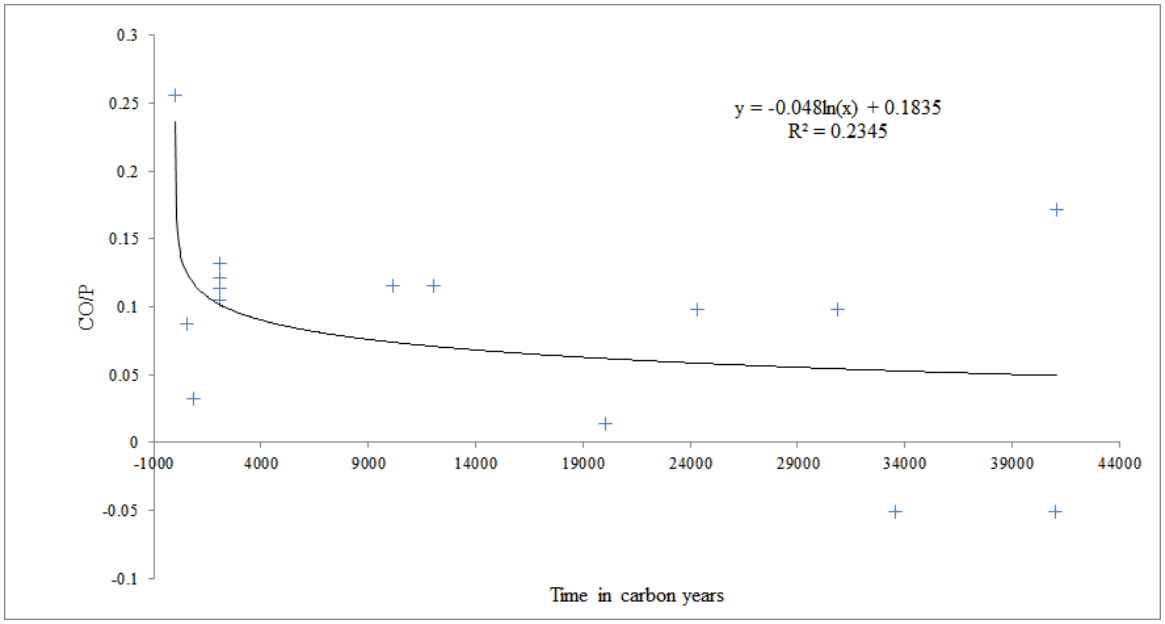

Figure 4.11 | Collagen decay estimated from CO/P ratios of 14 ancient bone samples. Four samples had two radiocarbon results, and each of those was plotted separately, making eight data points for them, totaling 16 data points overall. Modern bone had the highest CO/P ratio, consistent with the idea that CO/P approximates collagen loss over time. However, the poor R^2 value of the logarithmic trend line and the wide variation in CO/P indicate that factors additional to protein decay significantly affected the results.

in a general sense by the look and feel of bone, since those with poor preservation are more friable and generally darker tinted than those with higher quality preservation, that collagen quality can vary widely even among samples in similar and nearby settings. These new results in Fig 4.11 suggest that phosphate crystal formation may vary even more widely than collagen decay, as this process would markedly affect CO/P ratios.

CO/P ratios that span from medieval to Mesozoic (i.e., excluding the single sample of modern bone) show a more linear than exponential trend. One might suggest on this basis that bone components can somehow exit the very orderly protein decay trend characterised in bone decay experiments[15,16] and enter a non-decaying, more linear preservation mode. However, most of the CO/P variation in the Mesozoic results also

appears in just the medieval results. It is possible that the CO/P ratio may have more value in estimating bone burial times via collagen decay within forensic time frames of within a decade or so, but not as much value in estimating collagen decay in older samples like those included in this study.

Overall, the data shown in Fig. 4.11 confirm that modern bone has a higher CO/P ratio than all other IR-analysed and dated ancient bone samples. However, they also reveal that CO/P ratios from a long time span do fall within a range, but too wide a range to detect a certain trend. Future efforts at using CO/P to estimate collagen decay in ancient bone should improve with more consistent and accurate sample processing procedures, as discussed above and explored in the next chapter. They may also improve with a better understanding of how recrystallisation of phosphate and possibly other diagenetic processes affect the CO/P ratio.

Macro for CO/P finder in Excel

In order to process the FTIR data using standard spreadsheet and graphing software, they were saved as .csv files. The proprietary spectral analysis software Omnic was used to interface with the Fischer Scientific Nicolet FTIR as described above. It has spectra-specific features that standard graphing and spreadsheets don't have, such as an integrated library that quickly compares any measured spectrum against a database of spectra for standard compounds and a "find peaks" function. In anticipation of having to identify and record dozens of carbonyl and phosphate peaks in ancient bone or artificially decayed bone sample spectra, a macro program called "CO/P Finder" was written for Microsoft Excel.

The strategy for identifying a peak of interest in a sample began with code that specified the typical wavenumber for a functional group. The macro was then directed to

search for the highest number five wavenumbers above and below that standard. The results were output to specific cells in the spreadsheet. The CO/P ratio was then automatically calculated and the result was output to a separate sheet.

The CO/P ratio results on dinosaur bone material using this macro looked very inconsistent. They ranged from -135 to 25, whereas the manually curated ratios shown in Table 4.3 ranged from -0.118255 to 0.255673. Therefore each peak of interest was collected manually and used to plot Fig. 4.11. Each spectrum was visually plotted and the peak of interest was either collected from a visible peak, or in the case of most Mesozoic material which showed no visually discernable carbonyl peak, whatever the near-baseline intensity was at 1650 cm^{-1} was collected.

The CO/P Finder code is as follows:

```
Sub CO_P_Finder()

Dim wb As Workbook
Dim ws As Worksheet
Set wb = ActiveWorkbook
Set ws = wb.Worksheets("Sheet1")
Set ws2 = wb.Worksheets("Sheet2")
Dim i As Integer
dColumn = 1 'Data Column
rRow = 1 'Results Row
nColumn = 4 'Name Column
On Error Resume Next


For i = 0 To 20 'number of times to run loop
   pRow = "Error"

   pRow = ws.Range(ws.Cells(1, dColumn), ws.Cells(8000,
dColumn)).Find("1650").Row 'row that is around the phosphate peak
   cRow = ws.Range(ws.Cells(1, dColumn), ws.Cells(8000,
dColumn)).Find("1035").Row 'row that is around the Carbonyl peak
   If pRow = "Error" Then
      End
   End If
   pPeak = Application.WorksheetFunction.Max(ws.Range(ws.Cells(pRow, dColumn +
1), ws.Cells(pRow + 11, dColumn + 1)))
   cPeak = Application.WorksheetFunction.Max(ws.Range(ws.Cells(cRow, 2),
ws.Cells(cRow + 11, 2)))
```

```
    Debug.Print ("------")
    Debug.Print (pRow)
    Debug.Print (cRow)
    Debug.Print (pPeak)
    Debug.Print (cPeak)


    ws2.Cells(rRow, 1) = ws.Cells(1, nColumn)
    ws2.Cells(rRow + 2, 1) = cPeak / pPeak

    dColumn = dColumn + 5
    nColumn = nColumn + 5
    rRow = rRow + 5
Next

End Sub
```

Ultimately the use of Omnic's "find peaks" function proved more efficient and consistent results than either manual collection or the above macro. However, it was discovered through the experimental process described in the next chapter that the Omnic consistently identified a carbonyl peak in artificially decayed bone samples up to 25 wavenumbers away from the ideal 1650. Therefore if CO/P Finder will find use in future studies, it would need adjustments. For example, it would need to search 25 instead of just 5 wavenumbers above and below the targeted wavenumber, while also recognizing and excluding adjacent peaks from within that range. Refinement of CO/P Finder was not pursued because the use of the more widely used algorithm in Omnic would output more familiar and comparable results for publication. Therefore, peak results were copied from Omnic's "find peaks" results and pasted into a Wordpad document for the subsequent analyses shown in Chapter 5.

Raman spectroscopy of ancient bone

In keeping with the use of the four XA Roman era porcine bone samples from the Hallaton shrine as a proxy for error bar determination in FTIR studies of ancient bone, the same four bones were selected as initial targets for Raman spectroscopy.

Fig. 4.12 shows the resulting spectra, collected from 300 to 1800 wavenumbers in order to capture the expected peaks from published modern bone scans. In this case XA bones were powderised but not sifted. Fig. 4.13 shows a published bone spectrum using the same excitation wavelength, in this case mouse cortical bone, after Mandair and Morris (2015)[17].

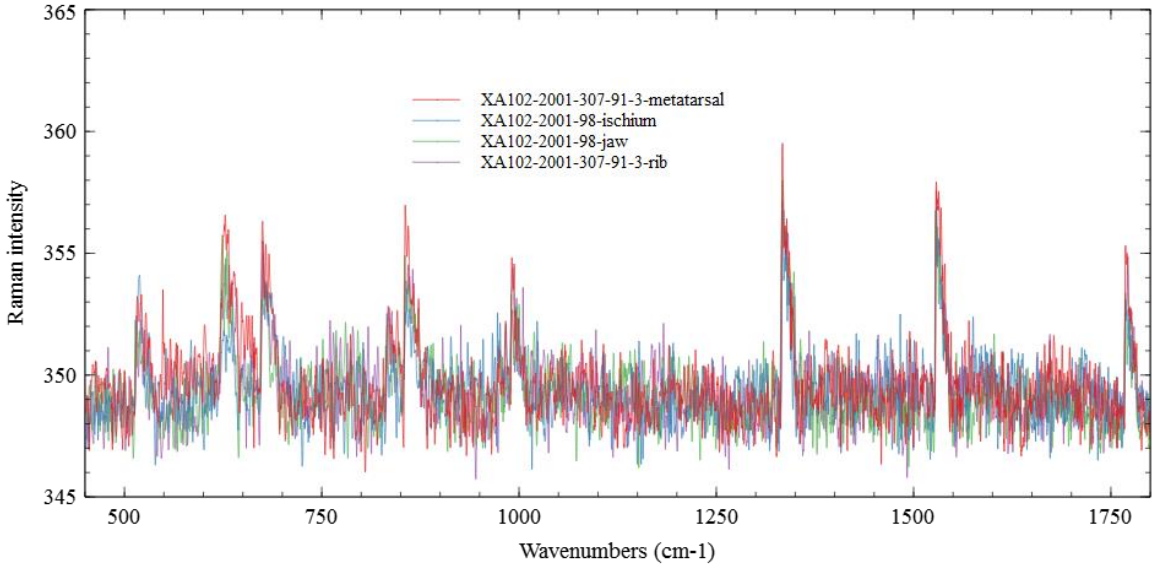

Figure 4.12 | Baselined Raman spectra of four Roman era porcine bones from the same context. Spectra acquired with a 785nm incident laser. The four spectra show minimal intensity variation, probably caused by differences in grain size between samples. Functional group assignments based on comparison with Fig. 4.12.

All four spectra show the same peaks at the same positions, consistent with their identical origins as discussed above and in Chapter 2. Peak identifications remain tentative, partly because Raman-sensitive diagenetic alterations of collagen functional groups remain largely unexplored. Comparisons with Fig. 4.13 give a basis for some

identification. Infrared laser sources such as 785 are generally preferred because they do not excite autofluorescence in biomolecules, which could easily overwhelm the Raman signal[18].

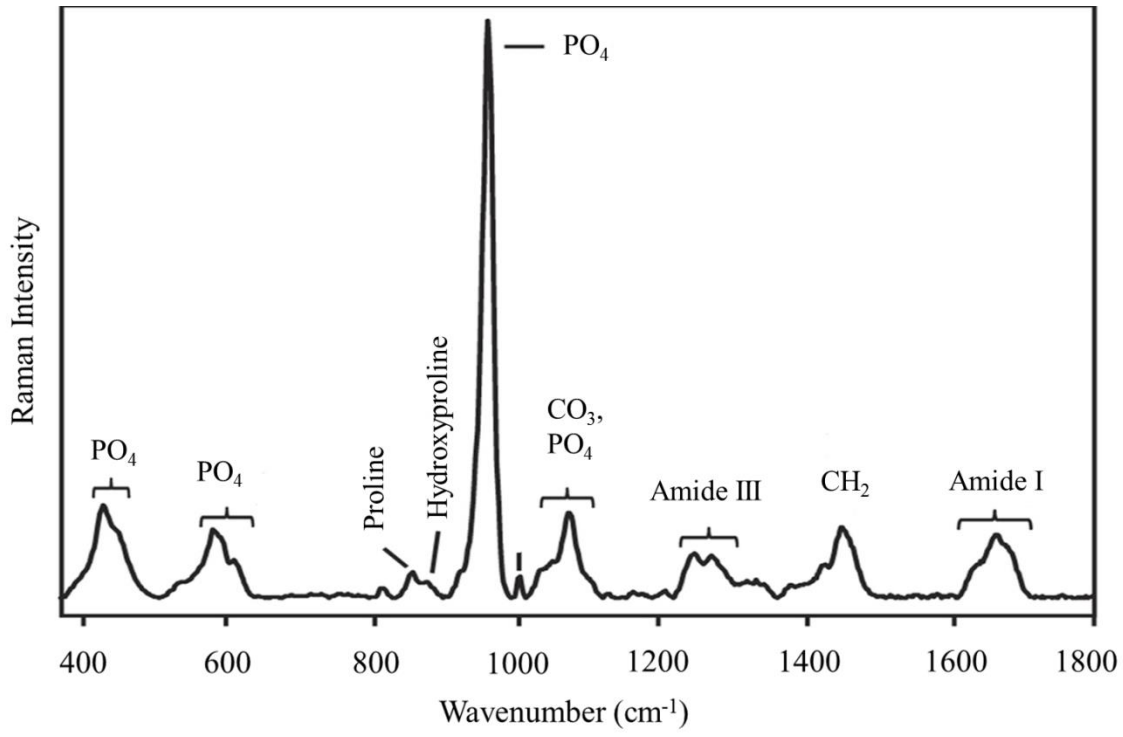

Figure 4.13 | Baseline-corrected Raman spectrum of modern mouse cortical bone acquired with a 785-nm laser. Modified from Mandair and Morris (2015)[17].

Differences between the published Raman spectrum for modern bone shown in Fig. 4.13 and the Raman spectra presented in this thesis indicate that functional group assignments should be considered preliminary. The phosphate positions in modern bone at ~590 and ~950 cm^{-1} seen in Fig. 4.13 hold similar positions in Roman era bone (Fig. 4.12). Both Figs were scanned at 785nm. However, the prominent 950 cm^{-1} peak in Fig. 4.13 appears severely reduced in both the ancient and modern bone samples shown in Fig. 4.14. This could be caused by recrystallalisation during diagenesis, where larger microcrystalline sizes alter the electronic configuration of phosphates in such a way as to diminish the intensity of their symmetric stretch at 784 cm^{-1}.

A second comparison references Schof *et al*., who used the Amide I peak collected at 785 cm^{-1} to perform 3D Raman imaging of collagen fiber structure in modern human femur bone[19]. They used the highest peak between 1600-1700 cm^{-1} to represent Amide I and thus collagen. The closest peak among these Hallaton specimens to this range lies at 1528cm^{-1}. This peak, as well as the ~1334 cm^{-1} peak, also occurred in modern, ice age, and medieval bone samples using the same experimental setup, as reported by Thomas *et al*. (2017)[4], shown here in Fig. 4.14. Another difference between the ancient bone Raman spectra of Fig. 4.13 and Fig. 4.11 is that in the former case the laser was directed onto the surface of bone thin sections, and in the latter case the laser was directed onto powderised, but not sifted (see next chapter) bone. This may also explain the scattered appearance of the Raman spectra of Hallaton bone samples. Thomas *et al*. (2017) identified the 1528 cm^{-1} peak as an Amide II stretch instead of Amide I as Fig. 4.12 shows at 1650cm^{-1}. Likewise they identified the 1334 cm^{-1} peak as an amide III vibrational mode. However, in view of the fact that even the modern bone spectrum collected in this study differed significantly from the published modern bone spectrum shown in Fig. 4.13, these assignments remain tentative.

Another obvious difference between the published spectra and the Hallaton spectra is the high level of signal noise, seen as scattered intensities along all wavenumbers in Fig. 4.12. This effect could be the product of bone powder preparation. Powderising bone affects sample crystallinity, to which Raman spectroscopy shows sensitivity.

One potentially key feature of Raman spectroscopy applied to bone is the hydroxyproline shoulder identified by Mandair and Morris (2015, Fig. 4.13). Hydroxyproline is a collagen-specific modified amino acid, so its detection in any bone sample reveals vertebrate-specific collagen, as opposed to contaminant, proteins. It was

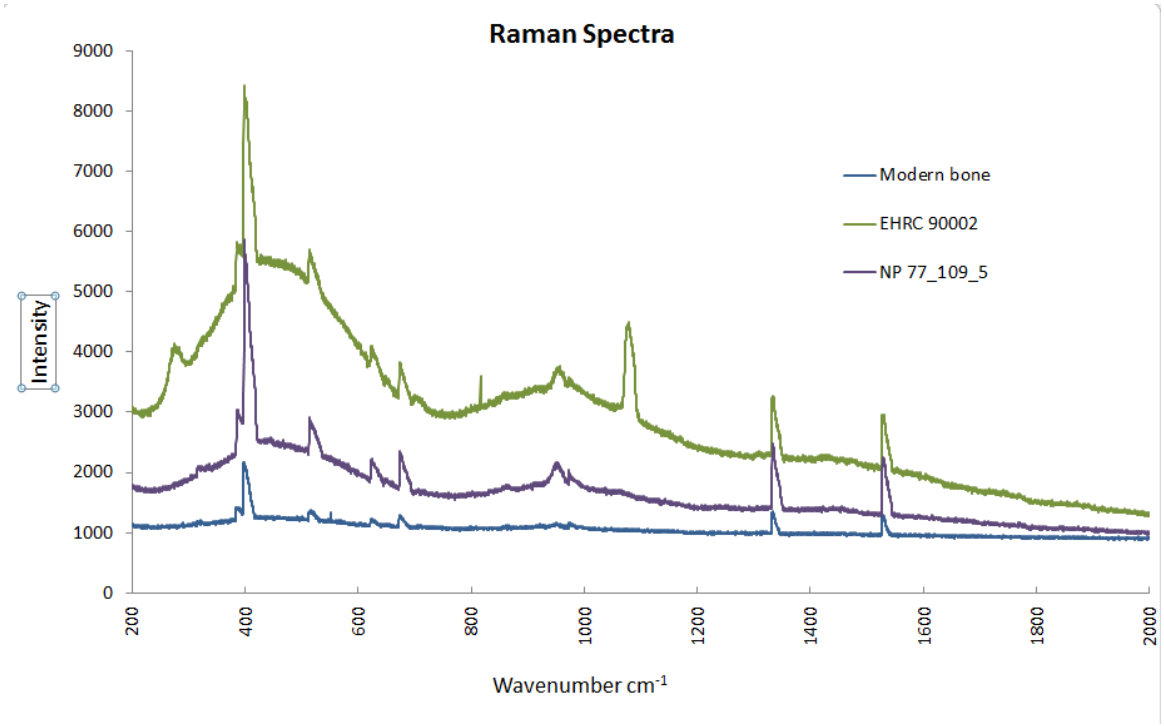

Figure 4.14 | Raw Raman spectra of modern, Pleistocene (EHRC 90002), and medieval (NP 77-109-5) bones. Spectra show slight shifting of peaks to higher wavenumbers over time, from Thomas *et al* (2017).

initially hoped that Raman spectroscopy could provide an inexpensive and efficient means of identifying endogenous collagen even in ancient bone via hydroxyproline shoulder detection, but as Fig. 4.14 shows, the experimental setup and/or sample preparation did not reveal a discernable peak at that position (~875 cm^{-1}, using a 785 nm source) in modern bone, let alone ancient bone samples.

Further research will be necessary to first re-capture the hydroxyproline peak as per Mandair and Morris (2015). Then, adjustments to the bone preparation and instrumental parameters would be necessary to more firmly identify collagen-indicators such as Amide I, II, and III peaks. Once these key peaks are identified, then additional research with Raman spectroscopy, perhaps on time-stamped artificially decayed bone collagen, could prove helpful in characterising the effect of age on protein-specific peak heights, positions, and shapes. For example, Fig. 4.14 shows a slight shift in wavenumber with

sample age, but three samples are too few to establish this as a trend. Thus far, instead of finding Raman spectroscopy a quick and accurate collagen detection technique, these results present an unforeseen realm of investigation into Raman spectroscopy on ancient bone.

The potential for spectral studies of ancient bone collagen

The results in Chapter 4 and 5 expand collagen decay characterization by FTIR and Raman spectroscopy enough to suggest their potential for use in efficient and user-friendly protocols that pre-screen samples for the presence of ancient or fossil bone proteins. For example, the TruScan RM Handheld Raman Analyzer by Thermo Scientific weighs only two pounds and could accompany future archaeologists in the field if a sufficient protocol were to be developed for it or a similar instrument.

However, the poor fit of CO/P ratios to a decay curve as shown in Fig. 4.10 suggested that some factor or factors in the analysis, approach, technique, and/or underground history (taphonomy) of the samples made the CO/P ratios captured here a poor proxy for collagen decay in ancient bone, as mentioned above. Ancient proteins expert Matthew Collins mentioned (personal communication, May 24, 2018) an unpublished paper by Kontopoulos *et al*. that characterized systematic FTIR spectral differences in both peak position and intensity with powdered bone grain size[9]. Therefore, an experiment was conducted to test the possibility that certain recommended procedures from that unpublished paper, especially including tighter control on grain size, could improve the precision of FTIR enough for it to find use in ancient as opposed to just forensic bone samples. This experiment is the subject of the next chapter.

1 Thompson, T., Gauthier, M. & Islam, M. The application of a new method of Fourier Transform Infrared Spectroscopy to the analysis of burned bone. *Journal of Archaeological Science* **36**, 910-914 (2009).
2 Thompson, T., Islam, M. & Bonniere, M. A new statistical approach for determining the crystallinity of heat-altered bone mineral from FTIR spectra. *Journal of Archaeological Science* **40**, 416-422 (2013).
3 Paschalis, E. P., Mendelsohn, R. & Boskey, A. L. Infrared assessment of bone quality: a review. *Clinical Orthopaedics and Related Research®* **469**, 2170-2178 (2011).
4 Thomas, B. *et al.* Second-harmonic generation imaging of collagen in ancient bone. *Bone reports* **7**, 137-144 (2017).
5 Huynh, V., Williams, K., Golden, T. & Verbeck, G. Investigation of falsified documents via direct analyte-probed nanoextraction coupled to nanospray mass spectrometry, fluorescence microscopy, and Raman spectroscopy. *Analyst* **140**, 6553-6562 (2015).
6 Smith, R., Wright, K. L. & Ashton, L. Raman spectroscopy: an evolving technique for live cell studies. *Analyst* **141**, 3590-3600 (2016).
7 Gu, C., Katti, D. R. & Katti, K. S. Photoacoustic FTIR spectroscopic study of undisturbed human cortical bone. *Spectrochim Acta A Mol Biomol Spectrosc* **103**, 25-37, doi:10.1016/j.saa.2012.10.062 (2013).
8 Koutsopoulos, S. Synthesis and characterization of hydroxyapatite crystals: a review study on the analytical methods. *Journal of Biomedical Materials Research: An Official Journal of The Society for Biomaterials, The Japanese Society for Biomaterials, and The Australian Society for Biomaterials and the Korean Society for Biomaterials* **62**, 600-612 (2002).
9 Ioannis Kontopoulos, S. P., Kirsty Penkman, and Matthew J. Collins. *Preparation of Bone Powder for FTIR-ATR Analysis: The Particle Size Effect* (University of York, 2018).
10 in *National Institute of Standards and Technology* (US Department of Commerce).
11 Kobrina, Y. *Infrared Microspectroscopic Cluster Analysis of Bone and Cartilage* PhD thesis, University of Eastern Finland, (2014).
12 Pevzner, P. A., Kim, S. & Ng, J. Comment on "Protein sequences from mastodon and Tyrannosaurus rex revealed by mass spectrometry". *Science* **321**, 1040; author reply 1040, doi:10.1126/science.1155006 (2008).
13 Reisz, R. R. *et al.* Embryology of Early Jurassic dinosaur from China with evidence of preserved organic remains. *Nature* **496**, 210-214, doi:10.1038/nature11978 (2013).
14 (National Oceanic and Atmospheric Administration).
15 Buckley, M. & Collins, M. J. Collagen survival and its use for species identification in Holocene-lower Pleistocene bone fragments from British archaeological and paleontological sites. *Antiqua* **1**, 1 (2011).
16 Collins, M. J., Gernaey, A. M., Nielsen-Marsh, C. M., Vermeer, C. & Westbroek, P. Slow rates of degradation of osteocalcin; green light for fossil bone protein? *Geology [Boulder]* **28**, 1139-1142, doi:10.1130/0091-7613(2000)028<1139:SRODOO>2.3.CO;2 (2000).
17 Mandair, G. S. & Morris, M. D. Contributions of Raman spectroscopy to the understanding of bone strength. *BoneKEy reports* **4** (2015).
18 Tuschel, D. Selecting an excitation wavelength for Raman spectroscopy. *Spectroscopy* **31**, 14-23 (2016).
19 Schrof, S., Varga, P., Galvis, L., Raum, K. & Masic, A. 3D Raman mapping of the collagen fibril orientation in human osteonal lamellae. *Journal of structural biology* **187**, 266-275 (2014).

Chapter 5: Artificial decay of bone collagen

Contents

Figures

Tables

Introduction

Use of SHG and FTIR to explore actually decayed (ancient) bone collagen *in situ* and to estimate bone collagen decay revealed two reasons why these same techniques should be applied to artificially decayed bone. Firstly, typical means of assessing collagen integrity involve collagen extraction prior to measuring molecular integrity, for example by sequencing, electrophoresis, or weighing. This makes results dependent on the variabilities of extraction yields and produces wide-ranging bone collagen decay estimates. In contrast, more precise FTIR and SHG measurements can assess bone collagen directly within bone, offering potential to increase measurement precision and a narrower decay range.

Lastly, FTIR or SHG-based assessments of ancient bone collagen integrity remained speculative without comparison to results from the same two techniques applied to experimentally decayed bone. Therefore an artificial bone decay experiment was conducted using similar procedures to published artificial collagen decay experiments, but this time using ATR-IR and SHG microscopy to evaluate the integrity of decaying collagen throughout the experiment.

In addition to evaluating the applicability of ATR-IR to decaying bone collagen, this experiment explores the question of what causes the poor fit shown in Fig. 4.10. Is FTIR sensitive enough to detect trace amounts of protein remnants in archaeological bone? Do the wide ranges in CO/P ratios for ancient bones reflect actual bone components, bone preparation procedures or something else? To address these questions, modern porcine bone was processed and heated at three different temperatures for one month each in order to generate an Arrhenius plot as per Collins et al[1]. CO/P ratios from FTIR spectra were used to quantify bone collagen decay as per Thompson et al[2], and SHG images were captured in parallel to give a qualitative perspective on bone collagen decay. The

experiment also gave opportunity to evaluate adjustments to bone preparation protocols as discussed below.

Methods

An artificial bone decay protocol was developed based on the methods used by Collins et al (1995)[3]. Those methods, modified in a 2000 paper, are reproduced here for context, followed by a description of modifications made to them:

> Bone powder was saturated to 95% relative humidity and sealed in Pyrex glass tubes, as described in Collins et al, 1998[4]. The tubes were heated in modified DNA hybridization ovens (±0.1 °C). Oven temperatures were maintained at 75 °C, 85 °C, and 95 °C. Oven modifications involved integration of a new heating element with a higher temperature capability. The tubes were removed at selected time intervals and stored frozen at –75 °C until analysis. For analysis, samples were demineralized in 10% wt/vol EDTA with protease inhibitors 4 days at 4 °C[4]. A total of four EDTA extractions were performed on each sample, and the four supernatants were pooled for immunoassay. The immunoassay (ELISA) measured collagen extracts as a percent of the ELISA signal of original (time 0), un-decayed bone[1].

The following protocol adjustments were made to the above. First, Modern porcine cortical metacarpal and metatarsal bone was obtained from a local market. Because protein decay is sensitive to temperature, it was recognized that air temperature variances within a dry oven could introduce significant scatter into resulting collagen decay plots. Also, initial attempts at using incubator ovens resulted in some of the high temperature (90 °C) vials exploding. Therefore, three separate water baths were used to maintain a more uniform temperature across all samples and to provide counter-pressure on the vials.

A high temperature of 90 °C instead of 95 °C was used to reduce data scatter, since lower temperature plots showed the highest R^2 values in published studies. Two replications each of two bone preparations were used for each of three temperatures. Temperatures of 90 °C, 86 °C, and 82 °C were selected to minimise the total length of the experiment, since it would take more than a month to establish a trend line using temperatures in the 70's °C.

Approximately 2 g of bone powder was separately placed into 25 ml ampules (Wheaton, Millville, NJ). This bone powder was saturated with deionized water. Porcine bone powder preparation presented unique challenges when what appeared to be endogenous bone lipids caused the grains to flocculate, making a paste that would not pass through the size-exclusion sifting screens (described below.) Therefore a drying step was added to the bone preparation procedure. Accordingly, the ampules were placed into an 80°C water bath and held for 30 minutes. Excess water was then decanted from the bone powder. This provided a moist but not soaked bone sample.

Ampules containing porcine bone were then heat-sealed and placed into water baths maintained at 82° C, 86° C, and °90 C. Two ampules were removed from each water bath according to a preset sampling schedule. Ampules were subsequently opened, bone content drained onto Falcon cell strainer (40 μm) filters, and bone shards removed from the powdered bone. The resulting 90 dried bone powder and shard samples were stored at 3 °C for further analysis.

Because FTIR assesses bone collagen decay essentially through quantifying a reduction in carbonyl peak heights, the freezing and demineralisation procedures of Collins *et al*. (2000) necessary to immunoassays were omitted here. Also, two key recommended procedures were adopted from unpublished work by Kontopoulos *et al*[5], who demonstrated systematic IR peak shifts with grain sizes. First, each replicated sample

was scanned in triplicate to ensure uniform spectral characteristics. This totaled 135 spectra for all three temperatures. Second, bone powder grain size was restricted to between 20 and 60 μm by sifting between stacked sieves (Fisherbrand 8 in. dia. x 2 in. depth).

ATR-IR spectra were collected according to the methods described in Chapter 4. Briefly, bone powder was crimped beneath the anvil on the diamond window of the Thermo Nicolet ATR module. Each spectrum averaged 16 scans. Spectral collection ranged between 2,000 and 600 wavenumbers. Default settings for optical velocity (1.8988) and Aperture (138) were used. Spectra were saved separately as both a .SPA and .CSV file. Each spectrum was plotted using Omnic, where the "find peaks" function was used. The tolerance slider was adjusted just until the software displayed the carbonyl (CO) peak at ~1650 cm^{-1}. This also captured the phosphate (P) peak of interest as well as other neighboring peak heights. CO and P peak intensities for all six reads (two replications of three reads each) were averaged for every temperature and time. These averages were used to calculate linear slopes for each temperature. The slope of the line of best fit calculated for the CO/P ratio versus time in days was used for the rate constant, k, for each of three temperatures, according to k = -slope. These slopes were then used to construct an Arrhenius plot, from which the values used in the Arrhenius equation can be determined. The equation estimates molecular decay at any temperature, thus:

$$k = Ae^{-Ea/(RT)}$$

where k is the rate constant specific to collagen, A is a constant that estimates a molecular collision rate, e is the base of natural logarithms, Ea is the energy of activation, R is the gas constant (8.3144598 kg $m^2s^{-2}K^{-1}mol^{-1}$), and T is temperature in °K.

SHG imaging was used as an independent and qualitative confirmation of the quantitative FTIR data. SHG imaging was performed as per Thomas et al, 2017. Bone

shards were mounted on glass slides and imaged under a Zeiss Plan-Apochromat 10×, NA =0.45 objective lens using a Zeiss Examiner Z1 two-photon excitation laser scanning confocal microscope (Carl Zeiss, Jena, Germany) coupled to a Coherent Chameleon titanium:sapphire laser (Coherent, Glasgow, UK). The laser was set to 920 nm for excitation. The SHG emission signal was collected at 458 nm (half the excitation wavelength).

A parallel autofluorescent signal was also collected at 760 nm. Cellular components including lipopigments and vitamin derivatives (Zipfel et al., 2003) as well as aromatic amino acids (Monici, 2005) autofluoresce and provide a context for comparison with the collagen histology. A dual channel Zeiss LSM BiG detector captured both the SHG and autofluorescent channels simultaneously. Focal planes and bone regions were selected to include sufficient collagen to visualise within the viewing frame. Frame sizes of 1932 × 1932 pixels were rastered at 5 s speed, taking the average of 4 reads per line.

Open source ImageJ software package Fiji was used to overlay parallel channels and adjust channel brightness[6]. Unless otherwise noted, intensity thresholds were generally set to 40–255 to visualize the strong and broad collagen signal seen in fresh bone, and 20 to 255 to visualize the faint and rare signal seen in artificially decayed bone.

Results

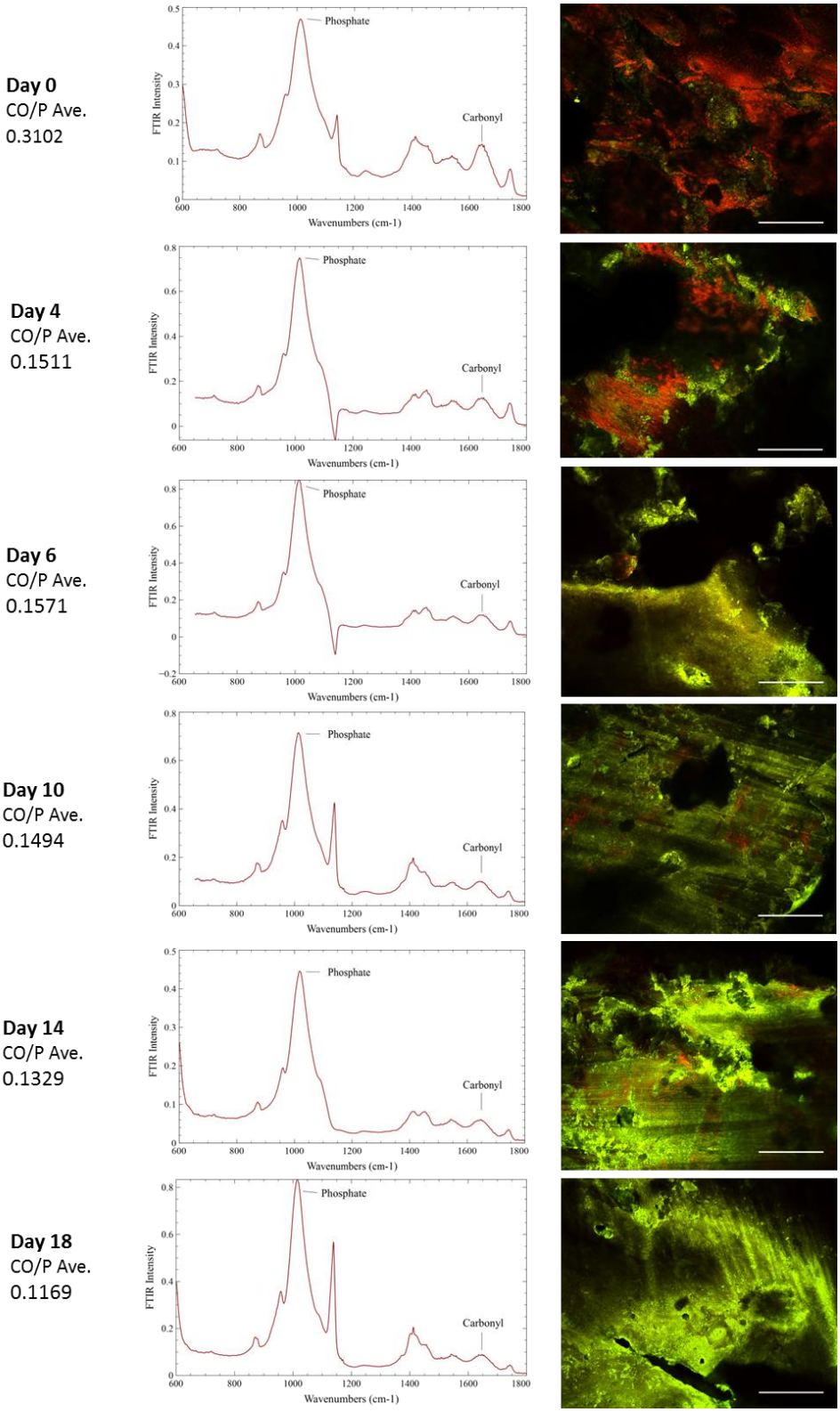

Figure 5.1 | Sample FTIR spectra and corresponding SHG images for bone artificially decayed at 82 ºC. CO/P refers to the ratio of peak heights indicated in the spectra, where CO = carbonyl and P = phosphate. Each average represents six scans—three each for two experimental replications. The CO/P dropped steadily over time, consistent with shrinkage of the CO peak

representing collagen decay. The spotty 1138 cm^{-1} spike on some spectra did not appear to affect the peaks of interest or the overall results. Figure shows representative data only. Scale bar for SHG images is 200 μm. Intensity thresholds were set as follows: Day 0 red = 0-75, green 0-145. Day 4 red = 0-75, green 0-145. Day 6 red = 0-75, green = 0-145. Day 10 red = 0-75, green 5-200. Day 14 red = 0-145, green 0-145. Day 18 red = 0-75, green 0-145.

Figure 5.1 shows six example spectra beside their corresponding SHG images taken from the 82 °C experiment. The decrease in red collagen signal seen in the SHG images qualitatively corroborates the steady decrease in quantitative CO/P ratios. SHG images in Fig 5.1 represent manually splintered instead of precision cut bone surfaces. Although precision cut surfaces are preferred as they supply more consistent imaging data, the required time for sample preparation may not appeal to researchers interested more in speed than quality of image acquisition. Overall, the qualitative perspective from manually prepared bone shards may have been just as effective as precision cut bone samples in illustrating decay, seen here as a diminishing red signal. The standardisation of bone particle size, in conjunction with other experimental constants such as use of the same bone as source material and each sample's exposure to virtually the same hydration, produced uniform spectral results shown in Fig. 5.1.

Of particular note from the 82 °C experiment, SHG of artificially decayed bone as shown in Fig. 5.1 very closely resembled decay characteristics of ancient bone images shown in Chapter 3. For example, the red collagen signal in Fig. 5.1 began to fade in intensity and coverage, eventually diminishing to tiny red dots. Similarly, SHG images of Medieval (e.g. Fig. 3.5) and Roman Era bones had faded in intensity and coverage as compared to modern bone, and many find their artificial equivalents in the range of approximately days 4-10. Further, the oldest bone samples imaged in Chapter 3 from ice age and Cretaceous sources showed small pockets with red dots, interpreted as tiny collagen fibre holdouts. These resembled the small red signal seen in some of the most decayed bones from the experiment, for example Day 18 from 82 °C in Fig. 5.1.

SGH images from the 90 °C spectral data lost visible collagen within 10 days. After that point, red collagenous remnants were not generally observed, and CO/P ratios began to fluctuate somewhat randomly instead of in a steady decline. Lower temperatures offered higher resolution perspective of collagen decay. Therefore the 82 °C data were used to illustrate gradual degradation of collagen from powderised bone as shown in Fig. 5.1.

Day	CO/P Ave, 90 ºC	CO/P Ave, 86 ºC	CO/P Ave, 82 ºC
0	0.3102	0.3102	0.3102
2	0.297296		
4	0.150254	0.164992	0.151097
6	0.105685	0.142077	0.157058
8	0.116257	0.121179	0.159201
10	0.094972	0.119364	0.149412
12	0.110388	0.126632	0.14436
14		0.100859	0.132884
16		0.092486	0.122954
18		0.121298	0.116875
20		0.112043	0.08874
22			0.098664

Table 5.1 | CO/P averages of three scans of two replications per day. Spectra were collected for most of the missing cells, but calculation of their CO/P ratios was discontinued after the time points when results from each temperature began to fluctuate instead of steadily decline. Some day two data were unavailable due to difficulties in bone preparation. The data shown here were used to construct the first Arrhenius plot for protein decay using FTIR, as shown below.

Whereas the first 100 or so scans resulted in almost exact duplications of their respective experimental replications and spectral triplications, some of the last few dozen scans began to veer from the baseline at the high and low ends of the 400 to 2000 wavenumber scan spectrum. The CO/P ratios from these “floating” spectra also veered from the systematic decay trend that all the preceding data had revealed. The floating spectra were treated as outliers. Such results proved the usefulness of the painstaking

process of collecting scans in triplicate, and of replicating the experiment. The Day two spectra were not yet available at the time of writing due to difficulties dessicating the powder enough to fit through the 60 µm mesh sieve without heating it (which would accelerate collagen decay and thus skew the results). The CO/P ratios of all non-outlier plots were averaged, and Table 5.1 shows these averages. The natural log was taken for each average as per Collins et al[4], then plotted versus time in Fig. 5.2. Slopes from the three plots were consistent with expected bone collagen decay rate differences between evenly spaced temperatures.

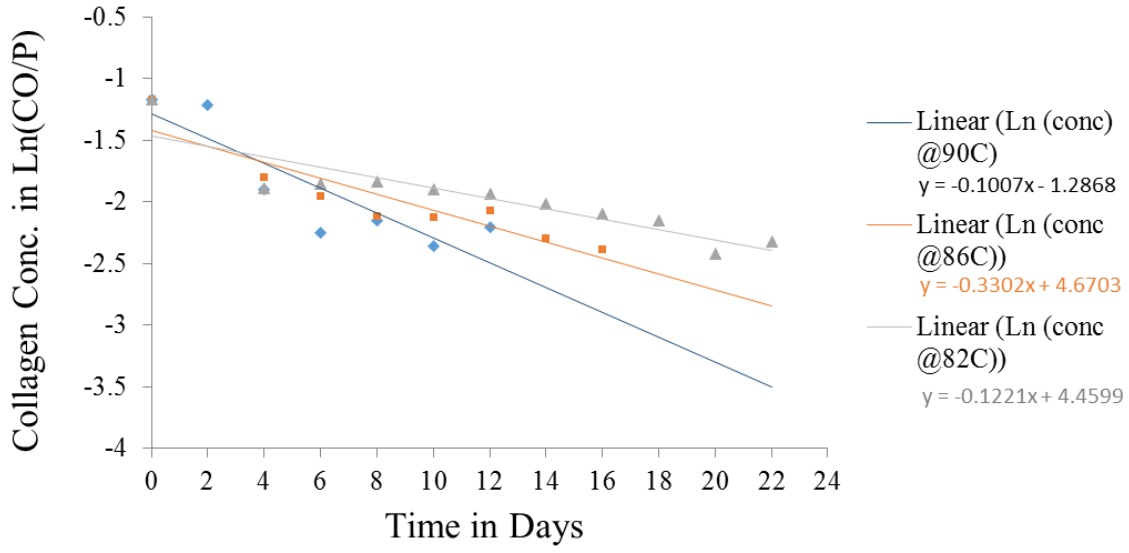

Figure 5.2 | Log plots of porcine bone collagen decay at three temperatures.

The linear regression function in Excel was used to calculate a slope for each of three experimental temperature data sets. Fig. 5.2 displays each slope in standard y = mx + b format. As in published versions of this experiment, the highest temperature experiment (90 °C, blue diamonds in Fig. 5.2) showed the widest scatter. The slopes from Fig. 5.2 were uniform and considered suitable to construct an Arrhenius plot, shown in Fig. 5.3.

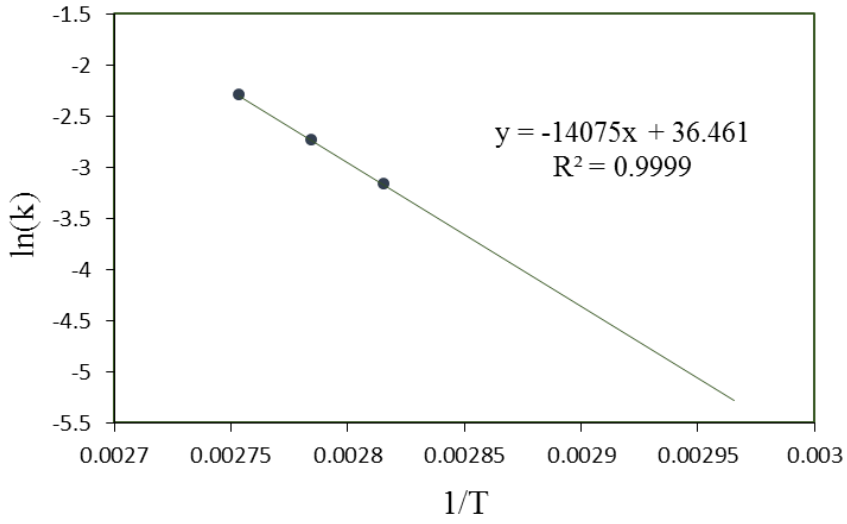

Figure 5.3 | Arrhenius plot of artificial collagen decay in porcine bone. The decay rate at 86 °C (the middle point) almost exactly equaled the average decay rate for all three temperatures, creating a nearly perfect fit of the data to a linear slope. Data represent CO/P ratios of FTIR spectral peaks for three temperatures, shown in Fig. 5.2.

The resulting Arrhenius plot showed an almost perfect R^2 of 0.9999. This highly correlated result was attributed in part to the high precision of the FTIR process used, which was independent of variations in extraction yields as it assessed the collagen carbonyl bond vibrational mode *in situ*. Fig. 5.3 represents the first use of FTIR to quantitatively assess bone collagen decay. The slope, again calculated using the linear regression function in Excel, was used to solve for Ea and A as per Collins et al[4]. Thus,

$$Ea = |Rb|$$

where b is the slope of ln(k), 1/T: Ea = 8.31445898(-5593.68681) = 46,508.48 kJ mol^{-1}.

$$A = Exp^{a}$$

where a is the y-intercept of the slope of ln(k), 1/T: A = $Exp^{36.46}$ = 6.833 x 10^{15}.

The resulting *Ea* for porcine bone of 117 kJ mol^{-1} is 36 % different than, but in the same order of magnitude as, the published 173 kJ mol^{-1} for bovine bone[7]. Further investigation will be required to determine the cause of this difference. Possible contributing factors include differences between porcine and bovine bone chemistry and

variations in the reactivity of bone components during artificial diagenesis, the novel use of FTIR to assess bone collagen decay, and temperature spacing between experimental setups.

Conclusions

The experiment-based solutions for *Ea* and A substitute into the Arrhenius equation (p. 159) to calculate decay rates for collagen decay at any given temperature. Table 5.2 gives three example temperatures. 10 ºC approximates the average annual temperature of England, 7.5 ºC of Montana, and ~25 ºC of tropical regions. These results affirm the high sensitivity of collagen decay to temperature as well as the empirical basis for expectations of bone collagen disappearance from sedimentary contexts below the upper Pleistocene.

Various temps (ºC)	Various temps (ºK)	Rate (k) at temp, using Arrhenius	Half-life (days) of rate k, using (ln2/k)	Half-life (~years)
10	283.15	1.76084E-06	393,645.36	1078
25.85	299	2.45556E-05	28,227.72	77
7.5	280.65	1.13086E-06	612,938.51	1678

Table 5.2 | Porcine bone collagen decay rates at three temperatures.

The discovery of just how fatty the porcine bone was, the fact that the ancient bone samples from England come from both porcine and bovine, and the difference between published and resulting *Ea* values suggest that this experiment needs to be replicated on bovine bone. Initial work on bovine bone has found that it is much drier (i.e., has an apparently lower lipid content), and thus promises to be easier to work with. Bovine results will enable direct comparison between decay rates of collagen from two differing mammalian taxa, as measured by FTIR-based CO/P ratios.

FTIR measured bone collagen decay with high precision, and SHG illustrated the same bone collagen deca y with high accuracy. The high R^2 values of the line of best fit

shown in Fig. 5.3 commends FTIR as a reliable new technique for direct assessment of bone collagen integrity in artificial collagen decay experiments. Its usefulness was predicated on the standardisation of powder grain size to between 20 and 60 μm, which effectively neutralised crystallisation effects on FTIR spectra. Future use of ATR-IR on ancient bone will benefit from this standardisation of protocol.

1 Collins, M. J., Gernaey, A. M., Nielsen-Marsh, C. M., Vermeer, C. & Westbroek, P. Slow rates of degradation of osteocalcin; green light for fossil bone protein? *Geology [Boulder]* **28**, 1139-1142, doi:10.1130/0091-7613(2000)028<1139:SRODOO>2.3.CO;2 (2000).

2 Thompson, T., Islam, M. & Bonniere, M. A new statistical approach for determining the crystallinity of heat-altered bone mineral from FTIR spectra. *Journal of Archaeological Science* **40**, 416-422 (2013).

3 Collins, M. J., Riley, M.S., Child, A.M., Turner-Walker, G. A basic mathematical simulation of the chemical degradation of ancient collagen. *J. Archaeol. Sci.* **22** (1995).

4 Collins, M., Child, A., van Duin, A. & Vermeer, C. Is osteocalcin stabilised in ancient bones by adsorption to bioapatite? *Ancient Biomolecules* **2**, 223-233 (1998).

5 Ioannis Kontopoulos, S. P., Kirsty Penkman, and Matthew J. Collins. *Preparation of Bone Powder for FTIR-ATR Analysis: The Particle Size Effect* (University of York, 2018).

6 Schindelin, J. *et al.* Fiji: an open-source platform for biological-image analysis. *Nature methods* **9**, 676 (2012).

7 Buckley, M., and Collins, M.J. . Collagen survival and its use for species identification in Holocene-lower Pleistocene bone fragments from British archaeological and paleontological sites. *Antiqua* **1**, 1:e1 (2011).

Chapter 6: Stable Carbon Isotopes and Molecular Preservation in Fossils

Contents

Figures

Tables

Appendixes

Justification of Stable Isotope Analysis

The first chapter of this thesis used a literature search to reveal the core question. Namely, fossil organics that include original biochemistry and even entire, flexible tissue-like structures most famously in Cretaceous fossils encounter limited reception in certain circles. This research project was therefore targeted at applying novel technologies to ancient bones with the premise that additional data would help resolve this controversy. Chapter 2 described the first step to that end, which was to adequately describe the provenance of, and properly catalogue, each specimen. Chapter 3 showed the positive results of a novel application of SHG to ancient bone. It revealed faint traces of collagen in Mesozoic samples. Chapter 4 investigated the same set of bones using infrared spectroscopy, and the artificial bone collagen decay experiment described in Chapter 5 erected a context to help interpret those results. It also introduced FTIR as a valid tool to quantify collagen loss over simulated time. The preceding efforts have thus far focused on the organic fraction of ancient bone, which consists primarily of Type 1 collagen. However, investigation of the the mineral fraction offers an indirect tactic to evaluate the fossil biochemical controversy. This chapter therefore describes stable isotope analyses of the mineral (bioapatite) fraction of Cretaceous samples. Also, the stable isotope results described here parallel Mass Spectrometry Group efforts to develop a field-deployable quadrupole mass spectrometer (QMS) with capability to detect key stable isotopes including ^{13}C and the far more abundant ^{12}C.

Linking Molecular Preservation with Stable Isotopes

Molecular preservation such as decayed bone collagen, peptides, and organic residues in fossils has been reported for decades, but the numbers of such publications, and especially the specificity of molecular identification have increased significantly in

recent years (see Chapter 1 and review by Schweitzer and Marshall)[1]. Several of the more impactful molecular preservation reports, especially including those sourced from bone collagen, derive from Montana's Hell Creek Formation (HCF) and a handful of other dinosaur fossil-rich beds in western North America. These sources of molecular preservation in, for example, *Tyrannosaurus rex*[2] and *Triceratops horridus*[3] offer intriguing new windows into the paleobiology, paleoecology, and paleoclimatology of the Late Cretaceous in North America[4]. Some HCF collagen samples have even furnished high enough molecular integrity for pioneering protein sequence comparisons with extant archosaurs[2,5]. Literature summarized in the next section of this chapter reveal a growing list of geologic settings that contain molecular preservation in fossils. These include from North America the HCF equivalent Lance Fm. Underlying these, the Judith River Fm. and Dinosaur Park Fm., the Niobrara Chalk Fm. of Kansas[6], and the Green River Fm[7] all supply Cretaceous material with published organics. Elsewhere, the Ciply Phosphatic Chalk of Belgium[8], the Lower Lufeng Fm. of China[9], and the Lower Gogolin Formation in Poland[10], among others, retain molecular preservation. These reports of molecular and, more rarely, primary tissue preservation do not include stable isotope data.

However, stable isotope ratios including $^{13}C/^{12}C$ ratio measurements ($\delta^{13}C$) from bioapatites have been used to convey meaningful paleodietary data from Cretaceous settings[11]. Results are reported in $\delta^{13}C$, where $\delta = (R_{sample}/R_{standard}-1)\cdot 1000‰$, $R = {}^{13}C/{}^{12}C$, and isotope values for the Vienna Pee Dee Belemnite (VPDB) are used as the standard for carbon. Stable isotope studies only supply meaningful data if they reflect primary isotopes. Establishing the presence of primary carbon is a necessary step for $\delta^{13}C$-based reconstructions to either reflect ancient diets or ecosystems or confirm or refute the hypothesis of primary Cretaceous organics. If dinosaur bone bioapatite and bone protein remnants preserve primary carbon isotope ratios, then both fractions should

contain largely original carbon. Arguments have been made in favor of primary carbon isotope ratios in fossil material via stable isotope tests such as comparing within-bone offsets and paleontological versus biological differences[12].

Secondary isotope alteration of bone bioapatite can occur by metamorphism or groundwater percolation that would facilitate dissolved carbonate interactions. Within-bone indicators of secondary isotopes include: (1) isotope exchange mismatches between stable isotope ratio patterns found in fossil versus modern bone, (2) randomized between-species or within-bone fraction offsets, and (3) homogeneity between fossil bones of different taxa within a site or microsite. Stated positively, primary bioapatite and proteinaceous carbon sources should exhibit (1) biological isotopic heterogeneities, (2) bone fraction and taxon-specific isotopic offsets, and (3) bone fractionation patterns between taxa or microsites that resemble those from comparable modern bone samples and ecosystems.

Finally, the co-occurrence in fossils of primary protein remnants and primary carbon isotopes may be related, but such co-occurrence must first be established prior to investigating possible causes. This chapter takes two steps toward investigating the co-occurrence of primary molecules and isotopes. First, it collates disparate literature from the two separate disciplines. Second, it includes two assessments for and against the presence of primary carbon isotopes in Hell Creek and Lance Formation bone fossils. These include comparisons between new stable carbon isotope ratios from dinosaur bone bioapatite to isotopes from 73 published dinosaur enamel and dentine results, and comparison between three within-bone fractions. The establishment of primary isotopes within specimens from the same settings as those with reported primary organics would confirm the primary proteins in fossils.

Background: Stable Carbon Isotope Ratios

Marine environments are enriched in ^{13}C compared to terrestrial environments[13]. On land, plants that use the more common C_3 photosynthetic pathway are more depleted in ^{13}C than C_4 plants. Trophic levels, taxon or age-specific bodily processes such as hibernation or weaning[14], or a particular mix of dietary components such as marine and terrestrial sources[15] can generate $\delta^{13}C$ offsets in differing body tissue fractions like the biominerals versus organics in teeth and bones. Measured biological differences across feeding modes and body tissues reflect known isotopic offsets to which fossil data can be compared. Conclusions about paleodiets may in turn inform plausible models of ancient ecosystems.

An array of papers has explored links between stable carbon isotope ratios and biome variances within extant[16] and extinct ecosystems[17]. These studies ultimately convey meaningful data with certainty only if original ratios are known or accurately inferred. Unfortunately, no purely objective test exists to verify the primary origin of isotope ratios. Differences in geologic settings such as matrix permeability and lithology, diagenetic processes such as hydrothermal circulation and crystallite reorganization, and metamorphic alteration can facilitate or inhibit isotopic exchange to various degrees in different tissue components. Strategies have therefore been developed to help assess whether or not, or to what degree, stable isotopes from fossils reflect primary or secondary sourcing. After applying appropriate sample cleaning and treatment protocols, these strategies include comparing isotope ratios from different taxa in one location, comparing different isolates from one body part, and comparing fossil isotope fractionations with biological fractionations, preferably with known parallels in extant biomes[11].

Experiments show that $\delta^{13}C$ values in bone or tooth apatite are higher (enriched) compared to collagen sampled from the same organism. Krueger and Sullivan[18] modeled this offset as a product of dietary carbohydrate carbons entering bone apatite and dietary proteins entering bone collagen. If undisturbed, ^{13}C content in organic versus inorganic bone fractions preserve food source signals plus isotope partitioning effects. Such differences between $\delta^{13}C$ values in apatite and collagen may be observed even after presumed diagenetic processes have occurred. As an example, Lee-Thorp et al[15] found that bone collagen in herbivore remains from southern Africa and Malawi represent a fractionation of ~ +5‰, and herbivore bone apatite ~+12‰, relative to the vegetation source.

Recently, stable carbon and oxygen isotopes in apatite of dinosaur and other fossil reptile femurs and teeth, plus several shells and bones, supplied sufficient data to begin reconstruction of East Asian dinosaur environments including regional paleoclimates[19]. Tütken's ^{13}C analysis of sauropod biominerals and extant plus extinct plant matter concluded that sauropods from the Morrison Formation and the Tendaguru Beds of Tanzania ate terrestrial C3 plants[12] . Stable isotope analysis of organic remains in a 10 cm long sauropod coprolite revealed a mean $\delta^{13}C$ value of -24.1‰, also consistent with preservation of C_3 plant matter[20]. Closer to the context of this present study, Fricke and Pearson[21] reconstructed dinosaur and garfish niche partitioning in the HCF using $\delta^{13}C$ and $\delta^{18}O$ ratios, standardized to VPDB and Vienna Standard Mean Ocean Water (VSMOW), respectively. Similarly, primary ^{13}C signatures have been interpreted from Dinosaur Park Formation, as well as from the dinosaur-rich, Two Medicine and Judith River Formations in Western North America[11].

If carbon isotopes from Hell Creek dinosaur bones show patterns that indicate extensive diagenetic alteration, for example virtually equal apatite-collagen offsets or

non-biological offsets, then further work would be suggested to evaluate the extent of isotope exchange. On the other hand, finding similar patterns to those of other workers suggests isotopic preservation. When joined to sites showing molecular preservation, investigation of causes for such co-occurrence could then begin. From a wider perspective, if the literature reveals primary isotopes in fossils lacking molecular preservation, or vice versa, then causal explanations should be sought to match those findings. However, the recognition of primary isotopes alongside molecular preservation would suggest causal explanations that could help account for both fossil features. Thus, Cretaceous specimens from geologic formations containing fossils with already published descriptions of original biochemistry were obtained and evaluated for $\delta^{13}C$ ratios.

Geologic Setting and Materials

The HCF outcrops in South Dakota and Wyoming show siliciclastic lithology containing laminar and cross-bedded sandstones, mudstones, and ironstones, as well as coal seams and coal lenses of various purities. Cretaceous fauna are preserved in its impure sandstones. These characteristic lithologies and paleofaunas also outcrop in the Williston Basin and Bighorn Basin in Wyoming to comprise the Lance Formation, illustrated in Fig. 6.1. In many areas, for example the HCF type locality in Flag Butte, north of Jordan, Montana, these coeval Formations contain a K-Pg boundary signature of two characteristic lignite beds near an iridium anomaly[4]. The GDFM fossils (see Chapter 2) from the HCF in this study included two *Triceratops horridus* femora and one hadrosaur femur collected from a private ranch near Glendive, Montana, 7.6 m below the narrow K-Pg coal seam marking the upper boundary of the HCF. A small portion of the triceratops brow horn described in Anderson and Armitage[3] as HTCH06 was tested alongside a separately catalogued fragment of the same horn core, GDFM 12001. The

sandstone layer from which these samples were extracted, approximately 3 m below the surface, was poorly cemented.

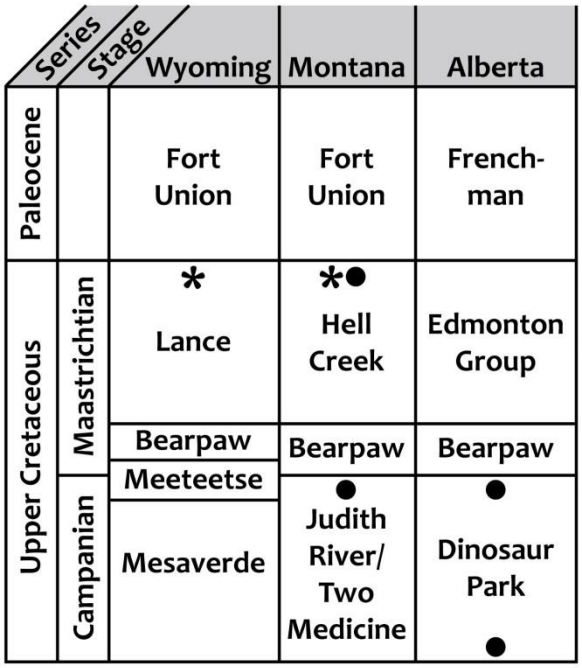

Figure 6.1 | Correlation chart of Formations and relative fossil locations. Asterisks mark positions of fossils sampled in this study. Dots mark positions of fossils sampled by Fricke and Pearson[21] and Fricke et al.[11]. Formations and Stages adapted from Rogers et al.[22] and Finn[23].

The HRS fossils from the Lance Fm. used in this study (see Chapter 2) came from a private ranch near Roxson, Wyoming. An unidentified dinosaur limb bone fragment from Rose quarry, and a Lambaeosaurus long bone fragment from the Southwest quarry are two of approximately twenty thousand dinosaur and other bones and fragments from the poorly cemented and poorly sorted Maastrichtian Lance sandstone lenses historically interpreted as fluvial deposits[24]. Here we present additional carbon isotope signatures from Hell Creek fossils and new results from two Lance Formation dinosaur bone fossils, and compare these signatures to published results on fossils from HCF, Judith River, and Dinosaur Park Formations. We hypothesize that strata with primary isotope indications within their fossils would be more likely than other strata to also contain fossils with original organics.

Fossil sites were selected based on a high likelihood of verifying both primary, largely unaltered OM and primary carbon isotopes as described in the literature. Lithology and paleofauna identify formation name equivalences shown in Figure 1. The Dinosaur Park Formation from eastern Montana and southeastern Alberta, Canada, would stratigraphically underlie the Hell Creek and Lance Formations if present in one geographic location. All three formations, plus Judith River, have already shown remarkable preservation of primary carbon sources. Figure 1 also illustrates geological proximities of primary bone proteins extracted from nearby formations in Western North America. Fossil site selection included consideration of similarities in lithology (for example deep sandstones)[25] with the assumption that lithology contributed to molecular and isotopic preservation.

Literature Search for Molecular and Isotopic Co-occurrence

Literature describing primary stable carbon isotopes was collected and compared to reports of primary OM from the same geologic settings. Table 6.1 shows nine co-occurrences of primary carbon and OM. Surprisingly, they represent Cenozoic, Mesozoic, Paleozoic, and Proterozoic strata. This observation suggests that taphonomic processes that may have contributed to preservation of both isotopes and biomolecules, for example rapid burial and lithification, have occurred throughout depositional history.

More co-occurrences will probably emerge from additional literature searches and data collections. For example, Table 6.1 shows that the results reported here from Lance Fm. dinosaur bone bioapatite $\delta^{13}C$, if considered primary, would add a tenth co-occurrence.

	Geologic formation	Primary ^{13}C signature (Reference)	Primary organic material (Reference)
1	Green River	Stromatolite laminae[26]	Lizard keratin[7]
2	Messel	Intraleaf structures[27]	Insect cuticle[28]
3	Hell Creek	Dinosaur tooth enamel, gar scale enamel[21] Probable dinosaur bone apatite[29]	*T. rex* bone collagen[2] Probable dinosaur collagen[29]
4	Lance	Probable dinosaur bone apatite[29]	Dinosaur bone collagen[30-33]
5	Dinosaur Park	Dinosaur tooth enamel[11]	Theropod bone collagen[32,34]
6	Judith River	Dinosaur tooth enamel[11]	Dinosaur bone amino acids[35] Brachylophosaur collagen, elastin, etc.[36]
7	Jehol Biota	Dinosaur, crocodile, and turtle tooth and bone apatites[19]	*Psittacosaurus* sp. probable integument proteins[37]
8	Morrison	Lacustrine carbonates[38]	Seismosaur protein[39]
9	Gunflint Chert	Microfossil components[40]	Cyanobacteria amide functional groups[41]
10	Emu Bay Shale	Cyanobacteria[42]	*Gloeocapsomorpha prisca* (cyanobacterium) N-alkanes[42]

Table 6.1 | Geologic Formations contain fossils with both primary stable carbon isotopes and endogenous biomolecular remnants. Line 3 shows that new results in this chapter verify published data, and line 4 shows where results described in this chapter may extend co-occurrence into Lance deposits.

Sample Treatments

Seven Upper Cretaceous dinosaur bones were collected and portioned into 15 samples. Taxa included eight samples from *Triceratops horridus*, one unknown taxon, and two hadrosaurids including a *Lambeosaurus lambei*. From these, fifteen $^{13}C/^{12}C$ ratio measurements are reported in $\delta^{13}C$. Table 6.2 shows the ^{13}C results from three different chemical preparation procedures were performed to isolate three different bone fractions from various specimens. One preparation isolated bone protein remnants (mostly collagen as discussed in Chapter 1 and below), a second isolated bioapatite, and a third included a mixture of bone biomineral plus organics. Stable carbon isotopes from each

fraction were compared to end members from corresponding biological bone fractions, expectations from diagenesis, and previously published data.

Commercial laboratories were used in order to avoid bias, ensure industry standard results, and obtain the highest possible accuracy to construct a baseline for future stable isotope studies toward testing a novel portable mass spectrometer currently under development (See poster presentations in Appendixes 6.1 and 6.2). Specifically, archaeological practice has over several decades firmly established decontamination procedures for bone isotope analyses[33]. In conjunction with the high resolution of AMS technology, well-tested decontamination protocols present perhaps the most accurate means of extracting primary isotope information from fossil bone. In particular, acid plus alkaline washes described below in the Arslanov and Svezhentsev[43] protocol have repeatedly demonstrated their effectiveness in removing organics, for example humic substances, that may have adsorbed onto bone crystallites or other microsurfaces, and thus in isolating primary material.

Accordingly, protein residue, bulk bone, and biomineral extraction protocols as standardised for archaeological use were performed by Geochron Laboratories and the University of Georgia's Center for Applied Isotope Studies (CAIS). Geochron Laboratories subcontracted the measurement of graphitized carbon isotope ratios, using accelerator mass spectrometry, and CAIS collected measurements using their compact National Electrostatics Corporation Model 1.5SDH-1 Pelletron 500kV accelerator mass spectrometer. The expense of these procedures limited sample numbers and results. Table 6.2 lists the six specimens investigated and their extracted fractions.

(Numbered bone) Taxon, Description	Apatite $\delta^{13}C$	Bulk $\delta^{13}C$	OM $\delta^{13}C$	Accession Number	Lab Number
1) *Triceratops* femur			-23.8	GDFM 08.027	UGAMS-03228b
2) Hadrosaurid femur			-22.7	GDFM 04.001	UGAMS-01937
3) *Triceratops* 1 femur			-20.1	GDFM 03.001	GX-32372
2) Hadrosaurid femur		-18.4		GDFM 04.001	GX-32678
4) *Triceratops* horn		-17.1		GDFM 12.001	UGAMS-11752
3) *Triceratops* 1 femur		-16.6		GDFM 03.001	GX-32647
2) Hadrosaurid femur		-16		GDFM 04.001	GX-32739
2) Hadrosaurid femur		-15.7		GDFM 04.001	UGAMS-01936
3) *Triceratops* 1 femur	-7.24			GDFM 03.001	UGAMS-17386
2) Hadrosaurid femur	-6.4			GDFM 04.001	UGAMS-01935
4) *Triceratops* horn	-5.51			HCTH 06	UGAMS-17387
1) *Triceratops* femur	-4.7			GDFM 08.027	UGAMS-03228a
4) *Triceratops* horn	-4.3			GDFM 12.001	UGAMS-11752a
5) Dinosaur	-2.6			HRS 08267	UGAMS-20476
6) *Lambeosaurus*	-2.4			HRS 19114	UGAMS-20477

Table 6.2 | ^{13}C measurements of stable carbon isotope ratios in ‰ for three chemically separated fractions of six dinosaur bones: 1) *Triceratops* femur, 2) Hadrosaurid femur, 3) *Triceratops* 1 femur, 4) Triceratops horn, 5) Unidentified taxon, and 6) Lambeosaurus. HTCH 06[3] represents a fragment of the same triceratops horn core as GDFM 12001. Organic matter (OM) extraction as per Arslanov and Svezhentsev[44] yields mostly collagenous residue mixed with trace proteinaceous remnants. HRS samples were sourced from Wyoming Lance Formation, and all others from Montana Hell Creek Formation.

Three different pretreatments isolated three bone fractions for differential isotope comparisons designed to assess the primary origin of carbon isotope ratios. First, the collagen extraction from the bone protocol from Arslanov and Svezhentsev[43] was followed. Bone was cleaned and washed using an ultrasonic bath, then dried. Dried bone was gently crushed to small fragments. The bone was treated with 5% HCl at 80°C for 1 hour, then washed and with deionized water on a fiberglass filter and rinsed with diluted (0.1N) NaOH at room temperature for 24 hours to remove any possible humic acids. The sample was treated with diluted HCl again, washed with deionized water, and dried at

60°C. The prepared samples were transferred to quartz tubes and combusted at 900ºC. The dried collagen was combusted at 575ºC in evacuated/sealed Pyrex ampoules in the presence of CuO and the resulting CO_2 captured for isotope analysis.

Brock et al.[45] confirmed that whereas the alkaline wash step increases protein purity, it also reduces collagen yield. Brock et al. used an extremely sensitive LC-MS/MS LTQ Orbitrap to identify specific products from typical protocols including the Arslanov method used in the present analysis. The Brock et al. analysis revealed a mixture. The vast majority of recovered protein was bone collagen, but with trace amounts of other protein remnants and inorganic complex residuals. Such a mixture follows from inefficiencies in collagen extraction by demineralisation and acidification. Brock et al. described no evidence for contamination, but they note that the term "protein residue" more accurately describes products of the Arslanov and similar methods than the typical use of "collagen." Therefore, the use of "collagen" in the present study denotes collagenous residue plus traces of other organics that almost certainly include diagenetic collagen products. The Arslanov method recovered no collagen in four of our seven bone samples. The three that did contain collagen showed high levels of decay, with average yields of only 0.275% by weight. This result was consistent with the rich literature of primary protein residuals described in Chapter 1.

Second, bioapatite bone fractions were separately recovered and analyzed. Again as per the protocols supplied by radiocarbon laboratories, the crushed bone was treated with diluted 1N acetic acid to remove surface adsorbed and secondary carbonates. Periodic evacuation insured that evolved carbon dioxide was removed from the interior of the sample fragments, and that fresh acid was allowed to reach interior micro-surfaces. The chemically cleaned sample was then reacted under vacuum with 1N HCl to dissolve the bone mineral and release carbon dioxide from bioapatite.

Third, standard archaeological bulk bone preparation was followed. Crushed bone was treated with 1N HCl at 4ºC for 24 hours. The residue was filtered, rinsed with deionized water and under acid condition (pH≈3), then heated at 80ºC for 6 hours. The resulting collagenous solution was then filtered, dried, and weighed. The bulk bone results thus combine isotopic signal from both bioapatite and organic bone components.

Evaluation of Primary Sourcing

To assess the degree of primary verses secondary carbon isotope ratios, results were first compared to known biological end members. They show an upper depleted maximum for collagen of -23.8‰ and for bone bioapatite of -7.24‰, giving a $\Delta\delta^{13}C_{apatite\text{-}collagen}$ of +16.56‰. We found a lower depleted minimum for collagen of -20.1‰ and for bone bioapatite of -2.4‰, giving a $\Delta\delta^{13}C_{apatite\text{-}collagen}$ of +17.7‰. The nearest proxy in the literature that compared bioapatite to collagen within the same ancient bone comes from mammalian bones that showed an ~+7‰ offset[15]. Possible causes of the large (~10‰) difference between archaeological mammal bone and dinosaur bone are discussed below.

A second assessment of our results included a comparison of our $\delta^{13}C$ measurements with those supplied by other authors including Fricke and Pearson[21] and Tütken[12]. In their supplemental information, Fricke and Pearson totaled 67 Hell Creek $\delta^{13}C$ enamel and dentine bioapatite measurements from ceratopsian and hadrosaurian teeth from several microsites, ranging from approximately -1.0‰ (their -0.4‰ result was treated as an outlier and removed from the data set) to -9.4‰, finding a roughly Gaussian distribution with a mean of -5.2‰. Their study, and others like it, assessed small isotopic heterogeneities *between* taxa in order to tie the degree of primary isotope ratios partly to dietary and habitat expectations. In our bone samples, however, the very large heterogeneity between within-bone bioapatite and “collagen” fractions occurred at a

much broader scale. Combining Fricke and Pearson's various dinosaur enamel bioapatite results decreased the resolution to a degree that permitted a generalised comparison between their tooth and the present bone bioapatites. Zooming out also enabled visualization of the large offsets between our bone bioapatite and organic components as Figure 6.2 shows below.

Seven dinosaur bone bioapatite $\delta^{13}C$ results ranged from -2.4‰ to -7.24‰ with a mean of -4.3‰. Figure 6.2 shows that these bone bioapatite results correspond to Fricke and Pearson's (2008) Hell Creek tooth bioapatite $\delta^{13}C$ range. We hypothesize that if certain taphonomies help preserve bone bioapatites, they may simultaneously preserve primary isotope ratios. Stated negatively, stable carbon isotope ratios that show evidence of mixing within inorganic bone fractions suggest the potential of contamination of the organic fraction also. Fricke and Pearson demonstrated primary isotope ratios in enamel bioapatites. Also, new reports show that some sites better preserve bone apatites than tooth apatites (as discussed below.) Therefore the overlap between bone and tooth $\delta^{13}C$ could signify that similar taphonomies helped preserve primary isotopes in Hell Creek and other localities.

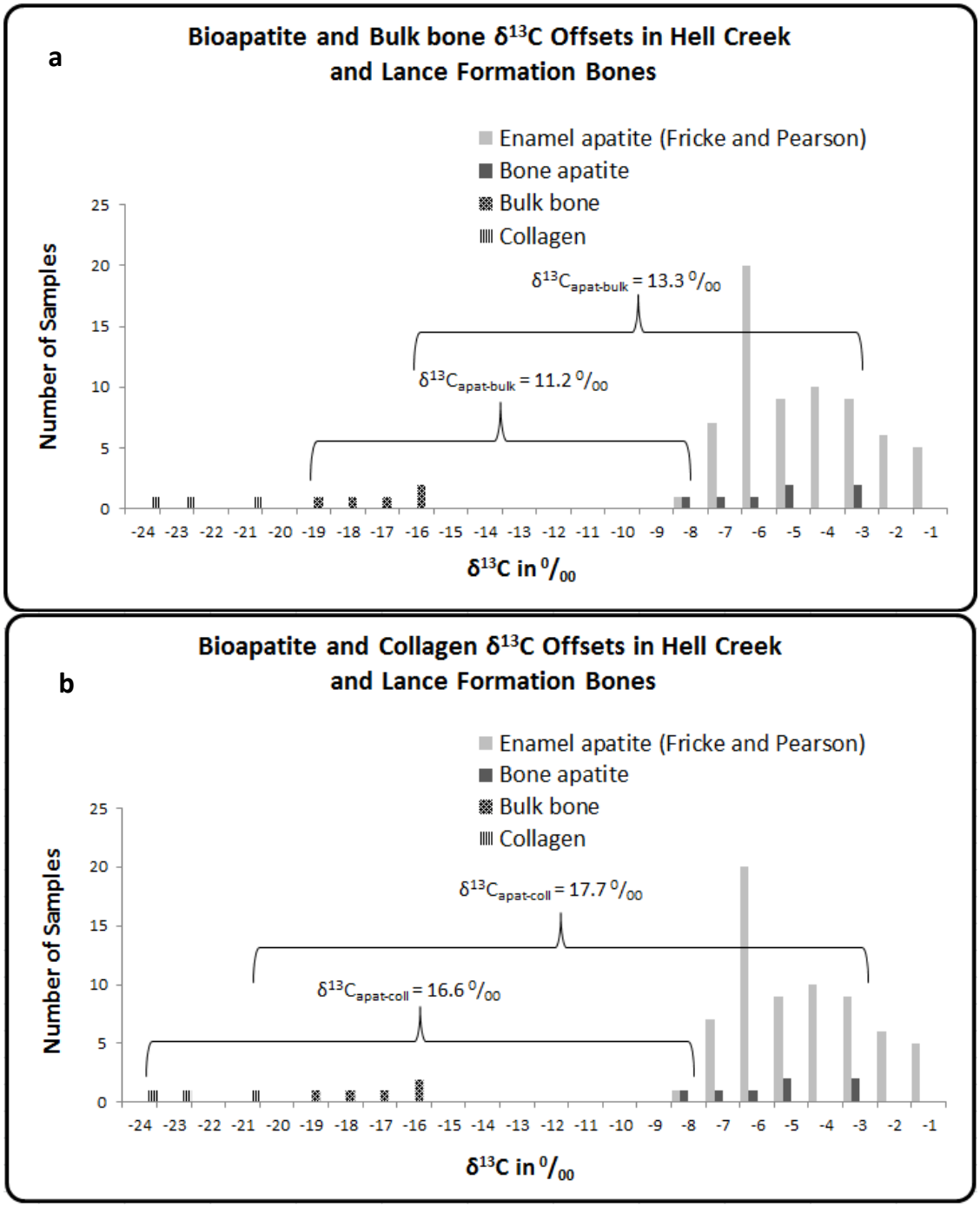

Figure 6.2 | Numbers of $\delta^{13}C$ measurements in ‰ $_{VPDB}$ binned in whole units by bone fraction. Light gray bars show 67 measurements of Hell Creek ceratopsian and hadrosaur enamel and dentine bioapatite reported by Fricke and Pearson (2008). In this study, black, hatched, and thin line bars show 15 $\delta^{13}C$ results from 7 different dinosaur bones. The black bars show seven measurements of hadrosaur and ceratopsian bone bioapatites. Thin line bars show that one hadrosaur and two ceratopsian protein remnant ("collagen") extracts contain heavily depleted $\delta^{13}C$ levels relative to bioapatite, somewhat similar to biological bone offsets. Hatched bars show five results from bulk treatments that yield unfractionated bone. **a,** Brackets indicate upper and lower end member offsets between apatite and bulk bone fractions. **b,** Brackets indicate an upper and lower end member offsets between apatite and collagen bone fractions.

Discussion: Cretaceous bone proteins

The co-occurrence of molecular preservation with carbon isotope ratio preservation in fossils could help alleviate tension over whether or not Cretaceous fossils retain primary biochemistry and inform discussions of preservation conditions that might contribute to this co-occurrence. The demonstrable preservation of any original isotopic information in the organic fraction would be consistent with many other descriptions of molecular preservation as discussed above and described in Chapter 1. Three tests were employed to assess isotopic preservation and possibly confirm molecular preservation in seven dinosaur bones. In one, ^{13}C ratios were collected directly from dinosaur bone using established archaeological collagen extraction procedures. In another, ^{13}C ratios were collected from dinosaur bone bioapatite and compared to published dinosaur tooth bioapatite signatures from equivalent geologic units. Similarly, they were compared to analogous biological (i.e., modern) bone fractions. In the third, comparison was sought internally between ^{13}C ratios of collagen and apatite fractions from the same bones.

Given the relative rarity of bone collagen preservation in Mesozoic sources, little to no recovery was initially expected. However, tiny amounts were recovered in three of the seven Hell Creek dinosaur bones included in this analysis. The alternative scenario to the recovery of primary proteins would be difficult to defend: i.e., that exogenous protein remnants were transported to the interior of these bones and survived standardized acid/base/acid decontamination protocols to finally masquerade as endogenous collagen. On the other hand, recovery of proteinaceous vestiges aligns with the many other descriptions of dinosaur bone protein remnants reviewed above. For example, Bertazzo et al.[32] described collagen microfiber-sized structures in six of eight dinosaur bones from the Dinosaur Park Formation (see Fig 6.1). They wrote that “the preservation of soft tissues

and even proteins is a more common phenomenon than previously accepted." The results reported here appear to echo this possibility.

Discussion: Comparison of $\delta^{13}C$ in tooth versus bone bioapatite

No extraction procedure yet invented can separate diagenetic from primary carbonate with 100% reliability. However, fossils contain clues that offer reasonable inferences. For example, Fricke and Pearson[21] (2008) made cogent inferences from their data set to argue that stable isotope ratios in Hell Creek enamel, dentine, and ganoine (garfish scales) bioapatite carbonates are largely or wholly primary. For example, they measured offsets in $\delta^{18}O$ and/or $\delta^{13}C$ between HCF taxa that mirrored offsets between extant taxa with similar ecologies. Also, they argued that diagenetic alteration would have homogenized isotope ratios from various taxa, obscuring or even obliterating the observed offsets. In order to discern whether or not isotope ratios preserve at least some original signals, "it is simply enough to know that isotopic offsets and differences in correlation coefficients among animals can be preserved only if isotopic alteration does not obscure original isotopic information" (Fricke and Pearson 2008), and their results revealed exactly these isotopic offsets and differences in correlation coefficients. They also found that the offset between dietary $\delta^{13}C$, inferred from organic matter extracts from sedimentary matrix, and herbivore enamel $\delta^{13}C$ from eight microsites ranging from upper Campanian to upper Maastrichtian and from western Montana to North Dakota consistently held to ~18‰. Since no known diagenetic process would manufacture such a consistent signal across such time and space, they concluded that their Hell Creek fossil carbonates retain primary isotopic information.

The considerable congruence between their tooth $\delta^{13}C$ range and our new bone apatite $\delta^{13}C$ range as revealed in Fig 2 suggests that Hell Creek bone $\delta^{13}C$ may also

preserve original isotopic signal. Our bone apatite $\delta^{13}C$ values fall within the range of Fricke and Pearson's (2008) enamel apatite values after pooling data from their various taxa together. Comparison between like taxa revealed similar tooth and bone bioapatite overlaps (data not shown) as lumping their taxa as shown in Figure 2. Also, the mean apatite value from Fricke and Pearson (2008) of -4.7‰ and the bone apatite mean value of -5.9‰ differ by only 1.2‰. (Inclusion of one outlier would raise this offset to 2.1 ‰.) Similar arguments made by Fricke and Pearson's for the primary origin of their enamel $\delta^{13}C$ signals (grey bars in Fig 6.1) should apply to the present bone apatite $\delta^{13}C$ values (black bars in Fig 6.1).

Many workers prefer analyzing tooth enamel, citing the argument that bone bioapatites are more susceptible to diagenetic alteration, for example isotope exchange with matrix carbonates facilitated by hydrothermal circulation. Reference to literature that described biological ^{13}C ranges in bone is offered in response to this. Tütken[12] found a similar overlap in 64 Jurassic sauropod long bone bioapatite and 19 tooth enamel results. Sauropods had a mean enamel $\delta^{13}C$ of -8.0 ± 1.2‰ (ranging from -9.1 to -4.1‰), and a mean bone bioapatite of -7.1 ± 1.4‰ (ranging from -10.9 to -4.7‰). Since both tooth and bone mean values fall far below the nearly zero values expected from contamination by isotopic exchange with matrix carbonates, both mineral sources appear to preserve a large fraction of primary isotopes. This conclusion confronts the common contention that enamel preserves primary isotopes with greater fidelity than bone. Review of this issue revealed a long-standing debate with some reporting evidence that some settings do preserve bone isotopes with as much or more fidelity as tooth isotopes. Could the HCF be grouped among those settings?

As described in Chapter 1, bone bioapatites occur as flattened rods of roughly 30Å X 400Å, whereas enamel crystallites range one or two orders of magnitude larger[46]; the

smaller crystal size of bone apatite is thought to be linked to increased susceptibility to recrystallization and diagenetic alteration. However, tooth enamel is not immune to isotopic exchange even in archaeological contexts[47,48]. Further, a recent review assessed comprehensive isotope data from about 150 bone and tooth samples. "The information provided by the carbon isotopic analysis of bone apatite is potentially as reliable as in enamel at least for the past 40,000 yr"[49]. After admitting that this initially "seems to challenge more than 30 yr of bone and enamel diagenesis research," Zazzo (2014) argues that the conflict is only apparent. He suggested that tight cross-linking between bone collagen and associated apatites stabilizes bone in the early stages of diagenesis to diminish recrystallization that leads to isotope alteration. Zazzo (2014) restricts his observations to archaeological timescales. However, far fewer bone apatite $\delta^{13}C$ results than might be expected have been collected from paleontological sources. This implies that the perception that bone preserves isotopes more poorly than enamel in all settings is not based on extensive data across various geologic or geographic settings. Could the cross-linking between collagen and bioapatite invoked to explain the persistence of primary isotopes across archaeological time scales also lead to persistence of primary isotope ratios across paleontological time scales? Reports other than the present chapter are consistent with this possibility.

For example, Lee-Thorp and van der Merwe[50], in their seminal study on fossil bone apatite, observed that the increase of diagenetic $\delta^{13}C$ signal is "initially rapid, then slowing" over paleontological timescales. Elsewhere, Lee-Thorp speculates regarding the variable alteration effects of burial conditions on archaeological bone: "Could the crucial difference be that the [heavily altered] specimens used in the former studies are on a pathway to destruction rather than fossilization, whereas those from Die Kelders, Klasies and Border Cave are buried in environments conducive to fossilization with minimal

chemical alteration?"[51] She observed that minimal isotopic alteration implies that recrystallization has not incorporated exogenous carbonates in the crystal structure. Instead, "Structural changes may have merely involved the rearrangement (Ostwaldian ripening) and/or incorporation of in situ 'raw material.'"[51]. The $\delta^{13}C$ data for bone apatite presented in the current study and in published reports may indicate that protection in archaeological environments "conducive to fossilization" could also apply to paleontological settings. Our results, along with others such as Tütken (2011), are too few to definitively answer this question as it applies to HCF and Morrison, respectively, but they suggest that paleontological bone sources may preserve more primary isotopic information than typically suspected.

Such considerations ultimately await empirical investigations of isotope exchange rates in various burial environments. Meanwhile, the data in Fig 6.1 are consistent with the hypothesis that some fossils preserve approximately primary HCF and Lance bone bioapatite isotope ratios.

Discussion: Comparison of within-bone "collagen" to bioapatite fractions

The non-random and internally consistent pattern of dinosaur bone fraction offsets shown in Figure 6.2 also matches expectations from primary ^{13}C ratios. In short, how could a single diagenetic process have altered separate bone fractions to produce the wide but consistent heterogeneity between bone collagenous material and bone apatite? Similarly, bulk bone preparations supply a cross-check of the degree to which an isotope signal is primary versus secondary in origin. Bulk bone incorporates both OM and mineral bone components. Therefore, primary bulk $\delta^{13}C$ values should indicate a mixture of the isotope ratios from each fraction. Their positions in Figure 2 show values between apatite and collagen that match this interpretation.

However, our observed dinosaurian $\delta^{13}C_{apatite\text{-}collagen}$ value (17‰) exceeds the ~+7‰ offset (Lee-Thorp et al 1989) in the nearest proxy available in the literature—biological bone fractions for mammalian herbivores—by ~10‰. ^{13}C ratios in modern versus paleontological bone collagen tend toward similar values, suggesting that this larger (~+10‰) offset results from either primary or secondary heterogeneities in the bone bioapatite fraction. If our bone apatite and Fricke and Pearson's (2008) enamel results are principally primary as already argued, and if bulk bone and collagenous remnants preserve primary isotopes also as already argued, then plausible paleobiological explanations for such a large offset should be considered. Fricke and Pearson (2008) offered several possibilities to account for biological carbon enrichment they found in their dinosaur enamel bioapatite results, including:

1. Extinct hadrosaurian and ceratopsian digestive systems differed from extant mammals and birds in ways that enabled them to acquire sufficient nutrients from the tough, fibrous plant matter that contributed to their diets. Their unknown metabolic systems may have enriched heavy carbon isotopes that selectively incorporated into their bioapatites.
2. Different environments including uniquely Cretaceous microhabitats, and unique dinosaurian behaviors including competition for available resources may have affected dietary uptake of $\delta^{13}C$.
3. Marine influences, including changes in sea level along widespread tidal flats, could favor growth of C_3 plants enriched in $\delta^{13}C$.
4. Available food may have comprised leaves exposed to direct sunlight. This canopy effect causes up to 10‰ higher $\delta^{13}C$ values compared to understory foliage.

Other authors have suggested or measured additional factors that influence carbon isotope fractionation:

5. Want et al[52] suggested that the higher partial pressure of CO_2 indicated by Cretaceous System fossils, likely producing a greenhouse effect, albeit of debated intensity, may affect carbon isotope ratios in plant tissues.
6. Fernandes et al[53] found that body size may positively correlate with $\Delta^{13}C_{bioapat\text{-}diet}$, with pigs showing a larger apatite-diet offset than rats, and rats larger than mice. Possibly, the larger dinosaur body sizes also increased their $\Delta^{13}C_{bioapat\text{-}collagen}$ ratios.
7. Tütken[12] also noted known $\delta^{13}C$ differences that arise from soil moisture, water use efficiency, plant growth cycles, different plant organs, and substrate salinity.
8. Jim et al[54] discovered a controlled isotope diet that generated a +11‰ offset between bone apatite and collagen in mice. They wrote, "On diets in which the $\Delta^{13}C_{prot\text{-}engy}$ is negative, e.g. … where protein is C3 and energy is C4, $\Delta^{13}C_{coll\text{-}bchol}$ [bone collagen-bone cholesterol offset] will be small (~+3‰) and both $\Delta\ ^{13}C_{apat\text{-}bchol}$ [bone apatite-bone cholesterol offset] and $\Delta^{13}C_{apat\text{-}coll}$ [bone apatite-bone collagen offset] will be large (~+14 and +11‰, respectively…)."

This final scenario would explain Hell Creek herbivorous dinosaur apatite-collagen offsets if not for the fact that C_4 flora are not known in Cretaceous deposits. However, possibly some dinosaurian plant sources and/or metabolisms led to uptake of protein from C_3 plant sources, but carbohydrates more often from carbon-enriched vegetation other than C_4 plants. For example, sea grasses from inland salt marshes might be invoked, although the only known Cretaceous seagrass fossil is in the Netherlands[55]. In any case, a combination of some or all of these eight or other factors could have caused part or all of the observed 17‰ carbon offset. Although these paleobiological considerations do not

rule out the possibility of some level of isotope exchange, at a minimum they leave open the possibility of primary within-bone isotopic heterogeneities.

On the whole, literature clearly demonstrates primary isotope ratios that co-occur with primary OM in at least nine geologic settings including certain Upper Cretaceous sites in Western North America. If considered primary, the $\delta^{13}C$ results reported here add a tenth co-occurrence, in the Lance Fm. These observations are consistent with the suggestion of Zazzo (2014) that certain taphonomic conditions favor preservation of stable isotopes in bone. Future research might find that some or all of those conditions also favor molecular preservation.

Conclusions

Scientific literature increasingly describes direct detection of molecular preservation in fossils. Some of these reports include results from the gold standard of detection, bone collagen sequencing, as described in Chapter 1. This study adds to that trend by presenting the first report of $\delta^{13}C$ values taken directly from collagenous remnant extracts of dinosaur bone, shown in lines 1-3 of Table 6.2. Literature also describes a co-occurrence of primary isotopes and molecular preservation. The present study used three assessments of preservation in an attempt to evaluate the co-occurrence already described in the Hell Creek Fm., and to test for its extension into the equivalent Lance Fm. In one assessment, primary $\delta^{13}C$ from dinosaur teeth were compared to dinosaur bone bioapatites from HCF, showing congruent signals. Though rare and of poor quality, recovery of sufficient collagenous remnant enabled a second assessment by comparing isotopes from within-bone fractions. Very large heterogeneities between bioapatite and OM are more consistent with primary isotopes than they are with secondary replacements which should have homogenized the signals. However, some degree of isotopic alteration

cannot be completely overruled in light of the challenge in accounting for the very large (~+17‰) collagen-apatite offset. Paleobiological scenarios that could have produced or contributed to the large $\delta^{13}C$ offsets were reviewed from the literature. Third, comparison of within-bone bioapatite carbon isotope ratios to bulk bone fractions, which contain a mixture of apatite and OM, revealed offsets between apatite and collagenous remains. These offsets confirm the collagen-apatite offset and thus the hypothesis that mostly primary isotopes are preserved in HCF and Lance bones. The results of these three assessments therefore suggest that molecular and isotopic preservations also co-occur in Lance Fm. fossils. These conclusions lead to two outcomes. First, the co-occurrence of primary carbon isotope ratios and molecular preservation can inform future investigations into preservation modes that preserve both primary isotopes and molecules even extending to Cretaceous deposits. Last, AMS measurements of $\delta^{13}C$ in fossil bone supply a reference point for future QMS measurements, as illustrated in the attached appendices. This investigation happened to include unstable carbon isotope measurements for fossils, and these data revealed unexpected systematic trends set forth in the next chapter.

1 Schweitzer, M. H., and Marshall, M. *The Complete Dinosaur, Second Edition*. Second edn, 281 (Indiana University Press, 2012).

2 Asara, J. M., Schweitzer, M. H., Freimark, L. M., Phillips, M. & Cantley, L. C. Protein sequences from mastodon and Tyrannosaurus rex revealed by mass spectrometry. *Science* **316**, 280-285, doi:10.1126/science.1137614 (2007).

3 Armitage, M. H. & Anderson, K. L. Soft sheets of fibrillar bone from a fossil of the supraorbital horn of the dinosaur Triceratops horridus. *Acta Histochem* **115**, 603-608, doi:10.1016/j.acthis.2013.01.001 (2013).

4 Hartman, J. H. *et al.* Context, naming, and formal designation of the Cretaceous Hell Creek Formation lectostratotype, Garfield County, Montana. *Geological Society of America Special Papers* **503**, 89-121 (2014).

5 Buckley, M. *et al.* Comment on "Protein sequences from mastodon and Tyrannosaurus rex revealed by mass spectrometry". *Science* **319**, 33; author reply 33, doi:10.1126/science.1147046 (2008).

6 Lindgren, J., Caldwell, M. W., Konishi, T. & Chiappe, L. M. Convergent evolution in aquatic tetrapods: insights from an exceptional fossil mosasaur. *PLoS One* **5**, e11998, doi:10.1371/journal.pone.0011998 (2010).

7 Edwards, N. P. *et al.* Infrared mapping resolves soft tissue preservation in 50 million year-old reptile skin. *Proc Biol Sci* **278**, 3209-3218, doi:10.1098/rspb.2011.0135 (2011).

8 Lindgren, J. *et al.* Microspectroscopic evidence of cretaceous bone proteins. *PLoS One* **6**, e19445, doi:10.1371/journal.pone.0019445 (2011).
9 Reisz, R. R. *et al.* Embryology of Early Jurassic dinosaur from China with evidence of preserved organic remains. *Nature* **496**, 210-214, doi:10.1038/nature11978 (2013).
10 Surmik, D. *et al.* Spectroscopic Studies on Organic Matter from Triassic Reptile Bones, Upper Silesia, Poland. *PLoS One* **11**, e0151143, doi:10.1371/journal.pone.0151143 (2016).
11 Fricke, H. C., Rogers, R. R., Backlund, R., Dwyer, C. N. & Echt, S. Preservation of primary stable isotope signals in dinosaur remains, and environmental gradients of the Late Cretaceous of Montana and Alberta. *Palaeogeography, Palaeoclimatology, Palaeoecology* **266**, 13-27 (2008).
12 Tütken, T. The diet of sauropod dinosaurs: Implications from carbon isotope analysis of teeth, bones, and plants. *Biology of the sauropod dinosaurs: Understanding the life of giants*, 57-79 (2011).
13 Hoefs, J. *Stable isotope geochemistry*. 35 (Springer-Verlag, 1987).
14 Bocherens, H., Fizet, M. & Mariotti, A. Diet, physiology and ecology of fossil mammals as inferred from stable carbon and nitrogen isotope biogeochemistry: implications for Pleistocene bears. *Palaeogeography, Palaeoclimatology, Palaeoecology* **107**, 213-225 (1994).
15 Lee-Thorp, J. A., Sealy, J. C. & Van der Merwe, N. J. Stable carbon isotope ratio differences between bone collagen and bone apatite, and their relationship to diet. *Journal of archaeological science* **16**, 585-599 (1989).
16 Grey, J. & Jones, R. I. Carbon stable isotopes reveal complex trophic interactions in lake plankton. *Rapid Communications in Mass Spectrometry* **13**, 1311-1314 (1999).
17 Kohn, M. J. & Cerling, T. E. Stable isotope compositions of biological apatite. *Reviews in mineralogy and geochemistry* **48**, 455-488 (2002).
18 Krueger, H. W. & Sullivan, C. H. Models for carbon isotope fractionation between diet and bone. *Stable isotopes in nutrition* **258**, 205-220 (1984).
19 Amiot, R. *et al.* Environment and ecology of East Asian dinosaurs during the Early Cretaceous inferred from stable oxygen and carbon isotopes in apatite. *Journal of Asian Earth Sciences* **98**, 358-370 (2015).
20 Ghosh, P. *et al.* Dinosaur coprolites from the Late Cretaceous (Maastrichtian) Lameta Formation of India: isotopic and other markers suggesting a C3plant diet. *Cretaceous Research* **24**, 743-750 (2003).
21 Fricke, H. C. & Pearson, D. A. Stable isotope evidence for changes in dietary niche partitioning among hadrosaurian and ceratopsian dinosaurs of the Hell Creek Formation, North Dakota. *Paleobiology* **34**, 534-552 (2008).
22 Rogers, R. R., Swisher III, C. C. & Horner, J. R. 40Ar/39Ar age and correlation of the nonmarine Two Medicine Formation (Upper Cretaceous), northwestern Montana, USA. *Canadian Journal of Earth Sciences* **30**, 1066-1075 (1993).
23 Finn, T. M. in *U.S. Geological Survey Digital Data Series DDS-69-V* 1-14 (USGS, 2010).
24 Clemens, W. A. in *Publications in Geological Sciences* Vol. 48 12-17 (University of California, 1964).
25 Asara, J. M. *et al.* Interpreting sequences from mastodon and T. rex. *Science* **317**, 1324-1325, doi:10.1126/science.317.5843.1324 (2007).
26 Frantz, C. M. *et al.* Dramatic local environmental change during the Early Eocene Climatic Optimum detected using high resolution chemical analyses of Green River Formation stromatolites. *Palaeogeography, Palaeoclimatology, Palaeoecology* **405**, 1-15 (2014).
27 Grein, M., Roth-Nebelsick, A. & Wilde, V. Carbon isotope composition of middle Eocene leaves from the Messel Pit, Germany. *Palaeodiversity* **3**, 1-7 (2010).

28 McNamara, M. E., Briggs, D. E. & Orr, P. J. The controls on the preservation of structural color in fossil insects. *Palaios* **27**, 443-454 (2012).
29 Thomas, B. *Collagen Remnants in Ancient Bone* phD thesis, University of Liverpool, (2019).
30 Pawlicki, R., Dkorbel, A. & Kubiak, H. Cells, collagen fibrils and vessels in dinosaur bone. *Nature* **211**, 655-657 (1966).
31 Schweitzer, M. H. Soft tissue preservation in terrestrial Mesozoic vertebrates. *Annual Review of Earth and Planetary Sciences* **39**, 187-216 (2011).
32 Bertazzo, S. *et al.* Fibres and cellular structures preserved in 75-million-year-old dinosaur specimens. *Nat Commun* **6**, 7352, doi:10.1038/ncomms8352 (2015).
33 Lee, Y. C. *et al.* Evidence of preserved collagen in an Early Jurassic sauropodomorph dinosaur revealed by synchrotron FTIR microspectroscopy. *Nat Commun* **8**, 14220, doi:10.1038/ncomms14220 (2017).
34 Schweitzer, M. H., Wittmeyer, J. L., Horner, J. R. & Toporski, J. K. Soft-tissue vessels and cellular preservation in Tyrannosaurus rex. *Science* **307**, 1952-1955, doi:10.1126/science.1108397 (2005).
35 Ostrom, P. H., Macko, S.A., Engel, M.H., Silfer, J.A., Russell, D. Geochemical characterization of high molecular weight material isolated from Late Cretaceous fossils. *Advances in Organic Geochemistry* **16**, 1139-1144 (1990).
36 Schweitzer, M. H. *et al.* Biomolecular characterization and protein sequences of the Campanian hadrosaur B. canadensis. *Science* **324**, 626-631, doi:10.1126/science.1165069 (2009).
37 Vinther, J. *et al.* 3D Camouflage in an Ornithischian Dinosaur. *Curr Biol* **26**, 2456-2462, doi:10.1016/j.cub.2016.06.065 (2016).
38 Dunagan, S. P. & Turner, C. E. Regional paleohydrologic and paleoclimatic settings of wetland/lacustrine depositional systems in the Morrison Formation (Upper Jurassic), Western Interior, USA. *Sedimentary Geology* **167**, 269-296 (2004).
39 Gurley, L. R., Valdez, J. G., Spall, W. D., Smith, B. F. & Gillette, D. D. Proteins in the fossil bone of the dinosaur, Seismosaurus. *J Protein Chem* **10**, 75-90 (1991).
40 Williford, K. H. *et al.* Preservation and detection of microstructural and taxonomic correlations in the carbon isotopic compositions of individual Precambrian microfossils. *Geochimica et Cosmochimica Acta* **104**, 165-182 (2013).
41 Alleon, J. *et al.* Molecular preservation of 1.88 Ga Gunflint organic microfossils as a function of temperature and mineralogy. *Nat Commun* **7**, 11977, doi:10.1038/ncomms11977 (2016).
42 Hall, P. A., McKirdy, D. M., Halverson, G. P., Jago, J. B. & Gehling, J. G. Biomarker and isotopic signatures of an early Cambrian Lagerstätte in the Stansbury Basin, South Australia. *Organic Geochemistry* **42**, 1324-1330 (2011).
43 Arslanov, K. A., Svezhentsev, Y.S. An improved method for radiocarbon dating fossil bones. *Radiocarbon* **3**, 387-391 (1993).
44 Arslanov, K. A. & Svezhentsev, Y. S. An improved method for radiocarbon dating fossil bones. *Radiocarbon* **35**, 387-391 (1993).
45 Brock, F., Wood, R., Higham, T.F.G., Ditchfield, P., Bayliss, A., Ramsey, C.B. Reliability of nitrogen content (%N) and carbon:nitrogen atomic ratios (C:N) as indicators of collagen preservation suitable for radiocarbon dating. *Radiocarbon* **54**, 879–886 (2012).
46 Wopenka, B., Pasteris, J.D. A mineralogical perspective on the apatite in bone. *Materials Science and Engineering C* **25**, 131-143 (2005).
47 Zazzo, A. & Saliège, J.-F. Radiocarbon dating of biological apatites: a review. *Palaeogeography, Palaeoclimatology, Palaeoecology* **310**, 52-61 (2011).
48 Hollund, H., Arts, N., Jans, M. & Kars, H. Are teeth better? Histological characterization of diagenesis in archaeological bone–tooth pairs and a discussion of the consequences for

archaeometric sample selection and analyses. *International Journal of Osteoarchaeology* **25**, 901-911 (2015).

49 Zazzo, A. Bone and enamel carbonate diagenesis: a radiocarbon prospective. *Palaeogeography, Palaeoclimatology, Palaeoecology* **416**, 168-178 (2014).

50 Thorp, J. L. & Van Der Merwe, N. J. Carbon isotope analysis of fossil bone apatite. *South African Journal of Science* **83**, 712-715 (1987).

51 Lee-Thorp, J. A. in *Biogeochemical approaches to paleodietary analysis* 89-115 (Springer, 2002).

52 Wang, Y. *et al.* Paleo-CO2 variation trends and the Cretaceous greenhouse climate. *Earth-Science Reviews* **129**, 136-147 (2014).

53 Fernandes, R., Nadeau, M.-J. & Grootes, P. M. Macronutrient-based model for dietary carbon routing in bone collagen and bioapatite. *Archaeological and Anthropological Sciences* **4**, 291-301 (2012).

54 Jim, S., Ambrose, S. H. & Evershed, R. P. Stable carbon isotopic evidence for differences in the dietary origin of bone cholesterol, collagen and apatite: implications for their use in palaeodietary reconstruction. *Geochimica et Cosmochimica Acta* **68**, 61-72 (2004).

55 Voigt, E. Upper Cretaceous bryozoan-seagrass association in the Maastrichtian of the Netherlands. *Recent and Fossil Bryozoa: Olsen & Olsen, Fredensborg*, 281-298 (1981).

Establishing a Baseline for a Portable Stable Carbon Isotope Detection System

Brian Thomas (Brian.Thomas@liv.ac.uk)[1], David McIntosh[1], Timothy Clarey[2], and Stephen Taylor[1,3]

[1]Dept. Electrical Engineering & Electronics, University of Liverpool, UK; [2]The King's University, Southlake, TX; [3]Q Technologies Ltd, Liverpool, UK

OVERVIEW

Purpose: Demonstrating the accuracy of an on-site QMS radiocarbon detection system will require comparison to a baseline of industry standard results.
Methods: Stable carbon isotope ratios from three fractions of ancient bones were collected using AMS. They were compared to published results using IRMS in order to set expectations for what an on-site QMS should detect in similar bone samples.
Results: Comparisons of ^{13}C between within-bone fractions and between AMS and IRMS results revealed patterns of authenticity that a QMS instrument should also detect.

1. INTRODUCTION

Radiocarbon dating measurements are routinely performed using very precise, but large, laboratory-housed AMS systems at high costs and turnaround times of weeks to months. Miniature QMS systems cannot currently resolve the 0.00 1amu difference between the mass of $^{12}C^{16}O^{18}O$ (45.99407 Da) and the target species $^{13}C^{16}O^{16}O$ (45.99307 Da).

New detection and data analysis technologies may theoretically be capable of increasing the resolution of a QMS system enough to resolve these masses and increasing QMS sensitivity to $1:10^{14}$, approximating ^{14}C trace amounts in ancient samples. For example, use of hyperbolic rather than round electrodes can double resolution. Also, ideal hyperbolic fields can be augmented with magnetic fields to improve QMS resolution. Once developed, such a portable system would allow on-site deployment and sample turnaround times of hours, that time depending mostly on pre-treatment protocols.

However, to be considered reliable, this instrument would need to be thoroughly benchmarked. An on-site QMS should first prove that it can detect ^{13}C since the ^{13}C signal is much easier to resolve than ^{14}C on account of the natural abundance of ^{12}C being much higher (~100:1) than the $^{14}C/^{12}C$ ratio. Therefore this study only examines ^{13}C. Comparison to results from well-established AMS and the stable isotope industry standard IRMS systems would help determine the reliability of an on-site QMS prototype. If AMS and IRMS can detect the same patterns that characterize stable ^{13}C isotopes ratios in archaeological and paleontological bone samples, then a reliable QMS prototype should detect those same patterns.

2. METHODS

Small samples (~1.0g) of dinosaur bone fossils were acquired from three repositories for isotope analyses. Five fossils came from the Hell Creek Formation in Montana and two from its equivalent Lance Formation in Wyoming. Two different commercial laboratories performed standard pre-treatments to extract the mineral (bioapatite), organic (collagen), or bulk (organic plus mineral) bone fractions for AMS analysis. Fifteen total ^{13}C results were obtained then analysed for reproducible patterns.

In addition, our 15 results were compared with 67 previously published ^{13}C results from dinosaur teeth excavated from the Hell Creek Formation [1]. We looked for reproducibility between our AMS results and their IRMS results. Results from within-bone fractions were also compared.

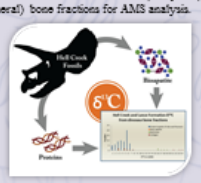

Fig. 1: Overview of 13C pattern detection in dinosaur fossils

3. RESULTS I

Fig. 2: Limb bone fragment of unknown dinosaur taxon in situ at Rose Quarry, Wyoming, shows loose matrix of Lance Formation that resembles Hell Creek lithology.

Similarities in biostratigraphy, lithology, and geologic context equate the Lance Formation to the Hell Formation (HCF), enabling direct stable isotope comparisons from both Formations. We collected $\delta^{13}C$ results, where
$\delta = (R_{sample}/R_{standard}-1)\cdot 1000‰$,
$R = {}^{13}C/{}^{12}C$, and VPDB as the carbon standard.

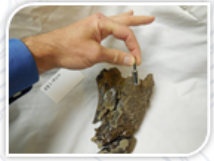

Fig. 3: Diamond-tipped coring bit used to extract sample from clean areas on HCF or Lance dinosaur bones or bone fragments.

Fricke and Pearson (2008) used IRMS to collect $^{13}C/^{12}C$ ratios from over 60 hadrosaur and triceratops teeth collected from the Hell Creek Formation in Montana [1]. We therefore sought fossils from similar geologic settings for AMS stable isotope comparisons. Two dinosaur bone fossils came from a private ranch in Wyoming Lance Formation (Fig 2). Also, Five Hell Creek Formation dinosaur bone fossils were assessed, totaling 15 stable carbon isotope analyses, shown in Table 1.

Specimen	Description, Notes	Laboratory and Sample No.	Bioapatite δ13C ‰	Bulk δ13C ‰	Collagen δ13C ‰	Lab. Number
HCF1	Triceratops femur (collagen)	CDOT 1			-22.1	UCL1318-22134
	Hadrosaurid femur (CO3 collagen)	CDOT 2			-22.1	UCL1318-21927
collagen	Triceratops femur (collagen)	CDOT 3			-22.1	GU-22272
collagen		CDOT 4				
bulk	Hadrosaurid femur (bioapatite)	CDOT 5		-16.4		GU-22273
bulk	Cretaceous Triceratops femur (bulk)	CDOT 6		-17.1		UCL1318-21722
bulk	Triceratops femur (femur, Cretaceous Hadrosaurid femur, bulk)	CDOT 7		-16.6		GU-22267
bulk		CDOT 8		-16.8		GU-22720
bulk	Hadrosaurid femur (bioapatite)	CDOT 9		-16.7		UCL1318-21928
apatite	Triceratops femur	CDOT 10	-7.3			UCL1318-17721
apatite	Hadrosaurid femur (apatite)	CDOT 11	-6.6			UCL1318-21929
apatite	Triceratops femur	MCTRO2	-6.8			UCL1318-17727
apatite	Triceratops femur	CDOT 12	-6.7			UCL1318-17722
apatite	Triceratops femur	CDOT 13	-6.2			UCL1318-17723
apatite	Triceratops femur	MCTRO3	-6.2			UCL1318-17724
apatite	Dinosaur, Jurassic (Bed)	MOR 2007	-5.6			UCL1318-22674
apatite	Ceratopsian rib	MOR 2014	-5.6			UCL1318-22677
		Lowrance	-6.7 ± 0.8		-22.1	

- CDOT - Creekmore Laboratories
- UCL1 - Center for Applied Isotope Studies, University of Georgia

Table 1: δ13C AMS results from seven dinosaur bones from Hell Creek and Lance Formations.

Each of seven bones was submitted to two or three different pre-treatments in order to extract ^{13}C data from two or three separate bone fractions: bioapatite, organic, and bulk bone. All seven yielded bioapatite results, and five gave bulk results. Only three showed enough collagen to analyse. The two Lance Fm. fossils, designated HRS in Table 1, showed slightly higher amounts of ^{13}C than HCF fossils.

4. RESULTS II

The seven AMS results from bone bioapatite were compared to 67 published IRMS results from tooth bioapatite. HCF tooth ^{13}C values range between 1.5 and -9.4 ‰, with a very roughly Gaussian distribution with a mean of -5.1 and mode of -6.1‰. This distribution entirely overlaps the AMS results from bone bioapatite that ranged between -2.4 and -7.24 ‰, with a mean of 4.74 ‰.
Two patterns emerged that any successful QMS instrument should also detect: 1. Dinosaur bioapatites from either bone or teeth should have $\delta^{13}C$ values of -5±5 ‰.
2. Lance and HCF bioapatites should also have $\delta^{13}C$ values of -5±3 ‰.

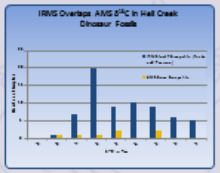

Fig. 4: Comparison between AMS 13C results from bone bioapatite (yellow bars) and IRMS 13C results from tooth bioapatite (blue bars) in HCR and Lance Fm. dinosaurs.

5. RESULTS III

Next, all three bone fractions were compared to each other and to tooth apatite. The first pattern to emerge from these comparisons was a distinct offset between the bioapatite and bulk bone preparations from within the same bones (Fig. 5). Figure 5 includes the 67 tooth apatite results for context. Brackets show the offsets between bioapatite and bulk bone stable carbon ratios. Bioapatite carbon is extracted from bone via CO_2 captured from phosphoric acid pre-treatments [2].

The standard bulk bone extraction includes acetic acid, NaOH, then HCl treatments to capture total organic content. This includes bioapatite plus any original organic residuals. Figure 5 shows the lower end member offset is 11.2 and the maximum is 13.3‰.

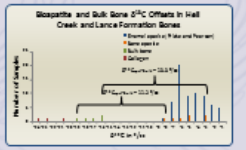

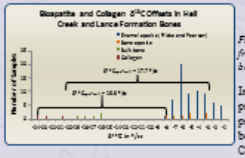

Fig. 6: Stable carbon isotope comparison of three bone fractions plus dinosaur tooth reveals a distinctive offset between bone and tooth bioapatite and bone collagen.

Fig. 5: Stable carbon isotope comparison of three bone fractions plus dinosaur tooth reveals a distinct offset between bone and tooth bioapatite and bulk bone.

In addition to bioapatite and bulk bone preparations, standard collagen extraction protocols use ~2M HCl rinses to demineralize bone, and the rubbery collagen is combusted to CO_2 for AMS analysis. Figure 6 shows the lower end member offset between bone apatite and collagen is 16.6, and the upper is 17.7 ‰.

6. CONCLUSIONS

On-site carbon isotope detection using a portable QMS has the potential to save time and money, as well as to multiply carbon isotope data collection. Concurrent with the development of such a device, a potential benchmarking procedure is under development. To help evaluate future QMS results, we collected stable carbon isotope ratios using AMS from similar paleontological sources that supplied the same data using IRMS.

Our QMS should detect $\delta^{13}C$ patterns in Hell Creek or Lance Formation fossils:

1. Dinosaur bone and tooth bioapatites should reveal a mean of -5±5‰.
2. Within-bone comparison should show an upper end member offset between bioapatite and bulk bone fractions of ~13.3 and a lower end member offset of ~11.2‰.
3. Within-bone comparison should show an upper end member offset between bioapatite and collagen of ~17.7, and a lower end member offset of ~16.6‰. However, only three of seven bones contained enough collagen to make this third pattern.

Radiocarbon and ^{13}C data from valuable archaeological bone, if destructible samples can be procured for QMS analysis, could add another set of patterns to further evaluate the accuracy of an on-site QMS device with enhanced sensitivity that resolves 0.001amu.

REFERENCES

[1] Fricke, H.C. and Pearson, D.A. Stable isotope evidence for changes in dietary niche partitioning among hadrosaurian and ceratopsian dinosaurs of the Hell Creek Formation, North Dakota. Palaeobiology 34,534–552 (2008)
[2] Cherkinsky, Alexander. Can We Get a Good Radiocarbon Age from "Bad Bone"? Determining the Reliability of Radiocarbon Age from Bioapatite. Radiocarbon 51.2,647–655 (2009)

Appendix 6.1 | American Society of Mass Spectrometry (ASMS) Conference poster, June 2016.

Appendix 6.2 | ASMS Conference poster, June 2017.

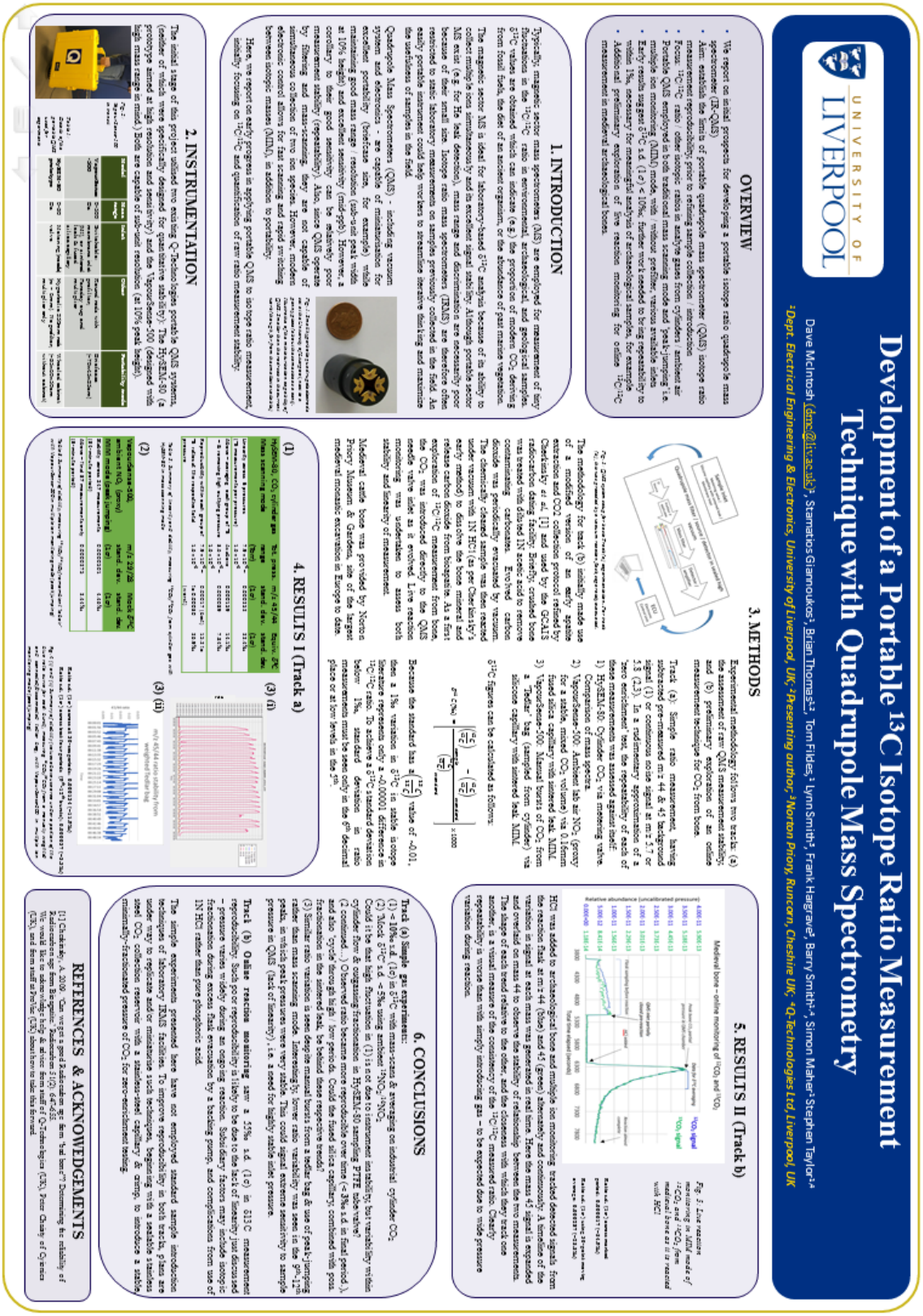

Development of a Portable ^{13}C Isotope Ratio Measurement Technique with Quadrupole Mass Spectrometry

Dave McIntosh (dmc@liv.ac.uk)[1], Stamatios Giannoukos[1], Brian Thomas[1,2], Tom Fildes,[1] Lynn Smith[1], Frank Hargrave[2], Barry Smith[2,4], Simon Maher[1] Stephen Taylor[1,4]

[1]Dept. Electrical Engineering & Electronics, University of Liverpool, UK; [2]Presenting author; [3]Norton Priory, Runcorn, Cheshire UK; [4]Q-Technologies Ltd, Liverpool, UK

OVERVIEW

- We report on initial prospects for developing a portable isotope ratio quadrupole mass spectrometer (IR-QMS)
- Aim: establish the limits of portable quadrupole mass spectrometer (QMS) isotope ratio measurement reproducibility; prior to refining sample collection / introduction
- Focus: $^{13}C/^{12}C$ ratio (other isotopic ratios in analyte gases from cylinders - ambient air
- Portable QMS employed in both traditional mass scanning mode and 'peak-jumping' i.e. multiple ion monitoring (MIM) mode, with 'without prejudice' various available suites
- Early results suggest $\delta^{13}C$ s.d. (1σ) < 10‰; further work needed to bring repeatability to within 1‰, necessary for meaningful analysis of archaeological samples, for example
- Additional preliminary exploration of line reaction monitoring for online $^{13}C/^{12}C$ measurements in modern archaeological bones.

1. INTRODUCTION

Typically, magnetic sector mass spectrometers (MS) are employed for measurement of tiny $\delta^{13}C$ values in the $^{13}C/^{12}C$ ratio in environmental, archaeological, and geological samples. $\delta^{13}C$ values are obtained which can indicate (e.g.) the proportion of modern CO_2 derived from fossil fuels, the diet of an ancient organism, or the abundance of past marine vegetation.

The magnetic sector MS is ideal for laboratory-based $\delta^{13}C$ analysis because of its ability to collect multiple ions simultaneously and its excellent signal stability. Although portable sector MS exist (e.g. for He leak detection), mass range and discrimination are necessarily poor because of their small size. Isotope ratio mass spectrometers (IRMS) are therefore often restricted to static laboratory measurements on samples previously collected in the field. An easily portable instrument could help workers to streamline iterative thinking and maximize the usefulness of samples in the field.

Quadrupole Mass Spectrometers (QMS) - including vacuum system and electronics - are capable of miniaturisation for excellent portability (footprint ~1m, for example) while maintaining good mass range resolution (sub-unit peak width at 10% height) and excellent sensitivity (mid-ppb). However, a corollary to their good sensitivity can be inherently poor measurement stability (repeatability). Also, since QMS operate by filtering and mass-scanning, they are not capable of simultaneous collection of two ion species. However, modern electronic control allows for fast scanning and rapid switching between isotopic masses (MIM), in addition to portability.

Here, we report on early progress in applying portable QMS to isotope ratio measurement, notably focusing on $^{13}C/^{12}C$ and quantification of raw ratio measurement stability.

2. INSTRUMENTATION

The initial stage of this project utilized two existing Q-Technologies portable QMS systems, (neither of which were specifically designed for quantitative stability). The HiSENSE-80 (a prototype aimed at high resolution and sensitivity) and the 'Vapourdense-500' (designed with high mass range in mind.) Both are capable of sub-unit resolution (at 10% peak height).

3. METHODS

Experimental methodology follows two tracks: (a) the assessment of raw QMS measurement stability; and (b) preliminary exploration of an online measurement technique for CO_2 from bone.

Track (a): Sample ratio measurement, having subtracted pre-measured m+1 44 & 45 background signal (1) or continuous noise signal as m+1 7 or 5.5 (2,3). In a rudimentary approximation of a 'zero enrichment' test, the repeatability of each of these measurements was assessed against itself:

1) HiSENSE-80 Cylinder CO_2 via metering valve. Comparison of mass spectra.
2) 'Vapourdense-500' Ambient lab air NO_2 (proxy for a stable, mixed CO_2 volume) via 0.18mm fused silica capillary with sintered leak MIM.
3) 'Vapourdense-500' Manual bursts of CO_2 from a 'Dafter' bag (sampled from cylinder) via silicone capillary with sintered leak MIM.

$\delta^{13}C$ figures can be calculated as follows:

$$\delta^{13}C\,(‰) = \left[\frac{\left(\frac{^{13}C}{^{12}C}\right)_{sample} - \left(\frac{^{13}C}{^{12}C}\right)_{standard}}{\left(\frac{^{13}C}{^{12}C}\right)_{standard}} \right] \times 1000$$

Because the standard has $\left(\frac{^{13}C}{^{12}C}\right)$ value of ~0.01, then a 1‰ variation in $\delta^{13}C$ is stable isotope literature represents only a ~0.000001 difference in $^{13}C/^{12}C$ ratio. To achieve a $\delta^{13}C$ standard deviation below 1‰, standard deviation in ratio measurements must be seen only in the 6th decimal place or at low levels in the 5th.

4. RESULTS I (Track a)

5. RESULTS II (Track b)

Fig. 3: Line reaction monitoring on MIM mode of $^{12}CO_2$ and $^{13}CO_2$ from medieval bone as it is reacted with HCl

HCl was added to archaeological bone and multiple ion monitoring tracked detected signals from the reaction flask at m+1 44 (blue) and 45 (green) alternately and continuously. A timeline of the variation in signal at each mass was generated in real time. Here the mass 45 signal is expanded and overlaid on mass 44 to observe the stability of relationship between the two measurements. The shape of each trend relative to the other, and the closeness with which they track one another, is a visual measure of the consistency of the $^{13}C/^{12}C$ measured ratio. Clearly repeatability is worse than with simply introducing gas – to be expected due to wide pressure variation during reaction.

6. CONCLUSIONS

Track (a) Simple gas experiments:
(1) ~10‰ s.d. (1σ) in $\delta^{13}C$ with mass-scans & averaging on industrial cylinder CO_2
(2) Mock $\delta^{13}C$ s.d. <5‰ using ambient $^{14}NO_2$:$^{15}NO_2$
Could it be that high fluctuation in (1) is not due to instrument instability but variability within cylinder flow & outgassing fractionation in HiSENS-80 sampling PTFE tube-valve?
(2 continued...) Observed ratio became more reproducible over time (< 3‰ s.d. in final period.), and also 'cycle through high / low periods. Could the fused silica capillary, combined with post fractionation in the sintered leak, be behind these evaporative trends?
(3) Similar ratio variation is seen despite manual bursts from a Dafter bag & use of peak-jumping rather than mass scanning mode. Interestingly, lower ratio variability was seen in the ^{13}C-12^{12}C peaks, in which peak pressures were very stable. This could signal extreme sensitivity to sample pressure in QMS (lack of linearity), i.e. a need for highly stable inlet pressure.

Track (b) Online reaction monitoring saw a 55‰ s.d. (1σ) in $\delta^{13}C$ measurement reproducibility. Such poor reproducibility is likely to be due to the lack of linearity just discussed – pressure varies widely during an ongoing reaction. Subsidiary factors may include isotopic fractionation during excess flask evacuation by a backing pump, and complications from use of 1N HCl rather than pure phosphoric acid.

The sample experiments presented here have not employed standard sample introduction technologies of laboratory IRMS facilities. To improve reproducibility in both tracks, plans are under way to replicate and/or miniaturise such technologies, beginning with a sensible stainless steel CO_2 collection reservoir with a stainless-steel capillary & crimp, to introduce a stable, moderately-fractionated pressure of CO_2 for zero-enrichment testing.

REFERENCES & ACKNOWLEDGEMENTS

[1] Chakraborty, A 2008 "Can we get a good Radiocarbon age from 'old bone'?" Determining the reliability of Radiocarbon age from Biogenetic." Radiocarbon 50(2), 647-660.

We would like to acknowledge help & advice from staff of Q-Technologies (UK), Peter Chaney of Cytecs (UK), and from staff at Pet/Cat (UK) about how to take this forward.

Chapter 7: Radiocarbon

Contents

Figures

Table

Radiocarbon but not carbon dating

The present thesis centers on the characterisation of endogenous collagen in archaeological bone and the contested question of endogenous collagen in fossil bone (or other biomineralised material like tooth or shell). Most chapters have dealt directly with collagen. The prior and current chapters (6 and 7) deal with the broader question of general preservation quality with the idea that higher preservation quality samples should have a higher likelihood of collagen preservation. Accordingly, carbon isotopes from both the organic (collagen) and inorganic (bioapatite) bone fractions were counted and considered. The prior chapter (6) presented $\delta^{13}C$ results with emphasis on Mesozoic specimens, with the conclusion that the ratios represent a large degree of paleobiological as opposed to diagenetic values. The current chapter (7) presents ^{14}C results in a second indirect effort to explore links between isotope ratios and the likelihood of collagen preservation in ancient bone.

^{14}C data are usually obtained for the purpose of precise radiocarbon age determinations in archaeological contexts. However, an alternative purpose was noted in chapter 6. Very precise AMS determinations of carbon isotopes were needed to benchmark the precision of similar measurements taken with a portable mass spectrometer (QMS) under development for the purpose of a field deployable device to obtain isotope measurements. AMS results yielded ^{14}C as well as ^{13}C data for the sample set under investigation.

Thus, rather than temporal constraints, the main purpose herein concerns isotopic patterns that may relate to the degree of diagenesis versus preservation in ancient bone. As a result, discussions omit certain details found in most radiocarbon-related literature, like chronological error bars and calibrations. Instead focus is placed on broad trends with bearing on the degree to which isotopic signals are primary versus secondary. In

particular, proteinaceous signatures identified by FTIR, and more specifically collagenous signatures identified by SHG imaging, plus ^{13}C patterns show general consistency with the hypothesis that some Mesozoic bone samples retain endogenous materials including proteins, as is consistent with the abundant literature reviewed in Chapter 1. Independent of these observations, ^{14}C trends could also verify or contradict this hypothesis.

43 radiocarbon results were gathered from prior projects or newly obtained from 22 archaeological or paleontological bone samples, plus three controls, using six commercial laboratories. An emphasis was placed on carbon isotope analysis of dinosaur bone samples for two reasons. First, these were available in more abundance than archaeological samples. Last, dinosaur collagen is the most controversial and thus deserved the most attention. Table 7.1 displays basic radiocarbon results according to bone fraction, and Table 7.2 below lists each laboratory sample number. It excludes error bars and ignores calibrated versus uncalibrated results for the reasons noted above. It reports results in percent modern carbon (pMC). This relates to radiocarbon years (C years) via:

$$pmC = 100 * 0.5^{C-yrs/5568}$$

5,568 refers to Willard Libby's original radiocarbon half-life. 1960 measurements supplied the more accurate value of 5,730, but for consistency's sake the original Libby estimate (some labs round it to 5,570) has been used by convention to calculate percent modern carbon.[1] ''Modern'' is defined as 95% of the radiocarbon concentration in AD 1950 of NBS Oxalic Acid I (SRM 4990B) normalized to $\delta^{13}C_{VPDB}$ = -19 per mil. After AD 1950, so-called bomb carbon from nuclear testing increased atmospheric radiocarbon via neutron release, thus increasing the ^{14}C ratios in the biosphere. A half-life correction was applied during calibration for age determinations of most of the Medieval and Roman Era material, since it had been radiocarbon dated to answer questions of chronological

Identifier	Description	bulk pMC	apatite pMC	collagen pMC
NP77_109_34	Bovid radius		89.8	89.0
NP77_109_34	Bovid radius		87.8	88.1
NP77_109_5	Bovid femur			94.6
NP77_109_5	Bovid tibia			93.1
NP77_109_5	Bovid tibia			93.1
NP71_12_9	*H. sapiens* ulna			90.1
NP73_34_81	*H. sapiens* rib			92.0
XA102_2001/307a	*Sus* metatarsal & rib			77.4
XA102_2001/98b	*Sus* jaw & ischium			77.4
EHRC90001	Camelid		28.2	22.3
EHRC90002	*Megatherium sp.*		8.24	<collagen
CM00088	Stegosaurid	1.03	6.61	
CM21728	*Diplodocus longus*	0.71	3.52	
CM00094	*Diplodocus longus*		1.12	<collagen
HRS08267	Dinosaur		0.57	<collagen
HRS19114	*Lambeosaurus sp.*		1.64	<collagen
GDFM12.001a	*Triceratops horridus* horn	1.53	0.61	
HCTH06 (GDFM12.001b)	"		0.88	
GDFM03.001	*Triceratops horridus* femur		2.08	
"	"		4.83	2.16
"	" (Beta)	1.38		
GDFM08.011	*Triceratops horridus* femur		0.76	2.36
GDFM04.001	Hadrosaurid femur		5.72	5.59
"	"	4.36	4.09	
"	" (Beta)	6.17		
EHRC90004	*Mucrospirifer profundus*	>0.30		
GDFM03.001	Matrix (*Triceratops*)	8.48		
GDFM04.001	Humics (Hadrosaurid)	72.7		
"	Concretion (")	78.5		

Table 7.1 | Radiocarbon results. "<collagen" indicates that the sample contained insufficient collagen for radiocarbon age determination. ">" indicates an infinite carbon age, where the sample pmC overlaps that of the machine blank. "(Beta)" refers to the original beta-counting method of radiocarbon dating, not AMS.

placement. These results, recorded in Table 7.1, appear as calibrated years (cal BP). Mesozoic samples appear uncalibrated, since the present purposes do not require age determination. Some commercial laboratories present results both in pMC and radiocarbon years, but others just radiocarbon years (and sometimes in calibrated radiocarbon years). The above formula was used to convert C years to pMC where pMC was not provided, and thus complete the data set for Table 7.1. All results in Table 7.1 were corrected for fractionation (called normalization) using the measured $^{13}C/^{12}C$ ratios. This calculation subtracts fractionation effects that occur when different biological materials deposit various ratios of heavy versus light carbon isotopes.

Results from collagen fractions of GDFM03.001, GDFM08.011, and GDFM04.001 were the least expected because they do not follow the generalised concept of fossilization, diagrammed in Fig. 7.1. Rather than large-scale infilling, spongy bone within the dinosaur samples analysed herein had porous cavities, as various figures in Chapter 2 revealed. Thus, although secondary mineralisation may have occurred, it did not manifest at a macroscopic scale in the sampled Mesozoic material. Fig. 7.1, taken from Keenan, 2016, also illustrates loss of organics[2]. However, results throughout this thesis demonstrate conclusively that although perhaps most fossils have experienced this loss, at least some have not. The three exceptional samples noted here contradict the diagrammed process, and thus deserve exploration and explanation.

In the process of collecting the results shown in Table 7.1, several strategies were implemented to evaluate the degree of primary signal in carbon isotopes, especially in Mesozoic samples. First, ^{14}C was isolated from the bioapatite fraction of a medieval bone (NP77_109_34) in order to compare it with the collagen fraction of the same bones, and to compare these within-bone similarities to the same fraction preparations from two ice age

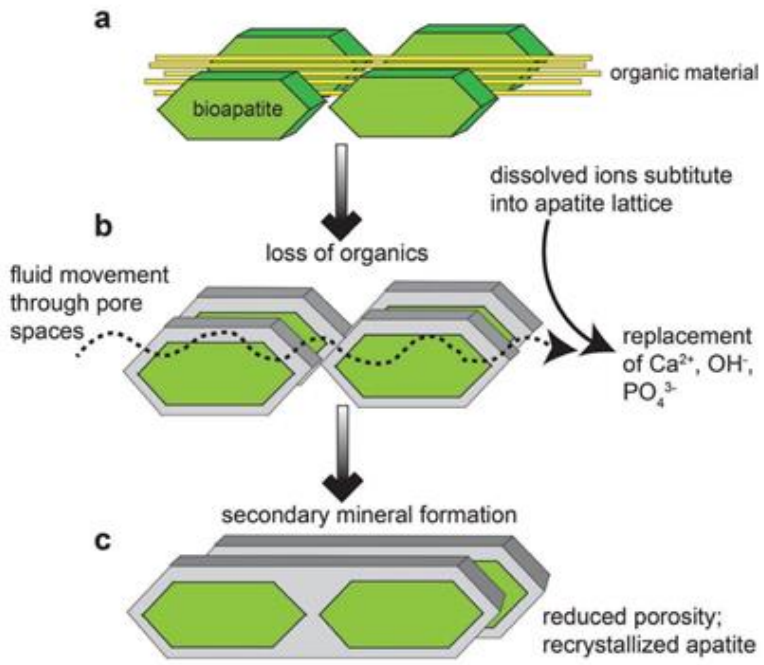

Fig. 7.1 | Illustration of bone diagenesis. From Keenan (2016) **a**, In vivo, collagen matrix (yellow stripes) binds bioapatite crystallites (green). **b**, After burial, the organic matrix biodegrades or chemically decays. This opens pore spaces to permit fluid movement, which can dissolve or redeposit minerals. **c**, Secondary mineralisation decreases porosity.

(EHRC90001, EHRC90002) and three Mesozoic (GDFM03.001, GDFM04.001, GDFM08.011) samples. Second, NP77_109_34 collagen and bioapatite were re-tested for radiocarbon using a different laboratory to evaluate consistency of results between measurements and laboratories. Third, Cretaceous specimens GDFM03.001 and GDFM04.001 were analysed by multiple labs and using three fractionation protocols as tests for exogenous radiocarbon sourcing. Next, the submission forms for Mesozoic samples, did not identify taxa, and listed “Pleistocene” as the expected age. Otherwise, modern AMS laboratories might refuse material this old. Fifth, brachiopod shells (EHRC90004, Devonian) were obtained for this study upon the discovery that modern brachiopods use collagen as the organic binding component of their carbonate shell

biomineral.[3] However, the standard radiocarbon preparation for shell resembles a bulk bone preparation, described below, instead of collagen extraction. Finally, three controls were submitted for analysis. Sedimentary matrix (Hell Creek Fm. sandy material described in Chapter 2) that surrounded the outer bone surface of GDFM03.001, and an iron-rich concretion directly adhered to the outer bone surface of GDFM04.001. Carbon isotope analysis of the humic acid extract (described below) was also obtained for GDFM04.001.

Lab #	**Identifier**	**Description**	**pMC**
UGAMS-17385	NP77_109_34	Bovid radius	89.8
QUBC-24093	NP77_109_34	"	89.0
QUBC-24091	NP77_109_34	"	87.8
UGAMS-20473	NP71_109_5	"	840
QUBC-24092	NP77_109_5	Bovid femur	94.6
QUBC-24093	NP77_109_5	Bovid tibia	93.1
Beta-368271	NP77_109_5	"	93.1
Beta-425286	NP71_12_9	*H. sapiens* ulna	90.1
Beta-425288	NP73_34_81	*H. sapiens* rib	660
Poz-22846	XA102_2001/307a	*S. scrofa* metatarsal & rib	77.4
Poz-22871	XA102_2001/98b	*Sus* jaw & ischium	77.4
UGAMS-20474	EHRC90001	Camelid	28.2
AA-106299	EHRC90001	"	22.3
UGAMS-20475	EHRC90002	*Megatherium sp.*	8.24
AA106302	EHRC90002	"	<coll
UGAMS-13302a	CM00088	Stegosaurid	6.61
UGAMS-13302b	CM00088	"	1.03
UGAMS-13303a	CM21728	*D. longus*	3.52
UGAMS-13303b	"	"	0.71
UGAMS-20478	CM00094	*D. longus*	1.12
UGAMS-41490	HRS08267	Dinosaur	0.57
AA-106301	HRS08267	Dinosaur	<coll

UGAMS-20477	HRS19114	*Lambeosaurus sp*	1.64
AA-106300	HRS19114	*Lambeosaurus sp*	<coll
UGAMS-11752	GDFM12.001a	*T. horridus* horn	1.53
UGAMS-11752a	"	"	0.61
UGAMS-17387	GDFM12.001b	"	0.88
UGAMS-17386	GDFM03.001	*T. horridus* femur	2.08
UGAMS-04793a	"	"	4.83
GX-32372	"	"	2.16
GX-32647	"	" (Beta)	1.38
UGAMS-03228a	GDFM08.011	*T. horridus* femur	0.76
UGAMS-03228b	"	"	2.36
GX-32739	GDFM04.001	Hadrosaurid femur	5.72
UGAMS-01937	"	"	5.59
UGAMS-01936	"	"	4.36
UGAMS-01935	"	"	4.09
GX-32739	"	" (Beta)	6.17
AA-108983	EHRC90004	*M. profundus*	>0.30
UGAMS-02444	GDFM03.001	Matrix (*T. horridus*)	8.48
UGAMS-01938	GDFM04.001	Humics (Hadrosaurid)	72.7
GX-31950	"	Concretion (")	78.5

Table 7.2 | Sample numbers and descriptions. UGAMS (Center for Applied Isotope Studies, University of Georgia, GA, USA), QUBC (Queen's University Belfast (CHRONO), Ireland), Beta (Beta Analytic, FL, USA), Poz (Poznan Radiocarbon Laboratory, Poland), GX (Geochron Laboratories, MA, USA), AA (University of Arizona AMS, AZ, USA).

Preparation of three bone fractions

Bioapatite was one of three bone fractions isolated for ^{14}C analysis. Bioapatite includes the carbonate (CO_3) fraction of bone, which generally comprises 0.6% to 0.75% of total bone bioapatite. Carbonate displaces some phosphate in bone hydroxyapatite during a creature's lifetime. The standard procedure of bone bioapatite preparation for ^{14}C analysis uses a dilute solution of acetic acid under vacuum to remove the superficial,

diagenetic CO_3. Then, the CO_3 fraction from bone bioapatite is dissolved in the much stronger but dilute hydrochloric acid and collected as CO_2 under vacuum. The CO_2 is then processed in the usual method (AMS) to obtain carbon isotope analysis. The superficial, diagenetic CO_3 can also be collected under vacuum and carbon-dated (C dated). "This approach confirms that CO_3 in calcined bone is very resistant to post-burial isotopic exchange and is the most reliable source of inorganic carbon for ^{14}C dating regardless of the environmental conditions," according to *Radiocarbon Dating of Biological Apatites*[4]. One experiment with long-submerged archaeological bone showed no detectable carbonate exchange with bioapatite, suggesting that with proper cleaning, even ancient bone provides an appropriate source of carbon for both radioisotope and stable isotope studies. As with collagen, the oldest C age of bioapatite is considered to represent the more precise age for the original carbon formed during the lifetime of the once-living animal.

Collagen was another of three bone fractions isolated for ^{14}C analysis. It is a large, insoluble, fibrous protein integral to metazoan connective, epithelial, and muscular tissues. The modified Longin method by Arslanov[5] and Sullivan[6] was used in attempts to extract collagen from dinosaur bones. Three of six attempts did retrieve collagen, but the percent weight for all three was below three—insufficient for radiocarbon age determinations, but sufficient to confirm its presence. The typical extraction protocol combines two methods of purification. Briefly, the bones were mechanically cleaned, then pulverized and treated at between 4°C and 6°C by two to three fresh solutions of 0.5-1.0 N Hydrochloric acid (HCl) for a few days (depending on preservation condition) until mineral components completely dissolved, leaving collagen protein. Respective RC labs then washed the collagen in distilled water until calcium and other minerals were no longer visible, added 0.1 N NaOH at room temperature for 24 hours, rewashed it, and

added weak HCl solution (pH = 3) at 80°C–90°C for six to eight hours. Humic acid residue was then separated from the gelatin solution by centrifugation, and the solution was evaporated. Benzene was synthesized from the dried gelatin by burning in a "bomb" or by dry pyrolysis. The purpose of the benzene is to compact the carbon, which in benzene is 92%. Thus, the collagen was purified by acid washing and by burning. Using this method, Arslanov et al. carbon dated bones that ranged in age from 20,620 ± 300 to 31,150 ± 400 RC ybp, results that partially overlap the current data set.[5] This procedure is commonly used today because it gives the oldest RC ages for collagen intrinsic to the bone. Typically, the older age determination from multiple fractions of the same bone is considered the most accurate, and the collagen fraction usually contains the lowest ^{14}C fraction.

"Bulk organics" refer to insoluble organics like collagen, plus the biomineral bone fraction. Secondary organics called humic acids include alkali-soluble material plus water-soluble contaminants. Humics are removed by standard Acid-Base-Acid (ABA, elsewhere Acid-Alkali-Acid, AAA) pretreatment as outlined above. Once the humics are removed, carbon is collected from a combination of the remaining bone organics and inorganics (bulk). The base (B) or alkali removes taphonomic or diagenetic humic acids, for example from surrounding soil or matrix. This pretreatment can be shown to effectively remove soil contaminants by precipitating the humic acids for separate AMS determinations. The large offset between any Mesozoic bone fraction (Average pMC from Table 7.1 = 2.75) and the pretreatment humic acid filtrate from GDFM04001 (72.7, Table 7.1) revealed the secondary sourcing of humic acid carbon, as well as the certain removal of humics during sample preparation. However, the high humic acid pMC value suggests that even very small inefficiencies in humic acid removal could affect ^{14}C ratios in any of the three bone fractionation techniques. Therefore other observations were made

to search for modern humic acid contamination of Mesozoic materials, described below. In the preparation of all three fractions, stringent sample processing removed externally associated ^{14}C sources. There are three logical sources for the detected ^{14}C: The original animal, secondary ^{14}C that became intrinsic to the crystalline sample material, or more likely a combination of these two.

Anomalous radiocarbon in the literature

Even traces of ^{14}C as shown in Tables 7.1 and 7.2 are not expected from fossils. Therefore a literature search was undertaken for precedents. Surprisingly, similar-looking results have been published from carbonaceous earth materials including fossils. Several materials presumed as carbon-dead have been routinely tested in searches for machine blanks, but they consistently show pMC values well within the detection limits of modern AMS devices, which are sensitive to one ^{14}C atom per 10^{15} total carbon atoms, or ~0.01pMC[7]. These include anthracite with detectable ^{14}C[8,9]. Marble has a history of ^{14}C detection[10,11], as does graphite from various sources[12,13]. Attempts to find carbon-dead sources in diamond also yielded ^{14}C[14]. Such data are routinely attributed to contamination or in situ nuclear synthesis, although neither scenario adequately accounts for the geologic depth or geographic breadth of relevant results. For example, contamination should be isolated (rare) and not ubiquitous like it appears to be. Also, rates of in situ nuclear synthesis are orders of magnitude lower than what would be required to generate the observed ^{14}C in earth materials[15].

Radiocarbon from fossils includes a larch wood section brought to the surface by oil drilling from 183 m depth at Prudhow Bay that showed >43,300 C years[11]. The collagen fraction then 2N HCl treatment of *Coelodonta antiquitatais* (wooly rhinoceros) collected in 1929 from Ukraine, extracted using pretreatments of benzene and ethyl alcohol to

remove preservatives, yielded 23,235 ± 775 RC years when tested by scintillation counting in 1972[10]. Standard radiocarbon methods have also been applied to other ice age fossil bones, including mammoths[16], saber tooth tigers[17], giant bison[18], and a dire wolf[16]. All contained detectable levels. Much older fossil material includes cortical bone from a mosasaur fossil found in Belgium chalk beds with a pMC of 4.68 (~24,600 C years)[19]. Standard acid-base-acid (ABA) pre-treating to remove contaminants such as calcite and humic acid were applied, making contamination an unlikely carbon source for this mosasaur as well as for other published examples. If the standard preparations do not remove sufficient secondary carbon from these materials, then nor should they remove sufficient secondary carbon from the untold numbers of carbon-dated artefacts. The mosasaur team tentatively attributed part of their result to cyanobacteria on the bone surface. However, they detected too few microbes to account for the obtained results. Even if cyanobacteria were present, their ^{14}C levels should reflect the levels within the bones upon which they feed.

^{14}C in foraminifera from sea cores proved a challenge for Nadeau et al (2001) to interpret[20]. The authors suggested "ubiquitous contamination" as a possible source for the more than 100 unexpectedly high ^{14}C levels they measured. Fossil wood with 0.16[21] and another wood sample with 0.16 pMC[22] add to the list. Finally, possibly the oldest fossiliferous ^{14}C was detected in the chitin fraction of a Cambrian sponge *Vauxia gracilenta*, at 0.57 pMC[23]. In much the same way that a robust body of published scientific literature supports the conclusion that original biochemistry persists in fossils, published radiocarbon results support the possibility that ^{14}C may also persist in some fossils.

pMC per era

Fig. 7.2 shows ^{14}C results of the total bone collection arranged in order of largest to smallest pMC. They conform to age constraints known via Medieval, Roman Era, and ice age burial contexts, but show a much smaller than expected gap between ice age and Mesozoic contexts. They also fail to distinguish between Cretaceous and Jurassic results. Therefore attention was given to interpret the enigmatic Mesozoic results. This included a search for sources of contamination, summarised in Table 7.3 below.

Searching in-bone for contamination

Carbon dating multiple fractions of the same sample helps evaluate the reliability of age determinations. Large differences between the collagen and apatite fractions are taken to indicate contamination[24]. Typically for samples with large ^{14}C offsets between fractions, the oldest fraction is claimed to be correct, and the youngest rejected on suspicion of incorporating some measure of modern carbon. However, this tendency is reversed in some cases where the older age contradicts contextual interpretations[25]. Thus, there seems to be no objective means to discern between addition of modern carbon into only one fraction versus subtraction of ancient radiocarbon from one fraction or the other. This lack of objectivity leaves open the logical possibility (though not often invoked in radiocarbon literature) that the younger of two fractions is closer to the age since deposition, and that the older of the two fractions has experienced ^{14}C leaching. Table 7.3 summarizes differences in ^{14}C measurements from inorganic and organic components.

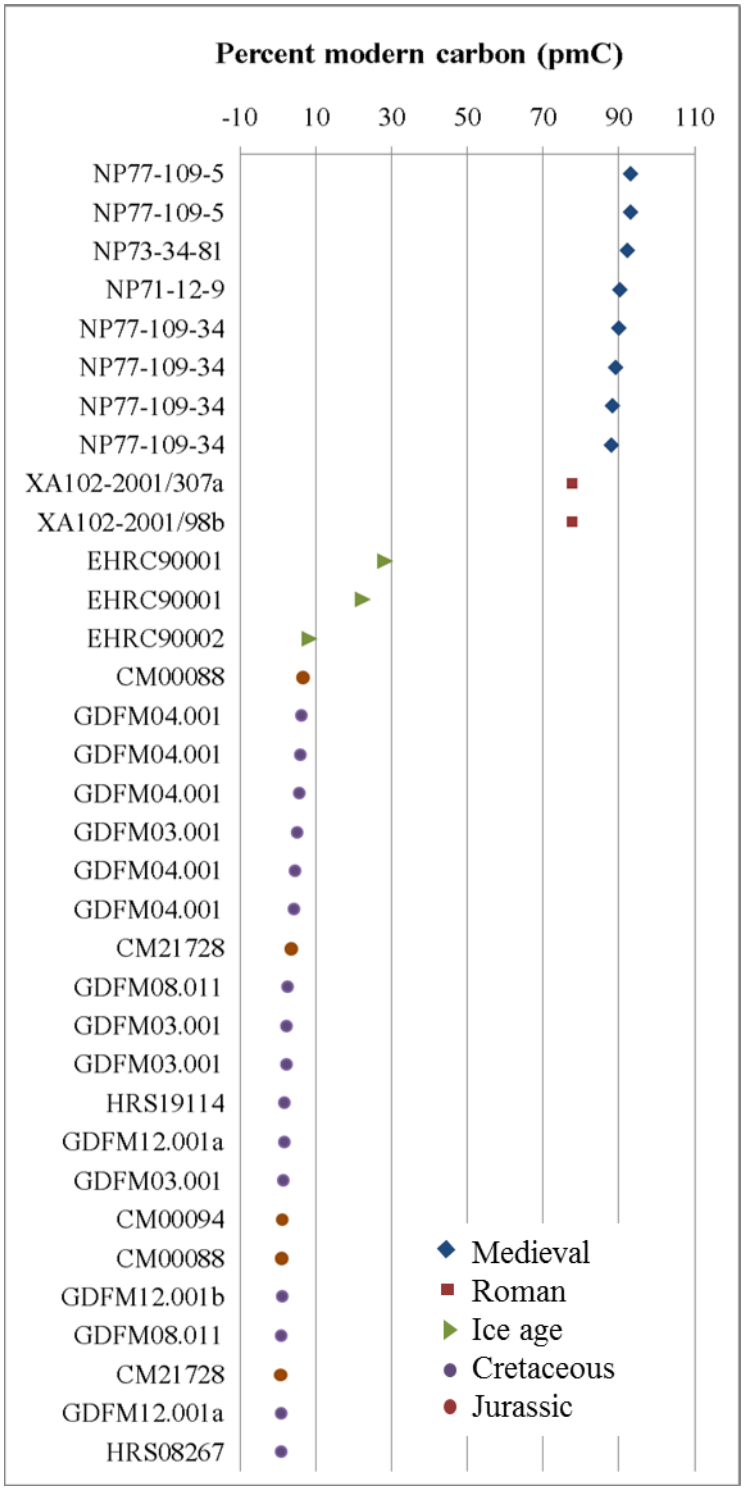

Fig. 7.2 | 14C results per sample arranged according to pMC.

Table 7.3 results suggest a trend of increasing differences between bone fraction with age of sample, except for GDFM04.001. It shows an even greater similarity between fractions than the Medieval material. Additional data may reveal a trend, but these six samples

Identifier	pMC apatite	pMC collagen	Absolute difference	Percent difference
NP77_109_34	89.8	89.0	0.80	8
NP77_109_34	87.8	88.1	0.30	3
EHRC90001	28.2	22.3	5.90	21
GDFM03.001	4.83	2.16	2.67	45
GDFM08.011	0.76	2.16	1.40	65
GDFM04.001	5.72	5.59	0.13	2

Table 7.3 | Differences between bioapatite and collagen bone fractions.

show no consistent pattern. Even if offsets increase with time since burial, that does not mean that either or both bone fractions represent contamination. Bone fraction ^{14}C differences point to some kind, but do not identify what kind, of diagenetic alteration of isotopes. If one were to think more highly of radiocarbon age determinations for samples with smaller differences between bone fractions, then the GDFM04.001 result would score the highest. One argument in favor of the primary origin of at least a majority of the measured Mesozoic ^{14}C comes from the first isolations of dinosaur collagen for isotope analysis in GDFM03.001, GDFM04.001, and GDFM08.011. The collagen fraction is considered to be the 'gold standard' for radiocarbon age determinations in archaeological contexts.

Fig. 7.3 is a plot of only the Mesozoic material by pMC, similar to Fig. 7.2, and identifies the bone fraction tested for each sample. No particular fraction groups at any position along the pMC continuum. Instead, the various fractions distribute somewhat randomly. If the apatite fraction preferentially incorporated secondary, recent carbon, then bioapatite results should congregate nearer the top right of Fig. 7.3. Instead, bioapatite results span the range of measured values. This matches the findings of Zazzo and Saliège, who evaluated a large archaeological sample set of bone and tooth fractions. The present data appear to confirm the conclusion that their result "confirms that carbonate in calcined bone is very resistant to post-burial isotopic exchange and is the

most reliable source of inorganic carbon for ^{14}C dating regardless of the environmental conditions[4].”

Searching for contamination elsewhere

Exogenous carbon sourcing would diminish the case that prior chapters have built for endogenous biochemistry and isotopes in ancient bone. Some pMC differences between bone fractions suggest inconsistencies, but do not identify them. Therefore alternative signals or sources of secondary carbon incorporation were considered. Table 7.4 lists 15 possible sources of contamination and an evaluation for each.

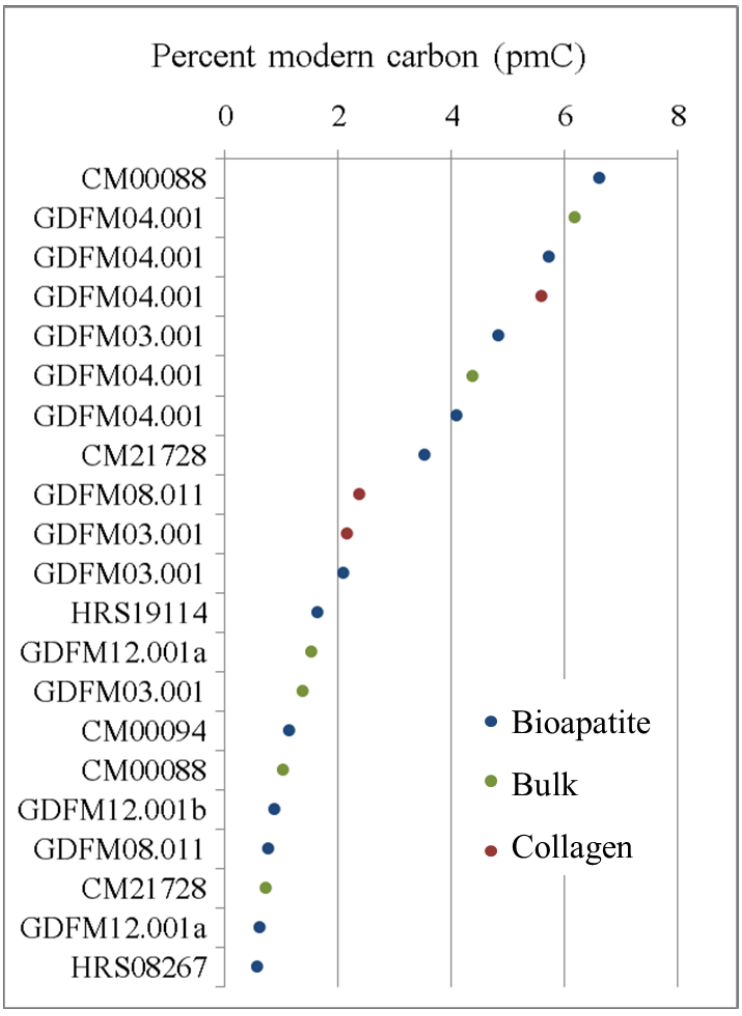

Fig. 7.3 | Mesozoic ^{14}C results arranged according to pMC and bone fraction.

Possible Contaminants a	**Pretreatments And/or Alternate Tests Performed**	**Contaminant Detected**
Young burial carbonate **b**	Hot dilute acetic acid under vacuum **h**	None
Old burial carbonate	Hot dilute acetic acid under vacuum	None
Young humic acid **c**	Hot dilute acid-base-acid (ABA) **i**	None
Old humic acid	Hot dilute acid-base-acid (ABA)	None
Collagen impurities	Test other bone fractions for reproducibility and/or test for ^{14}C in extracted precipitate from alkaline liquid **j**	None
In-situ bone carbonate	After removal of burial carbonate the bone sample is treated in dilute HCl under vacuum to collect CO_2 for ^{14}C testing **k**	None
Cluster decay of U & Th generate ^{14}C from N in collagen **d**	Analysis for U and Th showed only ppm U and Th in bones that contained small amounts of collagen (Appendix 7.1). **l**	None
Incomplete removal of contaminants **e**	Reproducibility across multiple labs and between bone fractions **m**	None
Shellac type preservatives on museum bones **f**	Refluxing in a mix of two hot organic solvents until discolorations dissipate followed by ABA etc. removes both shellac, clue and PVC coatings **n**	None
Reservoir effect causing possible old ages **g**	Source of dinosaur nutrition unknown, therefore the ^{14}C ages are considered the oldest possible ages; Reservoir effect far too small	None
Bacteria and fungus	Microbes completely and routinely removed by ABA pretreatment; bacteria would be the same age as their food source **o**	None
^{14}C signature an artifact of low sample size	General concordance between 21 separate pMC results	None
^{14}C signatures an artifact of geological or geographical province	pMC concordance between dinosaur material from 3 divergent geographical and geological provinces from the Western US	None
^{14}C signatures an artifact of sample location within or upon fossil	Age concordance between samples collected from a variety of locations within bone samples	None
^{14}C signature an artifact of faulty or outdated detection technique	Age concordance between samples tested by AMS sensitive to 40ka, AMS sensitive to 60ka, and Beta counting technologies	None
Isotopic exchange	All methods indirect: comparison of ^{13}C ratios or pMC differences in bone fractions	Some possible

Table 7.4 | Preliminary evaluation of secondary ^{14}C sourcing. a. Bone fragments to be tested for ^{14}C content are first crushed to mm-sized particles before pretreatments designed to remove contaminants. **b**. Young or old carbonates can adsorb onto bone microsurfaces during burial and are removed from surfaces by dilute acetic acid isolates the primary fossil carbonate. **c**. Young or old humic acids from new or old vegetation are routinely and effectively removed by alkali (base) dissolution. When total organics including collagen is fractionated, that portion of the bone sample is treated with dilute HCl to remove both bone burial and in situ carbonate. Collagen is extracted by the Arslenov method discussed in text. If the collagen is not a golden color or the percent of collagen is very low or non-existent, as in most dinosaur bones, then other portions of the bone are extracted for total organics and/or in-situ biological carbonate for ^{14}C content testing

to ensure reproducibility and reliability. **d**. U decay cross sections are far too low to produce even 1pMC. For Uranium's beta decay to have supplied the detected levels of ^{14}C shown in Table 7.1, the majority of each fossil and its surroundings would have to have been composed of U. **e**. Incomplete removal of organic contaminants could result in ages approximating thousands of years, but testing at five different labs and three separate bone fractions, yielding a relatively tight range of (6.61 pMC (21830 C years) to 0.57 (41490 C years), is inconsistent with incomplete removal of organics as a contaminating source. **f**. Shellac type preservatives, if present, could yield a much younger C age if tested in place of bone. However, visual inspection and deliberate avoidance of sample surfaces mitigate this option. **g**. The reservoir effect inflates ^{14}C ages, as evidenced by living plants with pMC's below 7, from absorbing old carbon. **h**. Acid dissolution of adsorbed carbonates were employed by all labs. **i**. ABA pretreatment was used when total bone organics or whole bone was to be C dated. **j**. Collagen was extracted using the conventional Arslenov method with the resultant collagen weighed and then tested when available, as for GDFM03.001, GDFM04.001, and GDFM08.011. Also a general concordance was observed between bioapatite and collagen fractions (Fig. 7.3). **k**. Primary carbonate was extracted with strong but dilute HCl under vacuum after acetic acid pretreatment to remove burial carbonate. Intrinsic contamination would yield wide-ranging pMC's, thus the reproducibility of the data set appears more consistent with the hypothesis of primary ^{14}C. **l**. Cluster decay, if U and/or T are present in large amounts, could transmutate N in collagen to ^{14}C only by greatly exaggerating either the uranium decay rates or available quantities of uranium. However, concentrations from Hell Creek Fm., Montana were far too low, at 0.020 mg/kg for U and 0.078 mg/kg for T (Appendix 7.1). **m**. Incomplete removal of contaminants is refuted by reproducibility of similar age ranges from 9 different dinosaurs plus a published Cretaceous mosasaur result. **n**. Shellac-type protective coatings could skew radiocarbon results. Thus two samples were specially treated to test for contamination via preservatives. Hot, organic solvent pre-treatments were applied to CM00088, which was collected in the early 20th century, as well as to an exterior sample from GDFM08.011, which had a modern paleontological PVC-based coating. The results were indistinguishable from other bone fractions. **o.** Microbes, postulated as a possible source of the 24,600 carbon year age for the mosasaur from Belgium would have been removed by the ABA pretreatment noted in that report[19].

Of the options considered and tested, only uniform, intrinsic contamination by isotopic exchange may help explain the presence of radiocarbon in the sample set. However, as argued above and shown in Fig. 7.4 below, the uniformity of pMC values across samples makes isotopic exchange difficult to defend as a means to incorporate recent carbon into very old bone. In particular, such exchange must have occurred before the secondary radiocarbon decayed. The relatively large difference between fractions in certain samples, and the large $\delta^{13}C$ offsets shown in Chapter 6 do suggest that some degree of isotopic exchange has possibly occurred. However, the present data do not

demand taphonomies with isotopic exchange. Even assuming enough isotopic exchange to decrease confidence in age determinations from these pMC results, it becomes difficult to imagine enough, exchanged recently enough, to supply all the ^{14}C required to produce these results.

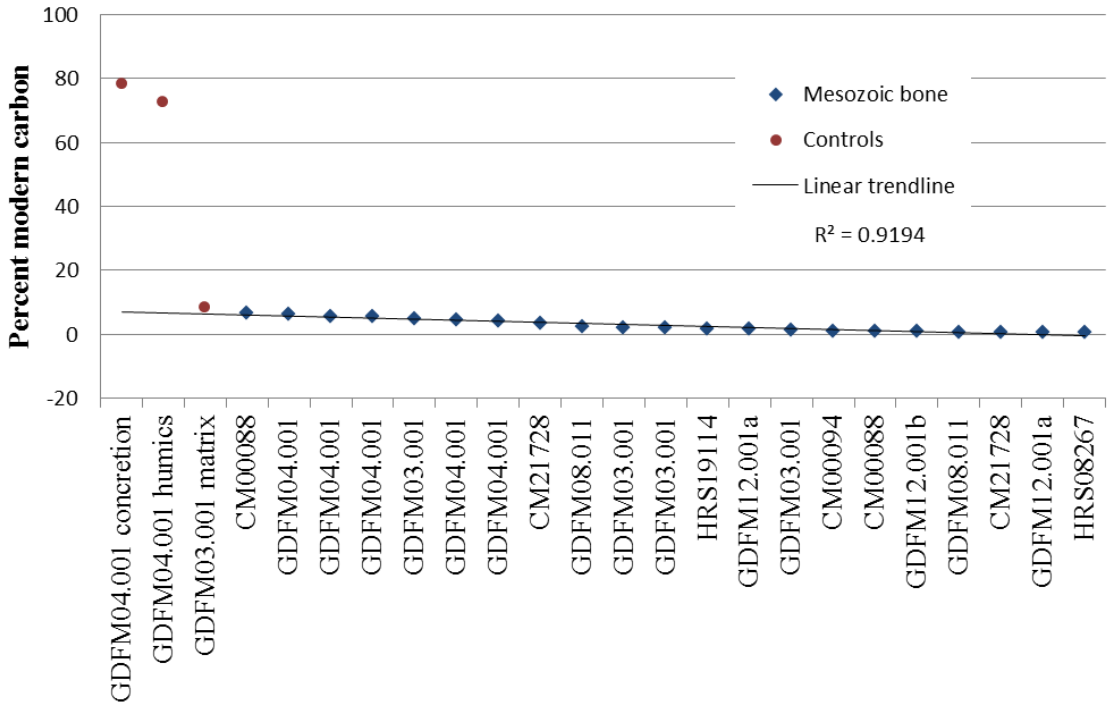

Fig 7.4 | A trendline separates Mesozoic ^{14}C results from known contaminants.

Fig. 7.4 includes a linear trend that intersects, at the displayed magnification, all the Mesozoic bone samples and none of the controls. One would expect on the basis of bone material leaching outward from the bone into its surroundings that the concretion adhered to the outer bone surfaces would have a pMC value more similar to the bones than that of the matrix. Humic acid extract gave a relatively much higher pMC of 72.7, showing that the 21 results from any of three bone fractions are much lower than humic acids. Overall, the noticeable difference between the pMC values of controls and the

trendline suggest a qualitative difference between the fossil bone materials and their surroundings. Further data are required to confirm this trend. If validated, a trendline such as this could be used to identify outliers as spurious.

Field-deployable radiocarbon detection?

The original research aim involved development of a field-deployable QMS device with both the sensitivity to detect those extremely rare ^{14}C atoms, and the precision (reproducibility) required for useful isotope data collection on-site. Although QMS modeling suggested these as theoretical possibilities of ^{14}C measurement from evolved CO_2, the goal has not been achieved so far in a real-world instrument. Isotopic ^{14}C is present in evolved CO_2 from pre-cleaned oxidized bones along with other isotopic combinations of C (^{12}C, ^{13}C and ^{14}C) and O (^{18}O and ^{16}O). However $^{14}CO_2$ is masked by other mass spectrometric peaks (isotopologues) which occur at the same nominal mass. The interfering peaks (e.g. $^{12}C^{18}O^{16}O$) completely swallow the much smaller $^{14}C^{16}O^{16}O$ peak even with improved electronic control. To measure the $^{14}C^{16}O^{16}O$ independently requires extremely high resolution and sensitivity which are not currently possible in a portable instrument. In the process of discovering what apparently cannot be done, the present AMS results were collected as benchmarks in case the QMS developed according to its theoretical potential. Once the large gap between theory and practice became clear, the AMS data set was analysed on its own merits to produce this chapter.

Conclusions

43 pMC results from known provenances showed expected decreases for Medieval, Roman era, and ice age samples, but failed to show the expected step-downs to Cretaceous and Jurassic fossils. Data collection from Cenozoic fossils, which span the

temporal gap between Mesozoic and Pleistocene strata, could shed light on this phenomenon. To that end, collaboration is currently under development to procure Cenozoic material from a remarkably well-preserved site on Ellesmere Island, Canada. The literature search revealed previously published radiocarbon in carboniferous material including fossils from Mesozoic and earlier deposits. This showed that although unexpected, the present data already have precedents.

The first detectable pMC results from dinosaur collagen are presented. A survey of six collagen versus apatite pMC differences suggested that some Mesozoic material has experienced a degree of isotopic alteration. However, literature review revealed that this test does not objectively identify which, if any, fraction represents primary isotopic data and which, if any, fraction represents isotopic alteration. Next, 21 pMC values from nine Mesozoic bone samples sorted by three bone fractions (collagen, apatite, and bulk) showed a largely randomised distribution that does not confirm the expectation that isotopic alteration would affect one fraction more than another. Finally, a linear trendline intersects all Mesozoic bone material, but none of the three control materials at the resolution displayed. This both commends primary Mesozoic ^{14}C and shows potential as a diagnostic tool to discern between primary and secondary pMC measurements.

Taken together, all these results are most consistent with the hypothesis that ^{14}C in Mesozoic and possibly older materials represent a combination of primary and secondary sources, with the caveat that no known cause of secondary sourcing stands out. Further testing, perhaps by additional sampling or improved analytical strategies, will be helpful to verify this hypothesis.

1 Godwin, H. Half-life of radiocarbon. *Nature* **195**, 984-984 (1962).
2 Keenan, S. W. From bone to fossil: A review of the diagenesis of bioapatite. *American Mineralogist* **101**, 1943-1951 (2016).
3 Jope, M. Brachiopod shell proteins: their functions and taxonomic significance. *American Zoologist* **17**, 133-140 (1977).

4 Zazzo, A. & Saliège, J.-F. Radiocarbon dating of biological apatites: a review. *Palaeogeography, Palaeoclimatology, Palaeoecology* **310**, 52-61 (2011).
5 Arslanov, K. A., Svezhentsev, Y.S. An improved method for radiocarbon dating fossil bones. *Radiocarbon* **3**, 387-391 (1993).
6 Sullivan, C. H. & Krueger, H. W. Carbon isotope analysis of separate chemical phases in modern and fossil bone. *Nature* **292**, 333 (1981).
7 Holloway, C. A new world of biomedical research-the Center for Accelerator Mass Spectrometry. *Science and Technology Review* (1997).
8 Grootes, P. M., Stuiver, M., Farwell, G. W., Leach, D. D. & Schmidt, F. H. Radiocarbon dating with the University of Washington accelerator mass spectrometry system. *Radiocarbon* **28**, 237-245 (1986).
9 Beukens, R. P., Gurfinkel, D. M. & Lee, H. W. Progress at the IsoTrace radiocarbon facility. *Radiocarbon* **28**, 229-236 (1986).
10 Stuckenrath, R. & Mielke, J. E. Smithsonian Institution radiocarbon measurements VII. *Radiocarbon* **14**, 401-412 (1972).
11 Stuckenrath, R. & Mielke, J. E. Smithsonian Institution radiocarbon measurements VIII. *Radiocarbon* **15**, 388-424 (1973).
12 Arnold, M., Bard, E., Maurice, P., Valladas, H. & Duplessy, J. C. 14 C Dating with the Gif-sur-Yvette Tandetron Accelerator: Status Report and Study of Isotopic Fractionation in the Sputter Ion Source. *Radiocarbon* **31**, 284-291 (1989).
13 Vogel, J. S., Nelson, D. & Southon, J. R. 14 C background levels in an accelerator mass spectrometry system. *Radiocarbon* **29**, 323-333 (1987).
14 Taylor, R. & Southon, J. Use of natural diamonds to monitor 14C AMS instrument backgrounds. *Nuclear Instruments and Methods in Physics Research Section B: Beam Interactions with Materials and Atoms* **259**, 282-287 (2007).
15 Zito, R., Donahue, D. J., Davis, S. N., Bentley, H. W. & Fritz, P. Possible subsurface production of carbon-14. *Geophysical Research Letters* **7**, 235-238 (1980).
16 Vasil'Chuk, Y., Punning, J.-M. & Vasil'Chuk, A. Radiocarbon ages of mammoths in Northern Eurasia: implications for population development and Late Quaternary environment. *Radiocarbon* **39**, 1-18 (1997).
17 Berger, R., Horney, A. G. & Libby, W. Radiocarbon dating of bone and shell from their organic components. *Science* **144**, 995-1001 (1964).
18 Harington, C. & Morlan, R. E. Evidence for human modification of a Late Pleistocene bison (Bison sp.) bone from the Klondike District, Yukon Territory, Canada. *Arctic*, 143-147 (2002).
19 Lindgren, J. *et al.* Microspectroscopic evidence of cretaceous bone proteins. *PLoS One* **6**, e19445, doi:10.1371/journal.pone.0019445 (2011).
20 Nadeau, M.-J. *et al.* Carbonate 14 C background: does it have multiple personalities? *Radiocarbon* **43**, 169-176 (2001).
21 Kirner, D. L., Burky, R., Taylor, R. & Southon, J. R. Radiocarbon dating organic residues at the microgram level. *Nuclear instruments & methods in physics research. Section B, Beam interactions with materials and atoms* **123**, 214-217 (1997).
22 Gulliksen, S. & Thomsen, M. S. Examination of background contamination levels for gas counting and AMS target preparation in Trondheim. *Radiocarbon* **34**, 312-317 (1992).
23 Ehrlich, H. *et al.* Discovery of 505-million-year old chitin in the basal demosponge Vauxia gracilenta. *Sci Rep* **3**, 3497, doi:10.1038/srep03497 (2013).
24 Grootes, P. M., Nadeau, M.-J. & Rieck, A. 14C-AMS at the Leibniz-Labor: radiometric dating and isotope research. *Nuclear Instruments and Methods in Physics Research Section B: Beam Interactions with Materials and Atoms* **223**, 55-61 (2004).
25 Cherkinsky, A. Can we get a good radiocarbon age from “bad bone”? Determining the reliability of radiocarbon age from bioapatite. *Radiocarbon* **51**, 647-655 (2009).

Appendix 7.1 | Elemental analysis of GDFM03.001 and GDFM04.001

TestAmerica

THE LEADER IN ENVIRONMENTAL TESTING

ANALYTICAL REPORT

TestAmerica Laboratories, Inc.
TestAmerica St. Louis
13715 Rider Trail North
Earth City, MO 63045
Tel: (314)298-8566

TestAmerica Job ID: 160-350-1
Client Project/Site: Bone Sample

For:
H. R. Miller
1215 Bryson ROad
Columbus, Ohio 43224-2009

Attn: Mr. Hugh R Miller

Authorized for release by:
8/6/2012 5:43:24 PM

Ivan Vania
Project Manager I
ivan.vania@testamericainc.com

LINKS

Review your project results through TotalAccess

Have a Question? Ask The Expert

Visit us at: www.testamericainc.com

This report has been electronically signed and authorized by the signatory. Electronic signature is intended to be the legally binding equivalent of a traditionally handwritten signature.

Results relate only to the items tested and the sample(s) as received by the laboratory.

Login Sample Receipt Checklist

Client: H. R. Miller

Job Number: 160-350-1

Login Number: 350
List Number: 1
Creator: Daniels, Brian

List Source: TestAmerica St. Louis

Question	Answer	Comment
Radioactivity either was not measured or, if measured, is at or below background	True	
The cooler's custody seal, if present, is intact.	True	
The cooler or samples do not appear to have been compromised or tampered with.	True	
Samples were received on ice.	True	
Cooler Temperature is acceptable.	True	Received ambient
Cooler Temperature is recorded.	True	
COC is present.	False	
COC is filled out in ink and legible.	N/A	
COC is filled out with all pertinent information.	N/A	
Is the Field Sampler's name present on COC?	N/A	
There are no discrepancies between the sample IDs on the containers and the COC.	N/A	
Samples are received within Holding Time.	True	
Sample containers have legible labels.	True	
Containers are not broken or leaking.	True	
Sample collection date/times are provided.	False	
Appropriate sample containers are used.	True	
Sample bottles are completely filled.	True	
Sample Preservation Verified.	True	
There is sufficient vol. for all requested analyses, incl. any requested MS/MSDs	True	
VOA sample vials do not have headspace or bubble is <6mm (1/4") in diameter.	N/A	
Multiphasic samples are not present.	True	
Samples do not require splitting or compositing.	True	
Residual Chlorine Checked.	N/A	

Detection Summary

Client: H. R. Miller
Project/Site: Bone Sample

TestAmerica Job ID: 160-350-1

Client Sample ID: TRICERATOPS #1 FEAUR — Lab Sample ID: 160-350-1

Analyte	Result	Qualifier	RL	MDL	Unit	Dil Fac	D	Method	Prep Type
Lead	1.3		0.30	0.10	mg/Kg	2		6020A	Total/NA
Silver	0.16	J B	0.20	0.014	mg/Kg	2		6020A	Total/NA
Aluminum	93		12	4.2	mg/Kg	5		6020A	Total/NA
Arsenic	9.4		1.0	0.20	mg/Kg	2		6020A	Total/NA
Barium	2900	B	20	0.57	mg/Kg	20		6020A	Total/NA
Beryllium	18	^	0.10	0.017	mg/Kg	2		6020A	Total/NA
Calcium	320000		1200	140	mg/Kg	50		6020A	Total/NA
Cadmium	0.070		0.050	0.016	mg/Kg	2		6020A	Total/NA
Cobalt	23		0.20	0.043	mg/Kg	2		6020A	Total/NA
Chromium	7.0		2.5	1.1	mg/Kg	5		6020A	Total/NA
Iron	9100		5.0	3.3	mg/Kg	2		6020A	Total/NA
Potassium	42		25	7.5	mg/Kg	5		6020A	Total/NA
Magnesium	860		120	9.5	mg/Kg	5		6020A	Total/NA
Manganese	1300		1.2	0.18	mg/Kg	5		6020A	Total/NA
Sodium	4100		50	17	mg/Kg	5		6020A	Total/NA
Nickel	49		0.50	0.082	mg/Kg	2		6020A	Total/NA
Selenium	0.28	J	0.50	0.16	mg/Kg	2		6020A	Total/NA
Thorium	0.12	J	0.20	0.078	mg/Kg	2		6020A	Total/NA
Thallium	0.92		0.20	0.10	mg/Kg	2		6020A	Total/NA
Uranium	12		0.10	0.020	mg/Kg	2		6020A	Total/NA
Vanadium	8.3		2.5	1.8	mg/Kg	5		6020A	Total/NA
Zinc	61		5.0	1.3	mg/Kg	2		6020A	Total/NA
Boron	12	J	25	8.3	mg/Kg	5		6020A	Total/NA

Client Sample ID: HADROSAUR #2 BADLANS — Lab Sample ID: 160-350-2

Analyte	Result	Qualifier	RL	MDL	Unit	Dil Fac	D	Method	Prep Type
Lead	1.7		0.30	0.10	mg/Kg	2		6020A	Total/NA
Silver	0.13	J B	0.20	0.014	mg/Kg	2		6020A	Total/NA
Aluminum	640		12	4.2	mg/Kg	5		6020A	Total/NA
Arsenic	3.9		1.0	0.20	mg/Kg	2		6020A	Total/NA
Barium	2900	B	20	0.57	mg/Kg	20		6020A	Total/NA
Beryllium	19	^	0.10	0.017	mg/Kg	2		6020A	Total/NA
Calcium	320000		1200	140	mg/Kg	50		6020A	Total/NA
Cadmium	0.16		0.050	0.016	mg/Kg	2		6020A	Total/NA
Cobalt	19		0.20	0.043	mg/Kg	2		6020A	Total/NA
Chromium	7.3		2.5	1.1	mg/Kg	5		6020A	Total/NA
Iron	7300		5.0	3.3	mg/Kg	2		6020A	Total/NA
Potassium	100		25	7.5	mg/Kg	5		6020A	Total/NA
Magnesium	960		120	9.5	mg/Kg	5		6020A	Total/NA
Manganese	1600		1.2	0.18	mg/Kg	5		6020A	Total/NA
Sodium	4600		50	17	mg/Kg	5		6020A	Total/NA
Nickel	33		0.50	0.082	mg/Kg	2		6020A	Total/NA
Selenium	8.2		0.50	0.16	mg/Kg	2		6020A	Total/NA
Thorium	0.92		0.20	0.078	mg/Kg	2		6020A	Total/NA
Thallium	0.52		0.20	0.10	mg/Kg	2		6020A	Total/NA
Uranium	9.3		0.10	0.020	mg/Kg	2		6020A	Total/NA
Vanadium	7.7		2.5	1.8	mg/Kg	5		6020A	Total/NA
Zinc	46		5.0	1.3	mg/Kg	2		6020A	Total/NA
Boron	14	J	25	8.3	mg/Kg	5		6020A	Total/NA

Chapter 8: Suggestions for further work and conclusions

Contents

Figures

Appendix

The status of ancient bone collagen studies

How ancient can bone proteins get? The literature review in Chapter 1 found no temporal boundary, as various reports describe primary organics in fossils collected from representatives of most geologic systems, including the Precambrian. The trend of slowly but recently increasing numbers of publications shown in Fig. 1.1 suggests that future research may add those remaining three Systems to the list. How broadly do ancient bone proteins extend across earth? Fig. 1.2 showed that of the seven continents, only two have not yet divulged fossils with original biochemistry. The widespread geography of fossil biochemicals suggests that with resource allocation it may only be a matter of time until fossil biochemistry is found on all continents.

Of over a dozen techniques noted in Table 1.2, none has yet emerged as a widely accessible, standardised test to confirm bone collagen in ancient and especially fossil samples, and several are partially or wholly destructive to the sample. Therefore, the goal of this research was to explore inexpensive, user-friendly, broadly accepted, minimally-invasive, and minimally-destructive techniques that could facilitate future searches into the geologic and geographic extent of primary organics in the fossil record.

However, techniques do no good without adequate records and appropriate sample availability. Thus, chapter 2 described the core principles behind cataloging bone (and in principle any ancient) samples and brought together the disparate provenances of the three dozen bones loaned to the University of Liverpool for this project. In addition, a stable retrieval system that includes an accession or other catalog number to be identified in peer reviewed articles must be traceable to and retrievable from a permanent repository. More samples are entering this ongoing project, and other relationships have been initiated with recognised, permanent collection caretakers who foresee the value of

novel technologies like SHG, spectroscopic, or isotopic analyses to explore primary organics in ancient bone.

Progress and challenges: SHG imaging

Chapter 3 made progress toward the establishment of SHG imaging as a novel and revealing technique that targets bone collagen fibres. SHG fills a niche as a useful tool for biomedical research, but had never before been applied to ancient bone. Therefore four independent techniques were used to test if the SHG signals revealed in ancient and fossil bone correspond to bone collagen remnants: FTIR, Raman spectroscopy, collagen extraction for radiocarbon dating, and collagen extraction and sequencing of a medieval human rib that had also been imaged with SHG. The results were published in the journal *Bone Reports* and support the conclusion that SHG detects bone collagen remnants in archaeological and ice age samples.

In addition, paleontological samples were imaged in attempts to evaluate the literature that supports the contentious concept of collagen preservation in fossil bone. Results from both Mesozoic and ice age samples revealed that most but not all samples within the collection showed collagen traces, although faint and few. Thus, chapter 3 includes the first SHG images of dinosaur bone collagen signals in situ. Because collagen signals were so faint in the oldest bone samples, a technique was developed to generate bone surface images of the same area as SHG images. Resulting composite images provide context for trace SHG signals and could provide a basis for the use of SHG to quantify collagen in bone, including collagen loss from bone in decay experiments, e.g., Chapter 5. Chapter 3 also showed that SHG imaging is sensitive enough to capture collagen remnants in samples that yield too little collagen from extraction protocols aimed at isotope analyses. Therefore, in addition to providing new information on the 2-D

and 3-D structure of decayed bone collagen, SHG has potential as a screening tool that could efficiently detect bone collagen in samples of interest.

One weakness of SHG imaging is that it relies on a large, expensive, and uncommon device. This limits its applicability to broad fields such as archaeology or paleontology. A next logical step would involve the development of a portable SHG microscope for on-site bone collagen assessment.

Another weakness of SHG is that it interacts only with highly structural collagen fibres. Different approaches would be required to analyse smaller collagenous remnants like collagen subunits. For example, a matrix-assisted laser desorption ionisation (MALDI) Orbi-Trap mass spectrometer generates an ion image of a specified area of a sample surface. It has not been used on ancient or fossil bone, and offers at least three benefits. First, it could provide an independent verification of the specific distribution pattern of collagen on a particular bone sample surface, for example patterns revealed in SHG images. Second, it would precisely identify small molecules on the bone surface like collagen subunits and collagenous breakdown products. Last, the high sensitivity (>1ppm) of OrbiTrap detectors suggests that a MALDI OrbiTrap could map even smaller collagenous remnants than the collagen fibres that SHG visualizes, and detect even smaller concentrations. It would thus nondestructively help verify SHG imaging results of ancient bone collagen while providing new insights on bone protein decay in situ.

SHG imaging is also limited in its depth of penetration beneath the sample surface. Although micro-computed tomography (Micro CT) does not detect organics, it does map density differences within deep bone. Micro-computed tomography imaging uses X-rays to penetrate beneath sample surfaces to nondestructively image deep within a sample. As such, it can assess the general degree of permineralisation of a fossil bone. It can also specify the degree of permineralisation in small, internal regions or microregions of a

single bone sample. Such small regions should be considered likely zones of preservation that offer higher chances of containing original organics assuming a low temperature history for the bone. If density patterns correlate with likelihood of organic preservation, then micro CT scans could help identify regions for further exploration, including internal pockets of preservation in what would otherwise appear to be a fully mineralised bone.

Progress and challenges: Infrared spectroscopy

Infrared spectroscopy, including FTIR and Raman, are attractive to ancient bone research because of their low cost, ease of use, low sample destruction requirements, and because they can target very specific chemical bonds in situ. A particularly useful module for FTIR called Attenuated Total Reflectance (ATR) interfaces with finely powderised material. Its application to ancient bone collagen found use through the collagen-specific carbonyl-to-apatite peak ratio as recently established for forensic analysis of bone. Results in Chapter 5 confirmed that ATR-IR can quantitatively assess amide carbonyl bond content in artificially decayed bone.

FTIR was applied to several dozen ancient bone samples to assess its usefulness in detecting collagen remnants. Results described in Chapter 4 showed a general trend, as expected, of smaller CO/P ratios for older bones. However, the ATR-IR results from ancient bone were too scattered to plot a statistically significant collagen decay curve. Later, it was learned that crystallinity of the sample affects FTIR peak heights (and positions) and thus any ratios based on them. Protocol systematisation promises to open a door to obtaining a more informative curve by effectively normalising the contribution of crystallinity to ancient bone spectra. Chapter 5 included such a protocol to show the novel application of FTIR to precisely assess bone collagen in artificial decay experiments.

Although these two IR techniques can confirm the presence of amide bonds in a sample via the amide carbonyl, they share a weakness in their inability to identify specific proteinaceous sources. MALDI OrbiTrap would address this by identifying specific ionised proteinaceous biomaterials.

Neither infrared spectroscopy nor SHG imaging can effectively assess bone samples or regions within a bone most likely to preserve primary protein. Energy-dispersive X-ray spectroscopy (EDS) examines the distribution of elements at various points of an exposed bone surface. EDS can identify the elemental composition of original bone mineral, as opposed to secondary mineralisation, to explore general bone contexts that suggest likelihood of original bone protein preservation. It has been used as an independent verification of molecular techniques, and could be used to verify the spectroscopic, microscopic, and spectrometric techniques used in this thesis. In addition, the elemental mapping potential of EDS would more comprehensively establish the composition of the sample material.

Progress and challenges: Isotope analysis

Isotopic techniques were used to approach ancient bone collagen indirectly. $^{13}C/^{12}C$ ratios co-occur in geologic formations and archaeological settings that yield collagen remnants in bone. Analysis of AMS-based stable carbon isotope patterns in dinosaur bone samples led to two deductions. First, their range of values generally corresponded to those published for dinosaur teeth. This suggested that both teeth and bone from the Hell Creek Fm. may retain some or all original isotope values. Second, comparison of the $\delta^{13}C$ offset between organic and mineral bone fractions was equivocal; i.e., larger than in natural, modern biological bone as though it includes a portion of secondary isotope content, and yet consistently patterned as though it includes all or mostly primary isotope content. One

weakness of stable isotope analysis is its dependence on laboratory-bound instruments. Progress toward a field-deployable quadrupole mass spectrometer with sufficient resolution for isotope analysis was made within our Mass Spectrometry Group, as described in Appendix 6.2.

Finally, analysis of unstable carbon isotopes gathered from the various catalogued bones within the present collection provided two key results. First, ^{14}C was found in amounts far above the AMS theoretical detection threshold and high enough above background levels to assign finite carbon age estimates to 21 Mesozoic samples. Last, Chapter 7 reported ^{14}C results obtained directly from dinosaur bone collagen extracts. This was consistent with the many published descriptions of Mesozoic collagen as well as the first SHG images of collagenous remnants in Cretaceous bone as per Chapter 3. It remains possible that some of the detected ^{14}C was secondary, although none of a dozen or so possible sources of contamination were found to reasonably account for the results.

Initial results: MALDI-OrbiTrap

MALDI uses a soft-ionisation process whereby a sample is dissolved in or mixed with an appropriate chemical matrix. Laser ablation ionizes the uppermost molecules of the sample surface. Its soft ionisation can help preserve the integrity of labile, ancient proteins as they travel through the instrument. Internal vacuum pressure plus electric fields direct the ions toward the OrbiTrap, which separates and detects the milieu of ions within each sampling. The density of sample spots and total coverage of the rastered area can be adjusted to optimise efficiency of data collection.

Initial MALDI results were gathered from eight bones of various settings before the device, housed at the Laboratory of Imaging Mass Spectrometry at The University of North Texas (UNT), lost operability. Matrix was added to the surface of bone thinsection.

Each slice was affixed to the sample plate for mass imaging. Figure 8.1 shows a preliminary result. The output can profile the total ions in the imaged area or selected mass ranges. However, ion fragmentation was not performed, yet fragmentation patterns are required for precise chemical identification. Once the instrument is back online, future attempts to use it on ancient bone must include a fragmentation protocol, as well as expertise on interpreting fractionation patterns in mass spectra. MALDI OrbiTrap mass imaging has the potential to characterise protein remnants in situ, for direct comparison of collagen distribution revealed by SHG images of the same bone surfaces. Future use of MALDI OrbiTrap on ancient bone should both verify the collagenous remnants detected either directly or indirectly using other techniques, and reveal different, smaller, vertebrate-specific molecular remnants.

Initial Results: Micro CT Imaging

In micro CT imaging, density differences are mapped onto planar images captured from several rotated angles. Software renders these into 3D images that reveal internal morphologies. Figure 8.2 shows initial results using a Bruker benchtop micro CT scanner to produce digital cutaway segments of *Triceratops* femur GDFM03.001 and hadrosaur femur GDFM04.001. The dinosaur samples share many morphological characters of modern and medieval bone (data not shown), but also differences. Both bone sources share generalised patterns of bone trabecular spacing and a higher density of cortical bone. However, the dinosaur bone trabecular spaces were less regular in size, and contained small regions of higher density shown in blue in Fig. 8.2. These likely resulted from partial permineralisation within bone pore spaces. Considering the identification of traces of endogenous collagen in these samples using collagen extraction, FTIR, and SHG imaging, a preliminary observation follows that some molecular preservation occurs even

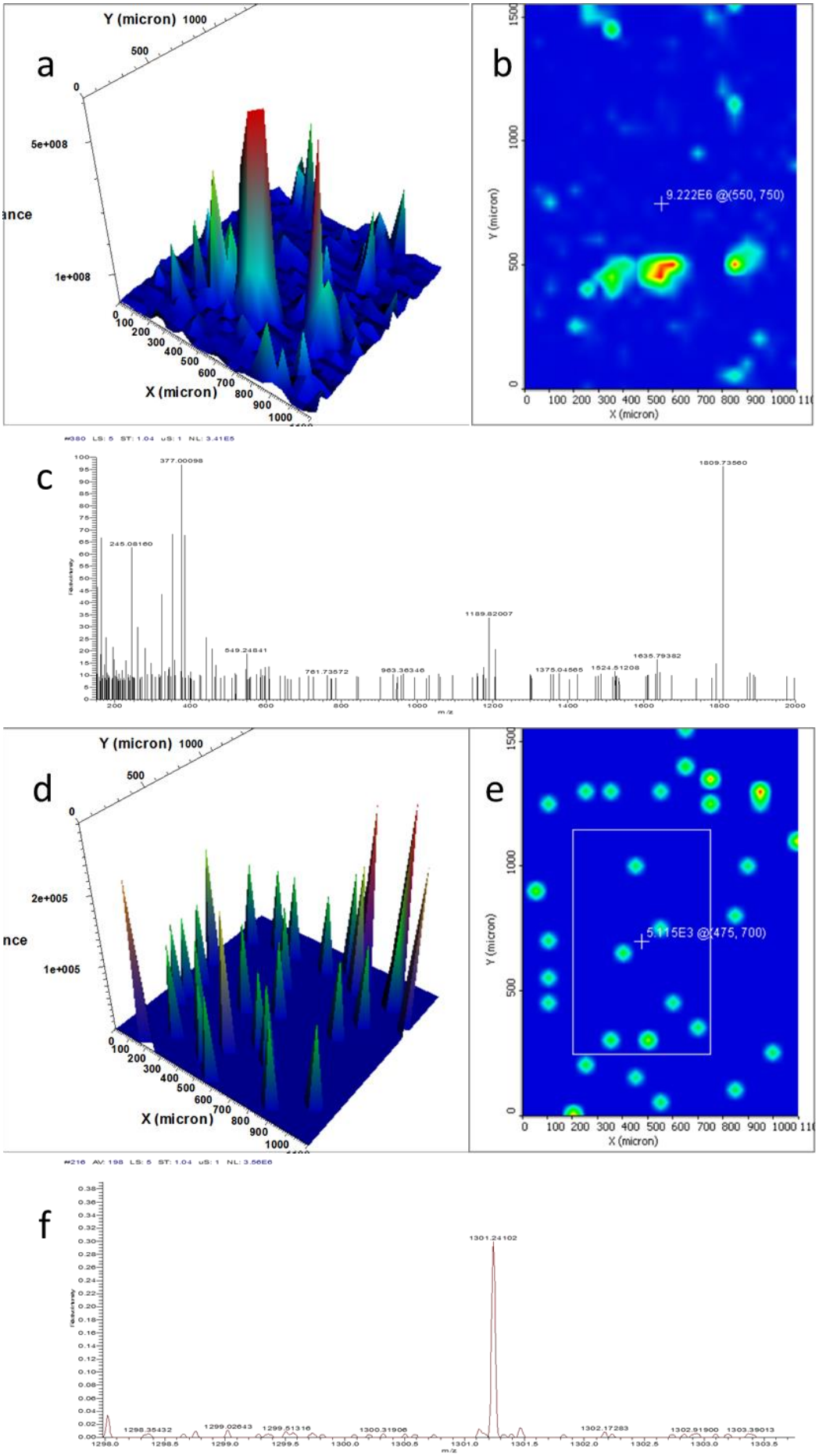
a
Y (micron) 1000
500
0
5e+008
1e+008
X (micron)
b
9.222E6 @(550, 750)
Y (micron)
X (micron)
c
377.00098
1809.73560
245.08160
1189.82007
549.24841
761.73572
963.36346
1375.04565
1524.51208
1635.79382
d
Y (micron) 1000
2e+005
1e+005
X (micron)
e
5.115E3 @(475, 700)
Y (micron)
X (micron)
f
1301.24102
1298.35432
1299.02643
1299.51316
1300.31906
1302.17283
1302.91900
1303.39013

Fig. 8.1 | MALDI OrbiTrap mass spectrometric imaging of medieval human bone surface. Data offer proof of concept that MALDI OrbiTrap can provide novel information of ancient bone surfaces. **a-c**, Total ion count (TIC) from *H. sapiens* rib NP73_34_81, Sk101. **d-f**, Mass 1302 from same sample. **a**, 3D distribution of TIC across the 1 mm^2 sampled bone surface. **b**, 2D distribution of TIC across sampled bone surface **c**, M/Z spectrum from cursor point shown in **b**. **d**, 3D distribution of mass 1302 across 1 mm^2 bone surface. **e**, 2D distribution of mass 1302 across the same bone surface. **f**, M/Z spectrum over the boxed area shown in **e**.

in bones that exhibit the partial permineralisation that Fig. 8.2 indicates. Further work with all these techniques on additional samples would be required to explore possible factors, for example depositional settings, contributing to the preservation of organics.

Initial results: EDS

With EDS, typically an X-ray beam excites electrons within various elements in the sample. Electrons that fall to lower-energy shells emit characteristic X-ray spectra. Figure 8.3 shows a portion of some initial EDS results obtained from the outer surface of *Edmontosaurus* specimen GDFM18.001 excavated in 2017. Houston Electron Microscopy was contracted to examine the specimen, and Figure 8.3 images were clipped from their resulting pdf file. It verified the presence of elements consistent with the mineral accretions expected from long burial. However, other points along the bone surface revealed the presence and proportions of elements very similar to biological bone, including calcium, phosphorus, oxygen, and carbon. This result was consistent with the FTIR spectrum of GDFM18.001, shown in Fig. 4.7, which generally aligned with modern bone. If EDS merely distinguishes between biomineral and secondary mineralisation, then FTIR would be a much more cost effective technique to investigate that same question. However, it appears that EDS could help identify regions within a bone sample that contain element ratios consistent with fresh bone and thus more likely to preserve primary organics.

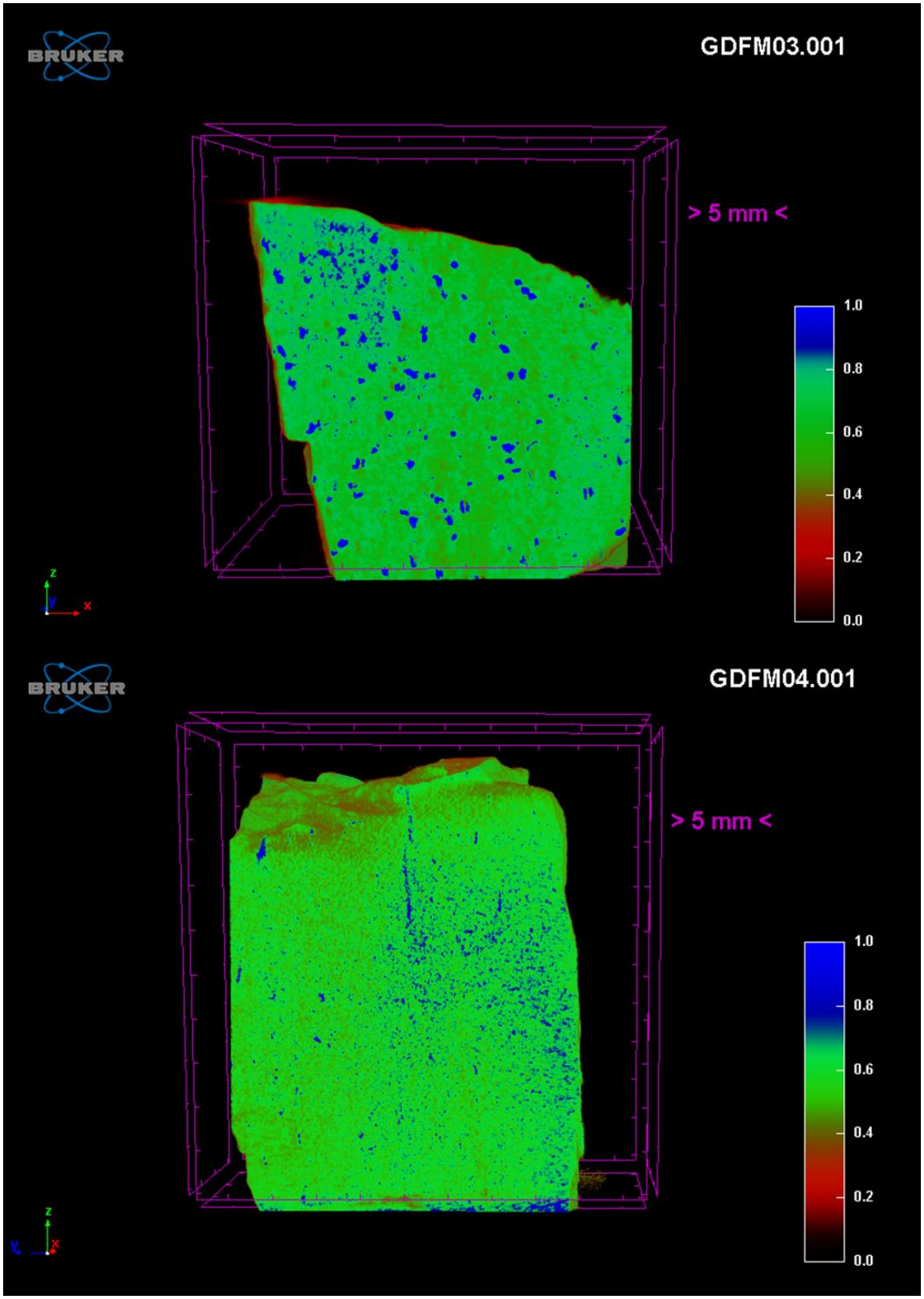

Fig. 8.2 | Sample micro-CT radiographs of two fossil dinosaur bone samples. Artificial color scale shows relative density in RGB, with blue as the highest density. Images courtesy of Tom Fildes (UoL).

a

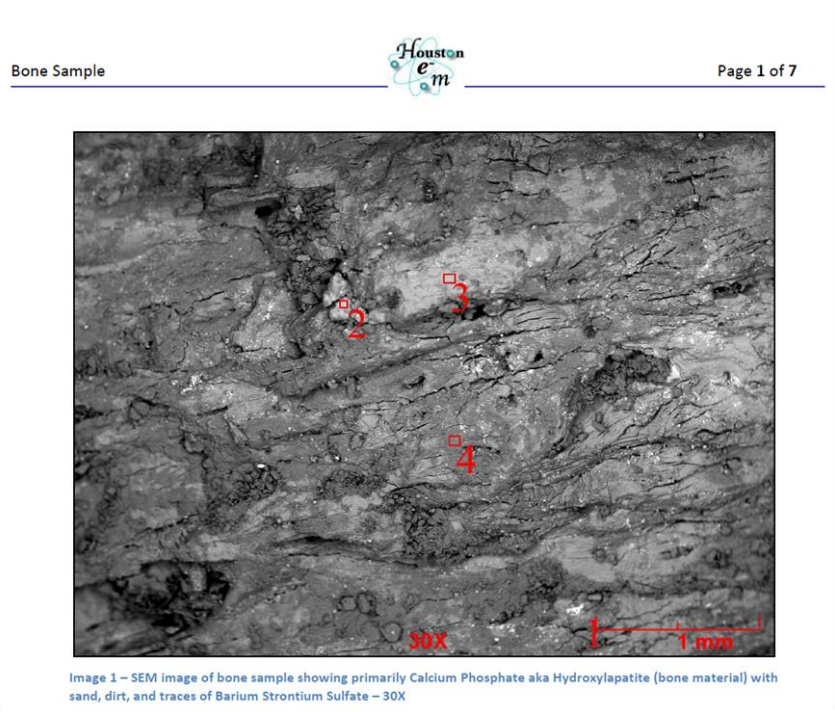

Image 1 – SEM image of bone sample showing primarily Calcium Phosphate aka Hydroxylapatite (bone material) with sand, dirt, and traces of Barium Strontium Sulfate – 30X

b

Table 1 – Semi-quantitative EDS analysis of bone sample and it's constituents shown above with significant elements highlighted; Wt. %

Spectrum	O	Al	Si	P	S	K	Ca	Fe	Sr	Ba
Overall	47.90	5.93	13.26	5.13	2.70	0.68	15.23	4.90		1.15
1 – Barium Strontium Sulfate	30.44	1.95			10.77	0.26	3.97	2.06	17.71	32.24
2 – Iron Oxide	19.36	3.18	6.10	1.87	0.58	0.24	3.48	61.96		
3 – Calcium Phosphate (Bone)	40.17	0.67	1.17	16.48	1.07		38.85	1.60		
4 – Al-Si Oxide (Silica)	45.80	11.05	27.37	1.49	0.40	1.32	4.36	6.12		

c

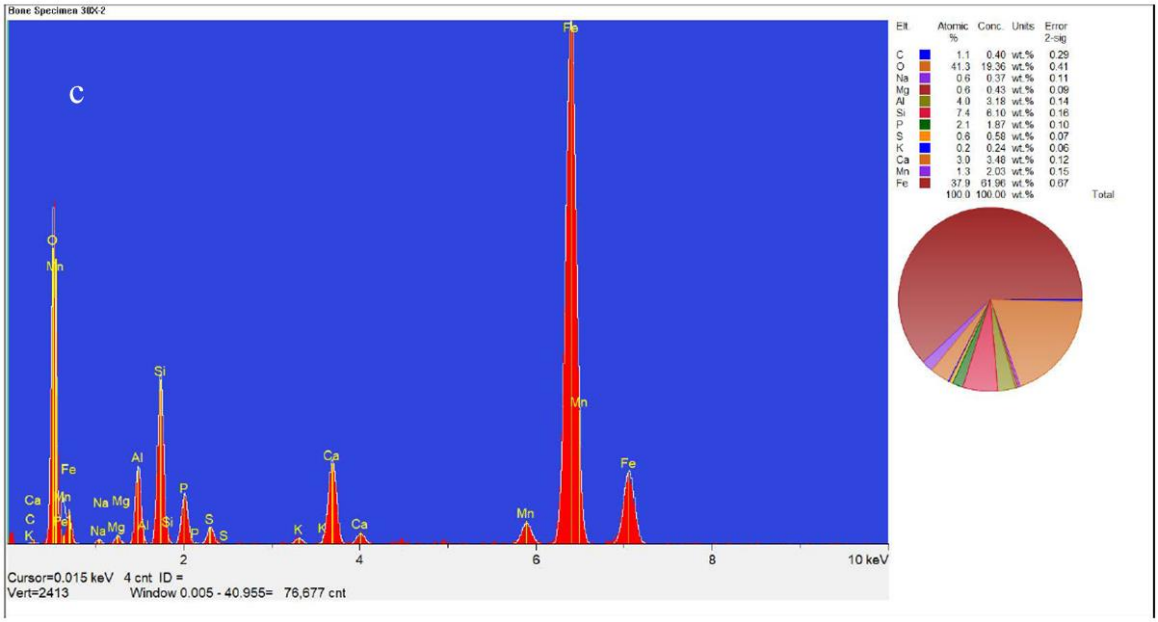

Fig. 8.3 | EDS results show elemental proportions consistent with biological bone on the surface of *Edmontosaurus* GDFM18.001. **a**, Scanning electron micrograph of fossil surface shows three still-biomineralised spots sampled by EDS **b**, Table of elemental constituents sampled from spots 2,3, and 4 in **a**. **c**, Sample fossil bone EDS spectrum. Results courtesy of Dan Biddle (Biddle Consulting Group).

Conclusion

Overall, the research results in this thesis verified rather than refuted the well-contended hypothesis that very ancient bone does indeed retain primary collagen. Further, the novel application of various techniques described herein, namely isotope analysis by AMS, infrared spectroscopy, and SHG imaging, were successfully applied to, and showed potential to reveal new information about, ancient bone collagen. Further development of portable QMS also promises to perform stable isotope analyses in the field. FTIR and SHG showed particular usefulness as technologies to quantify bone collagen decay and to provide information about the preservation of organics in medieval and Roman era bone collagen.

Appendix 8.1 | Papers, presentations, and posters

Journal papers:

Thomas, B., McIntosh, D., Fildes, T., Smith, L., Hargrave, F., Islam, M., Thompson, T., Layfield, R., Scott, D., Shaw, B. Burrell, C.L., Gonzalez, S., and Taylor, S. Second-harmonic generation imaging of collagen in ancient bone, *Bone Reports*, 7: 137-144 (2017).

Thomas, B., and Taylor, S. Second-Harmonic Generation Imaging of Medieval Human Bone. *Advances in Biotechnology and Microbiology*, 7(2): AIBM.MS.ID.555708 (2017).

Oral Presentations:

McIntosh, D., Giannoukos, S., Thomas, B., Fildes, T., Smith, L., Hargrave, F., Smith, B., Maher, S., and Taylor, S. Development of a Portable ^{13}C Isotope Ratio Measurement Technique with Quadrupole Mass Spectrometry. Presented on Wednesday, June 7, 2016. 65th ASMS Conference on Mass Spectrometry and Allied Topics, Indianapolis, IN., on behalf of the lead author. Abstract published in conference proceedings for access by ASMS members.

Thomas, B. Second-harmonic generation images reveal ancient bone collagen. Presented from 11:45-12:00, August 21, 2018. Ancient Proteins@20, Copenhagen, DK. Abstract online: [https://sites.google.com/palaeome.org/2018-ancient-proteins/programme/tuesday-21st-archaeology-programme/brian-thomas]

Poster:

Thomas, B. McIntosh, D., Clarey, T., and Taylor, S. Establishing a Baseline for a Portable Stable Carbon Isotope Detection System. Presented on Wednesday, June 8, 2015. 64th ASMS Conference on Mass Spectrometry and Allied Topics, San Antonio, TX. Extended abstract published in conference proceedings for access by ASMS members.

Conferences Attended:

11th HEMS Workshop. Harsh Environment Mass Spectrometry. September 18-21, 2017. Oxnard, CA.

SVP 75th Annual Meeting. Society of Vertebrate Paleontology. October 14-17, 2015. Dallas, TX.